An unstructured numerical method for computational aeroacoustics

PLEASE CITE THE PUBLISHED VERSION

PUBLISHER

© Lance O. Portas

PUBLISHER STATEMENT

REPOSITORY RECORD

Portas, Lance O.. 2015. "An Unstructured Numerical Method for Computational Aeroacoustics". figshare. https://hdl.handle.net/2134/16694.

An Unstructured Numerical Method for Computational Aeroacoustics

by

Lance O. Portas BSc MSc

A Doctoral Thesis

Submitted in partial fulfilment of the requirements for the award of
Doctor of Philosophy of Loughborough University
20 February 2009

Abstract

The successful application of Computational Aeroacoustics (CAA) requires high accuracy numerical schemes with good dissipation and dispersion characteristics. Unstructured meshes have a greater geometrical flexibility than existing high order structured mesh methods. This work investigates the suitability of unstructured mesh techniques by computing a two-dimensional linearised Euler problem with various discretisation schemes and different mesh types. The goal of the present work is the development of an unstructured numerical method with the high accuracy, low dissipation and low dispersion required to be an effective tool in the study of aeroacoustics. The suitability of the unstructured method is investigated using aeroacoustic test cases taken from CAA Benchmark Workshop proceedings. Comparisons are made with exact solutions and a high order structured method.

The higher order structured method was based upon a standard central differencing spatial discretisation. For the unstructured method a vertex-based data structure is employed. A median-dual control volume is used for the finite volume approximation with the option of using a Green-Gauss gradient approximation technique or a Least Squares approximation. The temporal discretisation used for both the structured and unstructured numerical methods is an explicit Runge-Kutta method with local time-stepping.

For the unstructured method, the gradient approximation technique is used to compute gradients at each vertex, these are then used to reconstruct the fluxes at the control volume faces. The unstructured mesh types used to evaluate the numerical method include semi-structured and purely unstructured triangular meshes. The semi-structured meshes were created directly from the associated structured mesh. The purely unstructured meshes were created using a commercial paving algorithm. The Least Squares method has the potential to allow high order reconstruction. Results show that a Weighted Least gradient approximation gives better solutions than unweighted and Green-Gauss gradient computation. The solutions are of acceptable accuracy on these problems with the absolute error of the unstructured method approaching that of a high order structured solution on an equivalent mesh for specific aeroacoustic scenarios.

Keywords: Computational Aeroacoustics, Unstructured Grids, Linearised Euler Equations, Finite-Volume Method, Weighted Least Squares, Green-Gauss, Benchmark Workshop Proceedings

The connection [between evolution and computers] lies in the counterintuitive observation that complex results arise from simple causes, iterated many times over. It's terribly simple to see this happening in a computer. Whatever complexities a computer produces - modeling wind turbulence, modeling economies or the way light dances in the eye of an imaginary dinosaur - it all grows out of simple lines of code that start with adding one and one, testing the result, and then doing it again. Being able to watch complexity blossom out of this primitive simplicity is one of the great marvels of our age, greater even than watching man walk on the moon.

Douglas Adams - October 2000

For my family

Acknowledgements

Firstly, I would like to thank Dr. Gary Page for giving me the opportunity to complete this research. I greatly appreciate his supervision and guidance and have thoroughly enjoyed my experience working for him. I am also grateful for the friendship he has shown me during my time studying abroad.

I would like to thank the people I worked with at Loughborough University, who helped me in many different ways at many different times. Many thanks to Indi Tristanto, who aided me in countless ways throughout my doctoral research. Thanks also to Lewis Balfour, Miles Trumper and Ioannis Veloudis who made the office an enjoyable and entertaining workplace.

Finally and perhaps most importantly I would like thank my family, especially my parents and my sister. My parents support, both financial and emotional, is one of the main reasons this work has been completed and without it, I never would have made it. Thanks also to my sister for her visits while I was away and her support throughout this endeavour, they made a world of difference.

Contents

List of Figures

List of Tables

Nomenclature

Latin Characters

a_0	non-dimensional speed of sound
a_1, a_2, a_2'	Least Squares gradient approximation coefficients
$A_{\Omega_{0'}}$	area of $\Omega_{0'}$ control volume
A_{Ω_0}	area of control volume Ω_0
d_0	number of vertices neighbouring vertex 0
e	internal energy of a fluid
E	total energy of a fluid
$\vec{f}$	vector form of body forces
f_x	body forces acting x direction
f_y	body forces acting y direction
F, G	linearised Euler equation flux term vectors
J_0	Bessel function of order 0
J_1	Bessel function of order 1
M_x	x component of mean velocity field
M_y	y component of mean velocity field
n_f	number of sides of polygonal control volume
n_G	number of Gaussian quadrature points
$n_{i\pm\frac{1}{2}}$	scaled normal vector
$n_{0i,1}, n_{0i,2}$	Green-Gauss gradient approximation edge segments
n_v	number of vertices compared for RMS error calculation
$\vec{n}_{0i}$	unit vector describing edge $0i$
$\vec{n}_{0i}$	Green-Gauss gradient approximation edge vector
NR	maximum number of mesh vertices in r direction
NT	maximum number of mesh vertices in θ direction

NX	maximum number of mesh vertices in x direction
NY	maximum number of mesh vertices in y direction
P	pressure variable
P	Least Squares gradient approximation weighting control term
P_0	initial magnitude of pressure field
$P(A)$	pressure variable associated with location A
$P(B)$	pressure variable associated with location B
$P(C)$	pressure variable associated with location C
q_1, q_2	Least Squares gradient approximation coefficients
$\dot{q}$	volumetric heat transfer of a fluid
Q	Least Squares gradient approximation formulation matrix
(r, θ)	cylindrical coordinates
r_ij	Least Squares gradient approximation coefficient
$\vec{r}_{0i}$	vector describing edge from vertex 0 to vertex i
R	Least Squares gradient approximation formulation matrix
$\text{Res}(W^{(i)})$	residual calculated using state vector $W^{(i)}$
RMS	root-mean-squared error value
S	linearised Euler source term vector
t	time variable
u	x component of velocity field $\vec{V}$
u_0	initial magnitude of velocity field
U_r	radial component of velocity field
U_θ	circumferential component of velocity field
v	y component of velocity field $\vec{V}$
V_{BC}	boundary vertex
V_{INT}, V_{INT2}	interior vertices associated with boundary vertex V_{BC}
V^*	virtual interior vertex associated with boundary vertex V_{BC}
$\vec{V}$	vector form of velocity field
w_{0i}	Gram-Schmidt decomposition terms for LS gradient approximation
w_j	quadrature weight factor
W	state variable vector
$W^{(i)}$	state vector at pseudo-timestep i
W^N	state vector at timestep N
W^{N+1}	state vector at timestep $N+1$
$\widetilde{W}$	finite volume gradient vector
$\widetilde{W}_{0i,L}$	reconstructed gradient vector at left endpoint of edge $0i$

$\widetilde{W}_{0i,R}$ reconstructed gradient vector at right endpoint of edge $0i$

$(\nabla W)_i$ gradient term calculated at vertex i

(x, y) Cartesian coordinates

Greek Characters

$\alpha_1 \ldots \alpha_4$ Runge-Kutta coefficients

Δ_i Barth-Jespersen limiting factor coefficient

Δs_{0i} length of control volume face $\partial \Omega_{0i}$

Δt Runge-Kutta time step

Δx mesh spacing in x direction

Δy mesh spacing in y direction

ϵ_0 number of edges of control volume 0

$\lambda(W)$ Barth-Jespersen limiting factor

ν_0 number of cells neighbouring vertex 0

ξ_{0i} Least Squares gradient approximation weighting factor

ρ density variable

ρ_0 initial magnitude of density

Φ function used to resolve flux approximation

Ω_0 control volume associated with vertex 0

$\Omega_{0'}$ control volume of all triangular cells surrounding vertex 0

$\partial \Omega_0$ surface of control volume Ω_0

$\partial \Omega_{0i}$ control volume face between Ω_0 and Ω_i

Subscripts, Superscripts and Overbars

$(.)_0$ mean flow variable component (for state variables ρ, u, v, and P)

$(.)'$ non-dimensional perturbation of state variable

$\widetilde{(.)}$ perturbation variable component

Acronyms

ACARE   Advisory Council for Aeronautics Research in Europe

ASD	Artificial Selective Damping
BC	Boundary Condition
CAA	Computational Aeroacoustics
DfT	Great Britain's Department for Transport
DG	Discontinuous Galerkin unstructured discretisation method
DRP	Dispersion-Relation-Preserving spatial discretisation method
EASA	European Aviation Safety Administration
FAA	Federal Aviation Authority of the United States
FE	Finite element discretisation method
GODRP	Grid-Optimized DRP spatial discretisation method
ICAO	International Civil Aviation Authority
ITRE	European Parliament's Committee on Industry, Research and Energy
IMM	Impedance-Mismatch Method boundary treatment
LDDRK	Low-Dispersion Low-Dissipation Runge-Kutta time discretisation method
NASA	National Aeronautics and Space Administration of the United States
PML	Perfectly Matching Layer boundary treatment
RK4	Standard Runge-Kutta 4-stage time discretisation method
SARP	Standards and Recommends Practices
SV	Spectral volume unstructured discretisation method
TVD	Total Variation Diminishing time stepping algorithm

Chapter 1

Introduction

The aerospace industry grows with each passing year. As it grows, the effect it has on the population, the economy and the environment grows as well. In the majority of industrialized countries there is a continual increase in airline traffic, air transport cargo and personal aircraft use. This increase has created the need for stricter guidelines on airport use as well as a more stringent design criteria for new aircraft. Current trends are forcing aircraft manufacturers to provide aircraft that have a longer range and a higher cruise speed, as well as aircraft that can carry greater numbers of people to more destinations in greater comfort. This trend has brought on the arrival of larger aircraft with engines that have increased power and fuel-efficiency. However the increase in power and efficiency of modern engines must be attained without an increased impact on the environment.

As the aircraft manufacturers work towards new designs to meet modern requirements the organisations in charge of regulating the industry constantly ensure that the criteria determined for the safety of passengers and the protection of the environment are met. The requirement of all aircraft to have certification from the industry regulators creates a situation where the demands of the aircraft operator are tempered with the demands of the safety agencies. This situation has created the need for a complex set of design tools and methods that can be used to evaluate current aircraft and develop new aircraft that fulfill the demands of performance while remaining within the design constraints set by both industry operators and regulators. One of the most important design constraints is that of noise associated with aircraft. Aircraft noise and engine pollution are the two factors that have the greatest impact on the environment and of the two, noise has been chosen as the purpose of this research. Noise emission

from aircraft is a closely studied topic in the aerospace industry. It is closely monitored by regulatory agencies and governmental departments and is a determining factor in whether or not an aircraft can enter service, or as noise regulations change whether an aircraft can continue service. The development of design tools to examine the generation and transmission of noise from aircraft is an important part of aircraft development. These design tools will have an important part in helping industry manufacturers meet the requirements of industry regulators.

1.1   The Structure of the Aerospace Industry

There are numerous regulatory agencies that have direct control over the use and required performance of aircraft and impact the entire aerospace industry. To better understand how the regulatory organisations work an explanation of how the aerospace industry is structured is required. The aerospace industry can be divided into two main sectors. The first is the aviation sector which deals solely with the operation of aircraft, and the second is the aeronautics sector which encompasses the study, design and manufacture of flight capable machines.

The aviation sector deals with two major categories of aircraft operation, the first for military aircraft and a second for civil aircraft. The civil aircraft category encompasses all scheduled air transport as well as all general aviation. Scheduled air transport refers to both passenger and cargo flights. General aviation refers to all non-scheduled passenger and cargo traffic, as well as business, hobby and personal air traffic. The largest sector of this industry is the scheduled air transport classification of civil aviation. This sector deals with the largest amount of traffic and therefore has the largest impact on the population and the environment. In more recent times, the general aviation field has also grown. As of the end of 2004, the United States alone has over 200,000 aircraft registered for use in general aviation as opposed to the 8000 aircraft registered for air carriers [54]. While the number of passengers is much greater with scheduled air transport the large number of aircraft associated with general aviation must also be considered when looking at the effect this industry has on the population and the environment. Since both scheduled air transport and general aviation are considered civil aviation, they are both regulated by the same industry standards.

1.2   The Regulation of the Aerospace Industry

The split of the aerospace industry into aeronautics research and aircraft operation is mirrored in the structure of industry regulators and it is important to understand how the operation of aircraft is regulated. Civil aviation has the greatest impact on population and the environment and therefore has the highest amount of certification and regulation. The International Civil Aviation Organization (ICAO), a specialised agency of the United Nations is concerned with maintaining the safety and regularity of international air transport for all countries associated with ICAO and deal with topics such as recognition and response to environmental concerns and the emergence of new technology [56]. Each nation also has its own Civil Aviation Authority that directly governs internal civil aviation and interacts with the ICAO. In the United Kingdom the Civil Aviation Authority is concerned with the regulation of all civil aviation within British borders. In the United States the Federal Aviation Administration (FAA) is responsible for regulation of civil aviation within American borders. In Europe, the European Aviation Safety Administration (EASA) is responsible for the certification of aircraft for use anywhere within the EU and determines the standards for design, manufacture, operation and maintenance of all civil aircraft as well as definition and application of technical requirements in regards to environmental impact for all aircraft [1].

These agencies have several concerns but one of the most important is that of the environmental impact of aviation, more specifically noise and pollution. The EASA states one of its main purposes as reducing environmental pollution and noise through the production of common rules for airworthiness within the EU [1]. In Great Britain the Department for Transport (DfT) also states that it plans to apply increasingly demanding technical standards to limit emissions and noise associated with aviation and wherever possible to see that aircraft emissions and noise are not only limited but decreased over time [25]. The ACARE has set a research target that by the year 2020 the perceived noise from aircraft should be reduced to half of what it is today [25]. Technical standards to limit civil aviation noise and engine emissions are also recommended by the ICAO. The ICAO noise standards are referred to by Chapter number. As of 2006, ICAO noise standard Chapter 4 has come into effect and will apply to all new aircraft types. It has an increased level of noise suppression as it requires new aircraft to be 10dB quieter than the previous Chapter 3 standard [53]. With the harsher guidelines set by agencies such as ICAO and ACARE require the use of design tools that focus on aircraft noise to ensure that the industry continues to grow in a controlled manner.

1.3 Industry Growth

Every year both the United Kingdom and the United States show an increase in airline passenger traffic and general aviation. National statistics from Great Britain show that in 2005, 228 million passengers went through UK airports as well as 2.4 million tonnes of air freight [26]. In the United States, 745 million passengers traveled through US airports and approximately 22,500 million lbs (10.3 million tonnes) of freight [55]. These statistics are reported as an increase over the previous year, and further investigation shows that there has been a steady increase in aviation traffic for decades. This trend is also predicted to continue. The Department for Transport predicts that by 2020 between 350 and 460 million passengers will use UK airports [25] and are planning accordingly. The DfT also predicts that freight loaded and unloaded at UK airports will double to over 5 million tonnes in the next 5 years [25]. Simply stated more people travel and transport goods on more planes each and every year. This increased traffic has a corresponding increase in environmental impact, for both noise and pollution.

1.4 Current Methods of Managing Aircraft Noise

Regulatory agencies such as ICAO and ACARE already have methods in place to deal with the Department for Transport and UK airports concerning the issue of managing aircraft noise. All of the ICAO member have already agreed to a four element approach that consists of reducing noise at the source (through aircraft certification), using noise abatement procedures for determination of flight path and taxi-way location, land use planning for the development of regions surrounding airports and operating restrictions that control the time of day certain aircraft are allowed operate within airport boundaries [53]. The Department for Transport is also supporting the ACARE research initiative into promoting development of low noise engine and airframe technologies [25]. The DfT has also required the removal of the noisiest and dirtiest aircraft from regular use and has adopted the use of economic incentives to encourage airport operators and airlines to use the best available technology to limit noise and engine emissions [25].

The most important approach of managing aircraft noise is the reduction of noise at the source, typically seen as developing and designing quieter aircraft. Most of the other management approaches are just dealing with the existing problem instead of examining the cause of it. The location of flight paths and control of takeoff and landing times are

useful attempts in dealing with the current situation, but as stated earlier, every year sees more planes completing more flights and creating more noise. The Department for Transport concedes that "today's aircraft are typically 75 percent quieter than jets in the 1960s" [25], but it also states that "action is needed to prevent a deterioration in the noise climate as growth in air traffic overtakes the rate of technological advance" [25]. There is no doubt as to the increase in air traffic. The requires that the aerospace industry must work to increase the level of technology when it comes to reduction of aircraft noise. In order to control the levels of noise created by aircraft, the sources and behaviour of the noise must first be understood. This means that perhaps the most important factor in reducing noise from aircraft is the determination of noise sources and the development of noise reduction techniques specific to particular noise sources.

1.5   Sources Of Noise

There are numerous sources of aircraft noise currently being studied in the development of acoustic technology. The work presented here is primarily interested in the noise sources of fixed-wing aircraft operating with turbofan engines. For fixed-wing aircraft noise-generating mechanisms can be separated into two general categories, mechanisms associated with the airframe and mechanisms associated with the engine. The engine noise sources are also separated into two subcategories, turbomachinery noise and jet noise.

The noise from the airframe is defined as "the noise generated by the aerodynamic flow interacting with the aircraft surfaces during flight" [59]. Possible sources of noise associated with the airframe include the main landing gear, the nose gear, the interaction between the gear and the flaps, the interaction between the jet and the flaps, the leading edge slats, the trailing edges and side edges of the flaps and the interaction between the wing and the flap [24, 59, 60]. The location of some noise source examples can be seen in Figure 1.1. Other sources of airframe noise include the wakes from the wing and the vertical and horizontal tail components [59]. The relative strength of airframe noise compared to engine noise is determined by flight speed, the aircraft geometry and the relative position of the aircraft components [60]. The airframe noise dominates the engine noise greatest during approach as the propulsion noise levels are lowest at this stage.

Examples of engine noise sources that can be classified as turbomachinery noise
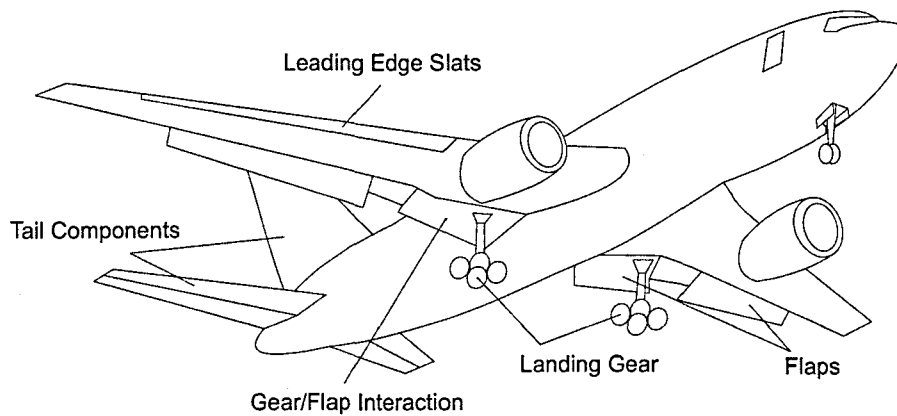
Figure 1.1: Examples of Airframe Noise Sources [60]

include turbine noise, combustion noise, and fan inlet noise. Similar to airframe noise, there are various noise generating mechanisms that have to do with the interaction of different components of turbomachinery. Engine noise sources include fan/outlet guide vane interaction, strut and pylon/fan interaction, booster/fan interaction and inflow/fan interaction. Noise is also generated from the fan and the outlet guide vanes, as well as the struts and pylons. Examples of noise sources that can be classified as jet noise include fan jet mixing, fan exhaust and the core jet [24, 59, 60]. The locations of the engines noise sources listed here can be seen in Figure 1.2. The relative dominance of the different components of engine noise are determined by engine bypass ratio. As the bypass ratio increases, the turbomachinery noise dominates over the jet noise [60].

There are noise sources, other than the standard airframe and aircraft engine components, that can have a significant contribution to the overall level of noise created. One such source is an auxiliary power unit (APU). APU systems have specific inlet and exhaust configurations due to the unit size and location on the aircraft that can create significant noise [31]. The fact that APU systems are often used on the ground near the terminal or hanger for extended periods of time without the plane in motion make them particularly noticeable to the public. Looking at different types of aircraft such as propeller or rotary-wing aircraft there are different noise creating mechanisms that may become more dominant that those with fixed-wing aircraft. With propeller aircraft, the important sources are free propeller noise and propeller/engine/airframe interaction in addition to the already present engine noise.

All of the examples of noise sources listed above can be separated into two different sound types. These two sound types are broadband noise and tone noise. Broadband
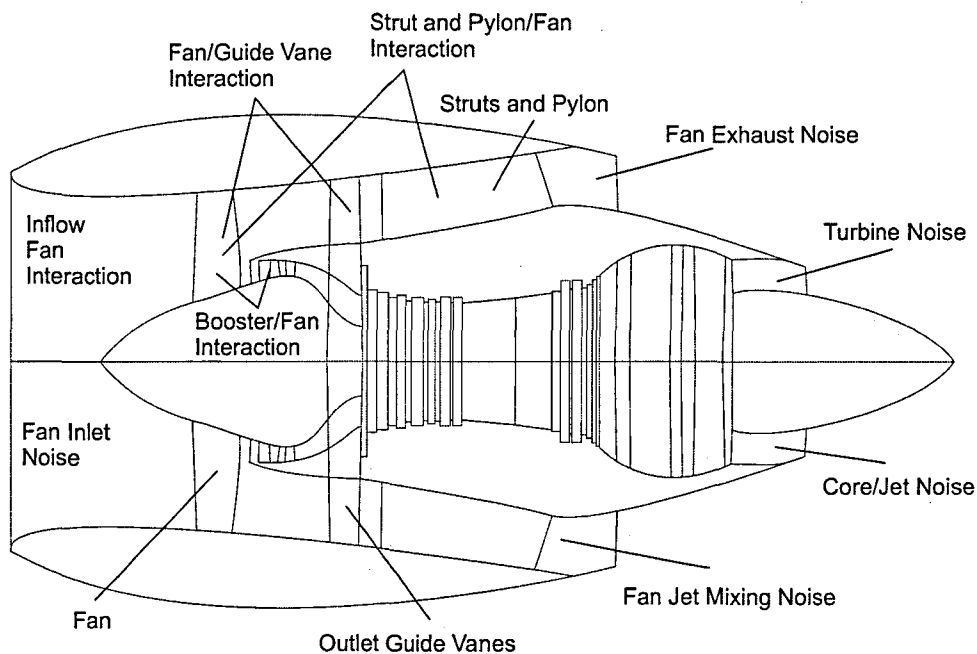
Figure 1.2: Examples of Engine Noise Sources [60]

noise has components over a wide range of frequencies. Tone noise has a discrete frequency or a very narrow range of frequency [19]. Sound sources that create broadband noise include the combustor and the jet as well as the interaction of the jet with the fan. The sources that can be listed as tone sources include those from the fan, compressor and turbine. Tone noise sources also include the stators, the pylons and the outlet guide vanes [24, 60]. The separation of noise sources due to frequency associated with the noise type creates the need for different approaches in noise reduction. Determining whether a noise source is mainly a tone noise or a broadband noise will also establish the best way to design some form of noise reduction.

1.6 Current Methods of Noise Reduction

Along with separation of noise types into broadband noise and tone noise, in order to develop methods of noise reduction it is also important to specify whether the noise is from an internal or an external source when determining a method of noise reduction. As stated previously, airframe noise sources such as flap/wing interaction, jet/flap interaction and gear, tail or other wing components are highly dependent upon two factors; the geometry of the airframe component and the relative position of the components

involved. The design of these two factors is therefore the best way to reduce noise. By designing airframe components specifically as noise sources instead of just aerodynamic or structural components, a great deal of external noise generation can be removed. This method has already been adopted in both experimental and computational research into new aircraft as well as evaluation of existing aircraft [23, 31, 59, 70].

Internal noise can generally be taken to mean engine noise. There are two approaches to suppressing internal engine noise. The first approach is to use basic design to minimise the amount of noise created and the second approach is to line interior surfaces of the engine with acoustically absorbent material [61]. Without any further investigation into exactly how engine noise is generated and behaves in a particular situation, there are a couple of design methods of dealing with noise sources that have been determined through past research and design modification. To minimize the amount of noise created a modification must "reduce the airflow disruption that causes the greatest amount of turbulence" [61]. There are several techniques used in engine design that accomplish this [61, 60]. The compressor wake intensity can be decreased by adjusting the spacing between the compressor blades and vanes. Also the ratio between rotating and stationary blades can be modified to contain noise within the engine. The noise created by the exhaust jet can be decreased as well by inducing a rapid or shorter mixing region. The introduction of deep corrugations or lobes into the the shape of the engine nozzle gives the greatest reductions in noise of these methods [61].

The use of acoustic liners in aircraft engines has proven extremely effective in reducing the amount of noise created by the engine without introducing large aerodynamic losses [19]. The acoustic liner is most often made up of a honeycomb-shaped material that is used to separate a perforated lining from a wall or other internal surface of the engine [19, 60, 61]. The combination of the porous material and the honeycomb layer creates a buffer that attenuates noise by capturing it before it impacts the wall of the engine and converting the acoustic energy into heat. The effectiveness of the honeycomb material that is used as an acoustic liner can be tailored to deal with specific noise sources. The specific depth of the honeycomb material is related to the frequency of the noise that is most absorbed by the acoustic lining, and the varying size and pattern of holes in the covering plate is related to the range of frequencies over which the acoustic lining absorbs sound [19].

The use of acoustic liners as well the optimization of how engine components interact with each other and how airframe components interact with each other have

certainly reduced the noise levels associated with aircraft. Nevertheless, with future industry guidelines concerning aircraft noise promising to be more strict there is a definite need for better noise reduction methods and a better understanding of both how the methods work and how noise behaves overall. Designers of modern aircraft are using computational aeroacoustics to gain this understanding. Aeroacoustics is the study of noise generated by aerodynamic forces interacting with surfaces and by turbulent fluid motion. Computational fluid dynamics (CFD) is a branch of fluid mechanics that deals with the numerical simulation of fluid flows. Computational aeroacoustics (CAA) is where CFD and aeroacoustics meet, it is the application of computer algorithms to numerically model aeroacoustic problems. The addition of CAA methods to the aeronautical design process is one of the main factors in how industry keeps up with international regulations when it comes to aviation noise.

1.7 Computational Aeroacoustics

The shift from experimental design and analysis of aircraft to computational design and analysis is a modern phenomenon. As computers have gotten faster and more powerful, the aeronautical industry has relied on them more and more as "key element[s] of design" [72]. Along with the increase in computing power, there has also been advances in numerical modeling. The ability to create a virtual model of an aircraft design (instead of a physical one) and accurately determine its aerodynamic and aeroacoustic characteristics has allowed for a greater understanding of not only how to design aircraft for specific purposes but of aerodynamics and aeroacoustics as well. Fabricating and testing scale models is expensive and the trial and error method of creating a single test model and running it through a series of tests doesn't always give the expected results [72]. CAA allows the "ability to assess change in noise due to change in geometry" [70] and give an important opportunity to "gain incites to the physics" [70] of aeroacoustics. The use of CAA allows for numerous configurations to be evaluated and for designs to be tailored to exactly match design requirements, such as aerodynamic performance, while staying within design constraints, such as noise generation.

The aeroacoustics branch of computational design is a relatively new addition to numerical modeling. A CAA model can be narrowly defined as the computation of the unsteady pressure at every location in the simulated field [49] and was generally a series of aeroacoustic calculations performed after the completion of an aerodynamic analysis. Previously there was a process to determine the aeroacoustic characteristics of a design.

First the component geometry was analyzed using CFD to determine the aerodynamic properties and then a noise model was applied to the CFD solution to ascertain the noise created from the component. With current CAA methods the aerodynamics and aeroacoustics are modeled together allowing for the change from CAA being a diagnostic tool to a design tool. Instead of needing a complete CFD solution to determine the aeroacoustic properties of a design, current CAA methods allow for the computation of acoustic waves directly. The direct computation of the acoustic properties allows the designer to observe how the acoustics and the aerodynamics develop together in a time-dependant simulation. There are however inherent difficulties in the simulation of acoustics. The acoustic phenomena studied with CAA can generally be categorized as pressure or velocity disturbances that have low magnitude and high frequency [62], characteristics that create difficulty with ordinary numerical modeling. Tam states that "the small magnitude of the acoustic disturbances... [are] usually smaller than the error incurred in the computation of the mean flow" [62]. This difficulty requires a specialized branch of computational methods specifically designed to deal with acoustic scenarios, namely computational aeroacoustics.

CAA numerical methods require high accuracy, low numerical dissipation and low numerical dispersion error in order to maintain the structure and resolution of the acoustic phenomena being modeled. The use of a higher-order accurate method allows for the approximation of more complex problems. The small magnitude and high frequency of acoustic disturbances can be easily lost in numerical simulations with low order accuracy. Dissipation error is vitally important in CAA because it dampens the already low magnitude of the acoustic disturbances. An example of the effect of dissipative error on a simple wave form can be seen in Figure 1.3. The velocity wave in plot (a) of Figure 1.3 has lost its well-defined shape in plot (b). A numerical method that is subject to a large amount of dissipation error may lose any trace of the acoustic phenomena it is modeling and be left with only a uniform velocity or pressure field. Sources of dispersive error are also of paramount concern. Dispersion is a phenomenon that causes the separation of a wave into components of varying frequency. Waves of different frequencies propagate at different phase velocities allowing oscillations to be superimposed on the previously smooth wave. The effect dispersion has on a simple waveform can be seen in Figure 1.4. The high frequency oscillations displayed in plot (b) of Figure 1.4 can easily overcome the acoustic disturbances being modeled allowing for the dispersive error to overshadow the acoustic phenomena. Any numerical method that is to be used effectively for CAA simulations must have the following specifications: high accuracy, low dissipation error
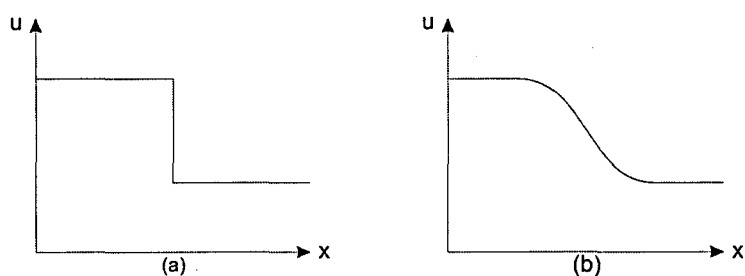
Figure 1.3: Effect of Numerical Dissipation [2]
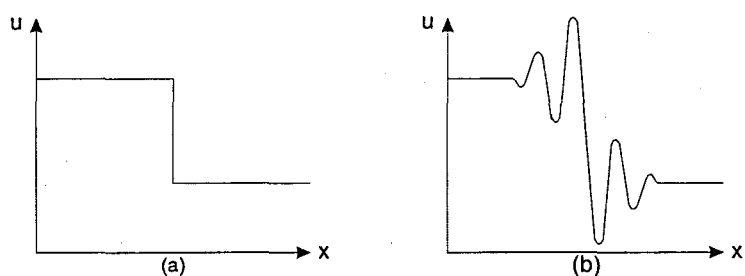
Figure 1.4: Effect of Numerical Dispersion [2]

and low dispersion error.

1.8   Current Numerical Methods Used For CAA

There are numerous methods currently being used for the investigation of computational
aeroacoustics. For the most part researchers employ structured methods in order to
have high enough accuracy to complete useful simulations. There are numerous types
of spatial and temporal discretisations employed with these methods. Few researchers
use unstructured methods because these methods often lack the high levels of accuracy
required for CAA problems. There are fewer types of discretisations either spatial
or temporal in use for unstructured methods. The unstructured portion of this field
has been left comparatively unexplored due to the lack of high order methods. The
structured methods often lack the ability to deal with complex geometries, and the
unstructured methods are often complex and computationally expensive. It is with
these facts in mind that the development of a new unstructured method is proposed.

1.8.1   Current Structured Methods Used For CAA

As stated previously, the majority of numerical methods used in Computational Aeroacoustics are developed for structured methods. Structured methods are used to maintain the high order of accuracy and low dispersion and dissipation characteristics needed to resolve acoustic phenomena. One of the best benefits of structured methods is the fact that the order of accuracy can often be raised merely by increasing the size of the stencil used by the discretisation approximation. This simple process of adding more neighbouring points to the calculation of derivatives and other terms is not as easily achieved with unstructured methods.

Spatial Discretisations

There are numerous types of spatial discretisation used by researchers in the field of acoustics, from simple low order methods to much more complex and higher order formulations. In some cases the use of a simple 2nd order accurate scheme, such as that employed by Djambazov and Pericleous [22] as well as Radvogin and Zaitsev [58] can be used with limited results. More often, however, a higher order approximation is required such as the 4th order accurate central-difference discretisation used by Nark [52]. Researchers typically opt for sixth-order accuracy or better and this high order accuracy is generally achieved by increasing the stencil size, such as with Tam's DRP method [68].

Another way to achieve high order accuracy, but without increasing the stencil is to use a compact scheme. Compact schemes use implicit factoring to increase the order of accuracy without increasing the stencil size. One example of a compact scheme is the 7-point Padé-type scheme used by Kim and Lee [46]. Another example is the 4th-order accurate compact scheme of Fung [27, 28]. Hayder et al. [36] use a 6th-order accurate compact scheme in far-field noise applications as well. Hixon [37] uses a 8th-order accurate compact scheme for his research which was formulated with inherent damping to deal with common errors associated with acoustic phenomena. This is an important addition to a compact scheme, as "compact difference schemes in general lack adequate numerical damping and filtering is often required to eliminate high frequency errors in the computational domain" [35]. Compact schemes have been shown to be quite useful in structured numerical methods, but the extension of the compact scheme onto unstructured meshes has it limitations. The work of Zingg and Lomax [74] as well as Tristanto [69] show that the compact schemes adapted for unstructured methods

suffer from a strong sensitivity to dispersion error and require equidistant neighbouring nodes as well as radial symmetry to guarantee accuracy. This makes the choice of compact schemes for aeroacoustics an unlikely one. The importance of having a low-dispersion numerical method in aeroacoustics has already been discussed and for this reason compact schemes are unsuitable.

Perhaps the most widely used higher order method is the Dispersion-Relation-Preserving (DRP) discretisation developed by Tam and Webb [68]. The DRP discretisation used a 7-point stencil to achieve sixth order accuracy and has been specifically tuned to have low dispersion error. The DRP method has been proven as an effective tool and numerous researchers have adopted it for the basis of their own aeroacoustic research, such as Zhuang and Chen [73], Chung and Morris [16], Hu et al. [44], Baysal et al. [10] and others. Other researchers have taken the DRP method as a starting point and adapted it for further applications. Cheong and Lee [14] have adapted the DRP scheme which was originally developed for uniform grids to the Grid-Optimized (GODRP) method which is designed for non-uniform and curvilinear meshes. Hixon et al. [38] also started with the DRP formulation but developed it into a MacCormack-type upwinding scheme maintaining a 4th-order accurate spatial discretisation. There is no doubt that the DRP method is a useful numerical method for aeroacoustics, but it is limited to use only on structured meshes and performs best on uniform unstructured meshes. It is not possible to take the structured DRP method and adapt it to unstructured meshes.

Taking the idea of increasing accuracy with an increased stencil size even further are spectral methods, a type of finite element method, some of which encompass 15 mesh points along each direction in the discretisation. These methods have been applied to CAA with success by researchers such as Bismuti and Kopriva [13], Hayder et al. [35] and Lin [47]. Bismuti and Kopriva use a Chebyshev spectral element approximation for the solution of CAA problems and Lin uses a Least Squares spectral element formulation. Hayder et al. use a spectral method to approximate derivatives normal to boundaries to improve dissipation characteristics. These spectral methods require very large stencils, but have extremely high-order accuracy. The spectral element methods are computationally expensive and numerically complex.

There is a gap in the research field between high-order structured methods and complex finite element methods and the investigation of this gap is the purpose of this present work, namely the development of a simple unstructured method that can

combine the functionality of unstructured meshes and the accuracy of the high-order structured methods.

Temporal Discretisations

There are not as many temporal discretisations being used for structured acoustic methods as the few that are used are quite effective. Many researchers use a standard Runge-Kutta time-stepping method. The Runge-Kutta method can be expanded similar to a Taylor series allowing for 3rd order (RK3) or even 4th order (RK4) accuracy. The increase in accuracy is accomplished with additional pseudo-timesteps and coefficient tuning. The RK3 temporal discretisation is employed by researchers such as Atkins [4], Radvogin and Zaitsev [58] and Lin [47]. The standard fourth-order RK4 temporal discretisation is used by many researchers, such as Morris et al. [50], Hayder et al. [36], Nark [52] and many others [13, 14, 46]. Tam and Webb [68] also developed a time-stepping algorithm to work directly with their DRP spatial discretisation. The low-dispersion, low-dissipation Runge-Kutta (LDDRK) temporal discretisation has optimized coefficients, transforming a standard Runge-Kutta scheme into one specifically designed to deal with acoustic phenomena. The combination of the DRP and LDDRK techniques creates a potent tool when dealing with aeroacoustics and are often utilized by other researchers. The LDDRK time-stepping algorithm is used by researchers such as Hu [44], Baysal et al. [10] and many others [37, 38, 63].

The standard and adapted RK timestepping methods are not the only temporal discretisations used in CAA. The compact scheme used by Fung [27, 28] employs an implicit time stepping algorithm. Djambazov and Pericleous use a semi-implicit 2nd-order accurate temporal discretisation as well.

Additional Treatments

For numerous applications the use of spatial and temporal discretisation methods is accompanied by some other treatment such as damping or a boundary treatment. Tam and Shen [63] use both the DRP/LDDRK formulation along with artificial selective damping (ASD) to deal with nonlinear acoustic pulses. The artificial damping terms are added to damp out short wave components while leaving the long wave components unaffected. Tam and Webb [68] also employ a damping of the physical waves to increase stability and allow for a larger time step when computing solutions to aeroacoustic

problems. Zhuang and Chen [73] use the DRP scheme with the addition of artificial viscosity terms to deal with spurious waveforms that are not controlled by the optimized discretisations. Chung and Morris [16] used the DRP/LDDRK method along with a special solid boundary treatment. Their Impedance-Mismatch Method (IMM) simulates a solid wall with a characteristic impedance that is set to a different value than the true wall, reflecting acoustic waves in-phase and acting like a true wall. As a general note, Colonius and Lele [17] state that "artificial dissipation that may be tolerable for hydrodynamic fluctuations can lead to unacceptable attenuation of acoustic waves" and since "acoustic radiation efficiency is invariably very low" numerical errors can upset the balance that is physically occurring within the acoustic field. One such example is mentioned is the acoustic cancellation process that accompanies the use of dipole or quadrupole sources [17]. The use of additional treatments, such as ASD or special boundary treatments must be carefully considered in aeroacoustic research as they may have unforeseen consequences in these specific situations.

One the most popular boundary treatments used for CAA problems is the Perfectly Matching Layer (PML) first developed by Berenger [11]. Berenger's PML technique was first developed for electro-magnetics, but was soon adapted for use with acoustic phenomena. Hu [40] was the first to apply the PML technique to aeroacoustics with success, and has since extended the use of PML methods from linear to nonlinear applications. One of the early requirements of the PML technique was that the variables needed to be split according to the spatial derivatives of the governing equations of the specified problem. Recently, Hu [41] has developed a new PML treatment where the splitting of the state variables is no longer necessary. The PML boundary treatment calls for the computational domain to be surrounded in an absorbing boundary layer. It is within this layer that the acoustic waves are damped out. One of the main benefits of the PML technique is that the interface between the internal domain and the PML domain does not reflect any waveforms, no matter what the frequency or angle of incidence.

Because of the complex nature of acoustic problems, there are many other numerical treatments that are used for CAA calculations. Examples include a domain decomposition strategy employed by Morris et al. [50] as part of the parallelization of their CAA algorithm. Hixon et al. [38] employ smoothing techniques to avoid problems with forcing functions and source terms. Kim and Lee [45] have developed an adaptive non-linear artificial dissipation model for dealing with complex acoustic phenomena. Nark [52] has developed a staggered mesh approach which allows for the tailoring of the flux cal-

culations at different grid points in the computational domain to better approximate how flow fields truly interact. There are other methods, both explicit and implicit that are used in CAA scenarios but the fact remains that these methods are all developed for structured meshes. The purpose of this present work is the investigation of unstructured methods. Further discussion of the various merits and consequences of using the discretisation and additional numerical treatments listed above can be found in the references, but these techniques remain unsuitable for unstructured applications.

1.8.2 The DRP/LDDRK Method

As stated previously one of the most popular and effective structured methods used for CAA approximations is the DRP/LDDRK method developed by Tam and Webb [63, 68]. For the simple reason that so many researchers choose the DRP/LDDRK method it was felt that a better explanation of what the algorithm entails was required. Since it is so widely used it is a useful reference in CAA research

To approximate the first derivative of a variable f at the kth node of a structured mesh a 7-point central differencing approximation can be written as defined by Tam and Webb as

$$\left(\frac{\partial f}{\partial x}\right)_k \simeq \frac{1}{\Delta x} \sum_{j=-3}^{3} a_j f_{k+j} \tag{1.1}$$

where Δx is the spacing of the mesh. If x is a continuous variable, the previous equation is a special case of the finite difference equation written as

$$\frac{\partial f}{\partial x}(x) \simeq \frac{1}{\Delta x} \sum_{j=-3}^{3} a_j f(x + j\Delta x) \tag{1.2}$$

To determine the Fourier wave number of the finite difference scheme, the Fourier transform of the previous equation is

$$i\alpha \tilde{f} \simeq \left(\frac{1}{\Delta x} \sum_{j=-3}^{3} a_j e^{ij\alpha\Delta x}\right) \tilde{f} \tag{1.3}$$

where $\sim$ refers to the Fourier transform and α is the Fourier wave number. Comparison

of the two sides of Equation 1.3 gives

$$\overline{\alpha} = \frac{-i}{\Delta x} \sum_{j=-3}^{3} a_j e^{ij\alpha\Delta x} \tag{1.4}$$

where $\overline{\alpha}$ is effectively the wave number of the finite difference scheme. Tam and Webb chose coefficients a_j so that the original derivative approximation of Equation 1.1 is accurate to $(\Delta x)^4$ when expanded in a Taylor series. The coefficients that remain are chosen according to the error defined by

$$E = \int_{-\eta}^{\eta} |\overline{\alpha}\Delta x - \alpha\Delta x|^2 \, d(\alpha\Delta x) \tag{1.5}$$

By choosing η so that $\overline{\alpha}$ is a close approximation of α over a wide band of wave numbers, the error E can be minimized. Tam and Shen [66] recommended $\eta=1.1$ giving the following coefficients:

$$
\begin{aligned}
a_0 &= 0 \qquad a_1 = \quad -a_{-1} \quad = 0.770882380518 \\
a_2 &= \quad -a_{-2} \quad = -0.166705904415 \\
a_3 &= \quad -a_{-3} \quad = 0.208431427703
\end{aligned}
\tag{1.6}
$$

which can be used along with Equation 1.1 as the DRP first derivative approximation.

Tam and Webb state the time discretisation of a variable f can be approximated using four levels as

$$f^{(n+1)} - f^{(n)} = \Delta t \sum_{j=0}^{3} b_j \left(\frac{\partial f}{\partial t}\right)^{(n-j)} \tag{1.7}$$

where the superscripts $(n+1),(n)$ etc. refer to the time level. The Laplace transform of Equation 1.7 with zero initial condition gives

$$-i \frac{i \left(e^{-iw\Delta t} - 1\right)}{\Delta t \sum_{j=0}^{3} b_j e^{ijw\Delta t}} \tilde{f} = \frac{\widetilde{df}}{dt} \tag{1.8}$$

where $\sim$ refers to the Laplace transform and w is the angular frequency . Tam and Webb state that the Laplace transform of the time derivative becomes $-iw\tilde{f}$. By comparing the two sides of the previous equation the effective angular frequency of the

time marching scheme $\overline{w}$ is defined by Tam and Webb as

$$\overline{w} = \frac{i\left(e^{-iw\Delta t} - 1\right)}{\Delta t \sum_{j=0}^{3} b_j e^{ijw\Delta t}} \tag{1.9}$$

The coefficients b_j were determined by Tam and Webb by requiring Equation 1.7 to be 2nd order accurate giving

$$
\begin{aligned}
b_0 &= 2.302558088838 \\
b_1 &= -2.491007599848 \\
b_2 &= 1.574340933182 \\
b_3 &= -0.385891422172
\end{aligned}
\tag{1.10}
$$

which can be used along with Equation 1.7 as the LDDRK time discretisation.

1.8.3   Current Unstructured Methods Used for CAA

Unstructured numerical methods are often overlooked when dealing with Computational Aeroacoustics as they often lack the required accuracy as well as the dispersion and dissipation characteristics needed to effectively deal with acoustic phenomena. There are numerous ways to adapt a structured method for aeroacoustics but there are few unstructured techniques that are available.

Spatial Discretisations

The most common spatial discretisation of an unstructured CAA method is the Discontinuous Galerkin (DG) method developed by Atkins and Shu [8]. The discontinuous Galerkin method has also been employed by Hu [43]. The DG method is similar to a standard finite element method in that instead of numerous nodes being employed to increase accuracy, fewer nodes are used with each node being described by a high-order polynomial. The DG method differs in that it is able to deal with basis functions that are discontinuous at cell interfaces. This allows for the application of the DG method in complex flows where shocks and other nonlinear flow phenomena are present. These methods are numerically complex in 2D and computationally expensive. The Atkins and Shu method contains a quadrature-free formulation that uses 5th order polynomials

to describe each of the elements within the domain.

One example of the few non-Galerkin unstructured methods is that of Wang [71]. The term non-Galerkin is used here to described a finite element method that does not require continuous basis functions. Wang developed a spectral volume (SV) method, which is related to the DG method and unstructured spectral method. Wang's SV method avoids the volume integral required in the DG method by introducing more interfaces where Riemann problems are solved. This is another example of the high level of complexity involved in the unstructured methods currently in use with CAA research.

All of these methods are numerically complex and computationally expensive. In the case of the DG method, for the simple benchmark test cases being investigated as part of this research the algorithm is too complex and computationally expensive - particularly in three dimensions. DG methods show great promise for CAA problems but as yet the computational cost is overly expensive for 2D and prohibitively expensive for possible 3D applications.

Temporal Discretisations

As with the structured numerical methods there are not very many different temporal discretisation techniques employed for CAA methods. The Atkins and Shu method contains a 3 stage TVD Runge-Kutta time stepping formulation [8]. The discontinuous method has also be employed by Atkins and Lockard [7] with a LDDRK time stepping algorithm in place of the TVD Runge-Kutta scheme.

Additional Treatments

Work done by Atkins [6] allows for a PML boundary treatment to be applied to deal with the acoustic waves. Hu and Atkins [42] employ a similar strategy to that of Hu except that instead of using a PML treatment Hu and Atkins use an exact characteristics split flux formula to separate the numerical wave modes into two forms. These two forms are the physically accurate mode and the spurious mode. The use of the split flux formula allows the spurious mode to become non-existent and allows for an accurate prediction of aeroacoustic flows. The application of unstructured methods to aeroacoustics is a difficult task. The requirements of high accuracy and control of dispersive and

dissipative error causes many researchers to remain using structured methods. Some researchers opt to use a commercial finite-element package [39] instead of developing their own method in an attempt to profit from the adaptability of an unstructured approach without having to deal with the common lower accuracy of a standard unstructured method.

1.8.4   The Discontinuous Galerkin Method

As discussed in the previous section, the discontinuous Galerkin method developed by Atkins and Shu is the most common unstructured method used for CAA applications. Since it is the most common approach for unstructured CAA problems further explanation of how it is implemented was warranted. This method is defined by Atkins and Shu [8] as being applicable to systems of first-order equations of the form

$$\frac{\partial U}{\partial t} + \nabla \cdot \vec{F}(U) = 0 \qquad (1.11)$$

defined on some domain Ω with a boundary $\partial\Omega$, where U refers to the velocity field made up of u, v components and $\vec{F}$ refers to fluxes $\vec{f_x}, \vec{f_y}$. The Ω domain can be expressed as a set of nonoverlapping elements Ω_i. Within each element Atkins and Shu solve the following equations:

$$\int_{\Omega_i} b_k \frac{\partial V_i}{\partial t} J_i d\Omega - \int_{\Omega_i} \nabla b_k \cdot \mathbf{J}_i^{-1} \vec{F_i}(V) J_i d\Omega + \int_{\partial\Omega_i} b_k \mathbf{J}_i^{-1} \vec{F}^R \cdot J_i \vec{ds} = 0 \qquad (1.12)$$

and

$$U \approx V_i = \sum_{j=1}^{N} v_{i,j} b_j \quad , \quad \mathbf{J}_i = \frac{\partial(x,y)}{\partial(\xi,\eta)} \quad , \quad J_i = |\mathbf{J}_i| \qquad (1.13)$$

for $k = 1, 2, \ldots, N$, b_k is defined as a set of basis functions, and N refers to the total number of nonoverlapping elements. Equations 1.12 and 1.13 are obtained by projecting Equation 1.11 onto each member of the basis set and then integrating by parts. Atkins and Shu define the basis set as the set of polynomials that are defined local to the element. The solution U is approximated as an expansion in terms of the basis functions; thus both V and $\vec{F}$ are discontinuous at the boundary between adjacent elements. The discontinuity is treated by Atkins and Shu with an approximate Riemann flux, which is denoted $\vec{F}^R$ in the above equation. The Jacobian of the transformation from global coordinates to elemental coordinates is defined as $\mathbf{J}_i$. In the usual implementation of the

DG method, the integrals are evaluated using quadrature formulas. In the quadrature free formulation of Atkins and Shu the integrals are reduced to a summation over the coefficients of the solution expansion. For the quadrature free approach, Atkins and Shu define the flux $\vec{F}$ to also be written as an expansion in terms of basis functions

$$\vec{F}(U) \approx \vec{G}(V_i) = \sum_{j=1}^{N} \vec{g}_j(V_i)b_j \qquad (1.14)$$

A similar expansion is required for the Riemann flux approximation. There are numerous other requirements involving the Jacobian and boundary integral terms which can be seen in [8].

1.8.5   Summary of Current CAA Methods

Computational Aeroacoustic problems are typically solved using numerical methods developed on structured Cartesian meshes. The most common of these methods is the DRP scheme of Tam and Webb [68]. The DRP scheme, along with the LDDRK time stepping formulation, is used time and again as the basis of CAA algorithms. Whether as the lone treatment for dealing with acoustic phenomena or as the discretisation method backed up by boundary treatments or numerical damping, the DRP/LDDRK combination has been used by many different researchers investigating aeroacoustics. The application of Berenger's electro-magnetic PML boundary treatments [11] onto aeroacoustic problems by Hu [40] is also a popular and effective choice. These methods, as well as the compact schemes and spectral element schemes, all have been employed successfully for CAA research but all have the same inherent flaw. They all require structured meshes and are therefore limited to simple geometries. The study of aeroacoustics has numerous applications in real life, almost all of them requiring the ability to deal with complex domains. The discontinuous Galerkin method of Atkins and Shu [8], the most prevalent unstructured CAA method, has the ability to deal with complex geometries but is numerically complex and computationally expensive. The DG method is used most frequently in these applications because it is the one exception to the typically low accuracy of unstructured methods.

Colonius and Lele [17] state that when solving problems of sound generation and propagation the numerical methods that are employed must be high-accuracy methods and suggest high-order accurate compact (Padé) and optimized finite difference and Runge-Kutta time marching schemes. They state that the particular care must be taken

when dealing with other known sources or error such as how the boundary conditions are imposed. Specifically they list that "careful attention must be accorded to issues of accuracy, artificial dissipation, non-reflecting and inflow/outflow BC and validation of results" [17]. Colonius and Lele stress that high fidelity methods, specifically DNS and LES schemes, should be chosen for roles in modeling the "flow physics and mechanisms of sound generation" citing "the importance of the resolving power of the discretisation as well as the computational efficiency of the overall scheme" [17].

In general, spectral and pseudo-spectral methods are very accurate and efficient for simple geometries and boundary conditions but lose effectiveness in complex geometries. The finite element and spectral element methods (such as DG methods) have been used by numerous researchers and show high accuracy as with high-order FD schemes but are more easily adapted to complex geometries with the use of complex unstructured meshes. The finite difference methods are most often used in CAA because they are easily extended to high-order accuracy but their greatest weakness is their reliance on structured grids. Each of the types of numerical methods have their strengths and weaknesses, but the basic trend is that greater accuracy can achieved at the cost of geometric complexity on one end of the spectrum, while at the other end solutions on a problem with an increasingly complex geometry are obtained with numerical methods that either have lower accuracy (as with standard unstructured methods) or are exceptionally complex and computationally expensive (as with the DG and FE methods).

The purpose of this research is to develop an unstructured numerical method that exists in the middle of these two extremes, a method that can handle complex geometries with an acceptable high order of accuracy high and low dispersion and dissipation error characteristics to be useful in the investigation of computational aeroacoustics.

1.9 Benchmark Workshops for CAA

As can be seen in the previous sections there are numerous methods currently employed by researchers in the field of aeroacoustics. When CAA was a relatively new branch of investigation a group of researchers devised a collection of benchmark problems to "address issues relevant to the acoustic propagation of sound generated by fluid flow" [33]. It was recognized that a collection of test cases focusing on the fundamentals of modeling aeroacoustics would allow for the validation of models that had been developed for CAA scenarios as well as the further development of better models for more complex

flows. The original Benchmark proceedings [33] were published in 1995 and included problems dealing with determining the numerical dispersion and dissipation properties of a computation scheme modeling linear waves. Other benchmark problems in the first proceedings included the propagation of a pressure pulse and vortex within an infinite domain as well as the simulation of a nonuniform mean flow within a semi-infinite duct. The primary focus of the original Benchmark Workshop was on numerical accuracy, especially relating to dissipation and dispersion. The Second Benchmark Workshop [64] was completed in 1997 and contained a series of more realistic benchmark problems such as the acoustic scattering from a cylinder or a sphere, sound propagation through and radiation from a finite length duct, gust interaction with a turbine cascade, and sound generation by a cylinder in uniform flow.

The Third CAA Workshop [20] was devised with the same emphasis in the second Workshop of computing acoustic problems that dealt with realistic scenarios. The main focus of the third Workshop was fan noise. The proceedings of the third CAA Workshop were published in 2000. For this series of test cases it was recognized that the complexity had increased so much as to warrant the comparison of the numerical approximations with well-documented experimental results. The benchmark problems from the third Workshop included modeling the propagation of sound through a narrow passage, the numerical approximation of the sound field generated by a rotor, the sound generation by the interaction of an airfoil with a vortical gust, modeling of rotor-stator interaction, the generation and radiation of acoustic waves from a 2-d shear layer, and an investigation into modeling automobile noise.

The proceedings of the Fourth Computational Aeroacoustics Workshop on Benchmark Problems [21] were published in 2004. The problems selected to be part of the fourth Workshop were also chosen to reflect realistic scenarios currently facing CAA researchers. These main focus of the Workshop included topics such as the issue of aliasing where spatial resolution errors affect the computation of sound, the interface condition problem, long-term stability and the accuracy of boundary treatments. Other test cases were chosen to highlight the ability of numerical methods to compute the sound interaction with surfaces which are geometrically complex, the approximation of sound generated by the interaction of airfoils and turbine cascades with vortical gusts, the simulation of sound transmitted through a turbulent shear layer, and the sound generated by viscous flows passing an object or cavity.

The main purpose of the research present within this dissertation is the development

of a simple unstructured numerical method to be used for aeroacoustics. The focus is on determining how this unstructured method deals with modeling basic acoustic phenomena. The numerical characteristics of the unstructured method are evaluated using benchmark problems taken from the first and second Benchmark Workshop proceedings. These less complex test cases were chosen as they provide a simple but direct test for determining how a numerical method deals with the accuracy required by an aeroacoustic approximation as well as the opportunity for dissipation and dispersion errors to render a method ineffective. The exact description of the benchmark problems chosen for the evaluation of the unstructured method are presented in the following chapters.

1.10 Objectives of Present Work

The aim of the current work is to develop a simple (i.e. non-Galerkin) unstructured numerical method that is accurate and adaptable enough to be used in place of a high-order structured method when solving CAA problems. It is required that the unstructured method has low dispersion and dissipation errors, and that the method does not show any mesh sensitivity

The objectives of the present work are:

1. To develop a 2-D linearised Euler structured method for the computation of solutions to CAA benchmark problems to provide baseline solution comparisons

2. To develop a basic unstructured method for the computation of solutions to CAA benchmark problems

3. To determine the best characteristics of the unstructured method by looking at the effects of:

    (a) gradient calculation methods

    (b) gradient reconstruction methods

    (c) mesh types

    (d) boundary conditions

4. To determine the best combination of the options listed above

5. To establish an approximate accuracy of the unstructured method

1.11   Outline of Thesis

The research presented here is contained within the following four chapters.

The general description of both the structured and unstructured numerical methods is contained within Chapter 2. The governing equations as well as the discretisations used in this research are described there as well. Also the various techniques (such as gradient calculation and reconstruction method) used to test the basic unstructured algorithm are included.

Chapter 3 includes the description of the first CAA Benchmark Workshop problem chosen to evaluate the unstructured method as well as the specified mesh requirements, initial conditions and boundary conditions. This chapter also contains a discussion of the results achieved by both the structured and unstructured methods for the specified problem. The various characteristics of the unstructured method are tested and compared to the structured method solution as well as the analytical one.

Chapter 4 contains the full description of the second CAA Benchmark Workshop test case as well as the results of the second series of calculations completed for this test case. The best combination of gradient approximation and reconstruction technique are taken from the previous chapter and used to test mesh dependency. The results are compared with both the structured calculation and solution taken from literature, as with the uniform mean flow problem.

The final chapter contains a summary of the results discovered in the previous chapters. These results are used to make conclusions about the objectives stated previously as well as generalisations about the effectiveness of the unstructured method. Chapter 5 also contains possible recommendations for future work.

Chapter 2

Numerical Method

2.1 Introduction

In the process of designing the unstructured method presented in this research, two separate sets of calculations were completed to ensure that an accurate and robust method was developed. Two different aeroacoustic benchmark problems have been chosen from literature [33, 64]. These problems are specifically devised to include aeroacoustic phenomena that an unstructured method must be able to simulate with a high level of accuracy. These phenomena include the expansion and convection of pressure waves, the convection of vortices and the interaction of pressure waves on solid surfaces. The aeroacoustic problems involve the approximation of a solution to the two-dimensional linearised Euler equations of the general form

$$\frac{\partial W}{\partial t} + \frac{\partial F}{\partial x} + \frac{\partial G}{\partial y} = S \tag{2.1}$$

2.2 The Linearised Euler Equations

The Euler equations describe the inviscid compressible flow of a fluid. They are used when neglecting the effects of viscosity as well as mass diffusion and thermal conductivity [2]. In two dimensions the Euler equations can be written as a group of four separate equations representing the conservation of mass, momentum (in each of the two dimensions) and energy. When written in Cartesian coordinates and in partial differential

form, the conservation of mass equation, also known as the continuity equation, is

$$\frac{\partial \rho}{\partial t} + \nabla \cdot (\rho \vec{V}) = 0 \tag{2.2}$$

where ρ represents the density of the fluid and $\vec{V}$ represents the velocity field.

The conservation of momentum in the x direction is written as

$$\frac{\partial (\rho u)}{\partial t} + \nabla \cdot \left(\rho u \vec{V} \right) = \frac{-\partial P}{\partial x} + \rho f_x \tag{2.3}$$

where u is the component of the velocity field $\vec{V}$ in the x direction, P represents the pressure field of the fluid and f_x represents body forces on the fluid in the x direction.

The conservation of momentum in the y direction is written as

$$\frac{\partial (\rho v)}{\partial t} + \nabla \cdot \left(\rho v \vec{V} \right) = \frac{-\partial P}{\partial y} + \rho f_y \tag{2.4}$$

where f_y represents body forces on the fluid in the y direction. The f_x and f_y vector components of the body forces in the previous two equations can also be written in a combined form of $\vec{f}$.

The conservation of energy equation can be written as

$$\frac{\partial}{\partial t} \left[\rho \left(e + \frac{V^2}{2} \right) \right] + \nabla \cdot \left[\rho \left(e + \frac{V^2}{2} \right) \vec{V} \right] = \rho \dot{q} - \frac{\partial u P}{\partial x} - \frac{\partial v P}{\partial y} + \rho \vec{f} \cdot \vec{V} \tag{2.5}$$

where e is the internal energy of the fluid, $\frac{V^2}{2}$ is the kinetic energy of the fluid, and $\dot{q}$ represents the volumetric heat transfer.

The total energy E of the fluid can be expressed as the combination of the internal as well as the kinetic energy, or

$$E = e + \frac{V^2}{2} \tag{2.6}$$

By neglecting any volumetric heat transfer and all external body forces, the 2-D Euler equations can be written in conservation vector form as

$$\frac{\partial W}{\partial t} + \frac{\partial F}{\partial x} + \frac{\partial G}{\partial y} = 0 \tag{2.7}$$

with

$$
W = \begin{bmatrix} \rho \\ \rho u \\ \rho v \\ E \end{bmatrix} , \; F = \begin{bmatrix} \rho u \\ P + \rho u^2 \\ \rho u v \\ u(E + \frac{P}{\rho}) \end{bmatrix} , \; G = \begin{bmatrix} \rho v \\ \rho u v \\ P + \rho v^2 \\ v(E + \frac{P}{\rho}) \end{bmatrix} \tag{2.8}
$$

The equations can be modified to describe small amplitude disturbances superimposed on a uniform mean flow [68]. The energy of the fluid can be expressed as a function of pressure and density, or $e = e(P, \rho)$, so that the linearised Euler equations which describe the disturbance are written as

$$
\frac{\partial \widetilde{W}}{\partial t} + \frac{\partial \widetilde{F}}{\partial x} + \frac{\partial \widetilde{G}}{\partial y} = 0 \tag{2.9}
$$

with

$$
\widetilde{W} = \begin{bmatrix} \tilde{\rho} \\ \tilde{u} \\ \tilde{v} \\ \tilde{P} \end{bmatrix} , \; \widetilde{F} = \begin{bmatrix} \rho_0 \tilde{u} + \tilde{\rho} u_0 \\ u_o \tilde{u} + \frac{\tilde{P}}{\rho_0} \\ u_0 \tilde{v} \\ u_0 \tilde{P} + \gamma P_0 \tilde{u} \end{bmatrix} , \; \widetilde{G} = \begin{bmatrix} \rho_0 \tilde{v} + \tilde{\rho} v_0 \\ v_0 \tilde{u} \\ \frac{\tilde{P}}{\rho_0} + v_0 \tilde{v} \\ v_0 \tilde{P} + \gamma P_0 \tilde{v} \end{bmatrix} \tag{2.10}
$$

where ρ_0 is the magnitude of the initial density field, P_0 is the magnitude of the initial pressure field and u_0 is the magnitude of the uniform mean flow. The '~' superscript describes the small amplitude disturbances in each of the state variables. The state variables can be constructed with the initial mean flow component and the small amplitude perturbation component in the form

$$
\rho = \rho_0 + \tilde{\rho} \tag{2.11}
$$

for density but similarly for u and v velocities and pressure P. The '0' subscript and '~' refer to the mean flow component and the disturbance component, respectively. The equations in 2.10 can be non-dimensionalised using a velocity scale of a_0, a density scale of ρ_0, and a pressure scale of $\rho_0 a_0^2$ to become

$$
\frac{\partial W'}{\partial t} + \frac{\partial F'}{\partial x} + \frac{\partial G'}{\partial y} = 0 \tag{2.12}
$$

where

$$W' = \begin{bmatrix} \rho' \\ u' \\ v' \\ P' \end{bmatrix} , F' = \begin{bmatrix} u' + M_x\rho' \\ M_yu' + P' \\ M_xv' \\ M_xP' + u' \end{bmatrix} , G' = \begin{bmatrix} M_y\rho' + v' \\ M_yu' \\ M_yv' + P' \\ M_yP' + v' \end{bmatrix} \tag{2.13}$$

where $M_x = \frac{u_0}{\rho_0}$, $M_y = \frac{v_0}{\rho_0}$, and $a_0 = 1$. The 'prime' notation refers to the variables as being dimensionless variables. For simplicity the 'prime' superscripts are dropped and the governing equations are defined as describing the non-dimensional perturbations of the state variables for the remainder of the discussion.

These governing equations represent a two-dimensional flow field, i.e. one that is not parallel to the x-axis. The two-dimensional velocity field can be represented by the terms M_x and M_y which refer to the x and y components respectively. The simplified form of the linearised Euler equations used as the basis of this research can be written as

$$W = \begin{bmatrix} \rho \\ u \\ v \\ P \end{bmatrix} , F = \begin{bmatrix} u + M_x\rho \\ M_xu + P \\ M_xv \\ M_xP + u \end{bmatrix} , G = \begin{bmatrix} M_y\rho + v \\ M_yu \\ M_yv + P \\ M_yP + v \end{bmatrix} \tag{2.14}$$

This form of the linearised Euler equations provide the basis of the two types of test case problems investigated as part of this research.

For each of the specified problems, a structured numerical method is used to complete a calculation that will later be compared with unstructured calculations to determine how accurate the unstructured method is. The structured methods use standard central-differencing spatial approximations, and a basic Runge-Kutta time discretisation. The structured methods also have simple boundary conditions.

Once the structured calculation was completed, the unstructured method was tested with different gradient approximation techniques and different quadrature formulations. The unstructured method also used three different meshes to complete a series of calculations. Once all of the unstructured calculations were completed, all of the different combinations were compared against analytical or published solutions as well as the structured calculation. This process allowed the most accurate choice of gradient approximation technique, quadrature formulation and mesh type to be chosen to make

the unstructured numerical method. The completion of a structured calculation, which has a specific order of accuracy, allows for the determination of the approximate order of accuracy of the unstructured method.

2.3 Structured Numerical Method

The structured numerical method developed for the two different benchmark problems both use a finite-difference approximation to solve the governing partial differential equation with the option to use either a sixth-order accurate central-difference formulation or a fourth-order accurate central-difference formulation. The two different problems investigated also use two different structured meshes, the uniform mean flow problem uses an H-type mesh while the scattering problem uses an O-type mesh. The two problems use similar adaptive stencils to maintain accuracy near boundaries as well. The adaptive stencils change from a standard central-differencing formulation to one with more interior points as the calculation point nears a boundary.

2.3.1 Spatial Discretisation

The standard sixth-order central-difference approximation used to solve the governing PDE was derived from Taylor series expansion [2] for use on uniform meshes. The partial derivative $\frac{\partial F}{\partial x}$ of the governing equation at any point on the numerical grid (i, j) is represented by a finite difference approximation that is sixth-order accurate by employing data from six neighbouring grid points in the following form:

$$\left.\frac{\partial F}{\partial x}\right|_{i,j} = \frac{F_{i+3,j} - 9F_{i+2,j} + 45F_{i,j} - 45F_{i-1,j} + 9F_{i-2,j} - F_{i-3,j}}{60\Delta x} \qquad (2.15)$$

where $i + 1, 2, 3$ refers to the mesh points to the right of the calculation point (i, j) and $i - 1, 2, 3$ refers to the mesh points to the left of (i, j).

The standard fourth-order central-difference approximation employs four mesh points in the following form

$$\left.\frac{\partial F}{\partial x}\right|_{i,j} = \frac{F_{i-2,j} - 8F_{i-1,j} + 8F_{i+1,j} - F_{i+2,j}}{12\Delta x} \qquad (2.16)$$

Although the derivative approximations described above are all expressed with the

variable F changing in the x direction (i.e. the stencil encompasses various i locations for a particular j) the same stencils can be used to calculate the derivative of variable G in the y direction by using various j locations for a particular i.

2.3.2   Temporal Discretisation

The time discretisation used in the structured method involves a basic Runge-Kutta four stage method (RK4). The standard RK4 scheme, which uses the current time step (W^N) to calculate the next time step (W^{N+1}), is written as:

$$
\begin{aligned}
W^{(0)} &= W^N \\
W^{(1)} &= W^{(0)} + \alpha_1 \cdot \Delta t \cdot \text{Res}(W^{(0)}) \\
W^{(2)} &= W^{(0)} + \alpha_2 \cdot \Delta t \cdot \text{Res}(W^{(1)}) \\
W^{(3)} &= W^{(0)} + \alpha_3 \cdot \Delta t \cdot \text{Res}(W^{(2)}) \\
W^{(4)} &= W^{(0)} + \alpha_4 \cdot \Delta t \cdot \text{Res}(W^{(3)}) \\
W^{N+1} &= W^{(4)}
\end{aligned}
\tag{2.17}
$$

where the superscripts (0),(1),... refer to pseudo-time steps, the α_i terms refer to the Runge-Kutta coefficients, Δt refers to the computational time step and $\text{Res}(W^{(i)})$ refers to the residuals calculated at each pseudo-time step. The residuals are the finite difference approximations of the flux terms of the governing equations, i.e. the $\frac{\partial F}{\partial x}$ and $\frac{\partial G}{\partial y}$ terms. The RK-4 coefficients are tuned to give fourth order temporal accuracy and are specified as

$$
\alpha_1 = \frac{1}{4}, \ \alpha_2 = \frac{1}{3}, \ \alpha_3 = \frac{1}{2}, \ \alpha_4 = 1
\tag{2.18}
$$

2.3.3   Mesh Specification

Uniform Mean Flow Problem

For the first Benchmark problem, the specified problem domain encompasses a region from $x = -100$ to $x = 100$ and from $y = -100$ to $y = 100$. The grid spacing throughout the entire domain has Δx and Δy equal to one, creating a uniform grid of 40,000 cells. The specified domain is extended a further ten grid cells in all directions to
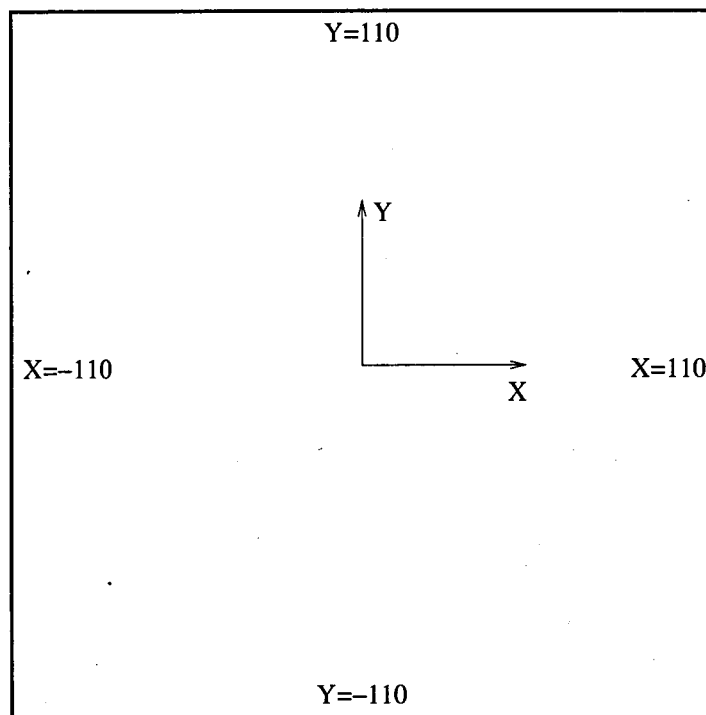
Figure 2.1: Specifications of Structured Mesh for Uniform Mean Flow Problem

ensure that neither the pressure pulse nor the vortex have any interaction with the boundary treatments. The new computational domain ranges from $x = [-110, 110]$ and $y = [-110, 110]$, although only the specified domain will be examined. A schematic of the mesh used to calculate solutions using the structured numerical method can be seen in Figure 2.1. The addition of an extended computational domain increased the number of cells in the structured mesh from 40,000 to 48,400 cells. The mesh is also defined as being NX by NY nodes (221×221), where the i and j indices begin at the lower left (x, y)=(-110,-110) corner. The NX and NY terms refer to the number of computational nodes in the x and y directions respectively.

Scattering Problem

The specified domain of the second Benchmark problem, the scattering problem, is described by a circular mesh with a diameter of 30 units (30 cylinder diameters). The entire cylinder is surrounded by continuous mesh which is divided into 600 equal circumferential segments and 290 equal radial segments. This creates a basic mesh with 174,000 cells. A schematic of the mesh used for the structured calculations can be seen in Figure 2.2.
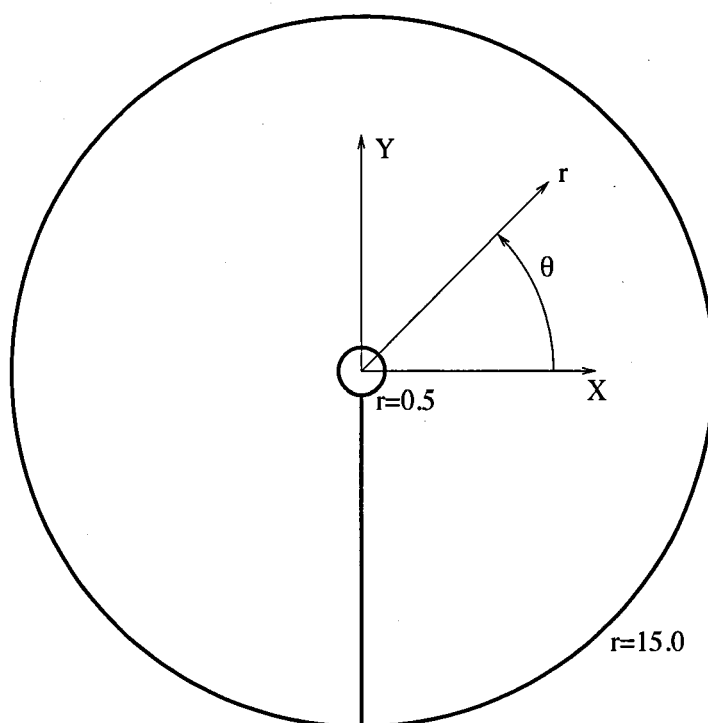
Figure 2.2: Specifications of Structured Mesh for Scattering Problem

The structured mesh also contains a cut along the line $x = 0$ from $y = -0.5$ to $y = -15$, or along $\theta = 270^o$. Along this cut, the continuity of the method is enforced with a periodic boundary condition using two phantom cells on each boundary to match the fourth-order accurate spatial discretisation. Phantom cells are non-physical cells that are added to the numerical mesh as a location to hold data that occurs across a periodic boundary but is required as part of the spatial discretisation. The specific location and use of phantom cells for this application is discussed below with the rest of the boundary treatments. For the application of the outflow boundary condition no phantom cell is included at the outer boundary, instead the condition is enforced on the

boundary vertex directly. Similarly, for the application of the solid boundary condition the no-flow condition is also enforced directly on the cylinder surface. The inclusion of the four periodic boundary cells creates a computational mesh of 175,160 cells (290 cells by 604 cells). The scattering problem mesh is also defined as being NR by NT nodes (291×605), where the i index begins at $r = 0.5$ and the j index begins at the left most boundary of the two phantom cells at $\theta = 270^{o}$. The NR and NT terms refer to the number of computational nodes in the radial and circumferential directions respectively.

2.3.4 Boundary Condition Implementation

Uniform Mean Flow Problem

The uniform mean flow problem has very simple outflow boundary conditions requiring a zero gradient for all of the state variables at the boundary. These conditions are applied directly on the external boundaries of the computational domain using a simple first-order gradient approximation. These boundary conditions can also be applied in a similar fashion for the upper and lower outflow boundaries using the same first order approximation.

Scattering Problem

The Benchmark Proceedings specifies only two boundary conditions for the scattering problem but because of the use of an O-type mesh, a third boundary condition is required. The two specified BCs are for the outflow boundary and the solid cylinder at the center of the mesh. The third boundary condition required is a periodic boundary condition to deal with the cut in the mesh below the cylinder.

Solid Boundary Condition   The outflow boundary conditions for the scattering problem require that the pressure gradient normal to the cylinder is equal to zero and that there is no radial component of the velocity field. As with the outflow boundary conditions of the uniform mean flow problem, these conditions are applied directly on the boundary vertex of the computational mesh. The pressure gradient is approximated using a simple first-order formulation and the radial velocity boundary condition is applied by explicitly setting the variable equal to zero at the boundary.

Outflow Boundary Condition The outflow boundary condition for the scattering problem requires the gradient of all three of the state variables to be equal to zero at the outer boundary. This boundary condition is applied in the same way as all the previous treatments, with a first-order approximation formulated using the last two vertices along each radial mesh line.

Periodic Boundary Condition The periodic boundary condition is used to maintain continuity in the mesh where an overlap exists. Two phantom cells are used on each end of the mesh for the entire radius, creating a seamless link and allowing information to pass through without any errors. The two cells are used to ensure that the fourth order accurate spatial discretisation is able to be used from one edge of the mesh to the other, without effecting the accuracy of the approximation. A schematic of the periodic boundary condition can be seen in Figure 2.3. where J refers to the vertex index and
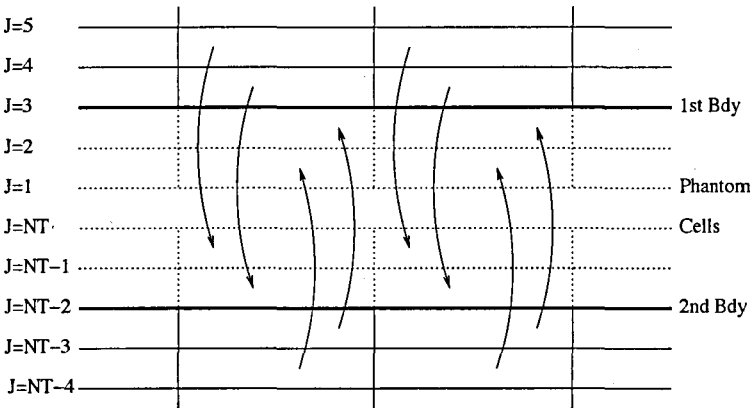
Figure 2.3: Schematic of Periodic Boundary Condition

NT refers to the total number of vertices along the circumference of the mesh. The first and second boundaries shown in Figure 2.3 actually lie one on top of the other, so that every time step the information from the cells bordering the first boundary are placed into the corresponding phantom cells bordering the second boundary, and vice versa.

2.3.5 Maintaining Accuracy of the Spatial Discretisation

As the location where the residual component is calculated nears the boundary, the number of mesh points available away from the center of the domain decreases and the approximation stencil needs to be adjusted. To maintain the accuracy used for

the calculation, seven mesh points are continually needed for sixth-order accuracy and five mesh points are needed for fourth-order accuracy. As the calculation point nears the boundary the stencil no longer has the correct number of mesh points available to use central-differencing. To maintain accuracy, the central-differencing approximation is replaced with an equivalent approximation that has more mesh points towards the interior of the domain. In this manner, the correct number of data points can always be used to determine the approximation of the gradients and the different combinations of coefficients allow for the calculation point to progress towards the boundary normally. A diagram of the different boundary treatments used for the structured method can be seen in Figures 2.4 and 2.5. For these figures the successive lines represent different stencil locations. The solid line represents the boundary of the computational domain, and the dashed lines represent the interior cells. The circular dots represent mesh point used to determine the residual terms around the calculation point, which is represented with the square.

In Figure 2.6, it can be seen that the periodic boundary treatment allows the fourth-order central-difference stencil to be used without adjustment up to the boundary. In this figure, the dotted line represents the phantom or boundary cells and the other lines represent the same mesh cells as with Figures 2.4 and 2.5. Since two phantom cells exist outside the boundary, the stencil does not need to be adjusted. The periodic boundary treatment can be used to determine the value of the data stored at the phantom cells.

Figures 2.4 and 2.5 show how different stencils are required to maintain accuracy as the calculation point nears the boundary, a treatment that is used on all of the boundaries in the uniform mean flow problem, and the inner and outer boundaries of the scattering problem.

Uniform Mean Flow Problem

In Figure 2.4 the impact of the calculation point nearing the boundary can be seen and its effect on the arrangement of the surrounding six data points used to maintain accuracy. The sixth-order stencil needs to be adjusted from a three-ahead three-behind format, to a six-behind format. The three-ahead three-behind stencil can be seen on the top line in Figure 2.4. The different stencils required as the calculation point nears the boundary can be seen on the successive mesh lines of Figure 2.4, ending with the calculation point on the boundary, and the stencil requiring the six preceding (six-behind) mesh points for accuracy.
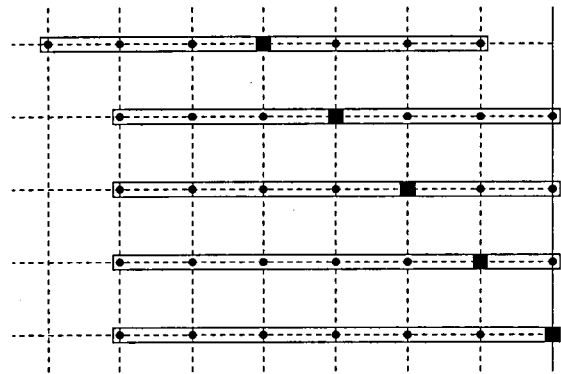
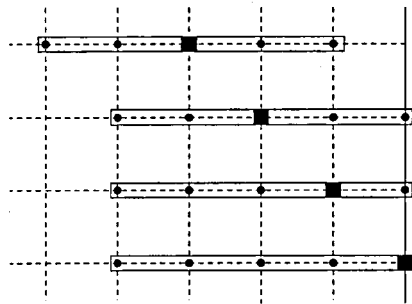Figure 2.4: Sixth-Order Accurate Stencil Schematic

Figure 2.5: Fourth-Order Accurate Stencil Schematic
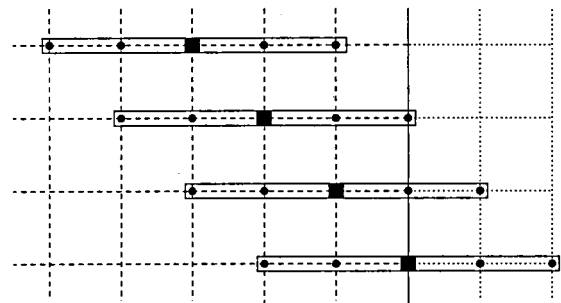
Figure 2.6: Periodic Boundary Stencil

The three different sixth-order stencils used as the calculation point nears the right and upper (maximum value of i) boundaries are determined from further expansion of the Taylor series used for the central-difference approximation [2]. These stencils are written as

$$\frac{\partial F}{\partial x}\bigg|_{i,j} = \frac{F_{i-4,j} - 8F_{i-3,j} + 30F_{i-2,j} - 80F_{i-1,j} + 35F_{i,j} + 24F_{i+1,j} - 2F_{i+2,j}}{60\Delta x} \tag{2.19}$$

$$\frac{\partial F}{\partial x}\bigg|_{i,j} = \frac{-2F_{i-5,j} + 15F_{i-4,j} - 50F_{i-3,j} + 100F_{i-2,j} - 150F_{i-1,j} + 77F_{i,j} + 10F_{i+1,j}}{60\Delta x} \tag{2.20}$$

$$\frac{\partial F}{\partial x}\bigg|_{i,j} = \frac{10F_{i-6,j} - 72F_{i-5,j} + 225F_{i-4,j} - 400F_{i-3,j} + 450F_{i-2,j} - 360F_{i-1,j} + 147F_{i,j}}{60\Delta x} \tag{2.21}$$

The equivalent process is used at the left and lower boundaries. The three different sixth-order stencils used to approximate the flux as the calculation point neared the left and lower (minimum value of i) boundaries are

$$\frac{\partial F}{\partial x}\bigg|_{i,j} = \frac{2F_{i-2,j} - 24F_{i-1,j} - 35F_{i,j} + 80F_{i+1,j} - 30F_{i+2,j} + 8F_{i+3,j} - F_{i+4,j}}{60\Delta x} \tag{2.22}$$

$$\frac{\partial F}{\partial x}\bigg|_{i,j} = \frac{-10F_{i-1,j} - 77F_{i,j} + 150F_{i+1,j} - 100F_{i+2,j} + 50F_{i+3,j} - 15F_{i+4,j} + 2F_{i+5,j}}{60\Delta x} \tag{2.23}$$

$$\frac{\partial F}{\partial x}\bigg|_{i,j} = \frac{-147F_{i,j} + 360F_{i+1,j} - 450F_{i+2,j} + 400F_{i+3,j} - 225F_{i+4,j} + 72F_{i+5,j} - 10F_{i+6,j}}{60\Delta x} \tag{2.24}$$

Scattering Problem

As with the uniform mean flow problem, the scattering problem also uses an adaptive stencil as the calculation point nears a mesh boundary. The two different fourth-order stencils used to approximate the residual term as the calculation point nears the maximum i boundary are

$$\frac{\partial F}{\partial x}\bigg|_{i,j} = \frac{-F_{i-3,j} + 6F_{i-2,j} - 18F_{i-1,j} + 10F_{i,j} + 3F_{i+1,j}}{12\Delta x} \tag{2.25}$$

$$\frac{\partial F}{\partial x}\bigg|_{i,j} = \frac{3F_{i-4,j} - 16F_{i-3,j} + 36F_{i-2,j} - 48F_{i-1,j} + 25F_{i,j}}{12\Delta x} \tag{2.26}$$

As the flux point nears the minimum i boundary, the two fourth-order stencils used

to calculate the first derivative approximation are

$$\left.\frac{\partial F}{\partial x}\right|_{i,j} = \frac{-3F_{i-1,j} - 10F_{i,j} + 18F_{i+1,j} - 6F_{i+2,j} + F_{i+3,j}}{12\Delta x} \tag{2.27}$$

$$\left.\frac{\partial F}{\partial x}\right|_{i,j} = \frac{-25F_{i,j} + 48F_{i+1,j} - 36F_{i+2,j} + 16F_{i+3,j} - 3F_{i+4,j}}{12\Delta x} \tag{2.28}$$

Although the derivatives approximations described above are all expressed with the variable F changing in the x direction the same stencils can be used to calculate the derivative of variable G in the y direction by using various j locations for a particular i, just as with the central-difference approximations used in Section 2.3.1.

2.4 Unstructured Numerical Method

The unstructured method developed for this research employs a finite volume formulation with the ability to use a combination of three different gradient reconstruction techniques and two different Gaussian quadrature approximations. The method was developed with a vertex-based data structure and a median dual control volume formulation. The three different gradient reconstruction techniques include a Green-Gauss approximation method, as well as a Least Squares reconstruction approach and a weighted Least Squares approach. The gradient reconstruction approximations are coupled with the option of using either single or dual point quadrature formulations. This combination of reconstruction techniques and quadrature options is also combined with a collection of three different calculation meshes to fully test the unstructured method for possible sources of error, possible mesh type dependency and any other characteristic behaviour when dealing with the CAA test cases.

2.4.1 Spatial Discretisation

As stated previously, the unstructured method used for this research is based upon a vertex-based median dual finite volume approximation of the linearised Euler equations. The vertex-based data structure was chosen because it most closely mirrored the data structure of the structured numerical method used for accuracy comparison. The vertex-based data structure also allowed for the application of the simple boundary conditions stipulated in the Benchmark test cases. Although all of the unstructured meshes used in this research contain triangular cells only, the use of a median dual control volume allows for the mesh cells to be any shape. The dual cell is constructed using cell centroids and edge midpoints. A median dual of five cells, such as those that are found in the meshes used here, is shown in Figure 2.7. The dual cell constructed from the five cells is associated with the vertex that the five cells share. The fact that each dual is associated with a single vertex agrees with the vertex-based data structure.

As stated previously the unstructured method developed for this research uses a finite volume approximation to solve the linearised Euler equations. With this in mind, the generic conservation equation [34] for any arbitrary volume Ω_0 can be stated by

$$\frac{\partial}{\partial t} \int_{\Omega_0} W_0 dA + \oint_{\partial \Omega_0} f(W) \cdot n ds = \oint_{\partial \Omega_0} g(W, \nabla W) \cdot n ds + \int_{\Omega_0} s(W, \nabla W) dA \quad (2.29)$$
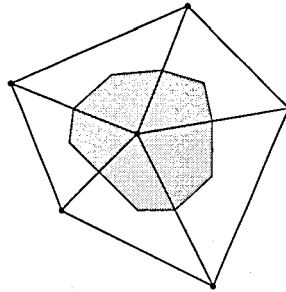
Figure 2.7: Median Dual Control Volume

where W refers to the state variable of the equation, Ω_0 refers to the control volume, $\partial \Omega_0$ refers to the surface of the control volume, and f, g and s refer to the terms in the general conservation equation.

Using the above equation as a base, the governing equations used for the unstructured method can be written as

$$\int_{\Omega_0} \frac{\partial W_0}{\partial t} dA + \oint_{\partial \Omega_0} f(\widetilde{W}) \cdot nds = 0 \tag{2.30}$$

In this particular case, W refers to the state vector which contains all of the state variables and $\widetilde{W}$ refers to the gradient vector defined for the general governing equation as

$$f(\widetilde{W}) = \frac{\partial F}{\partial x} + \frac{\partial G}{\partial y} \tag{2.31}$$

For this particular unstructured method, the value of the state variables in the control volume is taken as a constant across the entire volume at any time so that

$$\int_{\Omega_0} \frac{\partial W_0}{\partial t} dA = A_{\Omega_0} \frac{dW_0}{dt} \tag{2.32}$$

where A_{Ω_0} refers to the area of the control volume. The finite volume formulation of the general governing equation can then be rewritten as

$$A_{\Omega_0} \frac{dW_0}{dt} + \oint_{\partial \Omega_0} f(\widetilde{W}) \cdot nds = 0 \tag{2.33}$$

For a generic polygonal control volume such as the median dual control volume used in this method, the surface integrals computed along the polygonal surface of a control

volume with n_f sides become

$$A_{\Omega_0} \frac{\partial W_0}{\partial t} + \sum_{i=1}^{n_f} \int_{\partial\Omega_{0i}} f(\widetilde{W}) \cdot n\, ds = 0 \tag{2.34}$$

where $\partial\Omega_{0i}$ is the control volume face separating the current control volume Ω_0 and any neighbouring control volume Ω_i.

The fluxes are evaluated using Gaussian quadrature with n_G points and the source control volume is assumed constant to give

$$A_{\Omega_0} \frac{\partial W_0}{\partial t} + \sum_{i=1}^{n_f} \frac{\Delta s_{0i}}{2} \left\{ \sum_{j=1}^{n_G} w_j \left[f(\widetilde{W}) \cdot n \right]_{0i,\tilde{s}_j} \right\} = 0 \tag{2.35}$$

where Δs_{0i} is the length of the control volume face between control volumes Ω_0 and Ω_i, $\tilde{s}$ is a parameterised coordinate along the control volume face and w_j is the quadrature weight. The inviscid flux is calculated along the edge extending from the center of control volume Ω_0 to its neighbour Ω_i. Along this edge the inviscid flux is approximated by

$$\left[f(\widetilde{W}) \cdot n \right]_{0i} = \Phi \left(\widetilde{W}_{0i,L}, \widetilde{W}_{0i,R}; \hat{n}_{0i} \right) \tag{2.36}$$

where L and R refer to the left and right points of edge $0i$ respectively, Φ refers to the function used to resolve the flux approximation, $\widetilde{W}_{0i,L}$ and $\widetilde{W}_{0i,R}$ refer to the gradient vectors reconstructed at the left and right points of edge $0i$ respectively, and $\hat{n}_{0i}$ refers to the normal vector describing edge $0i$. For second order accurate Gaussian quadrature the midpoint rule is used giving

$$A_{\Omega_0} \frac{\partial W_0}{\partial t} + \sum_{i=1}^{n_f} \left[f(\widetilde{W}) \cdot n \right]_{0i} \Delta s_{0i} = 0 \tag{2.37}$$

Second order accuracy of the finite volume formulation is obtained by using

$$\Phi \left(\widetilde{W}_{0i,L}, \widetilde{W}_{0i,R}; \hat{n} \right) = \frac{1}{2} \left[\widetilde{W}_{0i,L} + \widetilde{W}_{0i,R} \right] \cdot \vec{n}_{0i} \tag{2.38}$$

where $\vec{n}_{0i}$ is the unit vector that describe the edge $0i$. With this flux approximation the general governing equation of the unstructured method becomes

$$A_{\Omega_0} \frac{\partial W_0}{\partial t} + \sum_{i=1}^{n_f} \frac{1}{2} \left[\widetilde{W}_{0i,L} + \widetilde{W}_{0i,R} \right] \cdot \vec{n}_{0i}\, \Delta s_{0i} = 0 \tag{2.39}$$

The reconstructed left and right state variables, $\widetilde{W}_{0i,L}$ and $\widetilde{W}_{0i,R}$ are computed using one of two different techniques depending on the choice of the number of quadrature points used. This formulation is only for a single control volume however. For the entire computational domain this calculation must be repeated for every vertex, taking into account every cell edge that is attached to each particular vertex.

Reconstruction Techniques

Two reconstruction techniques are used with the finite volume calculation methods. The first technique uses a single quadrature point located at the midpoint of each edge connecting the calculation vertex (0) with its neighbour (i). The $\widetilde{W}$ terms are determined using the two cell centroids (C1 and C2) of the primary cells adjacent to the calculation edge to reconstruct the state variable located at point Q, as shown in Figure 2.8(a). The variables are reconstructed as follows:

$$\widetilde{W}_{0i,L} = W_0 + \frac{1}{2}(\nabla W)_0 \cdot \vec{r}_{0i} \tag{2.40}$$

$$\widetilde{W}_{0i,R} = W_i - \frac{1}{2}(\nabla W)_i \cdot \vec{r}_{0i} \tag{2.41}$$

where W_0 is the value of the W state variable at the 0 vertex and $(\nabla W)_0$ is the calculated gradient of W at the 0 vertex. The terms W_i and $(\nabla W)_i$ are similarly defined, but for the i vertex. The $\vec{r}_{0i}$ term refers to the vector from vertex 0 to vertex i.

Instead of calculating the reconstructed values of W by using the entire $0i$ edge, the quadrature point Q can be referenced directly as in

$$\widetilde{W}_{0i,L} = W_0 + (\nabla W)_0 \cdot \vec{r}_{0Q} \tag{2.42}$$

and

$$\widetilde{W}_{0i,R} = W_i + (\nabla W)_i \cdot \vec{r}_{iQ} \tag{2.43}$$

where $\vec{r}_{0Q}$ refers to the vector from the 0 vertex to the quadrature point and $\vec{r}_{iQ}$ refers to the vector from the i vertex to the quadrature point. By calculating the reconstructed values in this way, it is easier to extend the same formulation to the use of two quadrature points.

The second reconstruction technique uses two quadrature points for each cell edge.
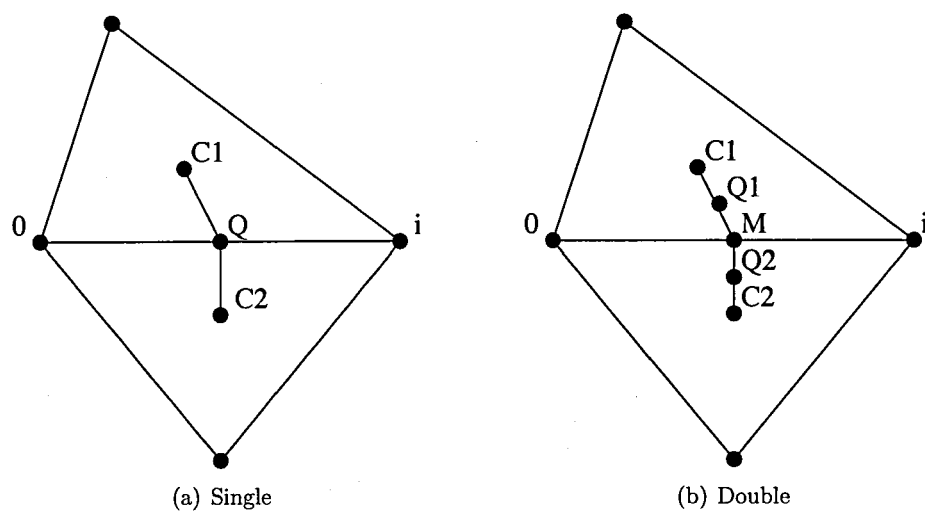
(a) Single   (b) Double

Figure 2.8: Quadrature Point Specification

The two quadrature points Q1 and Q2 are situated halfway between the midpoint of the calculation edge (M) and the corresponding primary cell centroids (C1 and C2, respectively). The locations of the quadrature points can be seen in Figure 2.8(b). The 0 vertex variables are reconstructed at each of the two quadrature points using

$$\widetilde{\mathrm{W}}_{0i,L} = \widetilde{\mathrm{W}}_{0i,L1} + \widetilde{\mathrm{W}}_{0i,L2} \qquad (2.44)$$

where $\widetilde{\mathrm{W}}_{0i,L1}$ refers to the term calculated using the Q1 quadrature point and the 0 vertex, and $\widetilde{\mathrm{W}}_{0i,L2}$ refers to the term calculated using the Q2 quadrature point and the 0 vertex. The i vertex term is reconstructed using

$$\widetilde{\mathrm{W}}_{0i,R} = \widetilde{\mathrm{W}}_{0i,R1} + \widetilde{\mathrm{W}}_{0i,R2} \qquad (2.45)$$

where $\widetilde{\mathrm{W}}_{0i,R1}$ and $\widetilde{\mathrm{W}}_{0i,R2}$ refer to the terms calculated with the i vertex and the Q1 and Q2 quadrature points, respectively. The $\widetilde{\mathrm{W}}_{0i,L1}$ quadrature component is calculated using

$$\widetilde{\mathrm{W}}_{0i,L1} = W_0 + (\nabla W)_0 \cdot \vec{r}_{0Q1} \qquad (2.46)$$

where $\vec{r}_{0Q1}$ is the vector from the 0 vertex to Q1. The $\widetilde{\mathrm{W}}_{0i,L2}$ quadrature component is calculated using

$$\widetilde{\mathrm{W}}_{0i,L2} = W_0 + (\nabla W)_0 \cdot \vec{r}_{0Q2} \qquad (2.47)$$

where $\vec{r}_{0Q2}$ is the vector from the 0 vertex to Q2. The right-hand $\left(\widetilde{\mathrm{W}}_{0i,R1} \text{ and } \widetilde{\mathrm{W}}_{0i,R2}\right)$ variables are reconstructed similarly.

Green Gauss Gradient Approximations

The first technique used in approximating the gradient of the state variables in the unstructured method uses the Green Gauss formulation. The Green Gauss theorem [9] can be written

$$\int_{\Omega_{0'}} \nabla W dA = \oint_{\partial \Omega_{0'}} W \vec{n} ds \qquad (2.48)$$

where $\vec{n}$ is the unit normal vector along surface $\partial\Omega_{0'}$. The derivative can be approximated as

$$(\nabla W)_0 = \frac{1}{A_{\Omega_{0'}}} \oint_{\partial\Omega_{0'}} W\vec{n}\,ds \qquad (2.49)$$

where $\Omega_{0'}$ is the area of all triangular cells surrounding vertex 0.

At interior vertices, the trapezoidal rule can be used to give

$$(\nabla W)_0 = \frac{1}{A_{\Omega_{0'}}} \sum_{i\epsilon\nu_0} \frac{1}{2}(W_i + W_{i+1})n_{i+\frac{1}{2}} \qquad (2.50)$$

where $n_{i+\frac{1}{2}}$ is a scaled normal vector and ν_0 is the number of cells neighbouring vertex 0. The sum is cyclic so the indices can be shifted to give

$$(\nabla W)_0 = \frac{1}{A_{\Omega_{0'}}} \sum_{i\epsilon\nu_0} \frac{1}{2}W_i(n_{i+\frac{1}{2}} + n_{i-\frac{1}{2}}) \qquad (2.51)$$

the sum of the normal is always equal to zero, so a constant was added giving

$$(\nabla W)_0 = \frac{1}{A_{\Omega_{0'}}} \sum_{i\epsilon\nu_0} \frac{1}{2}(W_0 + W_i)(n_{i+\frac{1}{2}} + n_{i-\frac{1}{2}}) \qquad (2.52)$$

The identities

$$n_{i+\frac{1}{2}} = 3n_{0i,1} - \frac{1}{2}n_{0i} \qquad (2.53)$$

$$n_{i-\frac{1}{2}} = 3n_{0i,2} + \frac{1}{2}n_{0i} \qquad (2.54)$$

can be used to give

$$(\nabla W)_0 = \frac{1}{A_{\Omega_{0'}}} \sum_{i\epsilon\nu_0} \frac{3}{2}(W_0 + W_i)(n_{0i,1} + n_{0i,2}) \qquad (2.55)$$

Using the fact that each dual edge consists of two segments, complexity is reduced by replacing the two segments $n_{0i,1}$ and $n_{0i,2}$ with a single term $\hat{n}_{0i}$ where

$$\hat{n}_{0i} = \frac{n_{0i,1}\Delta s_{0i,1} + n_{0i,2}\Delta s_{0i,2}}{\Delta s_{0i}} \qquad (2.56)$$

which allows the gradient of W to be approximated as

$$(\nabla W)_0 = \frac{3}{A_{\Omega_{0'}}} \sum_{i\epsilon\nu_0} \frac{1}{2}(W_0 + W_i)\hat{n}_{0i} \tag{2.57}$$

Also, the area of the median dual is equal to one third of the area of the surrounding triangles or

$$\frac{A_{\Omega_{0'}}}{3} = A_{\Omega_0} \tag{2.58}$$

giving

$$(\nabla W)_0 = \frac{1}{A_{\Omega_0}} \sum_{i\epsilon\nu_0} \frac{1}{2}(W_0 + W_i)\hat{n}_{0i} \tag{2.59}$$

The above equation is used to calculated the gradient of any control volume centered at vertex 0 using values of W at its adjacent neighbours, the control volumes associated with vertices i. Since the gradients are calculated on an edge by edge basis, the contribution of each adjacent i vertex is added to the total gradient stored at vertex 0. Once all of the edges have been passed over with this formulation, every median dual control volume has a gradient stored at its corresponding vertex.

Least Squares Approximations

The second and third techniques used in approximating the gradient of the state variables in the unstructured method both use the same formulation. The Least Squares gradient approximation technique is derived using the same equations as the weighted Least Squares formulation [3]. The difference between the linear Least Squares approximation method and the weighted Least Squares reconstruction method is controlled by the weighting variable P. For weighted Least Square gradient approximation, the neighbours of vertex 0 can be used to approximate gradients ∇W with

$$\begin{bmatrix} \xi_{01}(x_1 - x_0) & \xi_{01}(y_1 - y_0) \\ \xi_{02}(x_2 - x_0) & \xi_{02}(y_2 - y_0) \\ \vdots & \vdots \\ \xi_{0d_0}(x_{d0} - x_0) & \xi_{0d_0}(y_{d0} - y_0) \end{bmatrix} \left\{ \begin{matrix} \frac{\partial W}{\partial x} \\ \frac{\partial W}{\partial y} \end{matrix} \right\}_0 = \begin{bmatrix} \xi_{01}(W_1 - W_0) \\ \xi_{02}(W_2 - W_0) \\ \vdots \\ \xi_{0d_0}(W_{d0} - W_0) \end{bmatrix} \tag{2.60}$$

where d_0 refers to the total number of neighbours of vertex 0 and where

$$\xi_{0i} = \|r_i - r_0\|^{-P} \tag{2.61}$$

and the use of ξ determines whether the Least Square approximation is linear ($P = 0$) or weighted ($P > 0$). In the calculations completed as part of this research, weighted Least Squares was always used with $P = 1$ to give an approximation that contains a weighting factor that is inversely proportional to the distance between mesh vertices. The standard Least Squares gradient approximation method is calculated using a weighting factor that is directly proportional to the distance between mesh vertices. This change in the dependence of the method on the distance between vertices is the only factor that separates the two Least Squares methods.

Equation 2.61 can be written in the form of $Ax = b$ but with this particular formulation the A matrix is of the form $A^T A = I$ and is therefore ill-conditioned. A Gram-Schmidt method [32] can be employed by substituting $A = QR$ to improve the solution. In this formulation Q is a matrix d_0 rows by 2 columns and R is a matrix of size 2 by 2. This gives the new form of

$$QRx = b \tag{2.62}$$

which can be rewritten using $Q^T Q = I$ to give

$$x = R^{-1} Q^T b \tag{2.63}$$

This new formulation allows the approximation method greater accuracy without the effects of the ill conditioned matrix. The decomposed approximation technique can be further derived [34] with the a, q and r components of A, Q and R (respectively) using

$$[a_1|a_2] = [q_1|q_2] \cdot \begin{bmatrix} r_{11,0} & r_{12,0} \\ 0 & r_{22,0} \end{bmatrix} \tag{2.64}$$

or

$$a_1 = r_{11,0} q_1 \tag{2.65}$$

$$a_2 = r_{12,0} q_1 + r_{22,0} q_2 \tag{2.66}$$

The previous two equations can be inverted to give

$$q_1 = \frac{a_1}{r_{11,0}} \qquad (2.67)$$

$$q_2 = \frac{a_2}{r_{22,0}} - \frac{r_{12,0}}{r_{11,0} r_{22,0}} a_1 \qquad (2.68)$$

then the q_1 term can be rewritten as

$$q_1 = \frac{a_1}{\|a_1\|} = \frac{a_1}{r_{11,0}} \qquad (2.69)$$

where the $r_{11,0}$ coefficient can be stated as

$$r_{11,0} = \sqrt{\sum_{0i \epsilon \varepsilon_0} \xi_{0i}^2 (x_i - x_0)^2} \qquad (2.70)$$

In addition, a new term a_2' can be used with

$$a_2' = a_2 - (a_2 \cdot q_1) q_1 \qquad (2.71)$$

and the q_2 term can be rewritten as

$$q_2 = \frac{a_2'}{\|a_2'\|} \qquad (2.72)$$

Rewriting Equation 2.71 gives

$$a_2' = a_2 - \left(a_2 \cdot \frac{a_1}{r_{11,0}} \right) \frac{a_1}{r_{11,0}} \qquad (2.73)$$

which can then be rewritten as

$$a_2' = a_2 - \frac{1}{r_{11,0}} \sum_{0i \epsilon \varepsilon_0} \xi_{0i}^2 (x_i - x_0)(y_i - y_0) \frac{a_1}{r_{11,0}} \qquad (2.74)$$

The r_{12} term can be defined as

$$r_{12} = \frac{1}{r_{11,0}} \sum_{0i \epsilon \varepsilon_0} \xi_{0i}^2 (x_i - x_0)(y_i - y_0) \qquad (2.75)$$

and Equation 2.74 can then be written as

$$a_2' = a_2 - \frac{r_{12,0}}{r_{11,0}} a_1 \tag{2.76}$$

to give

$$\|a_2'\|^2 = a_2 \cdot a_2 - 2\frac{r_{12,0}}{r_{11,0}} a_1 \cdot a_2 + \left(\frac{r_{12,0}}{r_{11,0}}\right)^2 a_1 \cdot a_1 \tag{2.77}$$

which can then be written as

$$\|a_2'\|^2 = \sum_{0i\epsilon\varepsilon_0} \xi_{0i}^2 (y_i - y_0)^2 - r_{12}^2 \tag{2.78}$$

The $r_{22,0}$ term can be defined as

$$r_{22,0} = \sqrt{\sum_{0i\epsilon\varepsilon_0} \xi_{0i}^2 (y_i - y_0)^2 - r_{12}^2} \tag{2.79}$$

Going back to the matrix formulation of $x = R^{-1}Q^T b$ (Equation 2.63), the gradients can be approximated using

$$(\nabla W)_0 = \sum_{0i\epsilon\varepsilon_0} w_{0i}(W_i - W_0) \tag{2.80}$$

where the w_{0i} terms come from the Gram-Schmidt decomposition and are expressed as

$$w_{0i} = \left\{ \begin{array}{c} w_{x,0i} \\ w_{y,0i} \end{array} \right\} \tag{2.81}$$

where

$$w_{x,0i} = \frac{\xi_{0i}^2}{r_{11,0}^2}(x_i - x_0) - \frac{\xi_{0i}^2 r_{12,0}}{r_{11,0} r_{22,0}^2}\left[(y_i - y_0) - (x_i - x_0)\frac{r_{12,0}}{r_{11,0}}\right] \tag{2.82}$$

$$w_{y,0i} = \frac{\xi_{0i}^2}{r_{22,0}^2}\left[(y_i - y_0) - (x_i - x_0)\frac{r_{12,0}}{r_{11,0}}\right] \tag{2.83}$$

The weighted Least Squares gradients are calculated by looping over all edges of a polygonal control volume, and can be stored on a nodal basis, as with the Green-Gauss gradients. The formulation described above seems complex but computing the constant

r_{ij} coefficients during preprocessing allows for simplification.

2.4.2   Temporal Discretisation

The time discretisation for the unstructured method involves the same standard Runge-Kutta four stage method (RK4) as used for the structured calculations. The derivation of the RK4 scheme can be found in Section 2.3.2.

2.4.3   Mesh Specification

The different meshes tested with the unstructured method include two semi-structured meshes created using the structured mesh and a purely unstructured mesh created using a commercial mesh generation package. The two semi-structured meshes have a regular repeating pattern due to their construction. The meshes are created by cutting the structured mesh cells diagonally in half. A section of the original structured mesh used to create the triangular meshes can be seen in Figure 2.9. The two meshes, NEG and UK, are created by either cutting every cell in the structured mesh using a line with a negative slope (NEG mesh) or an alternating slope pattern creating a triangular mesh resembling a Union Jack flag (UK mesh), as can be seen in Figures 2.10 and 2.11. The purely unstructured mesh is created by specifying the boundaries of the structured mesh (for example $\Delta x = \Delta y = 1.0$ along $x = [-110, 110]$ and $y = [-110, 110]$ for the uniform mean flow problem) and using a paving algorithm to fill the interior. The purely unstructured meshes were created using a commercial program using a Delaunay formulation. A section of the TRI mesh can be seen in Figure 2.12). Test calculations on the semi-structured meshes are used to determine the influence of the orientation of the dominant diagonal edge on the numerical method. The NEG mesh has all the long edges aligned, which could cause distortion of the acoustic structures, and the UK mesh has an alternating pattern which may or may not have the same effect. In both the NEG and UK meshes, there exists an regular repeated pattern which also may have some effect. Test calculations on the TRI mesh are used to determine the influence of the random orientation of the cells on the numerical scheme.

In addition to the NEG and UK meshes, a third semi-structured mesh, POS, can be created by cutting the structured mesh cell diagonally in half using a line with a positive slope. This creates a mesh identical to the NEG mesh, merely rotated 90°. After completing preliminary calculations using both the POS and NEG meshes, it was
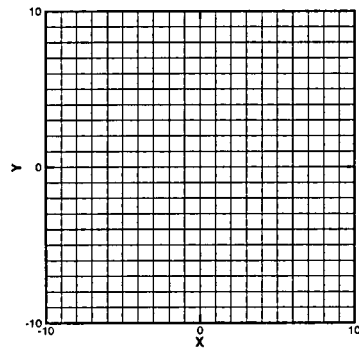
Figure 2.9: Section of Structured Mesh for Uniform Mean Flow Problem
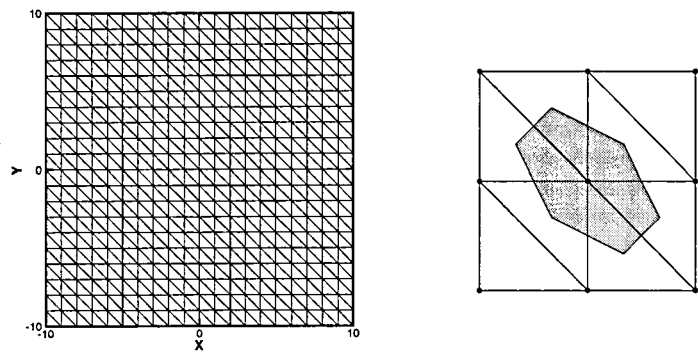

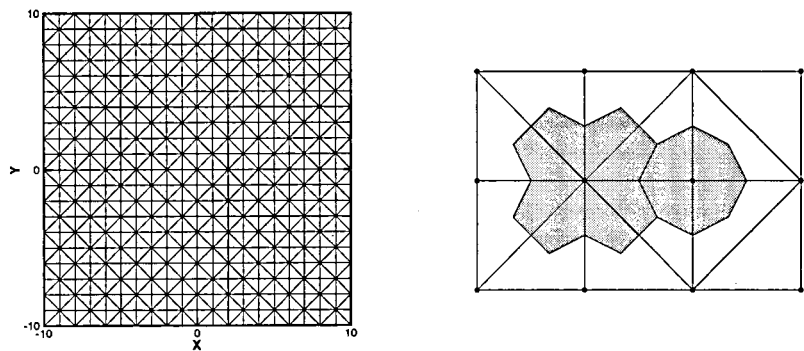Figure 2.10: Section of NEG Mesh and NEG Dual for Uniform Mean Flow Problem

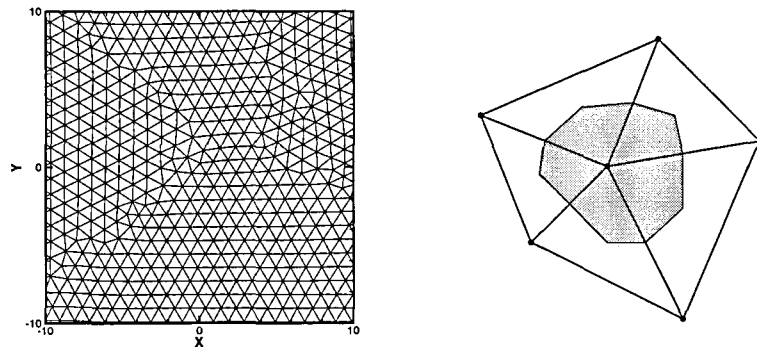Figure 2.11: Section of UK Mesh and UK Duals for Uniform Mean Flow Problem

Figure 2.12: Section of TRI Mesh and TRI Duals for Uniform Mean Flow Problem

determined that any possible mesh dependencies could be demonstrated using only the NEG mesh and the POS mesh would be reserved for confirming any possible mesh sensitivity characteristics that arise with the use of the NEG mesh. This decision was made based on the fact that both meshes had the same uniform orientation of long edges and neither had the alternating pattern of the UK mesh. For that reason, only the calculations completed on the NEG and UK mesh are used to demonstrate the effect of the semi-structured meshes.

Uniform Mean Flow Problem

As stated previously, the meshes used for the calculations were all enlarged beyond the domain specified in the Benchmark Proceedings to ensure that the boundaries were not encountered. The two semi-structured test meshes used for the uniform mean flow problem, UK and NEG, both have 48,841 vertices and 96,800 primary cells. Primary cells are cells that are defined by the mesh nodes and are not used as control volumes. For this unstructured method the median dual control volumes are constructed using mesh points and primary cell edges, not the primary cells themselves. The cells are all identical in area, and only differ in their orientation. The TRI mesh has 54,949 vertices and 109,016 primary cells. For data and error comparisons only vertices contained within the original domain were used. This created a region of 40,401 vertices for the UK and NEG meshes, and 44,858 vertices for the TRI mesh. The mesh specifications are summarised in Table 2.1.

Mesh Type	Total No. of Vertices	Total No. of Pri. Cells	No. of Vertices Compared
Structured	48841	48400	40401
NEG	48841	96800	40401
UK	48841	96800	40401
TRI	54949	109016	44858

Table 2.1: Statistics of Uniform Mean Flow Problem Meshes

Scattering Problem

Three unstructured meshes were created from the structured scattering problem mesh using the same method as described in Section 2.4.3. For the two semi-structured meshes, the quadrilateral cells of the structured mesh are cut into triangular cells to create the NEG and UK meshes. Each of these meshes have the same number of vertices and primary cells, 174,600 and 348,000 respectively, although with slightly different layouts. For the purely unstructured TRI mesh the inner and outer circular boundaries of the scattering problem structured mesh are used with the same paving algorithm employed with the uniform mean flow problem mesh, creating a computational area that encloses 960,863 vertices and 1,920,526 triangular primary cells. The mesh specifications are summarised in Table 2.2. Unlike the structured method used for the scattering problem, all three of the meshes used with the unstructured method only have two boundaries, the inner and outer circular boundaries and therefore only two boundary conditions.

Mesh Type	No. of Vertices	No. of Pri. Cells
Structured	176055	175160
NEG	174600	348000
UK	174600	348000
TRI	960863	1920526

Table 2.2: Statistics of Scattering Problem Meshes

2.4.4 Boundary Conditions

The calculations completed on the unstructured meshes all have boundary conditions that take advantage of certain mesh characteristics, simplifying the development. The

two types of boundary conditions used in the unstructured method are the outflow boundary condition and the solid boundary condition. The outflow condition is used for both the uniform mean flow problem and the scattering problem, but the solid condition is only used with the scattering problem.

Semi-structured Meshes

For the semi-structured meshes, the underlying structured mesh is still present and the existence of a mesh vertex lying directly normal to each boundary vertex is exploited. In Figure 2.13 it can be seen that each boundary vertex (V_{BC}) of the NEG mesh has a corresponding interior vertex (V_{INT}) that can be used to apply a simple boundary condition. The extra edges do not interfere with this formulation, as the data structure employs vertex-based storage of the state variables. The same scenario is used with the UK mesh, as seen in Figure 2.14. The interior vertex still lies directly normal to the boundary surface, one edge away from the corresponding boundary vertex.
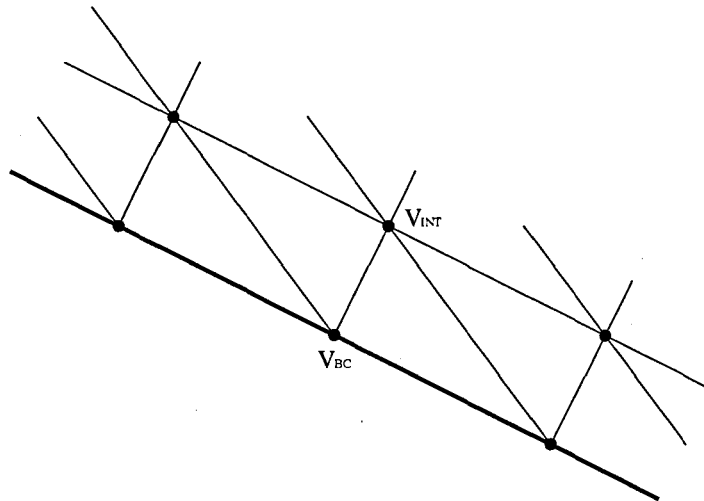

Figure 2.13: Schematic of NEG Mesh Boundary

Since the mesh was uniformly created, the boundary/interior vertex formulation can be used on both the outer and inner boundaries. The indices of the interior points are determined during preprocessing and are stored with their corresponding boundary vertices.
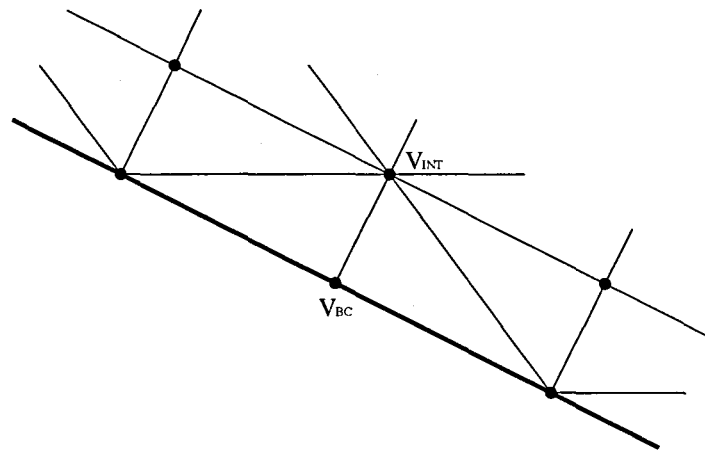
Figure 2.14: Schematic of UK Mesh Boundary

Outflow Boundary Condition   The outflow boundary conditions applied on to the semi-structured meshes are the same ones used for the structured method. For the uniform mean flow problem the boundary conditions require that the gradients normal to the boundary of all of the state variables are set equal to zero at the outer boundaries. These two separate boundary conditions can both be approximated using the same first order derivation as the one applied with the structured test case.

Solid Boundary Condition   The scattering problem solid boundary condition used with the semi-structured meshes is also identical to the one that is applied on the structured mesh. The pressure gradient normal to the cylinder is set equal to zero. This BC is applied in the same fashion as the other conditions, with the use of a first-order approximation. The radial velocity component boundary condition is explicitly applied by setting the variable to zero at the boundary vertex.

Purely Unstructured Mesh

A mesh characteristic that exists in the purely unstructured meshes can also be used to formulate simple boundary conditions, as with the semi-structured meshes. In the TRI mesh, the paving algorithm that was used determined the mesh by starting at the boundaries and working toward the middle of the mesh. This method created layers of isosceles triangular cells that are present at both the inner and outer edges of the mesh. These symmetric, triangular cells are no doubt caused by the fact that all of the

boundary edges that were specified from the structured mesh are of equal length.

For the TRI mesh boundary conditions, a virtual interior vertex is created directly normal to the boundary using two interior vertices from adjacent cells. The virtual vertex, labeled V^* in Figure 2.15, is created using two interior points, V_{INT} and V_{INT2}.
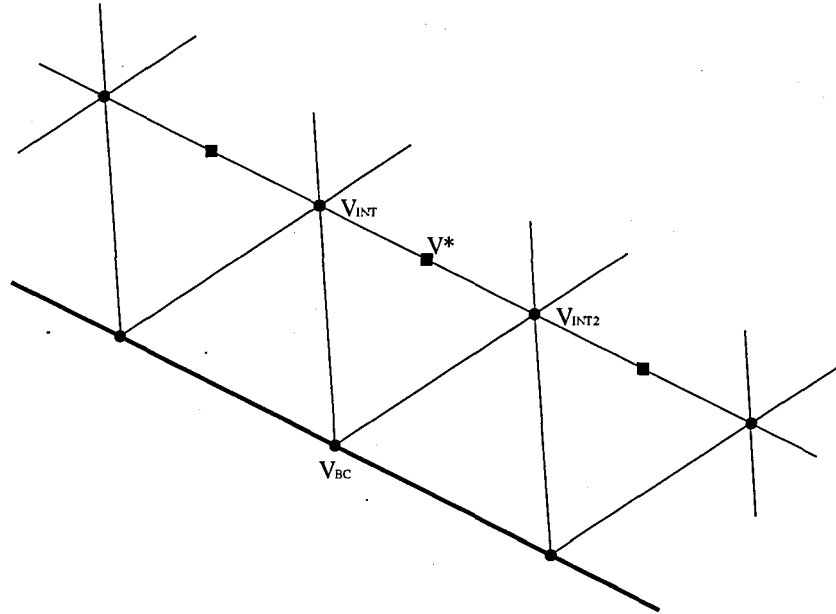

Figure 2.15: Schematic of TRI Mesh Boundary

In Figure 2.15 the actual vertices are shown with circular symbols and the virtual vertices are denoted with square markers. The value of the state variable at the virtual vertex is determined by averaging the variables at each of the interior vertices, or

$$W_{V^*} = \frac{W_{V_{INT}} + W_{V_{INT2}}}{2} \qquad (2.84)$$

The layers of isosceles triangular cells occur at both the inner and outer boundaries, and the virtual boundary vertices are created near both edges of the mesh. The interior cells used to create each virtual point are determined during preprocessing, and the indices of each are stored for use in applying the boundary condition. The value of the variables at each virtual vertex is not stored during calculation, instead the averaging of the existing data at the corresponding interior points is completed each time the boundary condition is applied.

Outflow Boundary Condition The outflow boundary condition for the purely unstructured mesh calculations remains the same as for the semi-structured and structured calculations as well. The gradients of all of the state variables normal to the boundary are set equal to zero at the boundary. The single difference is that for the interior vertex used in the first-order approximation of the boundary condition, the constructed variable from Equation 2.84 is used instead of one pertaining to a physical vertex.

Solid Boundary Condition The solid boundary condition applied on the purely unstructured mesh is the same as the one applied on both the structured and semi-structured meshes. The gradient of the pressure normal to the surface of the cylinder is set equal to zero. Also, the value of the radial velocity component is also set equal to zero at the cylinder surface. The solid boundary condition for pressure is applied using the same formulation as the outflow boundary condition for the unstructured mesh as stated above, and the radial velocity boundary condition is the same as specified for the semi-structured meshes and structured meshes.

2.4.5 Barth-Jespersen Limiter

Upon the completion of a few preliminary calculations using the unstructured method on the scattering problem, it was determined that a limiting function was required. Errors began to appear near the cylinder wall as the pressure pulse approached and by the time the end of the prescribed run had been reached these errors had polluted the entire domain. As a result a Barth-Jespersen limiting function [9] was employed for all unstructured calculations, removing the error and allowing the completion of a solution.

The two single-quadrature point reconstruction equations, Equations 2.40 and 2.41 can be rewritten with the limiting factor $\lambda(W)$ as

$$W_{0i,L} = W_0 + \frac{1}{2}\lambda_0(W)(\nabla W)_0 \cdot \vec{r}_{0i} \qquad (2.85)$$

and

$$W_{0i,R} = W_i - \frac{1}{2}\lambda_i(W)(\nabla W)_i \cdot \vec{r}_{0i} \qquad (2.86)$$

where the 0 and i subscripts on $\lambda(W)$ refer to the vertex used to calculate the limiter.

The limiting coefficient for vertex 0 has the condition that

$$0 \leq \lambda(W)_0 \leq 1 \tag{2.87}$$

Taking the approximation limiter equation for vertex 0, two terms can be defined

$$W_{\max} = \max_{0i \in \mathcal{E}_0} (W_0, W_i) \tag{2.88}$$

and

$$W_{\min} = \min_{0i \in \mathcal{E}_0} (W_0, W_i) \tag{2.89}$$

The coefficients that are used to determine the limiter are defined as

$$\Delta_{1,\max} = W_{\max} - W_0 \tag{2.90}$$

$$\Delta_{1,\min} = W_{\min} - W_0 \tag{2.91}$$

$$\Delta_2 = W_{0i} - W_0 \tag{2.92}$$

with the conditions that

$$\Delta_{1,\min} \leq \lambda_0(W)\Delta_2 \leq \Delta_{1,\max} \tag{2.93}$$

The value of the limiter function at vertex 0 is defined as the minimum of the limiter function calculated using all of the edges connected to vertex 0, or

$$\lambda_0(W) = \min_{0i \in \mathcal{E}_0} \lambda_{0i}(W) \tag{2.94}$$

where

$$\lambda_{0i}(W) = \begin{cases} \min\left(1, \frac{\Delta_{1,\max}}{\Delta_2}\right) & \text{if } \Delta_2 > 0 \\ \min\left(1, \frac{\Delta_{1,\min}}{\Delta_2}\right) & \text{if } \Delta_2 < 0 \\ 1 & \text{if } \Delta_2 = 0 \end{cases} \tag{2.95}$$

The Barth-Jespersen limiter function is used for all of the unstructured calculations completed for the scattering problem discussed as part of this research. The inclusion of a limiter may have negative effects on the formal accuracy of the unstructured method.

The limiting of the calculated gradient approximations may be powerful enough to remove the already low-magnitude disturbances which define the pressure pulse being scattered.

2.5   Calculation of Experimental Error Between Test Case Solutions

To compare the results of calculations numerically, a metric can be calculated relating the different calculated solutions to the analytical solution on the corresponding grid. The RMS error can be calculated for the density fields using Equation 2.96.

$$\text{RMS} = \sqrt{\frac{1}{n_v} \sum_{i=1}^{n_v} [\rho(i) - \rho^*(i)]^2} \tag{2.96}$$

where n_v is the total number of vertices compared, ρ is the density field of the calculated solution , and ρ^* is the density field of the analytical solution on the corresponding mesh. The exclusive use of density in determining RMS error for the uniform mean flow problem is due to the fact that the density field is the only state variable with an accurate depiction of both the pressure pulse and the vortex at any given time. For the second series of calculations, the pressure profiles were used for the graphical comparison as specified by the Benchmark Proceedings, and are therefore used for the numerical comparison as well. The formulation of the pressure RMS error is similar to that of Equation 2.96 but uses the three separate pressure profiles instead of the density field.

Along with the absolute error calculated using the RMS error equation a normalized RMS (NRMS) error was also calculated to give a percentage error between the test cases and the problem solutions. The NRMS is calculated using the RMS error and the maximum and minimum values of the solution data using

$$\text{NRMS} = \frac{\text{RMS}}{\rho^*_{\text{max}} - \rho^*_{\text{min}}} \tag{2.97}$$

for the uniform mean flow problem, where ρ^*_{max} and ρ^*_{min} refer to the maximum and minimum value of the density field of the analytical solution. The NRMS error of the scattering problem was calculated in a similar way using P^*_{max} and P^*_{min} instead. The use of the NRMS error allows for a percentage error to be obtained which can be easier

to relate to the data rather than an absolute error value.

2.6 Summary

This chapter has dealt with the explanation of the numerical methods used to perform the calculations that make up the basis of the research being presented. The were two methods developed for this work, the first is a standard structured method that was created as a reference point for the second method. The second method developed was a basic unstructured method with the option of three different gradient approximation techniques and the choice of how the quadrature was completed for reconstruction in the finite volume approach. The unstructured method was used to complete a range of test calculations on different meshes. The purpose of the different meshes as well as the different gradient approximations and reconstruction methods is to determine the numerical characteristics and accuracy of the unstructured method in different aeroacoustic scenarios. The full battery of tests is completed on the first Benchmark problem only, with the best combination of gradient approximation and reconstruction used for the second more difficult Benchmark problem. The results of the test cases are compared both graphically and numerically to determine sources of error such as numerical dispersion or dissipation caused by the formulation of the unstructured method.

The second Benchmark problem calculations are all performed using the same method, but on the different types of meshes discussed above. This second, limited battery of calculations is used to further investigate the behaviour of the unstructured method. The different mesh types will create different problems for the method and will show how effective it can be in the field of CAA.

Chapter 3

Uniform Mean Flow Problem

3.1 Introduction

The main purpose of the research presented is the development of a simple unstructured numerical method for use within the field of Computational Aeroacoustics. Along with the development of the numerical method was the requirement that it be tested on its ability to model different acoustic phenomena in order to determine if it was an accurate enough method to be used in place of high-order structured methods when needed. This method was designed to have the option of using different gradient reconstruction methods as well as the ability to be used on any type of unstructured mesh, giving it the advantage dealing with geometries too complex for structured methods. The testing procedure was to be used to determine which of the different gradient reconstruction methods included were the most effective for different scenarios. With this in mind, two standardized test cases were taken from NASA Benchmark Workshops for Aeroacoustics. These two problems were a uniform mean flow test case and a scattering test case. The uniform mean flow problem is a basic first-step scenario testing the ability of the numerical method to model the convection of a vortex and a pressure pulse with a uniform velocity field within an open domain. The scattering problem is more complex requiring the approximation of how a pressure pulse is scattered by traveling past a solid cylinder. These two problem represent fundamental aeroacoustic phenomena and provide an excellent opportunity to determine the merit of the unstructured numerical method developed.

The purpose of the uniform mean flow problem is to determine the ability of the

numerical method to simulate accurately the convection of a vortex as well as the convection and expansion of a pressure pulse within an open domain. The uniform mean flow problem description is taken from the Workshop on CAA Benchmark Problems [33] and is listed as Category 3, Problem 1. Numerical characteristics such as distortion, dispersion, mesh dependency and overall accuracy are used to evaluate the effectiveness of the method developed. The method is tested on different meshes with different gradient calculation techniques to ascertain the best combination for this aeroacoustic situation.

3.1.1   Test Case Description

The purpose of the uniform mean flow problem is to determine the ability of the numerical method to simulate accurately the convection of a vortex as well as the convection and expansion of a pressure pulse within an open domain. This benchmark test case was chosen because it deals with the very basic and important problem of simulating fundamental acoustic phenomena. If a numerical method in unable to accurately model a simple vortex and pressure pulse it will be unable to deal with any other more complex scenarios. This test case can be seen as the first step in the development of a more complex numerical method to deal with more diverse computational aeroacoustic situations. The uniform mean flow problem description is taken from the Workshop on CAA Benchmark Problems [33]. The description is listed as Category 3, Problem 1. A schematic of the problem can be seen in Figure 3.1.
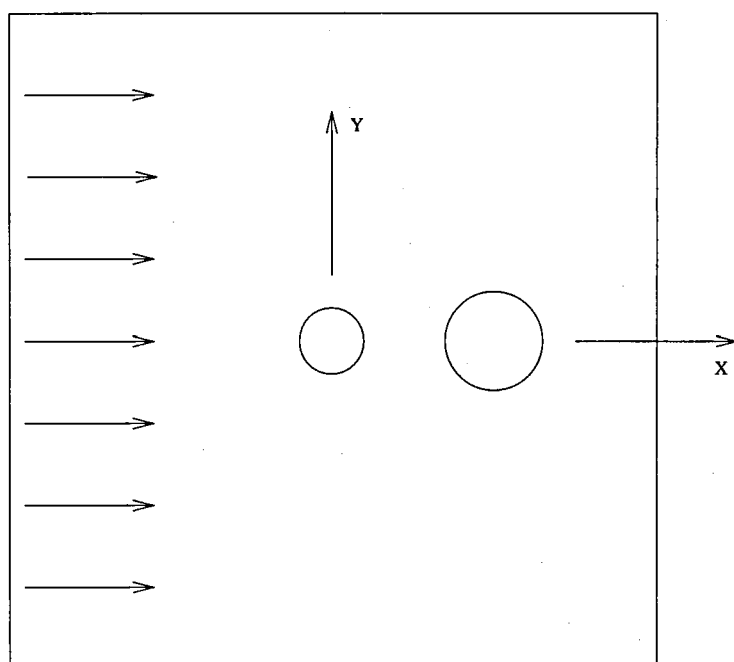
Figure 3.1: Schematic of Uniform Mean Flow Problem

3.1.2 Governing Equations

The governing equations are used to solve for the variables of density, pressure and velocity in two-dimensional Cartesian coordinates. The linearised Euler equations used for this specific problem previously seen as Equation 2.1, are written as:

$$\frac{\partial W}{\partial t} + \frac{\partial F}{\partial x} + \frac{\partial G}{\partial y} = S$$

where

$$W = \begin{bmatrix} \rho \\ u \\ v \\ P \end{bmatrix}, F = \begin{bmatrix} M_x\rho + u \\ M_x u + P \\ M_x v \\ M_x P + u \end{bmatrix}, G = \begin{bmatrix} M_y\rho + v \\ M_y u \\ M_y v + P \\ M_y P + v \end{bmatrix}, S = \begin{bmatrix} 0 \\ 0 \\ 0 \\ 0 \end{bmatrix} \tag{3.1}$$

The variables ρ, u, v, and P refer to the density, the x- and y-components of velocity and the pressure, respectively. The terms M_x and M_y refer to the x- and y-components of the mean velocity field. The variable t refers to time.

3.1.3 Test Case Domain

The specified problem domain encompasses a region from $x = -100$ to $x = 100$ and from $y = -100$ to $y = 100$. The grid spacing throughout the entire domain has Δx and Δy equal to one, creating a uniform Cartesian grid of 40,000 cells. The outer boundaries of the problem are devised to represent an infinite domain, with no solid walls or objects. Since the effect of a boundary condition is not being investigated with this calculation, the domain is extended a further ten grid cells in all directions to ensure that neither the pressure pulse nor the vortex have any interaction with it. The new computational domain ranges from $x = [-110, 110]$ and $y = [-110, 110]$, although only the specified domain will be examined. The addition of an extended computational domain increased the number of cells in the specified mesh from 40,000 to 48,400 cells.

3.1.4   Initial Conditions

The initial condition describes both a pressure pulse and a vortex which are to be convected through the domain. The pressure pulse is situated at the origin of the domain ($x = y = 0$). The vortex is initially set at a point downstream of the pulse at $x_{vi} = 67$ and $y_{vi} = 0$. The initial conditions are calculated using

$$\rho = \exp\left[-(\ln 2)\left(\frac{x^2 + y^2}{9}\right)\right] + 0.1\exp\left[\frac{(x - x_{vi})^2 + (y - y_{vi})^2}{25}\right] \tag{3.2}$$

$$u = 0.04y\exp\left[-(\ln 2)\frac{(x - x_{vi})^2 + (y - y_{vi})^2}{25}\right] \tag{3.3}$$

$$v = -0.04(x - x_{vi})\exp\left[-(\ln 2)\frac{(x - x_{vi})^2 + (y - y_{vi})^2}{25}\right] \tag{3.4}$$

$$P = \exp\left[-(\ln 2)\left(\frac{x^2 + y^2}{9}\right)\right] \tag{3.5}$$

where x_{vi} and y_{vi} refer to the center of the vortex at the start of the calculation ($t = 0$).

The specification of this test case sets the mean velocity components as $M_x = 0.5$ and $M_y = 0$. The time step used for all of the uniform mean flow problem calculations is defined as $\Delta t = 0.1$. This time step was taken directly from the Workshop manual [33]. Since the equations are non-dimensionalised with the length scale and time scale defined as the mesh spacing and speed of sound, respectively, the Courant-Friedrichs-Lewy condition collapses to an expression involving only time step. The standard definition of the Courant number in one dimension is $Cr = \frac{u\Delta t}{\Delta x}$ and with the reference length scale and velocity scale used in these equations the time step Δt is equal to the Courant number. With the time step specified in the literature the Courant number is sufficiently low to satisfy the CFL number conditions for decreasing dispersion error and increasing accuracy. The initial condition of density used for this calculation can be seen in Figure 3.2. This single state variable is shown because it displays the initial condition of both the pressure pulse and the vortex.
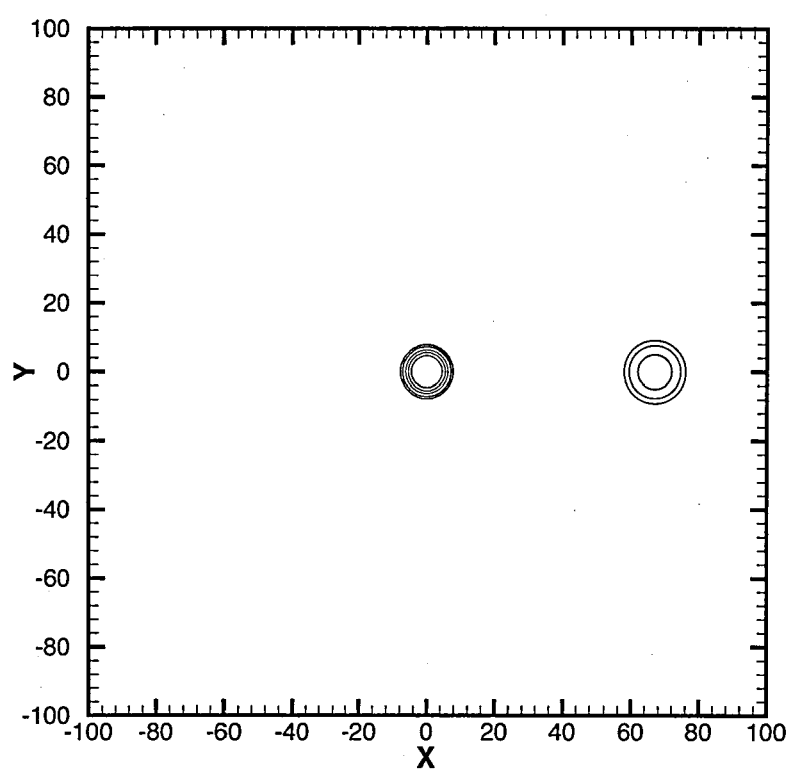
Figure 3.2: Density Contours of Initial Condition for Uniform Mean Flow Problem

3.1.5 Boundary Conditions

For this problem the boundary conditions are specified to be an inflow condition along the left hand side of the grid and simple outflow boundary condition along the other three sides. Since the purpose of this test case is to model the expansion and convection of the acoustic structures in free space there are no other boundary conditions applied. Along the left and right edges of the domain the boundary conditions can be written as

$$\left. \frac{\partial W}{\partial x} \right|_{x=\pm 110} = 0 \tag{3.6}$$

Similarly, along the top and bottom edges of the domain the boundary conditions can be written as

$$\left. \frac{\partial W}{\partial y} \right|_{y=\pm 110} = 0 \tag{3.7}$$

3.1.6 Test Case Solution

The analytical solution of the uniform mean flow problem [33] is given by

$$\rho = \frac{1}{2\alpha_1} \int_0^\infty e^{\frac{-\xi^2}{4\alpha_1}} \cos\left(\xi t\right) J_0\left(\xi \eta\right) \xi \, d\xi + 0.1 e^{-\alpha_2\left((x-x_{vi}-M_x t)^2+y^2\right)} \tag{3.8}$$

where x_{vi} refers to the center of the vortex at the start of the calculation and where

$$\alpha_1 = \frac{\ln 2}{9} \tag{3.9}$$

$$\alpha_2 = \frac{\ln 2}{2} 5 \tag{3.10}$$

$$\eta = \left[(x - M_x t)^2 + y^2 \right]^{\frac{1}{2}} \tag{3.11}$$

and J_0 represents the Bessel function equation of order zero (0). This solution is described in the CAA Workshop [33]. The analytical solutions of the remaining three variables are given by

$$u = \frac{x - M_x t}{2\alpha_1 \eta} \int_0^\infty e^{\frac{-\xi^2}{4\alpha_1}} \sin\left(\xi t\right) J_1\left(\xi \eta\right) \xi \, d\xi + 0.04 y e^{-\alpha_2\left((x-x_{vi}-M_x t)^2+y^2\right)} \tag{3.12}$$

$$v = \frac{y}{2\alpha_1 \eta} \int_0^\infty e^{\frac{-\xi^2}{4\alpha_1}} \sin\left(\xi t\right) J_1\left(\xi \eta\right) \xi \, d\xi - 0.04 y e^{-\alpha_2\left((x-x_{vi}-M_x t)^2+y^2\right)} \tag{3.13}$$
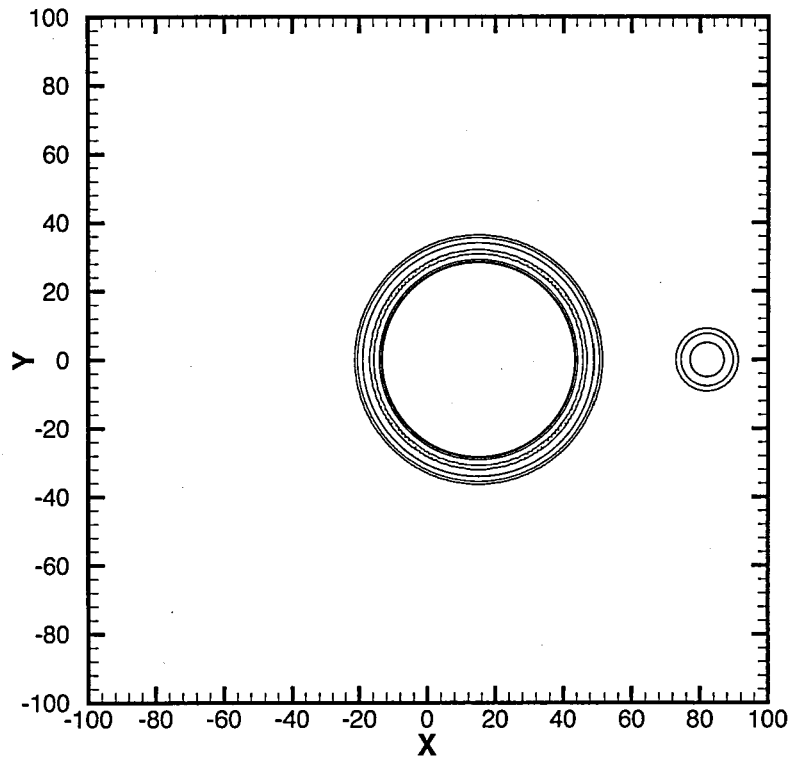
Figure 3.3: Density Contours of Uniform Mean Flow Solution

$$P = \frac{1}{2\alpha_1} \int_0^\infty e^{\frac{-\xi^2}{4\alpha_1}} \cos(\xi t) \, J_0(\xi \eta) \, \xi \, d\xi \qquad (3.14)$$

where J_1 represents the Bessel function of order one (1).

The analytical solution of the uniform mean flow problem at thirty computational time units ($t = 30$) can be seen in Figure 3.3. This is the solution that all test cases will be compared against to determine accuracy of both the structured and unstructured numerical methods.

3.2 Structured Method Solution

As stated previously, for both of the problems investigated as part of this research a structured numerical method is used as a reference in determining relative accuracy and sources of numerical error in the unstructured method. For the uniform mean flow problem, a sixth-order accurate formulation is used to approximate the first-order derivatives of the linearised Euler Equation. A contour plot of the structured method

solution to the test problem can be seen in Figure 3.4(a). The pressure pulse shows no dispersion or dissipation, and appears to have maintained the correct shape. The vortex also shows a lack of dispersion and dissipation errors and has also maintained the correct shape and dimensions. This result, while expected, shows the high accuracy of the standard central-differencing and time-stepping methods chosen. As a second form of visual comparison, a slice of the density solution is taken along the $y = 0$ line, and the calculated structured solution is compared with the analytical density field at the same $t = 30$ simulation time. The comparison, shown in Figure 3.4(b) has the solid line of the calculated density profile lying perfectly atop the dashed line of the analytical density profile for the entire length of the domain. In Figure 3.4(b) it can be seen that there is no discernable phase difference between the computed and analytical results, and no change in either the amplitude or the shape of the waves defining the pressure pulse or the vortex. These results show a lack of numerical dissipation in how the amplitudes all of the waves along the cut are correctly computed and a lack of numerical dispersion in the accurate prediction of the leading and trailing edges of the waveform. As a reference for later calculations, the RMS error calculated using the sixth-order accurate structured solution is 0.1826E-03 which gives a NRMS of 0.11% error.
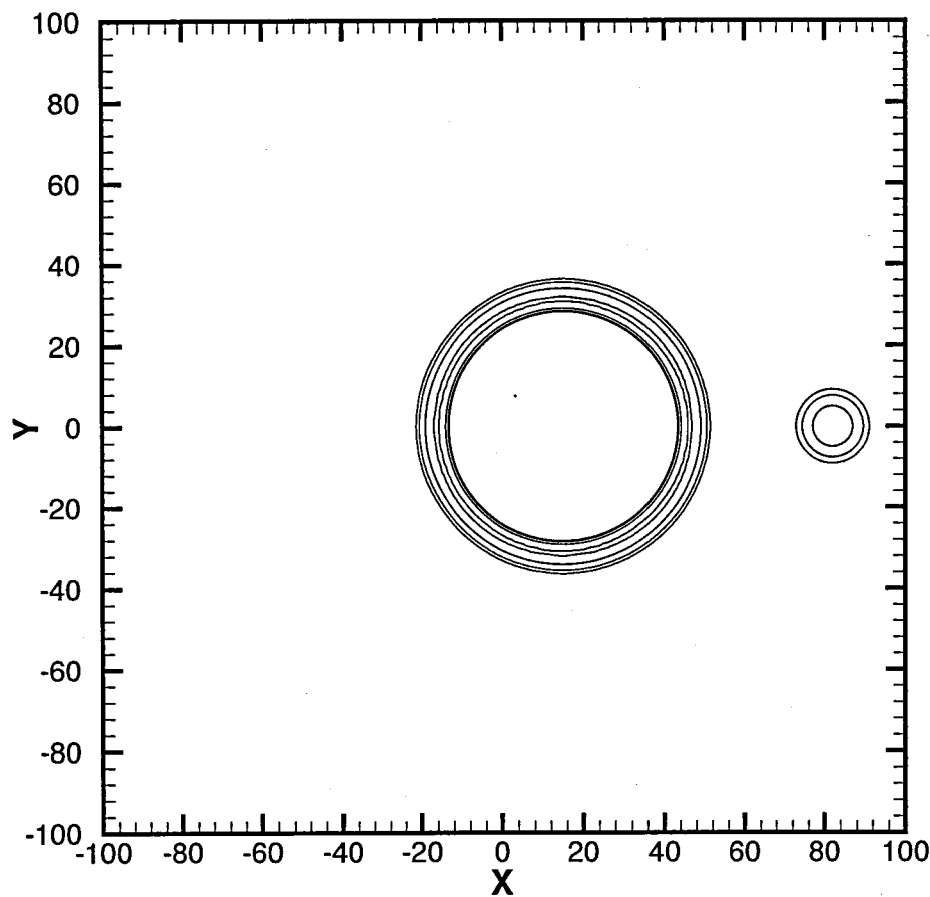
(a) Density Contours At t=30
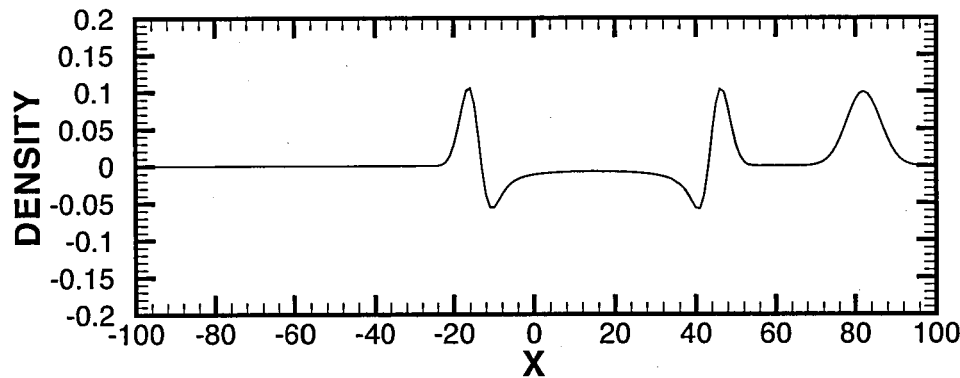
(b) Density Profile Comparison At t=30 (— Computed, - - - Exact)

Figure 3.4: Test Case Using Structured Method

For a more direct comparison between the calculated structured solution and the analytical solution, a second contour plot can be seen in Figure 3.5. For this comparison, the contour plot has been split along the $y = 0$ line. The top half contains the solution calculated using the structured method, and the bottom half of contains the analytical solution. Both halves are plotted using the same contour lines and the same scale. For this comparison the extents of the contour plot have been shortened, allowing for a closer view of the convected density field.

From Figure 3.5 it can been seen that the computed result closely resembles the analytical one. The sixth-order scheme has not caused any local time warping for either the pressure pulse or the vortex. The method has also correctly calculated the convection speed and the expansion of the pressure pulse. This is demonstrated by how closely all of the density contours line up across the $y = 0$ division and how closely the upper and lower regions mirror each other. The uniform grid appears to have had little effect on the shape of both the pressure pulse and the vortex, as expected. For this calculation the length of every cell edge of the mesh is identical, so there should not be any distortion caused by grid non-uniformity.

3.3   Unstructured Method Solutions

To determine accurately the effectiveness of the unstructured method that has been developed, it was tested with three different approximation methods and two different quadrature formulations on three different unstructured meshes. The purpose of this number of tests was to determine the best combination of gradient approximation, quadrature and mesh type for use in completing computational aeroacoustic calculations using the linearised Euler equations. For the sake of brevity, only the best combination of gradient approximation and quadrature is shown on each of the three meshes, and the worst case overall as a comparison. The solutions are compared visually as well as with an error metric calculated using an analytical solution. Results from all the test cases can be seen in Appendix B.

3.3.1   Summary of Uniform Mean Flow Test Case Error Calculations

Examination of the RMS and NRMS error was used to determine the accuracy of the calculations and choose the best combination of gradient approximation and quadrature
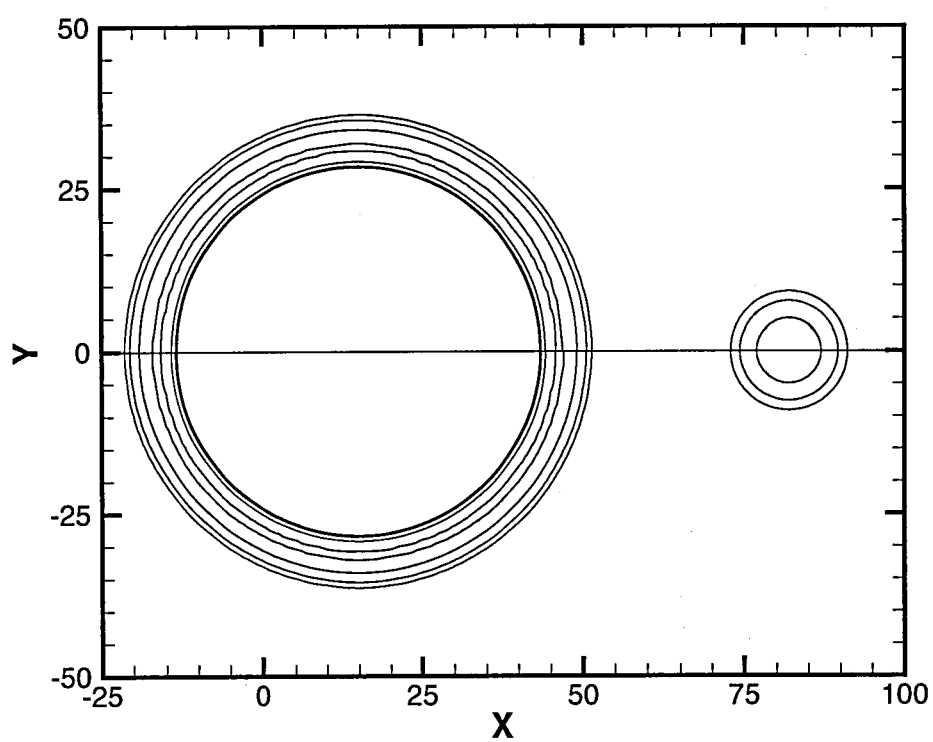
Figure 3.5: Density Contours At t=30 Using Structured Method

reconstruction. One early observation is that the use of two quadrature points instead of just one appears to have little benefit. The RMS errors calculated for the different gradient approximations on the different meshes are summarised in Tables 3.1 and 3.2. The normalized RMS error values for the test calculations can be seen in Tables 3.3 and 3.4. With these tables it can be seen that the accuracy of the gradient approximation is the key factor in these calculations rather than the addition of a second quadrature point. The use of two quadrature points would only be beneficial if if a higher order gradient approximation was used. In almost all cases, the TRI grid has the lowest error. Also, the weighted form of the Least Squares method has a great benefit, almost halving the error as compared to linear Least Squares and Green-Gauss gradient evaluations. It should be again noted that the spatially sixth-order structured method has an RMS error of 0.1826E-03, or 0.11% NRMS error, a tenfold reduction in error compared to the best unstructured calculation. Overall, the weighted Least Squares gradient approximation gives the lowest error when compared to the structured calculation. According to error calculations, the best combination of gradient approximation and mesh type is the use of a weighted Least Squares technique on the TRI mesh, with nearly identical error values with either a single or double quadrature points. The worst combination of gradient approximation method and mesh type is when a Least Squares technique is used on the NEG mesh. Again, the error values calculated with the use of one or two quadrature points is nearly identical.

Mesh	Gradient Approximation Method		
Type	GG	LS	WLS
NEG	0.3870 E-02	0.7317 E-02	0.4646 E-02
UK	0.3518 E-02	0.3403 E-02	0.1844 E-02
TRI	0.3135 E-02	0.3315 E-02	0.1830 E-02

Table 3.1: RMS Error of Single Quadrature Calculations At t=30

Mesh	Gradient Approximation Method		
Type	GG	LS	WLS
NEG	0.3886 E-02	0.7317 E-02	0.4646 E-02
UK	0.3523 E-02	0.3396 E-02	0.1833 E-02
TRI	0.3138 E-02	0.3318 E-02	0.1830 E-02

Table 3.2: RMS Error of Dual Quadrature Calculations At t=30

Mesh	Gradient Approximation Method		
Type	GG	LS	WLS
NEG	2.37	4.48	2.84
UK	2.15	2.08	1.13
TRI	1.92	2.03	1.12

Table 3.3: NRMS Error of Single Quadrature Calculations At t=30

Mesh	Gradient Approximation Method		
Type	GG	LS	WLS
NEG	2.38	4.48	2.84
UK	2.16	2.08	1.12
TRI	1.92	2.03	1.12

Table 3.4: NRMS Error of Dual Quadrature Calculations At t=30

3.3.2 Most Accurate NEG Mesh Calculation

The Green-Gauss approximation method used with one quadrature point is the most accurate calculation on the NEG mesh. The density contours of Figure 3.6(a) show that the pressure pulse and the vortex have both maintained the correct shape and size, and appear to have been calculated correctly. There are dispersion errors indicated by oscillations in the upper right and lower left quadrants of the pressure pulse at this stage, but the amplitude of the oscillations are quite small. This may be a result of the type of mesh used. The NEG mesh has a dominant edge that runs from upper left to lower right for each cell. This characteristic matches the small dispersion oscillations shown in Figure 3.6(a). The fact that these oscillations only occur in these locations seems to support the fact there might be some dependency on distance between nodes for the unstructured method. Looking at other tests completed using the NEG mesh (see Section B.2 in Appendix B) it can be seen that all have characteristic errors in the density contours that correspond to the mesh edge dominance. This error is present in different forms for all three reconstruction methods and with either single or dual quadrature points. The nature of the characteristic errors change with different gradient reconstruction techniques and always seem to have a greater impact on the pressure pulse than the vortex. The calculated density profile shows high accuracy when compared with the analytical solution as seen in Figure 3.6(b). There is a small oscillation and over-prediction of the leading edge of the right hand side of the pressure pulse and a dampening of the trailing edge. These indicate both dispersive and dissipative

effects that were not present in the structured calculation. The use of a Green-Gauss approximation method with one quadrature point on the NEG mesh has an RMS error of 0.3870 E-02 or 2.37% error, more than twenty times larger than that of the structured method.

As with the structured method in Figure 3.5, the unstructured method solution for this test case was also compared with the analytical solution as seen in Figure 3.7. Possible numerical errors created by the unstructured method are more apparent with the pressure pulse than with the vortex. There seems to be a slight acceleration of the interior of the pressure pulse. The outer density contour of the calculated pressure pulse almost perfectly mirrors that of the analytical pulse, but the interior density contour is slightly shifted outward. There is a greater discrepancy with the right hand interior contour than with the left hand contour. There are variations in the location and spacing of all of the interior density contours of the pressure pulse along the $y = 0$ cut, but as stated above all of the errors seem greater in the right hand section. This phenomenon does not appear to be directly related to the inflow condition because not all of the wave components are shifted in the positive x direction, as would be expected if the unstructured method was over-predicting the effect of the inflow velocity field. Since the positions of both the pressure pulse and vortex are correctly simulated by the unstructured method and the fact that the calculated vortex so closely mirrors the analytical one, it can be assumed that the method can accurately model the convection terms of the linearised Euler Equations.
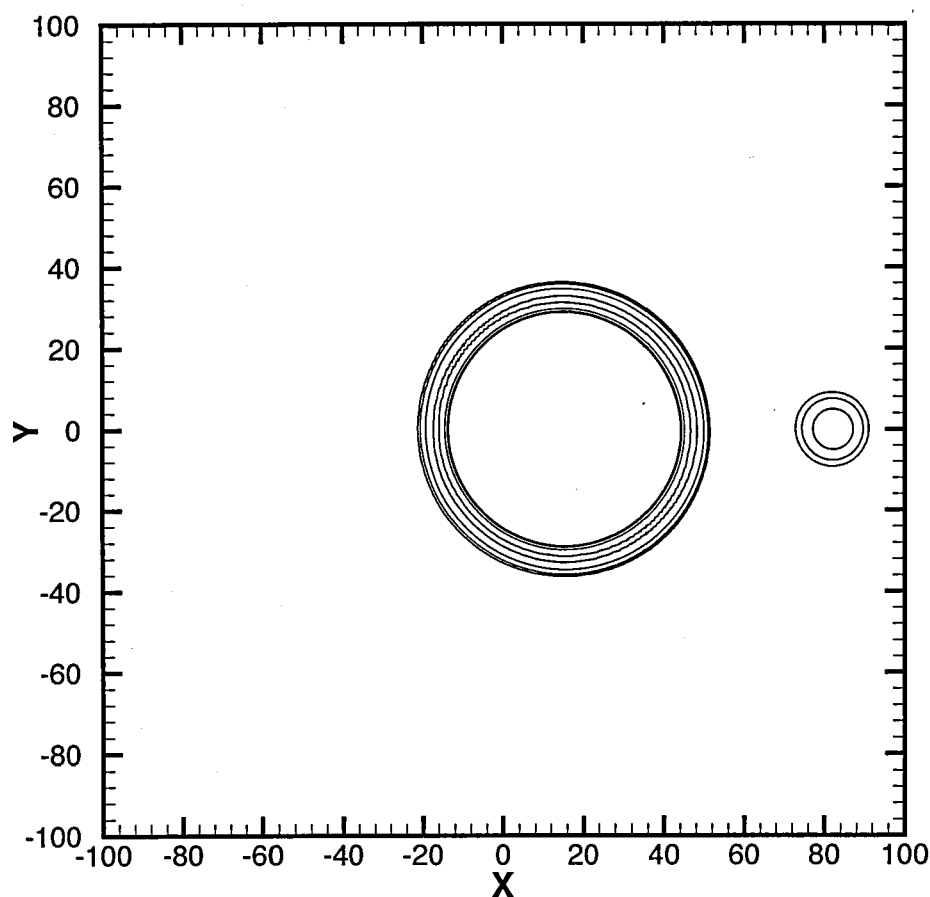
(a) Density Contours At t=30
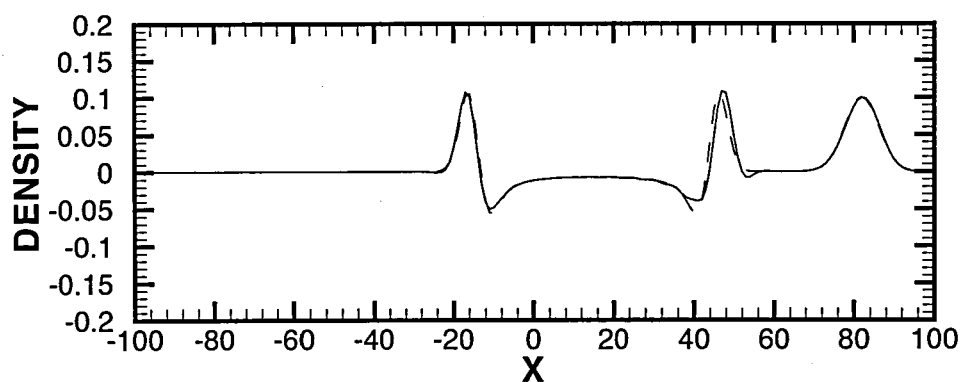
(b) Density Profile Comparison At t=30 (— Computed, - - - Exact)

Figure 3.6: Most Accurate Test Case on NEG Mesh
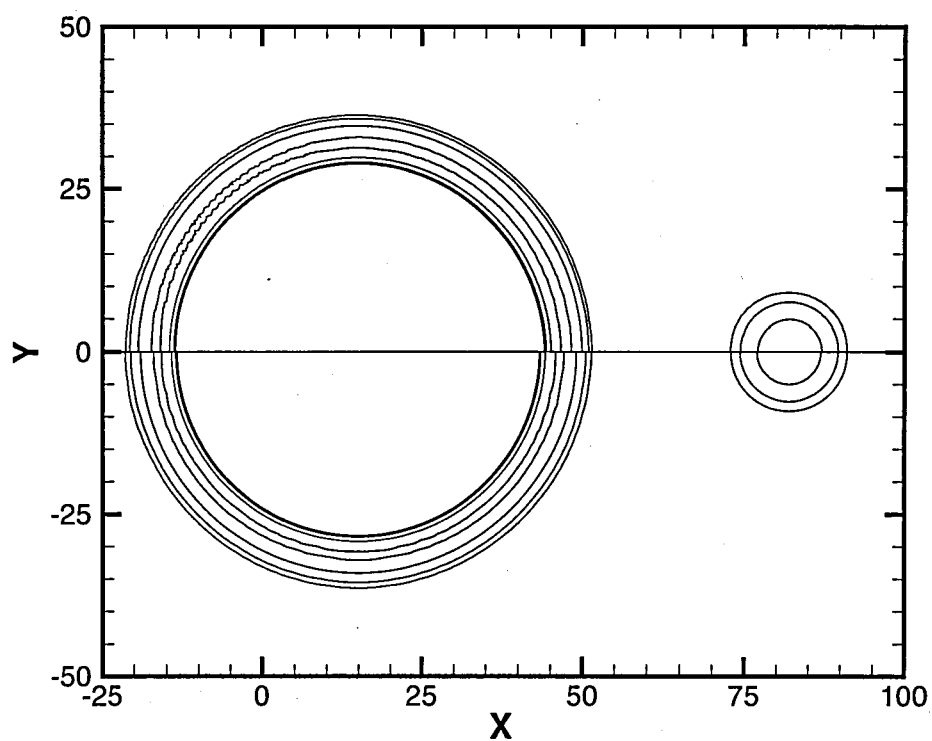
Figure 3.7: Density Contours At t=30 - Most Accurate Test Case on NEG Mesh (2)
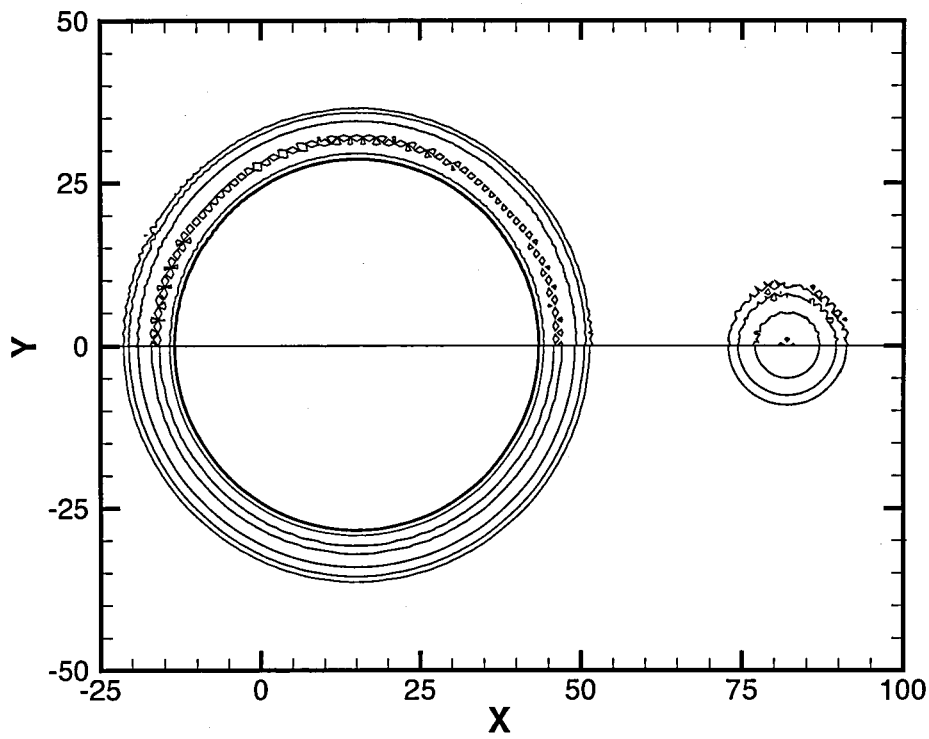
3.3.3   Most Accurate UK Mesh Calculation

The most accurate gradient calculation method used with the UK mesh is the weighted
Least Squares technique used with two quadrature points. As seen in Figure 3.8(a)
the contour plot of the density field after thirty computational time units displays low
amplitude oscillations on both the pressure pulse and vortex. The size and shape of
both the pulse and vortex appear correct, but the UK mesh has caused dispersion
errors. The presence of the alternating dominant cell-edge in the repeating pattern of
the UK mesh has apparently caused a decoupling effect resulting in these small scale
oscillations, however the effect is not strong enough to overpower the correct simulation
of the convection of both the pulse and vortex or the expansion of the pressure pulse.
The dispersive effect also seems to be non-uniform. There is a greater effect on the
interior contours of the density pulse than on the exterior contours, and the vortex
shows pockets of increased sensitivity to the errors. When compared to the rest of the
UK test cases, it becomes apparent that the decoupling dispersive error is caused by the
combination of the UK mesh and the weighted Least Squares reconstruction technique.
For both the Green-Gauss and Least Squares gradient reconstruction techniques the
error is much less visible, seen only as a very slight oscillation in the interior density
contours of the pressure pulse, and not present at all on the vortex, therefore the
dispersion is not directly associated with the use of the UK mesh on its own. The
Green-Gauss and Least Squares results can be seen in Section B.3 of Appendix B.

The density profile shown in Figure 3.8(b) displays the dispersion errors present in
the calculated solution. Although there are numerous areas of dispersive oscillations,
they are all shallow and have not affected the general profile of either the vortex or the
pulse. The vertical portions of the majority of the density profile perfectly correspond
to the analytical solution, except for the oscillations on the trailing edge of the vortex.
The amplitude of the wave is correctly predicted using the unstructured method. The
only errors present in this test case are those small perturbations, there appears to be
no dissipation and little dispersion associated with the combination of weighted Least
Squares gradient reconstruction and two quadrature points. The dispersion errors that
are present effect neither the slope of the faces of the waveforms nor the location and
amplitudes. The error calculated for this test case is 0.1833 E-02 (1.12%), roughly half
that of the best NEG mesh test case, but still an order of magnitude greater than the
error values of the structured test case.

From Figure 3.9 it can be seen that location of the calculated density contours of
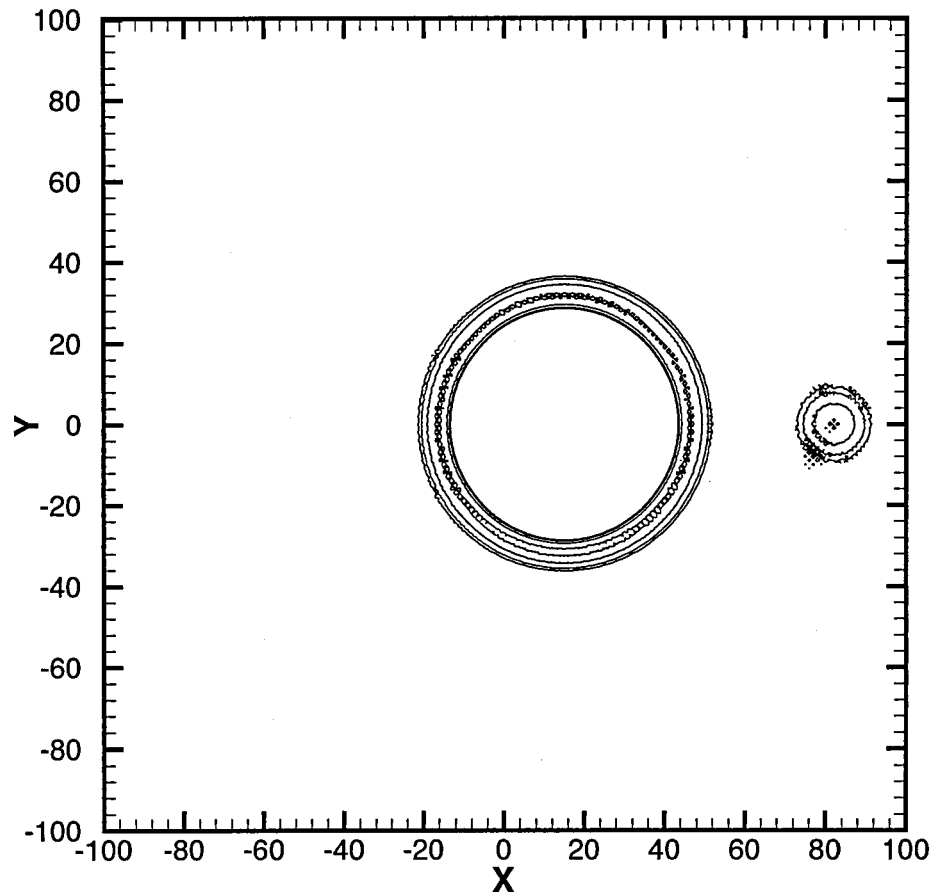
(a) Density Contours At t=30
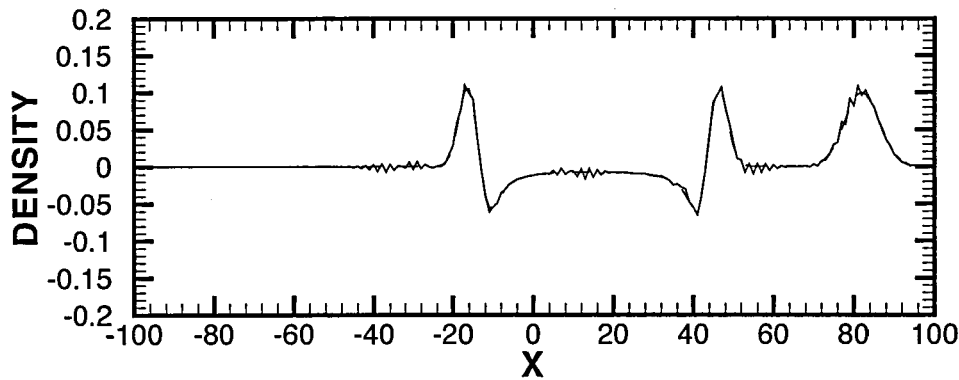
(b) Density Profile Comparison At t=30 (— Computed, - - - Exact)

Figure 3.8: Most Accurate Test Case on UK Mesh

both the pressure pulse and the vortex almost perfectly mirror those of the analytical solution. Even with the dispersion errors present in the interior of the pressure pulse, this test case appears to not to have the pulse expansion error that was present with the NEG meshes. When the other UK mesh test cases are compared to this one using the same 'split' plotting technique, it can be seen that the dispersion error is greatly reduced but the expansion error present in the NEG mesh test cases returns. When the Green-Gauss and Least Squares gradient reconstruction test cases are compared with the analytical solution in plots similar to Figure 3.9, the same outward shift of the interior density contours of the pressure pulse is observed. As with the NEG mesh test cases the outer density contours mirror the analytical solution perfectly, and there is a greater effect on the right hand section than the left. Since these errors span the different mesh types, they cannot be instantly identified as an indication of the unstructured method having a sensitivity to the type of mesh used. As this effect was removed with the use of weighted Least Squares, it appears to be related to the gradient reconstruction method.

Figure 3.9: Density Contours At t=30 - Most Accurate Test Case on UK Mesh (2)

3.3.4 Most Accurate TRI Mesh Calculation

The most accurate gradient approximation method used with the TRI mesh is the weighted Least Squares method with the use of two quadrature points. The contour plot seen in Figure 3.10(a) shows some error in the downstream portion of the pressure pulse. Overall, the pressure pulse show little distortion or dispersion errors, and other than the slight error introduced in the leading portion both the convection and the expansion of the pulse appear to be modeled accurately. The vortex is accurately convected, with little or no dispersion or dissipation. The shape and size of the vortex has been maintained for the duration of the calculation. The dispersion errors of the pressure pulse are contained within the waveform as the errors do not appear present on the most exterior or interior density contours. The interior density contours that are broken in the downstream portion of the pressure pulse appear to be relatively symmetrical about the x-axis. When the results of the weighted Least Squares gradient reconstruction method are compared with the Green-Gauss and Least Squares reconstruction methods, the dispersion errors disappear. The density contours for both the Green-Gauss and Least Squares techniques more closely resemble the concentric circles of the analytical solution. This means that the dispersion error of this TRI mesh test case (as with the UK mesh) appears to be dependent on the weighted Least Squares reconstruction method not the mesh type. The results of other test cases using the TRI mesh can be found in Section B.4 of Appendix B.

Looking at the comparison of the density profiles, as seen in Figure 3.10(b), a slight error in the leading edge of the pulse can be seen as the calculated profile shows dispersion error with a small oscillation just behind the front of the pulse. There appears to be a slight phase lag in the downstream portion of the pressure pulse. The vortex is accurately calculated and the small leading edge error has decreased at the following edge. The vortex seems to be perfectly convected downstream, and the only errors are associated with the pressure pulse. When compared to the TRI mesh test cases using the other two reconstruction techniques, the density profiles show different regions of error. The weighted Least Squares technique shows dispersion error and a slight phase lag in the right hand portion of the pressure pulse. The Green-Gauss and Least Squares techniques show a lower dispersion error and a slight phase shift ahead of the analytical solution. Since the mesh does not change for these tests, the errors mush be caused by the reconstruction technique, not the mesh type. As with the NEG and UK mesh expansion error, there is a greater error present with the right hand or downstream

portion of the pulse.

The lowest RMS error calculated on a TRI mesh was completed using the weighted Least Squares approximation and has an error of 0.1830 E-02 (1.12%), very similar to that of the weighted Least Squares calculation completed on the UK mesh. It is important to note that the error values when using the weighted Least Squares reconstruction technique for both the UK and TRI meshes are lower by a factor of two than with either of the other gradient methods, even though the contour plots show a closer resemblance between the other techniques used and the analytical solution.

By referring to Figure 3.11 it can be seen that for the first time there is a slight widening of the pressure pulse. The density contours of the pressure pulse calculated using the weighted Least Squares reconstruction method appear more widely spaced than the corresponding analytical contours. This error appears on both the downstream and the upstream sections of the pressure pulse. The dispersion error that was noticed with the UK mesh is still present, but only effects the pressure pulse. The vortex has been perfectly convected downstream and the density contours of the calculated solution mirror those of the analytical one. By comparing the result of this test case with all other calculations completed on the TRI mesh, it can be seen that in every case the vortex shows no dispersive or dissipative errors whatsoever. It can also be seen that there is a similar trend to how the gradient reconstruction method effects the pressure pulse. As with the UK meshes the use of the weighted Least Squares reconstruction technique changes the nature of the numerical errors in the calculated solution. When both the Green-Gauss and Least Squares techniques are used the density contour plot resemble each other and the error values calculated with both are similar as well. When the reconstruction technique changes to the weighted Least Squares method the contour plot changes, and the error is decreased by a factor of 2. For the test cases completed using the TRI mesh the same phenomenon seen with the UK meshes reappears namely the dispersion error is greatly reduced but the expansion error present in the NEG mesh test cases returns when the Green-Gauss and Least Squares gradient reconstruction techniques are used. As with the previous mesh types the solutions of all of the test cases completed on the TRI mesh can be seen in Appendix B, specifically in Section B.4.
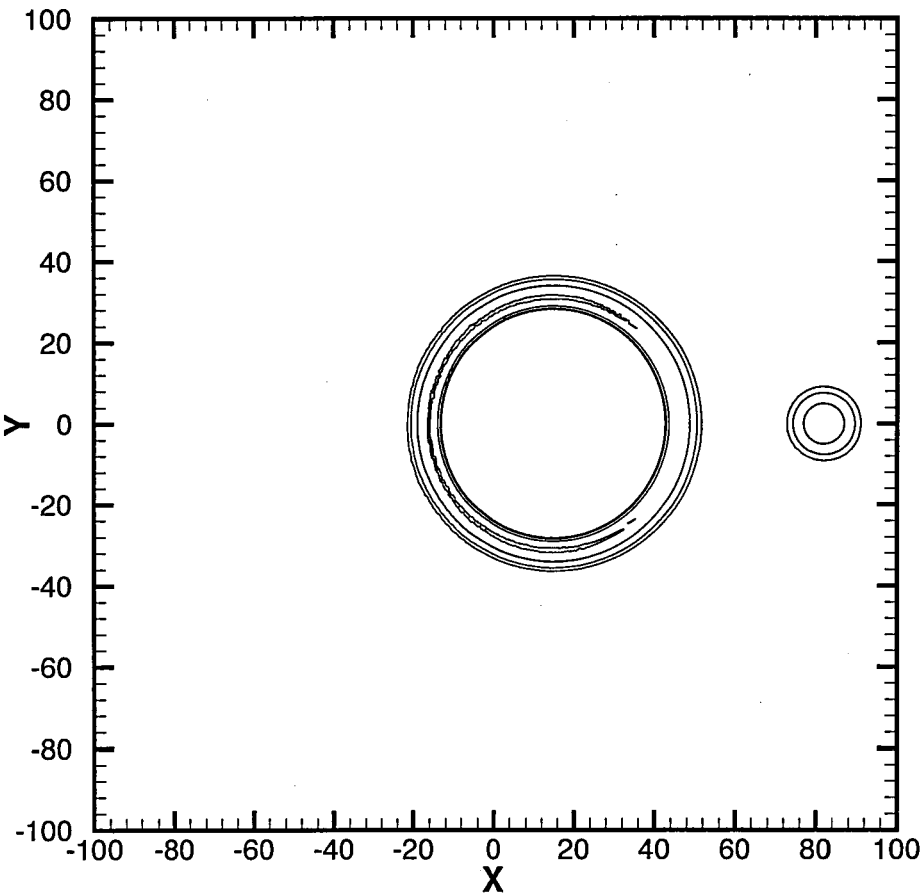
(a) Density Contours At t=30
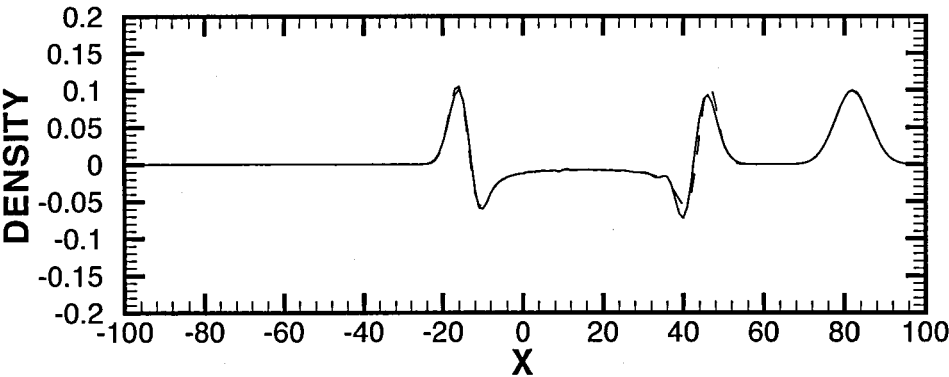
(b) Density Profile Comparison At t=30 (— Computed, - - - Exact)
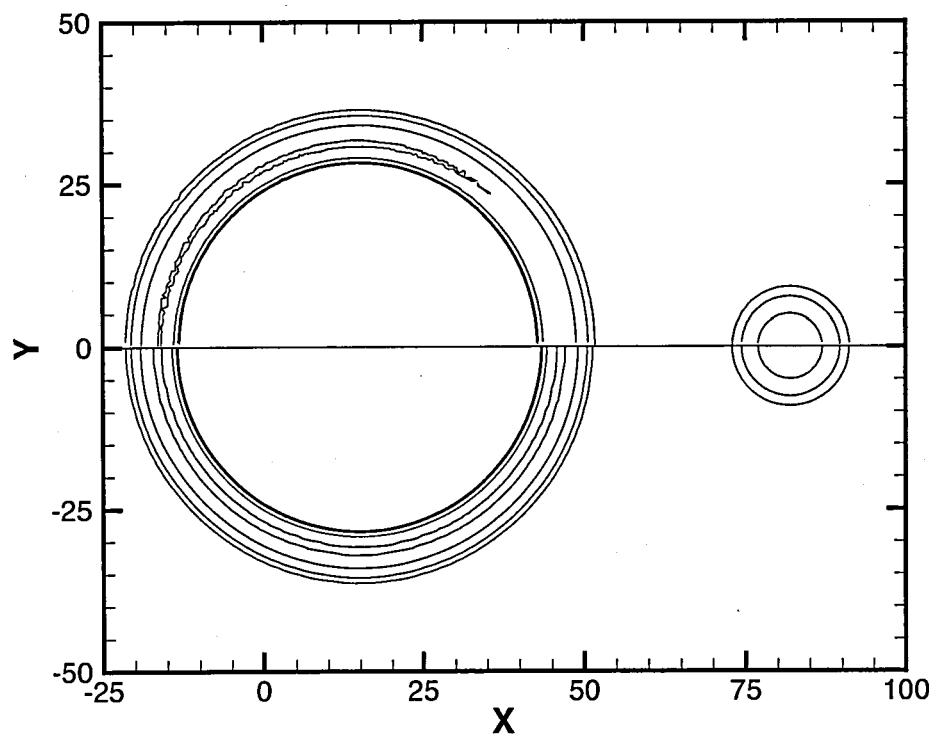
Figure 3.10: Most Accurate Test Case on TRI Mesh

Figure 3.11: Density Contours At t=30 - Most Accurate Test Case on TRI Mesh (2)

3.3.5 Least Accurate Calculation

This calculation shows that a poor selection of gradient approximation, quadrature and mesh type can combine to severely decrease the accuracy of the unstructured method. The least accurate combination of mesh type and gradient approximation used to calculate a solution for the uniform mean flow problem is the Least Squares method using two quadrature points on the NEG mesh. Looking at the contour plot of the calculated solution, as in Figure 3.12(a), it can be seen that the pulse has become elongated along the long-edge direction of the mesh. This error was present in the earlier NEG mesh calculations, but the combination of this mesh and the Least Squares reconstruction technique has amplified the effect. The peak of the pulse has been affected as well, and a leading edge error caused an oscillation in the lower left quadrant of the pulse. This error also lies along the same direction of the dominant edge of the NEG mesh. The vortex has also been affected, appearing slightly out of round at this point in the calculation. The pressure profile plot shown in Figure 3.12(b) confirms what was shown with the contour plot. There is a definite error in the pressure pulse, with both the leading edge and trailing edge of the pulse showing a slight phase error and oscillations. There is also evidence of the errors in the downstream section of the pressure pulse being more pronounced. The vortex also appears to be slightly out of phase,with the calculated peak in the profile just in front of the analytical peak. The Least Squares calculation on the NEG mesh has an RMS error of 0.7317 E-02 (4.48%) the largest error of the unstructured calculations completed and 40 times that of the structured test case.

The direct comparison of the density contours from this test calculation and those of the analytical solution can be seen in Figure 3.13. As stated previously the combination of the NEG mesh and the Least Squares gradient approximation appear to be the most vulnerable to error. Both the pressure pulse and the vortex show the effects albeit to different extents. The vortex appears to be less effected by the error with the density contours of the unstructured calculation slightly advanced compared to those of the analytical solution. It appears as though the location of the center of the vortex has been predicted ahead of where it should truly lie. The pressure pulse also shows a time warping effect as the pulse is slightly larger than it should be and shifted downstream. This expansion error, seen in previous test cases to a lesser degree, appears to be caused by the numerical method accelerating the expansion and convection of the pressure pulse.

To determine whether or not the strong error of the test case with a Least Squares
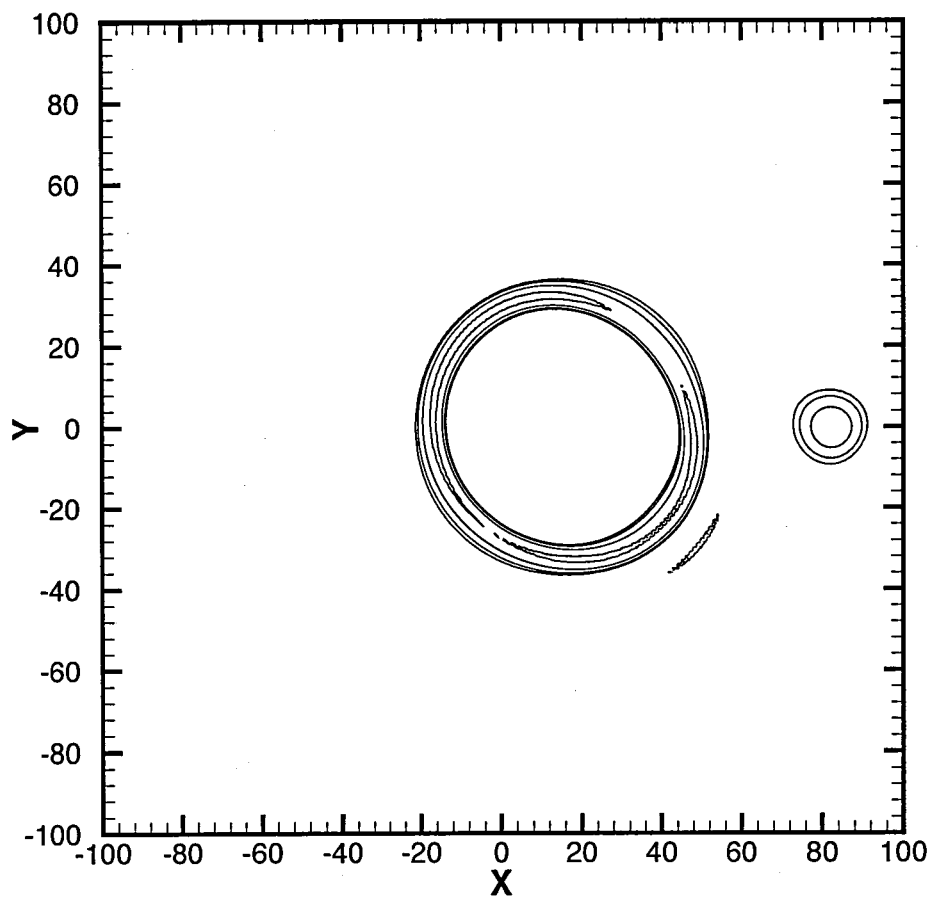
(a) Density Contours At t=30
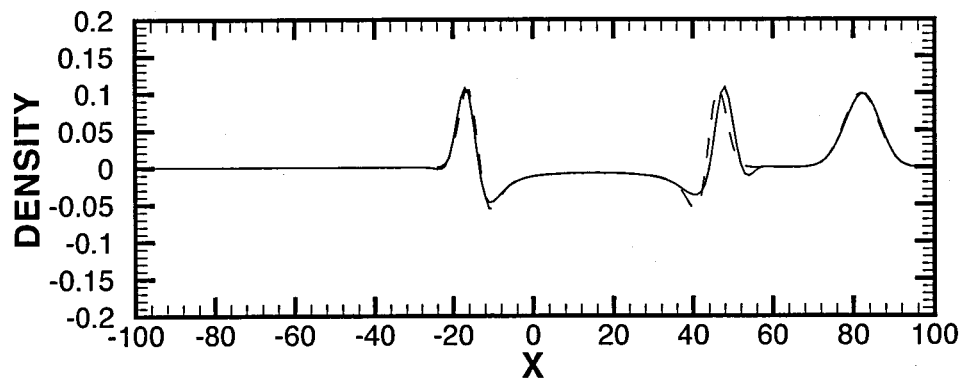
(b) Density Profile Comparison At t=30 (— Computed, - - - Exact)
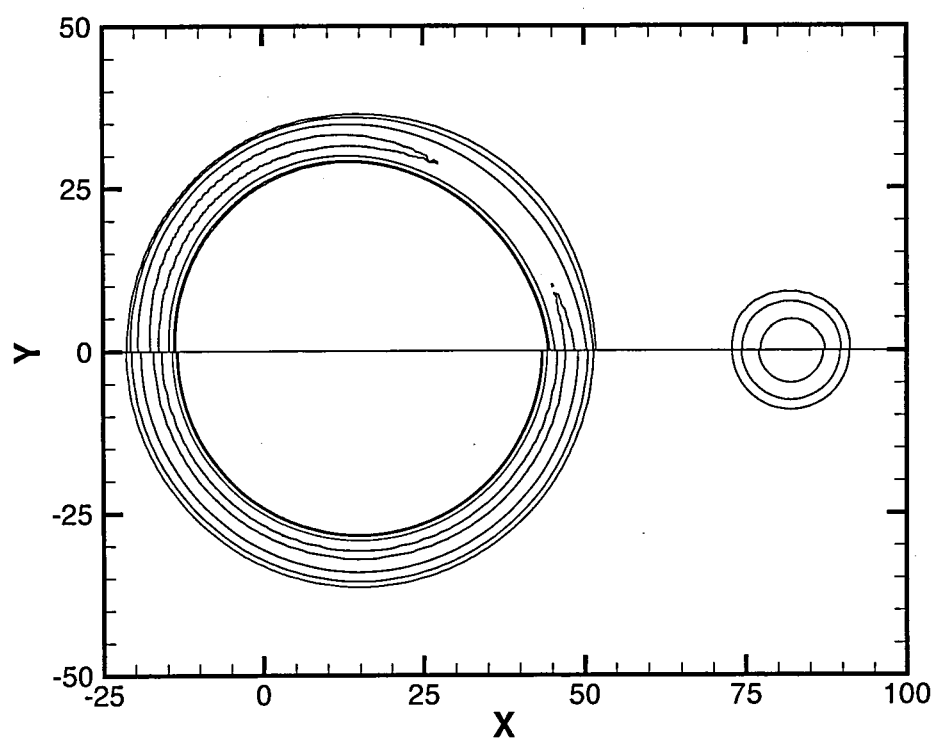
Figure 3.12: Least Accurate Unstructured Case

Figure 3.13: Density Contours At t=30 - Least Accurate Unstructured Case (2)

gradient approximation on the NEG mesh was directly dependant on the NEG mesh, an extra calculation was run. This test case involved the same specifications for the numerical method options, namely 2 quadrature reconstruction points and the Least Squares gradient approximation, but the NEG mesh was replaced with the similarly constructed POS mesh mentioned previously in Section 2.4.3 of Chapter 2. The POS mesh has the same repeating dominant primal cell edge as the NEG mesh, but instead of having negative slope, the dominant edges have a positive slope. The results of the POS mesh calculation can be seen in Figures 3.14(a) and 3.14(b). The density contours of Figure 3.14(a) confirm that the distortion and dispersion errors of the NEG mesh Least Squares approximation test case were caused by the NEG mesh. By changing the slope of the dominant edge the same pressure pulse/vortex distortion and dispersion error was recreated in a different location. The density contours of the POS mesh test case appear identical to those of the corresponding NEG mesh test case when flipped about the x-axis. The density profile of the POS mesh, seen in Figure 3.14(b), appears identical to that of the NEG test case. This was to be expected as the density profile is taken along the x-axis, the line of symmetry between the two cases. Along with this graphical comparison, the RMS error of the POS test case with 2 quadrature points and the Least Squares gradient approximation was 0.7315 E-02, an NRMS error of 4.48%, nearly identical to that of the corresponding NEG test case.

The comparison of the POS test case density contours and those of the analytical solution can be seen in Figure 3.15. The same pressure pulse acceleration error present in the corresponding NEG calculation can be seen along the comparison line as well as the dispersion error. The greatest effect of the dispersion error for this test case is the low-magnitude wave that has been cast off of the upper right quadrant of the pressure pulse. This dispersive wave was also present in the NEG calculation, but in the lower right quadrant corresponding to the orientation of the dominant cell edge. These results, especially taken with those seen in Figure 3.13, confirm the effect of the specific formulation of the NEG semi-structured mesh.
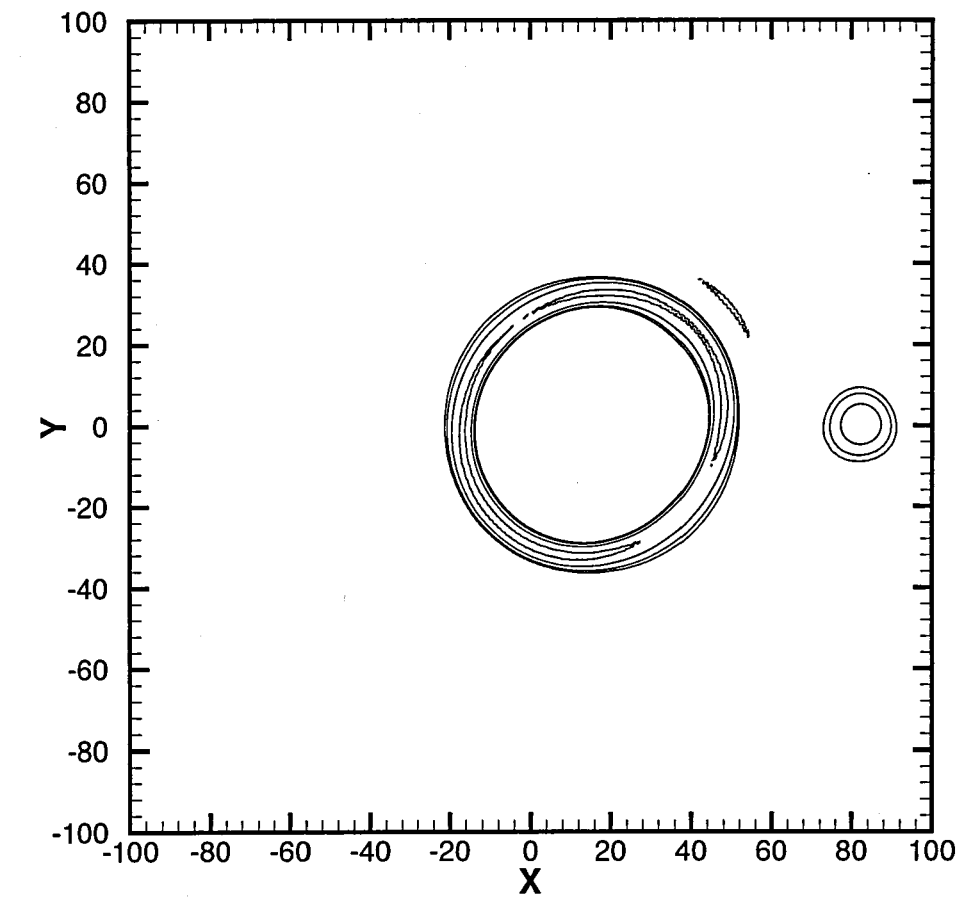
(a) Density Contours At t=30
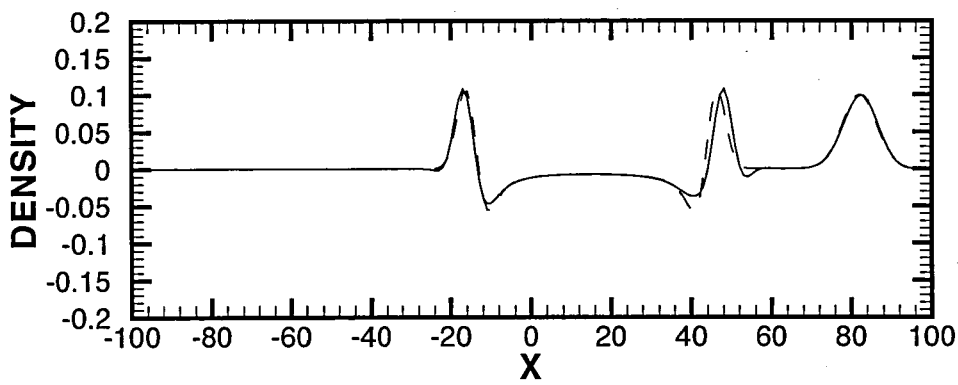
(b) Density Profile Comparison At t=30 (— Computed, - - - Exact)

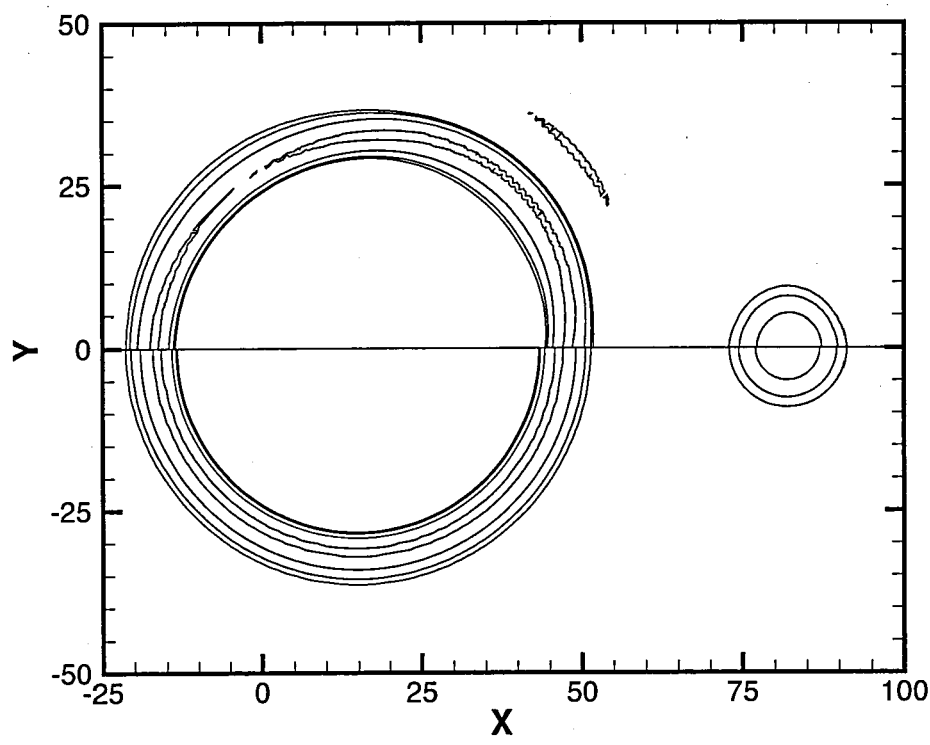Figure 3.14: POS Mesh Unstructured Case

Figure 3.15: Density Contours At t=30 - POS Mesh Unstructured Case (2)

3.4   Comparison of Test Case Solutions with Published Results

In the CAA Benchmark Workshop [33], there are six different researchers that also completed calculations for the uniform mean flow problem. All six of the papers included in the proceedings that completed these calculations used high-order accurate structured methods. Of the six sets of results discussed, most were completed using a spatial discretisation of fourth-order accurate or better. Only one paper of the six, that of Nark [51] used anything less than a fourth order accurate spatial discretisation and in this case Nark used a staggered scheme incorporating both a 2nd and 4th order accurate method. The results published by Nark confirmed that the 2nd order accurate spatial discretisation experienced dispersion errors and the method used lost resolution of the leading edge of the pressure pulse [51]. The remaining researchers all presented results with little or no discernible error, results which appear very similar to the calculations completed with the structured method developed as part of this research. The work presented by Tam et al. [67] was completed using Tam's DRP method. This method used a 7-point stencil to give an approximately 6th-order accurate spatial discretisation. The DRP stencil is coupled with Tam's LDDRK method, a modified 4th-order Runge-Kutta temporal discretisation specifically tuned for use with aeroacoustic problems. The results of Tam et al. mirror those of the structured calculation completed as part of this research and have been reproduced from the Benchmark Proceedings in Figures 3.16 and 3.17. The density contours displayed in Figure 3.16 refer to density levels different from the ones used to display previous results, but the overall shape and resolution of the pressure pulse and vortex can be observed. The density profile of Figure 3.17 is plotted in a similar fashion to previous density profiles. The calculated result is displayed as a solid line along with the analytical result, which is displayed as a dashed line. In this particular case, the two profiles lie directly on top of one other for the entire domain

The same DRP/LDDRK method was employed by Chung and Morris [15], along with selective artificial dampening, with similar results. Another method presented in the Benchmark Workshop is that of Fung et al. [30]. This method used a compact finite-difference method with implicit time discretisation to get calculations that were 4th order accurate in space and 2nd order accurate in time. The results published by Fung et al. in the CAA Benchmark Proceedings have been reproduced in Figure 3.18. As with the Tam et al. results reproduced above, the density contours depicted in Figure 3.18 are not the same contours specified with previous results. However, this does not
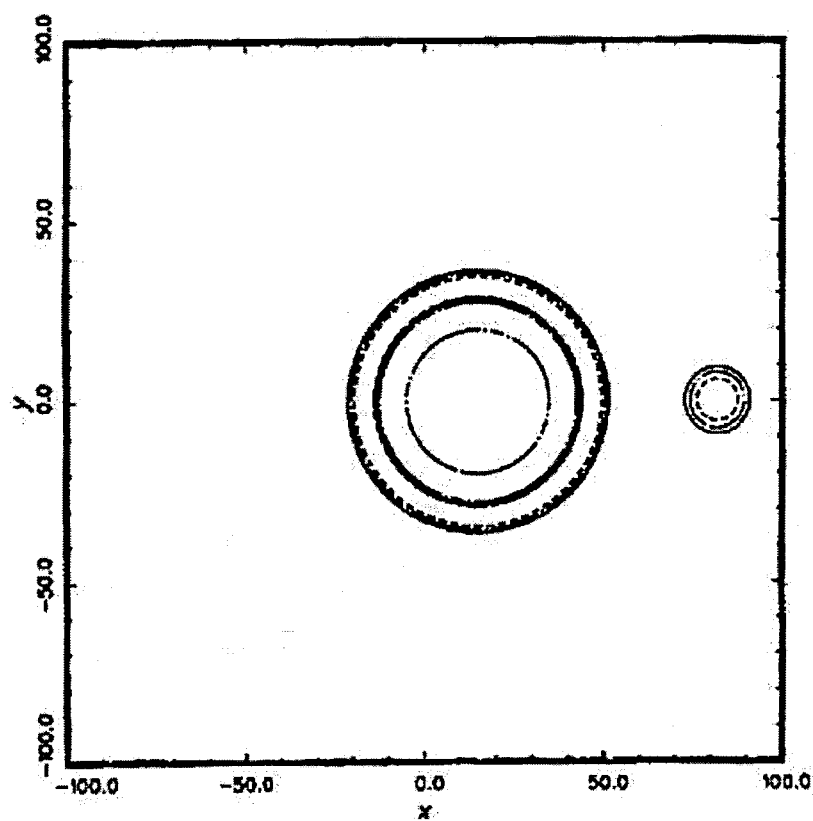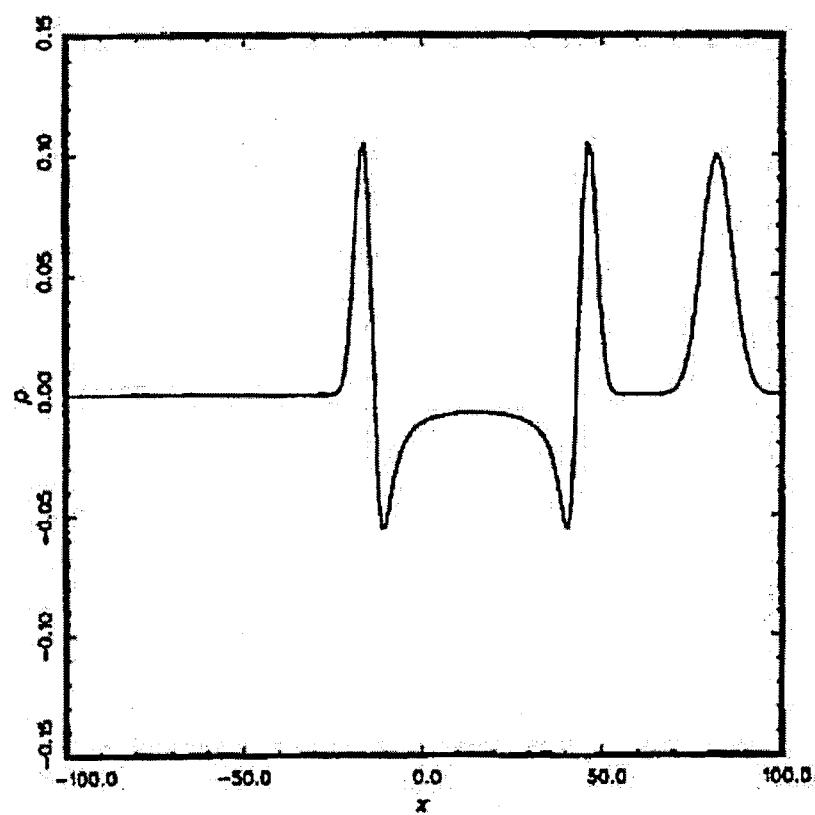
Figure 3.16: Density Contours At t=30 - Tam et al. [67]

Figure 3.17: Density Profile Comparison At t=30 - Tam et al. [67]
— Computed, - - - Exact

alter the observation that the results of Fung et al. show smooth and concentric density contours which give no indication of dispersion error. In this case, both the pressure pulse and the vortex appear to have been modeled accurately, indicating a numerical method with high accuracy and little or no dispersion or dissipation. Although the experimental results contained within the Benchmark Proceedings all seem to reflect the ability of numerous methods to accurately model this problem, they show no proof of being any more accurate than the very basic standard 6th-order accurate structured method completed as part of this research. What is important to note is that none of the methods described attempted to develop an unstructured approach for this problem.
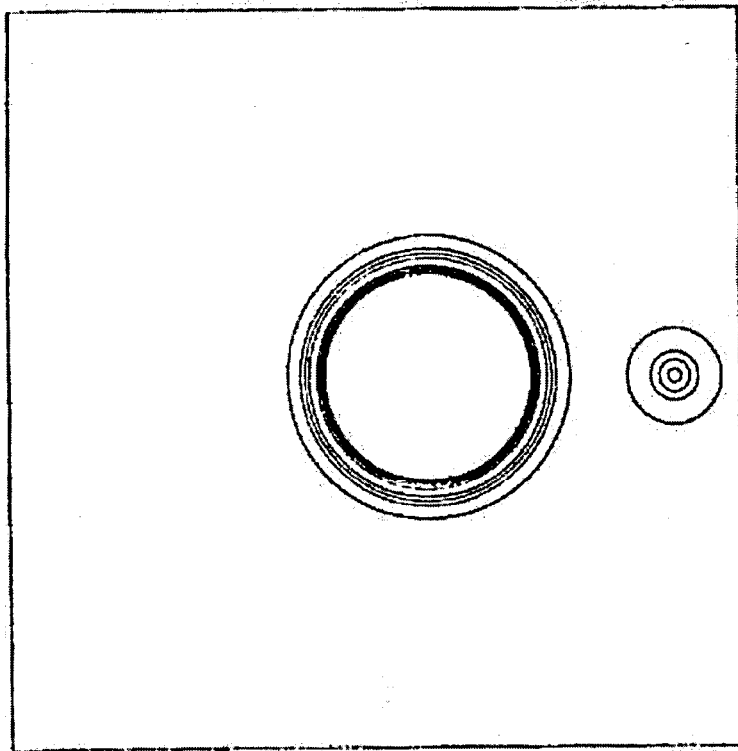
Figure 3.18: Density Contours At t=30 - Fung et al. [30]

3.5   Summary of Results

Upon completion of the series of uniform mean flow test cases the results were compared both numerically and graphically. The numerical comparison was completed by calculating the difference between the calculated density field and that of the analytical solution using RMS and NRMS error calculations. The graphical comparison was completed by visually inspecting contour plots of the density fields of the solutions as well as density profiles along the x-axis and comparing calculated results with the analytical solution. Using these two comparison methods the best combination of gradient approximation and quadrature reconstruction technique was determined. The effect of the different mesh types was also investigated.

When comparing the error values of the different test cases the NEG mesh had the highest error and the TRI mesh almost always had the lowest error. The dominant edge of the semi-structured NEG mesh and the fact that it is always in the same orientation for every cell appears to have an overpowering effect on the unstructured method. The use of the weighted Least Squares gradient approximation consistently created the lowest RMS error for different mesh types. It was therefore no surprise that according to RMS comparisons the best overall combination of mesh type and gradient approximation used to calculate solutions to the uniform mean flow problem included using a weighted Least Squares approximation on a TRI mesh. For this combination of gradient and reconstruction method, there was no discernable difference between the use of a single or dual quadrature points. In fact for all of the calculations the change between one and two quadrature points had little or no effect. This is believed to be due to the use of low order gradient approximations. If higher order gradient approximations were used it is believed that there would be a appreciable effect with the use of higher order quadrature reconstruction.

When comparing the test case solutions graphically the conclusions drawn were similar to those associated with the error calculations. The change from a single to dual quadrature reconstruction points has no discernable effect in the density contour plots or the density profile comparisons. The NEG mesh had the greatest effect on the test case results as well, causing warping of the pressure pulse and vortex. The pressure pulse was stretched in a direction corresponding to the dominant edge of the NEG mesh, a result of the repeating cell shape as confirmed by the POS mesh calculation. There also appeared to be an acceleration or compression of the pressure pulse when the Green-Gauss and Least Squares gradient approximation methods were used. This

acceleration error was present with all three unstructured mesh types and had a greater effect on the downstream portion of the pressure pulse than the upstream portion. Both the Green-Gauss and Least Squares formulations contain terms which make the approximated gradients directly proportional to the distance between calculation nodes (in this case the nodes correspond to cell vertices). In the weighted Least Squares formulation, similar terms make the approximated gradients inversely proportional to the distance between nodes. This proportionality is believed to be the cause of the acceleration error. This is supported by the fact that the test case completed with the weighted Least Squares gradient approximation on the UK mesh does not show this acceleration error at all, and on the TRI mesh the pulse seems to have been effected in the opposite way, with a deceleration or flattening of the pressure pulse.

Although the use of the weighted Least Squares gradient approximation was least effected by the acceleration error it appeared to be the only method with dispersion errors. These errors, though small, were visible on all three mesh types. The test case which showed the largest dispersion error was completed using the UK mesh. The combination of the dispersion error caused by the weighted Least Squares method and the alternating dominant edge of the UK mesh created a decoupling effect resulting in high frequency errors visible in both the contour plot and density profile. This dispersive error was also present in the TRI mesh test case, but to such a small degree that the error values were still the lowest of all the unstructured calculations. With these results in mind, the decision was made to use only the weighted Least Squares gradient approximation technique with a single quadrature point to complete calculations for the scattering problem. The method was still used with the three different mesh types to see if the same error characteristics remained with the more complex acoustic simulation.

Chapter 4

Scattering Problem

4.1 Introduction

The purpose of the scattering problem is to determine the ability of the unstructured method to simulate accurately the interaction of a pressure pulse and a solid cylinder. This problem mirrors the real-world scenario of the effect the fuselage has on the noise created by an engine on the wing of an aircraft. The scattering problem description is taken from the Workshop on CAA Benchmark Problems [64] and is listed as Category 1, Problem 2. As with the uniform mean flow problem, numerical characteristics such as dissipation, dispersion, mesh dependency and overall accuracy are used to evaluate the effectiveness of the method developed.

4.1.1 Test Case Description

The general layout of the scattering problem can be seen in Figure 4.1. To determine the effect the cylinder has on the flow field the pressure at three different locations in the domain is recorded throughout the simulation. The three pressure locations labeled A, B, and C are indicated along with their proximity to the cylinder. The cylinder used for the scattering problem has a diameter of one non-dimensional unit and is located at the origin. The three pressure locations are all located at 5 cylinder diameters away from the origin in the positions shown in Figure 4.1, $\theta_A = 90^o$, $\theta_B = 135^o$ and $\theta_C = 180^o$. The point labeled as S is the location of the initial pressure pulse, 4 diameters away from the origin at $\theta_S = 0^o$.

4.1.2 Governing Equations

The governing equations for this problem are used to solve for the variables of density, pressure and velocity. The linearised Euler equations used for this specific problem, previously seen as Equation 2.1, are written as:

$$\frac{\partial W}{\partial t} + \frac{\partial F}{\partial x} + \frac{\partial G}{\partial y} = 0$$

where,

$$W = \begin{bmatrix} u \\ v \\ P \end{bmatrix} , F = \begin{bmatrix} P \\ 0 \\ u \end{bmatrix} , G = \begin{bmatrix} 0 \\ P \\ v \end{bmatrix} \tag{4.1}$$

These equations differ slightly from those of the uniform mean flow problem. This is due to the fact that there in no uniform velocity field interacting with the pressure pulse, or $M_x = M_y = 0$. This creates a special condition where the continuity and energy equations collapse and become equivalent, so only one is needed. In this particular case the pressure is maintained and both the conservation of energy and conservation of mass equations are satisfied.

In order to ease the development of the structured code, the governing equations
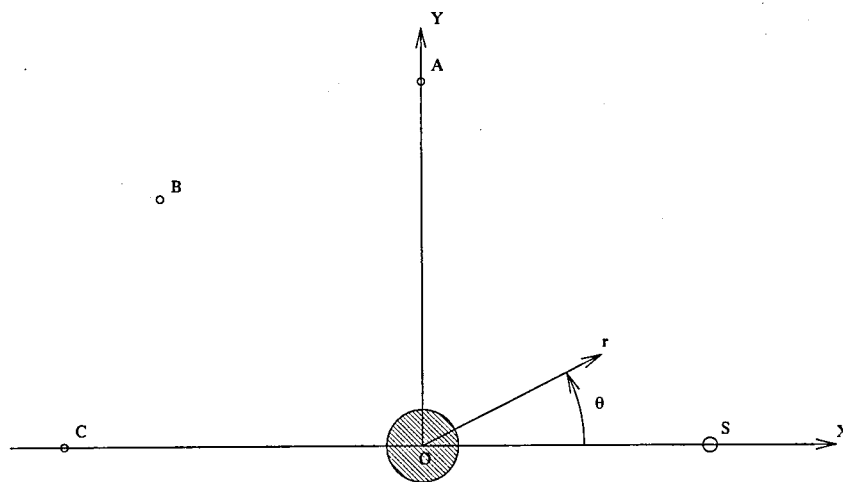
Figure 4.1: Schematic of Scattering Problem

for this problem are rewritten into cylindrical coordinates. The change from Cartesian coordinates to cylindrical coordinates is prompted by the boundary conditions. For this particular problem, the use of cylindrical coordinates makes the determination of boundary conditions along the curved surfaces and mesh edges far simpler than with the use of a Cartesian formulation. The governing equations, written in cylindrical coordinates, become

$$\frac{\partial U_r}{\partial t} + \frac{\partial P}{\partial r} = 0 \tag{4.2}$$

$$\frac{\partial U_\theta}{\partial t} + \frac{1}{r}\frac{\partial P}{\partial \theta} = 0 \tag{4.3}$$

$$\frac{\partial P}{\partial t} + \frac{\partial U_r}{\partial r} + \frac{1}{r}\frac{\partial U_\theta}{\partial \theta} + \frac{U_r}{r} = 0 \tag{4.4}$$

where the variables U_r and U_θ refer to the radial and circumferential velocities, respectively. In this Benchmark problem the freestream is at rest and $M_x = M_y = 0$.

4.1.3 Test Case Domain

The computational domain of the scattering problem is described by a circular mesh with a diameter of 30 units (30 cylinder diameters). The entire cylinder is surrounded by continuous mesh which is divided into 600 equal circumferential segments and 290 equal radial segments. This creates a basic mesh with 174,000 cells. There are only two boundaries for this problem, the first represented by the cylinder at the origin and the second external boundary 15 diameters from the center of the domain.

4.1.4 Initial Conditions

The initial condition specified for the scattering problem states that at $t = 0$ a pressure pulse located at $(4, 0)$ is created using

$$P = \exp\left[-(\ln 2)\left(\frac{(x-4)^2 + y^2}{(0.2)^2}\right)\right] \tag{4.5}$$

and all other variables are equal to zero, or $u = v = 0$. When written in cylindrical coordinates, this initial condition becomes

$$P = \exp\left[-(\ln 2)\left(\frac{r^2 - 8r\cos\theta + 16}{(0.2)^2}\right)\right] \tag{4.6}$$

with $U_r = U_\theta = 0$. The time step is set to $\Delta t = 0.01$ as defined in the Workshop manual [64] and the value of the pressure field at points A,B and C are recorded for the time $t = [6, 10]$.

4.1.5 Boundary Conditions

There are two boundary conditions specified for the scattering problem. There is an outflow boundary condition imposed at the outer circular boundary ($r = 15$) and a solid boundary condition imposed at the inner circular boundary ($r = 0.5$)

Solid Boundary Condition

The solid boundary condition used at the inner boundary is applied to only the pressure and radial velocity. To simulate accurately the solid wall of the cylinder, a condition is applied wherein the pressure gradient normal to the cylinder is equal to zero, and there is no radial component of the velocity field. That is

$$\frac{\partial P}{\partial r}\bigg|_{r=0.5} = 0 \tag{4.7}$$

and

$$U_r|_{r=0.5} = 0 \tag{4.8}$$

Outflow Boundary Condition

The outflow boundary condition used at the outer boundary is applied on all three of the state variables. The condition applied is used to force the normal gradient of both the velocity and pressure fields to be equal to zero at the outer edge of the domain. The condition is applied directly onto the last mesh vertices at $r = 15$ and can be written as

$$\frac{\partial W}{\partial r}\bigg|_{r=15} = 0 \tag{4.9}$$

4.1.6   Test Case Solution

The pressure profiles of the solution to the scattering problem can be seen in Figure 4.2. These pressure profiles were recreated from data published in the Second CAA Benchmark Workshop Proceedings [64]. These are the solutions that all test cases will be compared with to determine accuracy of both the structured and unstructured numerical methods.
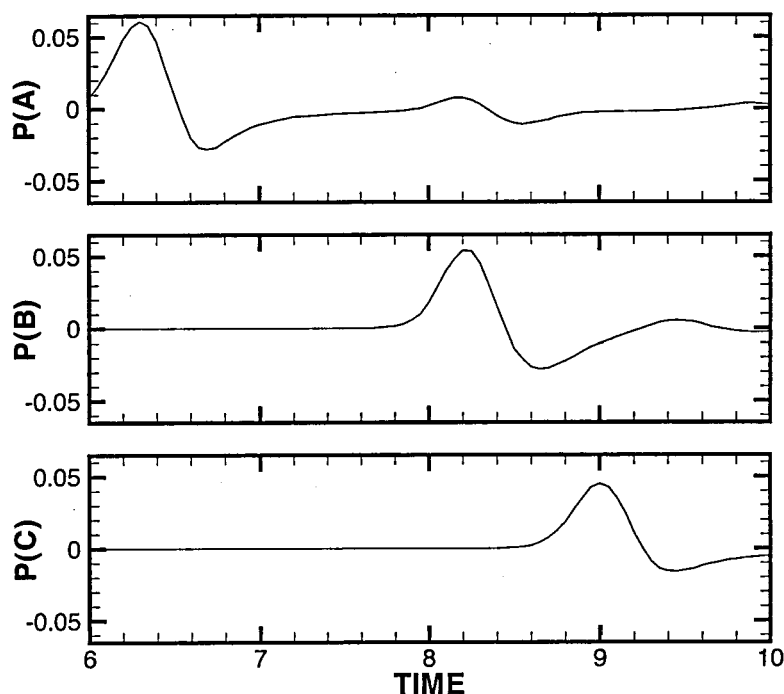
Figure 4.2: Pressure History for Reference Points - Reference Solution

4.2   Scattering Problem Solution on Structured Mesh

Before the unstructured calculations were completed, a structured method was used to determine a solution to the scattering problem to use as a comparison. The structured method used for this calculation has a fourth-order accurate central-difference spatial

discretisation. The pressure contours at ten time units of the structured method calculation can be seen in Figure 4.3. The pressure contours are symmetric about the x-axis for both the initial pressure pulse and the scattered pulse. The initial pulse has not shifted position, it is still centered at $(4,0)$ and the scattered pulse is centered on the cylinder. The correct shape and positioning of the two pulses indicate that there is little or no phase error in the approximation of the pressure pulse and also no local time warping causing a shift in the location of the center of the pulses. There is evidence of some low-magnitude dispersion with the small pressure wave ahead of the right-hand portion of the scattered pressure pulse. There appears to be no evidence of any dissipation error in the original pressure pulse as the pressure contours remain concentric and closely spaced after 10 time units ($t = 10$). These results demonstrate the high accuracy and low-error characteristics of a standard 4th-order central-differencing approximation.

When looking at how the pressure field develops over time, the accuracy and low dispersion and dissipation of the structured method is easily observed. The pressure contours shown in Figure 4.4 correspond to the pressure fields at 2.5, 5.0, 7.5 and 10.0 computational time units. All of the pressure fields are displayed with the same contour levels. All four of the pressure contour plots show that the pressure pulse has remained symmetrical and in the correct location for the entire calculation. The concentric nature of the pressure contours also indicate a low level of dispersive and dissipative error.

The pressure profiles from the structured calculation, displayed in Figure 4.5, show the high level of accuracy of the structured method. The first profile, corresponding to location A in Figure 4.1, shows no dispersion or dissipation. There is a small difference between the computed solution (indicated by the solid line) and the solution taken from literature [64] (indicated by the dashed line). The only discrepancies for the A profile occur as a slight phase shift on the peak at 6.3 time units and a small under-prediction of the pressure at 8.2 time units.

Looking at the profile associated with the point at location B in Figure 4.5, the accuracy of the structure method is confirmed further. There is only a slight phase difference with the pressure peak at 8.2 time units. There is also a very slight under-prediction of the pressure field from 8.6 time units until 10 time units. Overall, the second pressure profile agrees very well with the analytical solution.

The third pressure trace, that of point C in Figure 4.5, also displays the high accuracy of the structured method. The only visible errors appears as a slight phase shift in
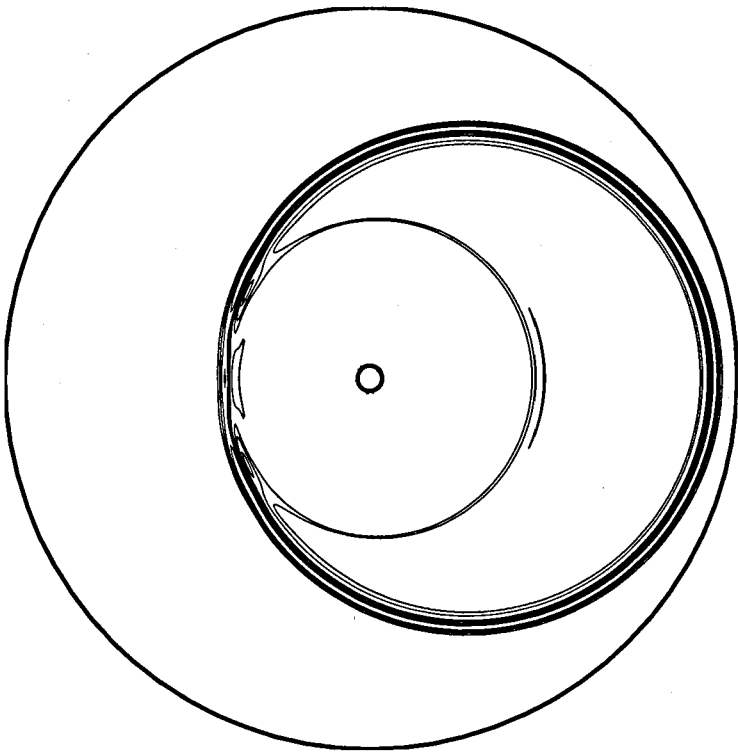
Figure 4.3: Pressure Contours At t=10 - Structured Method

(a) t=2.5   (b) t=5.0

(c) t=7.5   (d) t=10.0
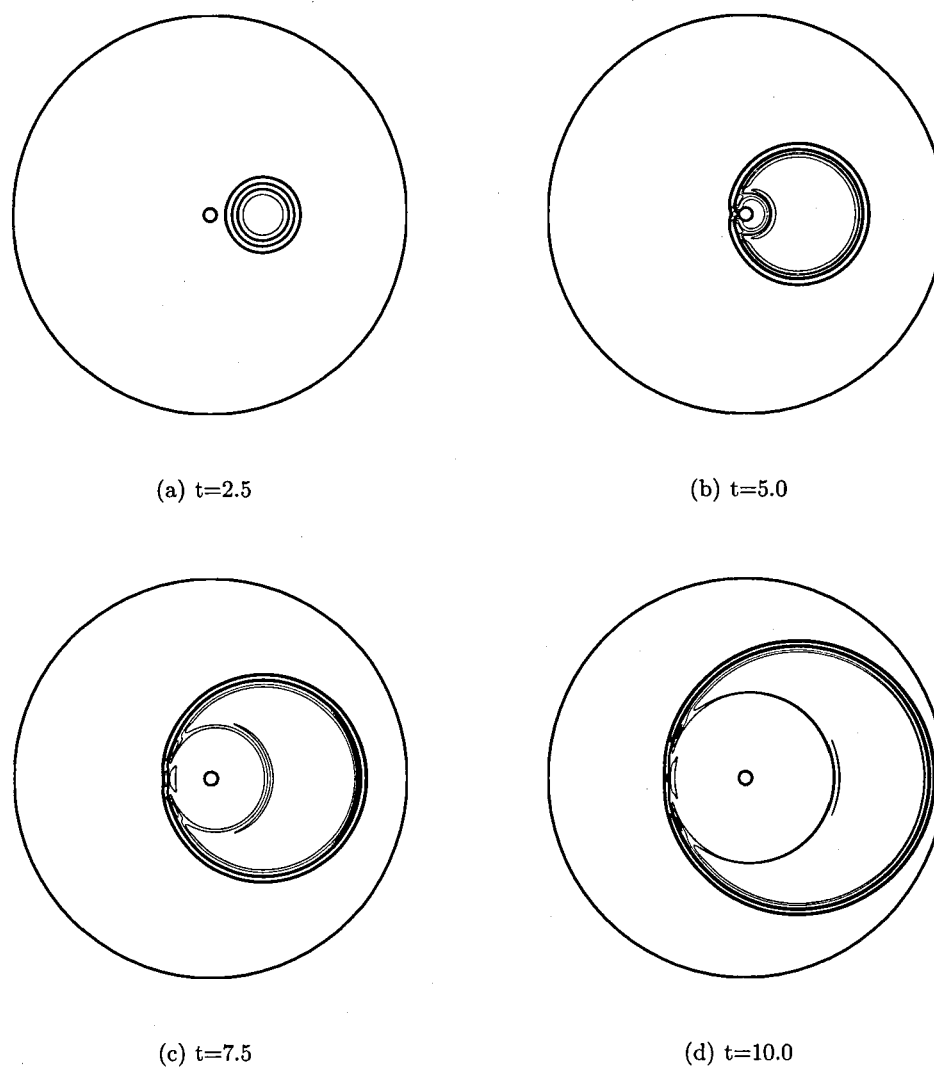
Figure 4.4: Pressure Contours At t=2.5, 5, 7.5 and 10 - Structured Method

the pressure peak at 9 time units and a very slight dispersive error at the leading edge
of the peak.

Overall, the solution computed using the structured method shows very high accu-
racy. All of the locations and amplitudes of the peaks in the pressure profiles for all
three pressure point locations are closely matched to the published solution.
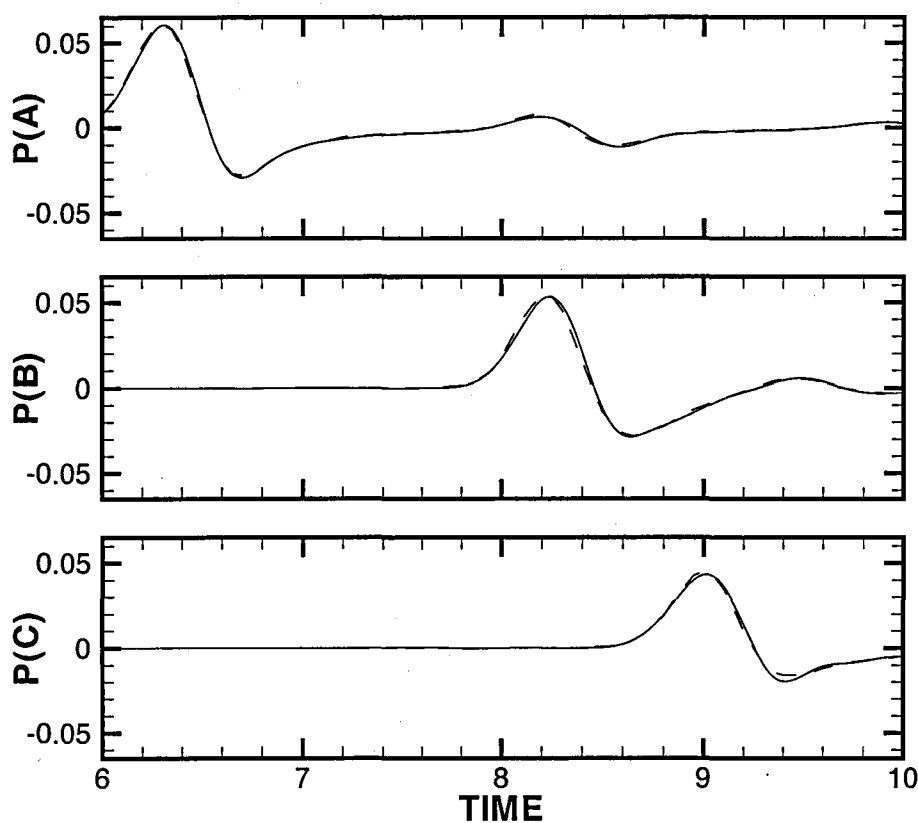
Figure 4.5: Pressure History for Reference Points - Structured Method
— Computed, - - - Exact

4.3   Scattering Problem Solution on Unstructured Meshes

As stated previously, only one gradient approximation method was used to calculate solutions to the scattering problem on the unstructured meshes. Also, only a single quadrature point was used. All three of the meshes (NEG, UK and TRI) were used with a weighted Least Squares formulation to determine possible mesh dependencies of the method. Only the weighted Least Squares calculations were completed because they were consistently the most accurate of methods tested on the uniform mean flow problem.

4.3.1   Summary of Scattering Problem Error Calculations

As with the uniform mean flow problem, examination of the RMS and NRMS errors was used to determine the accuracy of the calculations and the effects of the different mesh types. The two semi-structured mesh calculations both show higher levels of error when compared to the analytical solution. All of the RMS error calculations completed for the scattering problem, including that of the structured method, are summarised in Table 4.1. The values of the NRMS errors can be seen in Table 4.2. The structured solution has the lowest error for only two of the pressure point locations, points A and B. The unstructured TRI mesh solution has the lowest error for the C pressure location. The error values of the structured method and the unstructured method with the TRI mesh are similar for the pressure location C, with a difference of only 0.43% . The error values of the structured calculations are typically at least an order of magnitude smaller than that of the semi-structured mesh solutions. However, when the unstructured method is used with the purely unstructured TRI meshes the results are much more accurate overall and can be considered to be comparable (or in fact superior) to the error values associated with the structured calculations.

Mesh	Pressure Location		
Type	A	B	C
Structured	0.9156 E-03	0.1393 E-02	0.9534 E-03
NEG	0.1029 E-01	0.1016 E-01	0.8042 E-02
UK	0.1149 E-01	0.1074 E-01	0.9210 E-02
TRI	0.1502 E-02	0.2036 E-02	0.6524 E-03

Table 4.1: RMS Error of Scattering Problem Calculations

Mesh	Pressure Location		
Type	A	B	C
Structured	1.06	1.70	1.50
NEG	14.46	13.59	15.07
UK	12.91	12.98	15.03
TRI	1.69	2.46	1.07

Table 4.2: NRMS Error of Scattering Problem Calculations

4.3.2   Scattering Problem Solution on NEG Mesh

The first unstructured calculation was completed using the semi-structured NEG mesh. The contours of the resulting pressure field after ten time units can be seen in Figure 4.6. The pressure field shown in Figure 4.6 displays both dispersive and dissipative errors. The broken contours of the scattered pressure pulse and the increased number of contours in the lower left quadrant of the initial pressure pulse both indicate dispersion errors. The pressure contours are not symmetric about the x-axis indicating a mesh dependency in the method. The increase in the size of the initial pressure pulse at the right side of the domain also indicates dispersion error. This occurs on both the left and right sides of the domain. Although there is indications of dispersive errors, the initial pressure pulse and the scattered pulse appear to be the correct size and general shape demonstrating that the method maintains high enough accuracy to simulate the phenomenon of acoustic scattering.

The asymmetric regions of error are most likely caused by the semi-structured NEG mesh. Similar dominant error regions were observed with the uniform mean flow problem when the NEG mesh was used. Since the pressure field calculated using the NEG mesh is not symmetric about the x-axis the largest region of error is most likely due to the nature of the NEG mesh cells. The gradient approximation method used for this calculation was the weighted Least Squares method which incorporates terms relating the gradient to the distance between calculation nodes. The semi-structured meshes all contain non-equilateral triangular cells, but the dominant cell edges in the UK mesh alternates direction every cell and appears to have a different effect on the numerical simulation than the NEG mesh. With the NEG mesh the large cell edges align throughout the entire domain. This alignment is the only difference between the UK and NEG semi-structured calculations and must account for the difference in the pressure field.

As with the uniform mean flow problem, a graphical comparison was also used to
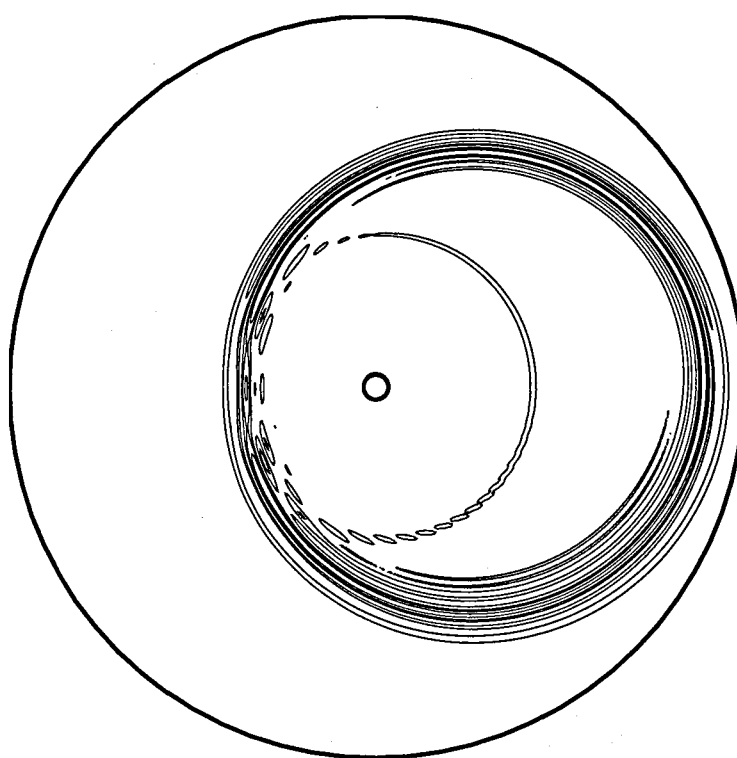
Figure 4.6: Pressure Contours At t=10 - NEG Mesh

determine the accuracy of the unstructured method. For this case however the analytical solution for the pressure field was not known, only the pressure profiles for the three monitoring locations were taken from literature. Therefore the pressure field solutions obtained with the unstructured method were compared to those of the structured case to determine any possible error characteristics. In Figure 4.7 the pressure contours of the unstructured method using the NEG mesh are plotted above the pressure contours of the structured method. The same contour levels were used as well as the same scale. Figure 4.7 shows that there is a fairly strong difference between both the initial and scattered pressure pulses between the two methods. The initial pressure pulse of the unstructured method is the same general size as the structured method pulse, the outer contours line up at both the far left and right sides of the pulses. The shape of the unstructured pulse is significantly different however. Looking at the right hand side of the pressure pulse, dispersive error has increased the overall width of the unstructured pressure pulse as well as increasing the number of contours, a sign of dispersive oscillations. There is also some proof that with the unstructured method, the pressure pulse is propagating at a slower rate than the structured method. The main structure (i.e. the closely spaced pressure contours at the center of pulse) of the initial pressure pulse of the unstructured method is inside the corresponding contours of the structured method. Similarly the scattered pulse of the unstructured pressure field is to the left of the structured pulse indicating a phase lag or wave speed error.

The pressure field of the NEG mesh unstructured method was taken at various stages of the simulation to determine how the final result evolved. The pressure contours of the NEG mesh calculation at 4 different time steps can be seen in Figure 4.8. The contour plots of Figure 4.8 confirm the observations made previously. The asymmetric error is present early in the calculations, as shown in Figure 4.8(a), and the relative size of the error grows as the pressure pulse grows as seen in Figures 4.8(b), 4.8(c) and 4.8(d). The dispersive error present in the scattered pulse appears to have a cumulative effect as the broken contours are not seen until after the t=7.5 pressure field seen in Figure 4.8(c).

The pressure distributions for all three of the pressure locations are shown in Figure 4.9. The profile associated with the pressure point at location A shows both dispersive and dissipative errors. The phase and amplitude of the peak at 6 time units is different from the analytical solution, and there is a slight oscillation in the computed solution throughout the entire time domain. Also, the calculated profile has lost the wave formation at 8.4 time units.
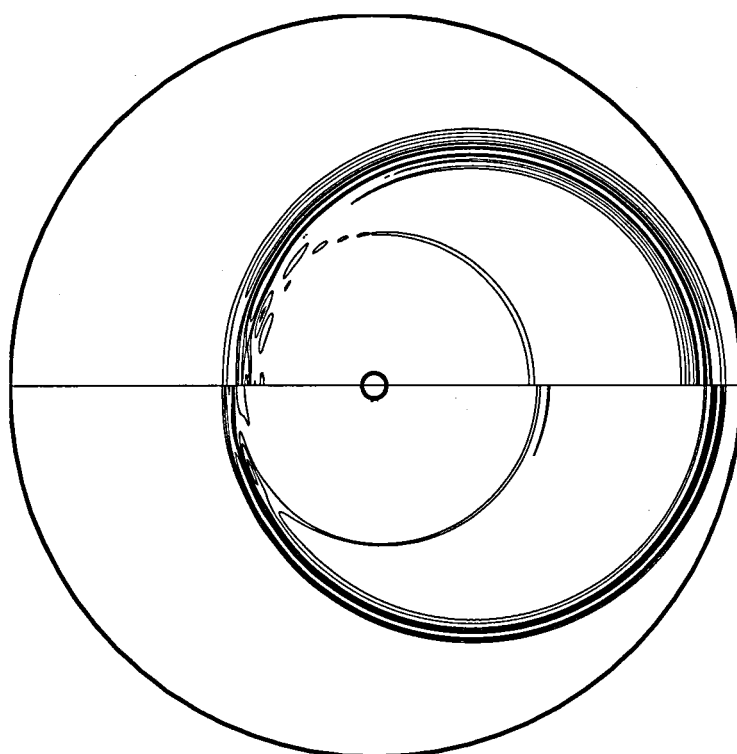
Figure 4.7: Comparison of Pressure Contours At t=10 - NEG Mesh vs Structured Method

(a) t=2.5

(b) t=5.0

(c) t=7.5

(d) t=10.0
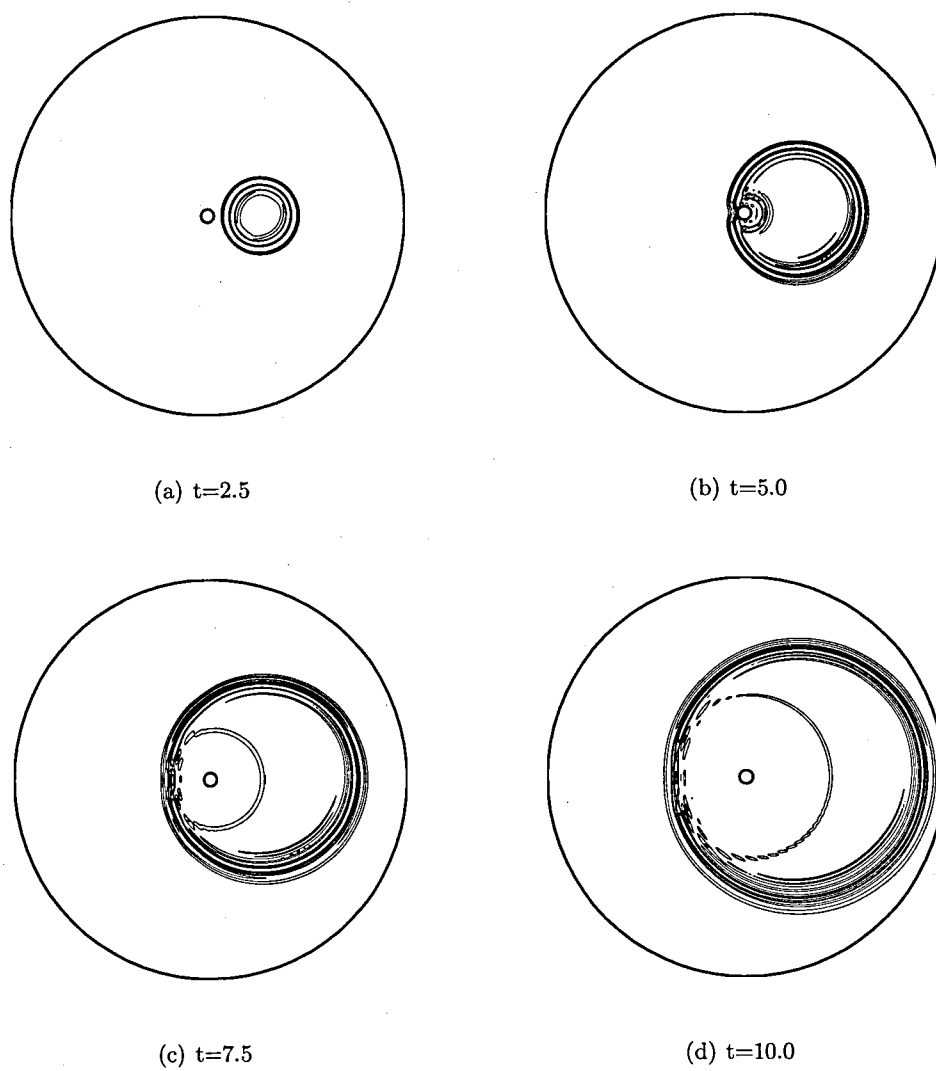
Figure 4.8: Pressure Contours At t=2.5, 5, 7.5 and 10 - NEG Mesh

The profile associated with the pressure point at location B also shows dispersive errors. The amplitude of the peak at 8.2 time units, as shown in the middle distribution of Figure 4.9, is damped and there is a phase shift as well as an induced oscillation from 8.6 time units until 10 time units. There is no error in the earlier part of the pressure profile because the pulse has not entered the null field that existed there previously.

The third and final pressure distribution in Figure 4.9 is associated with the pressure point at location C. For this point location, the peak also shows dispersive errors, in the under-prediction ahead of the pressure wave, and dissipative errors in the damping and widening of the base of the pressure peak.

Overall, the unstructured calculation completed using the NEG mesh show relatively high dissipation and dissipation errors for all three of the pressure point locations. All of the wave forms in the three distributions have been affected in some way, and most of the errors seem to have remained after the pressure pulse has passed. These results indicate how an unstructured method has difficulty in approximating the scattering phenomena on the semi-structured NEG mesh.
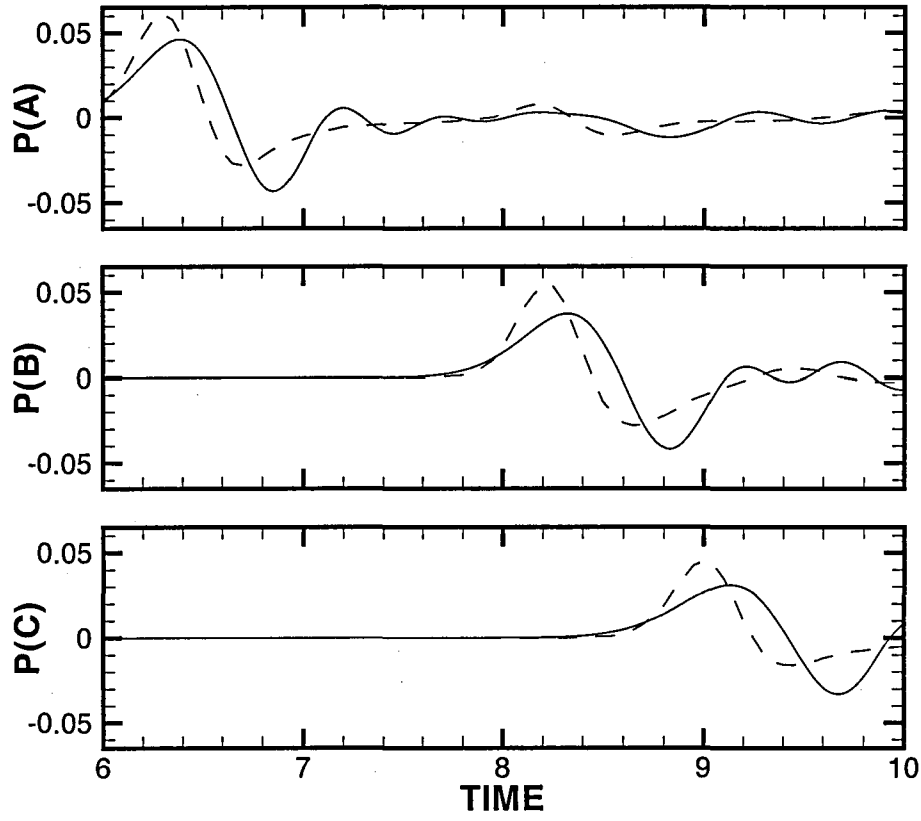
Figure 4.9: Pressure History for Reference Points - NEG Mesh
— Computed, - - - Exact

Comparison of NEG Mesh Results with POS Mesh Calculation

In order to confirm that the large error region of the pressure contours of the NEG mesh test case was caused by the dominant edge of the NEG mesh formulation the calculation was completed again using the the POS mesh. As stated earlier the POS semi-structured mesh is nearly identical to the NEG mesh, only rotated 90° about the origin of the domain. The contours of the resulting pressure field can be seen in Figure 4.10. The large region of error that was present in the lower right quadrant of the pressure contour plot with the NEG mesh is now present in the upper right quadrant of the pressure contour plot. This change in the location of the large region of error directly corresponds to the orientation of the dominant cell edge. Similarly the increased area of dispersive error present on the reflected or interior pressure pulse, i.e. the pulse nearest to the interior boundary, has also moved from the lower half of the contour plot to the upper half. The observation that the location and orientation of the large region of error present in both these calculations changes with the selection of either the NEG or the POS mesh indicates that the error is caused by the specific characteristics of the semi-structured mesh.

Further confirmation that the error is directly related to the semi-structured mesh is given by the fact that the two pressure fields computed using the NEG and POS meshes are so similar that when the regions with the largest amount of dispersive error are compared, as in Figure 4.11, they are mirror images of each other with the line of symmetry at $y = 0$. This symmetry in the dispersive error is identical to that of the two corresponding meshes which are also mirror images of each other with a line of symmetry extending along the x-axis. The mirror-image regions of error confirm that the dispersion error and the skewed pressure contours are created by the dominant edges of the NEG and POS mesh.
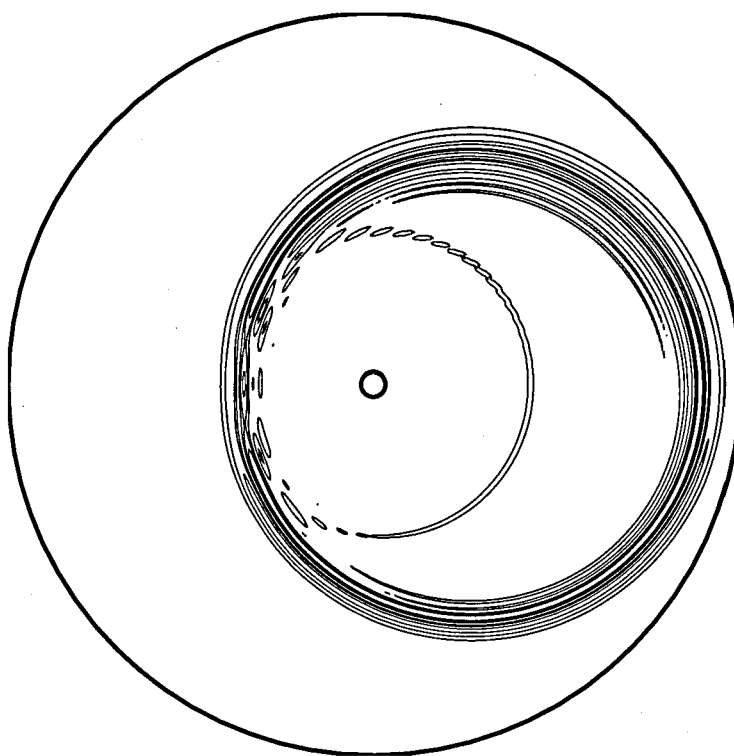
Figure 4.10: Pressure Contours At t=10 - POS Mesh
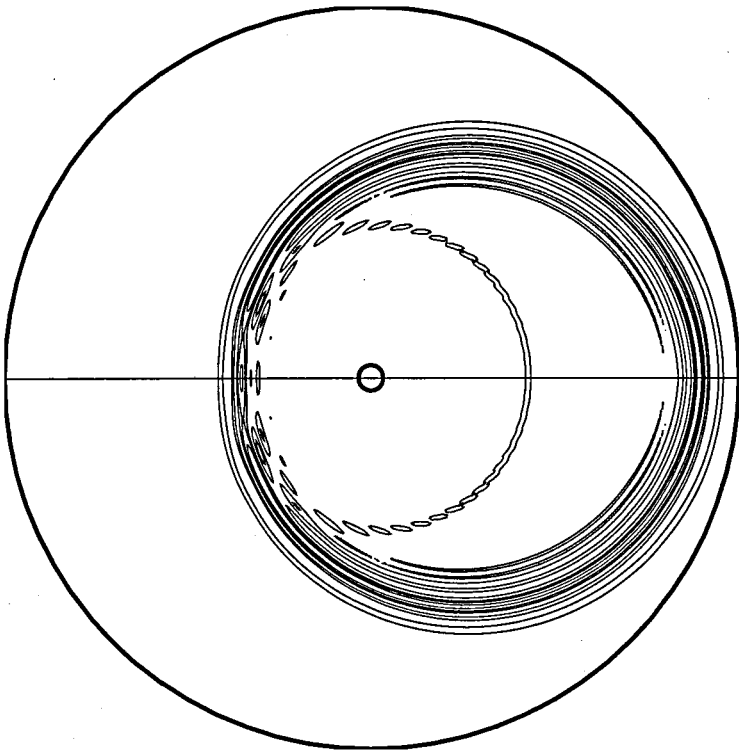
Figure 4.11: Comparison of Pressure Contours At t=10 - NEG Mesh vs POS Mesh

4.3.3   Scattering Problem Solution on UK Mesh

The second calculation completed using the unstructured method used the UK semi-structured mesh. The contours of the pressure field at ten time units ($t = 10$) can be seen in Figure 4.12. The pressure field of the UK mesh calculation is similar to that of the NEG mesh calculation. Both show the effects of dispersive error in both the initial and reflected pressure pulses. The UK mesh however has created a solution which is symmetric about the x-axis. This was to be expected as the UK mesh is symmetric as well. The asymmetric dispersive error of the NEG mesh calculation matches the asymmetric NEG mesh much in the same way the symmetric dispersive error of the UK mesh calculation matches the symmetric UK mesh. The most disruptive area of dispersion error is to the left of the center of the cylinder. This is also the area where the points used to monitor the pressure field are located. The dispersive oscillations in the pressure field in this region have created a series of broken pressure contours especially where the scattered pulse interacts with the initial pulse. These errors suggest that the unstructured method may have some difficulty dealing with the accurate simulation of this interaction.

The pressure field of the UK mesh calculation was also compared with the pressure field of the structured method calculation. The pressure contours of the two methods can be seen in Figure 4.13. Many of the same errors as the NEG mesh test case can be seen here as well. The general shape and size of the initial pressure pulse appear correct but the dispersion errors of the unstructured method have increased the width of the pressure pulse on the right side. The same propagation errors observed with the NEG mesh calculation are seen with the UK mesh calculation as the discrepancy between the pressure contours of both the initial and scattered pressure pulses are present in Figure 4.13.

Looking at the pressure field at 4 different time steps, as in Figure 4.14, it can be seen that the numerical method was able to maintain the symmetry of the problem for the entire calculation. The dispersive errors present just behind the right side of the initial pressure pulse appear in the same location above and below the x-axis. As with the previous mesh types, the dispersive error has the greatest effect on the left portion of the scattered pulse. This region contains the interaction of the initial and scattered pressure pulses. The broken contours of the scattered pressure pulse, as seen in Figure 4.14(d), occur mostly with the scattered pulse (i.e. closer to the cylinder) while the smooth, continuous contours are still present for the initial pressure pulse
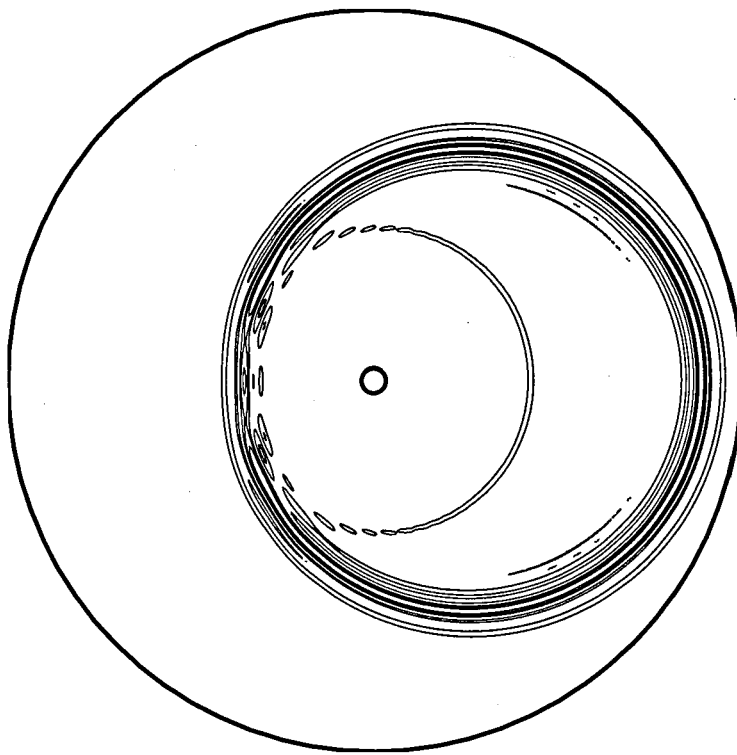
Figure 4.12: Pressure Contours At t=10 - UK Mesh
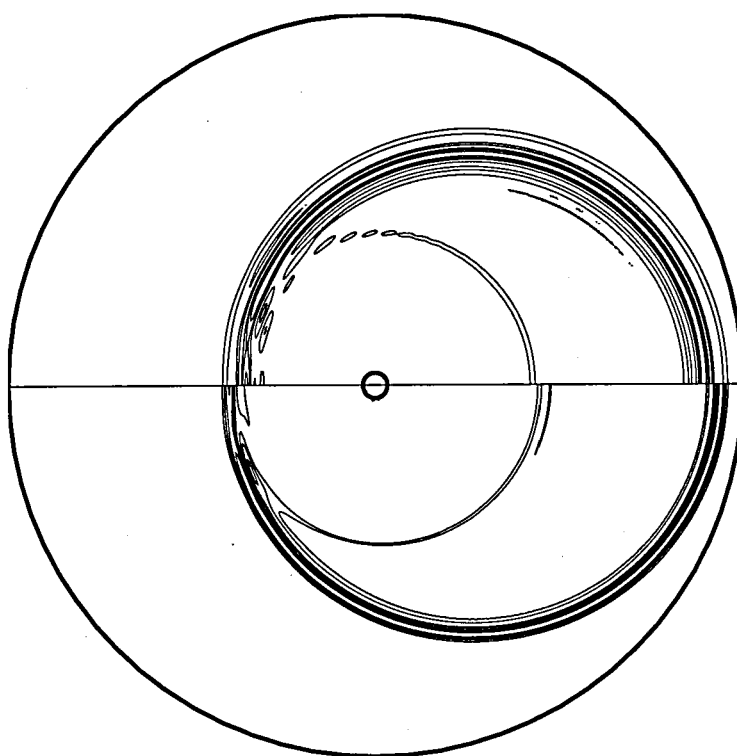
Figure 4.13: Comparison of Pressure Contours At t=10 - UK Mesh vs Structured Method

(i.e. farther away from the cylinder). This appears to be indicative the unstructured numerical method having difficulty simulating accurately the interaction between the scattered and initial pressure waves. As with the other calculations it can be observed that the dispersive error also has a cumulative effect, the earlier time steps show fewer broken contours where the initial and scattered pulse interact and a decreased width of the initial pulse.

The pressure distributions from this solution show the same types of errors as those of the previous NEG mesh calculation. The pressure profiles for all three of the pressure points can be seen in Figure 4.15. The pressure profile of point A show both dispersion and dissipation errors. The peak at 6.2 time units is damped and there are oscillations throughout the time domain. The phase of the peak has also been shifted, lagging behind the peak from the analytical solution.

The plot of the pressure trace associated with point B also shows dissipation and dispersion. The pressure pulse at 8.2 time units has been damped and shows a phase lag in the calculated solution. Also, there is an oscillation in the pressure distribution that began at approximately 9 time units and continued until the end of the calculation.

The pressure profile associated with the point at location C also shows dissipative error when compared to the analytical solution. The pressure pulse at 9.2 time units shows a drop in amplitude as well as a phase shift and an under-prediction of the pressure value on the trailing edge.

Comparing the pressure distributions associated with all three pressure locations and the analytical solutions, it can be seen that the solution calculated on the UK mesh has the same dissipation and dispersion errors as the solution calculated on the NEG mesh. This similarity points towards the semi-structured meshes as a source of error. It appears as though the unstructured method is unable to simulate accurately the scattering problem with a semi-structured mesh. Only after comparison of the TRI mesh calculation can the overall accuracy of the unstructured method be determined.

(a) t=2.5

(b) t=5.0

(c) t=7.5

(d) t=10.0
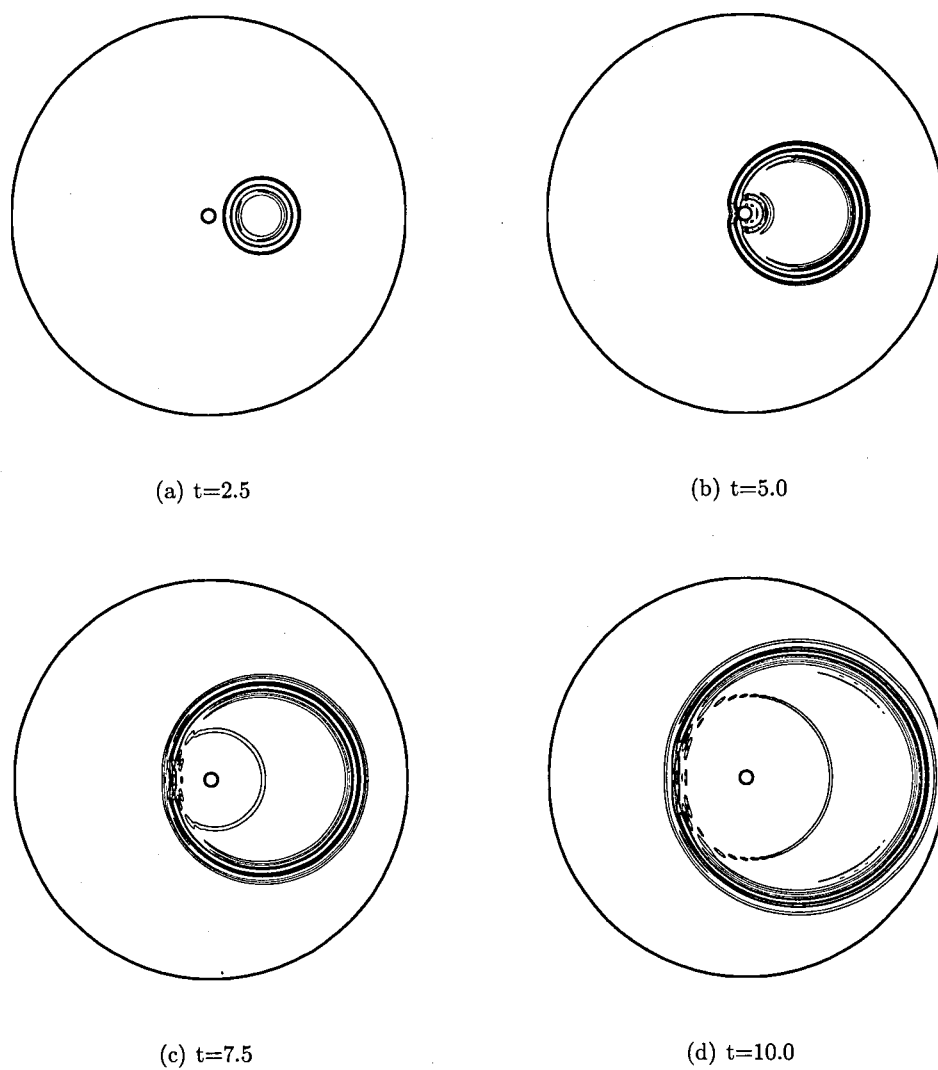
Figure 4.14: Pressure Contours At t=2.5, 5, 7.5 and 10 - UK Mesh
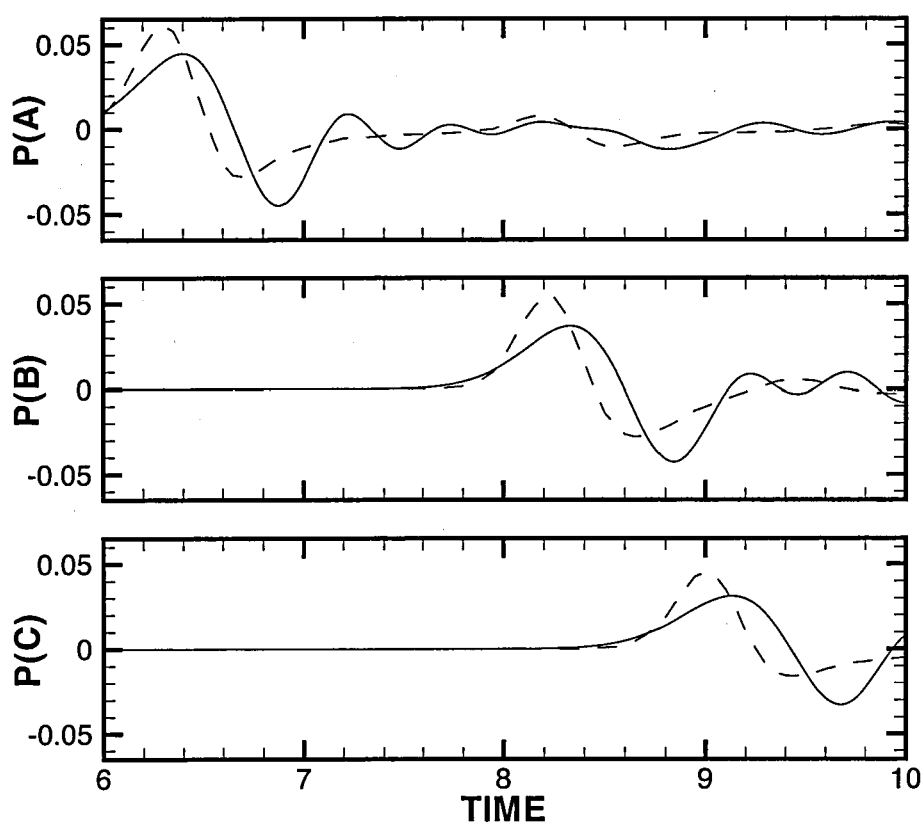
Figure 4.15: Pressure History for Reference Points - UK Mesh
— Computed, - - - Exact

4.3.4   Scattering Problem Solution on TRI Mesh

The third calculation completed using the unstructured method used the TRI mesh. The solution computed with this formulation shows high accuracy and very little discrepancy between the calculated and analytical solution. The contours of the pressure field at ten time units ($t = 10$) can be seen in Figure 4.16. The pressure contours of the TRI mesh calculation have two important differences to those of the semi-structured meshes. The first difference is the lack of broken contours in the region of interaction between the initial and scattered pressure pulses. This difference means the pressure field has a lower level of dispersive error in the region closer to the cylinder, as indicated by the continuous pressure contours. The second difference is the increase in the amount of trailing pressure contours inside the right side of the initial pressure pulse. This difference demonstrates that the pressure field has a higher levels of dispersion error in the region further out from the cylinder. These two regions of the pressure field indicate a possible link between the dispersive error calculated and the mesh size. For the semi-structured meshes, there was a linear correlation between the distance from the cylinder and the mesh cell size. This created an increase in dispersive error in the outer region of the test domain, but at levels that appear to be less intense than those of the TRI mesh calculations. For the TRI mesh the different method of cell size determination has created a different relation between the distance from the center of the domain and the dispersion error.

Aside from the two main differences listed above further inspection of the pressure contours for this test case, as shown in Figure 4.16, indicates a pressure field that is highly symmetrical about the x-axis, although there are some regions where there are minor discrepancies. The high level of symmetry is important because the test case solution is perfectly symmetrical about the x-axis. Unlike the UK semi-structured mesh case this particular numerical mesh is not symmetrical, the interior is instead filled with triangular cells in random orientations. As with the previous calculations the general shape and size of the pressure pulses are correct.

The pressure field of the TRI mesh calculation was also compared with the pressure field of the structured method, as seen in Figure 4.17. For this calculation there is a great similarity between the scattered pressure pulse of the unstructured method and that of the structured method. For the first time with the unstructured calculations the entire scattered wave appears to perfectly match that of the structured method along the x-axis cut line. There is only a small difference in the length of the small
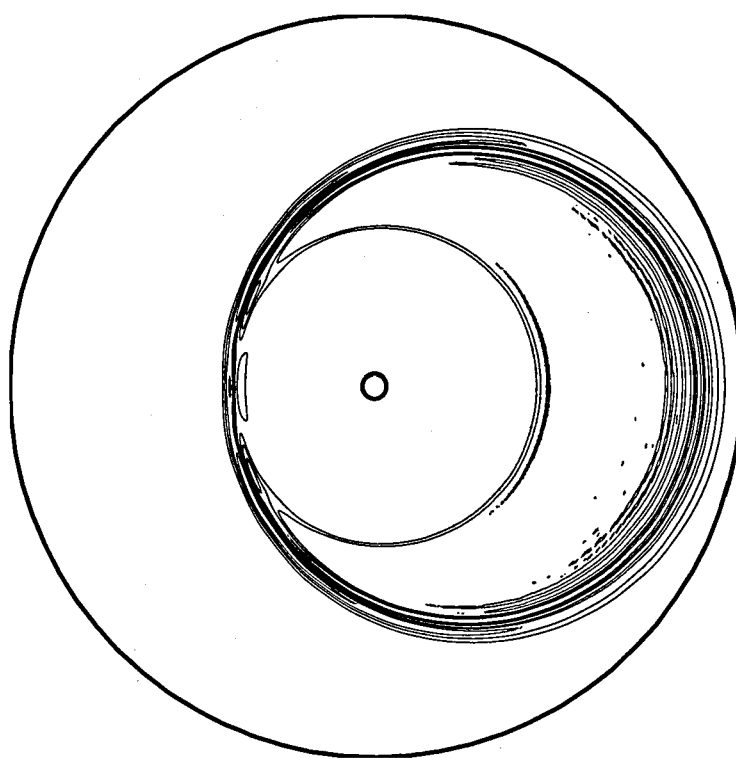
Figure 4.16: Pressure Contours At t=10 - TRI Mesh

pressure wave ahead of the right-hand portion of the scattered pressure pulse. The similarity between the structured and unstructured pressure fields does not extend for the initial pressure wave however. The contours of the unstructured pressure field near the right hand boundary show large dispersion error. There are numerous oscillations on the pressure field at this location creating the increased number of pressure contours. The dispersion error in this region has increased the width of the pressure pulse to approximately triple that of the structured calculation at the same point.

As with the previous mesh types, the pressure field calculated using the TRI fully unstructured mesh was also stored at 4 different time steps during the simulation. The resulting pressure fields can be seen in Figure 4.18. As with the pressure field shown in Figure 4.16 all of the time steps in this calculation show little dispersion error in the region of interaction between the initial and scattered pressure waves. The only area that shows any effect of dispersion is the right hand side of the initial pressure pulse. As with the other test calculations this appears to be a cumulative error as it is not present at 2.5 time units (Figure 4.18(a)) and grows to create a large region of oscillations at 10 time units (Figure 4.18(d)). Even with the dispersion error the pressure contours depict a pressure pulse that is the correct shape and maintains symmetry for each of the time steps.

The pressure distributions taken from the TRI mesh solution can be seen in Figure 4.19. The small errors that do exist appear to be very similar to the errors from the structured method calculation.

The pressure profile associated with the pressure point located at position A shows a strong agreement between the calculated pressure and the analytical pressure for almost the entire time domain. There is a slight phase shift in the pressure pulse peak at 6.2 time units, but the amplitude of the wave seems to be predicted correctly. There is also a slight phase difference in the pressure wave at 8.3 time units, but it is very minor.

The recorded pressure values corresponding to location B also show a high accuracy. There is no direct evidence of dispersion or dissipation and the only difference between the calculated and analytical solution appears as a slight phase lag in the pressure pulse at 8.2 time units.

The pressure distribution from pressure point C also displays an accurate approximation of the analytical solution. The only errors present in the profile appear to be a slight phase lag of the pressure wave at 9.2 time units as well as a small under-prediction
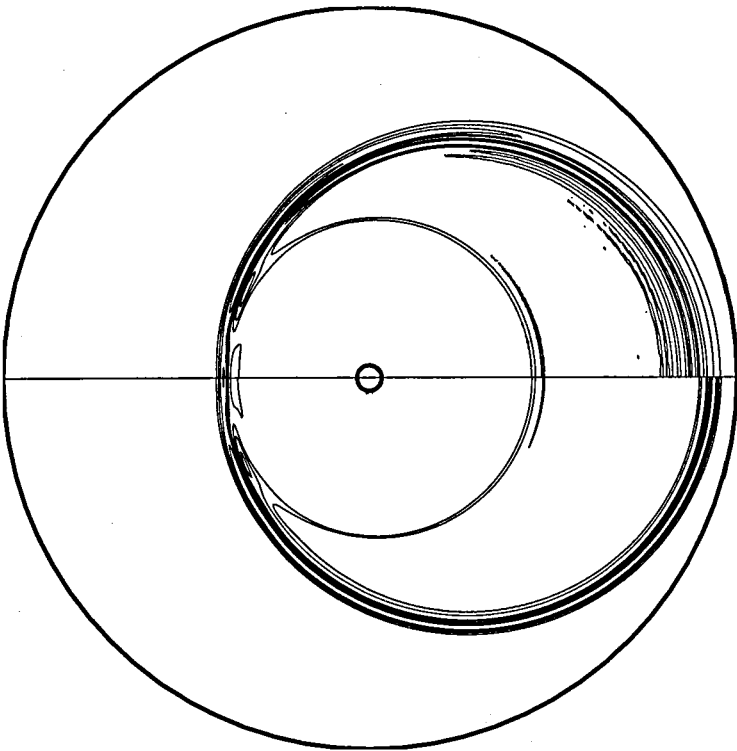
Figure 4.17: Comparison of Pressure Contours At t=10 - TRI Mesh vs Structured Method

(a) t=2.5

(b) t=5.0

(c) t=7.5

(d) t=10.0
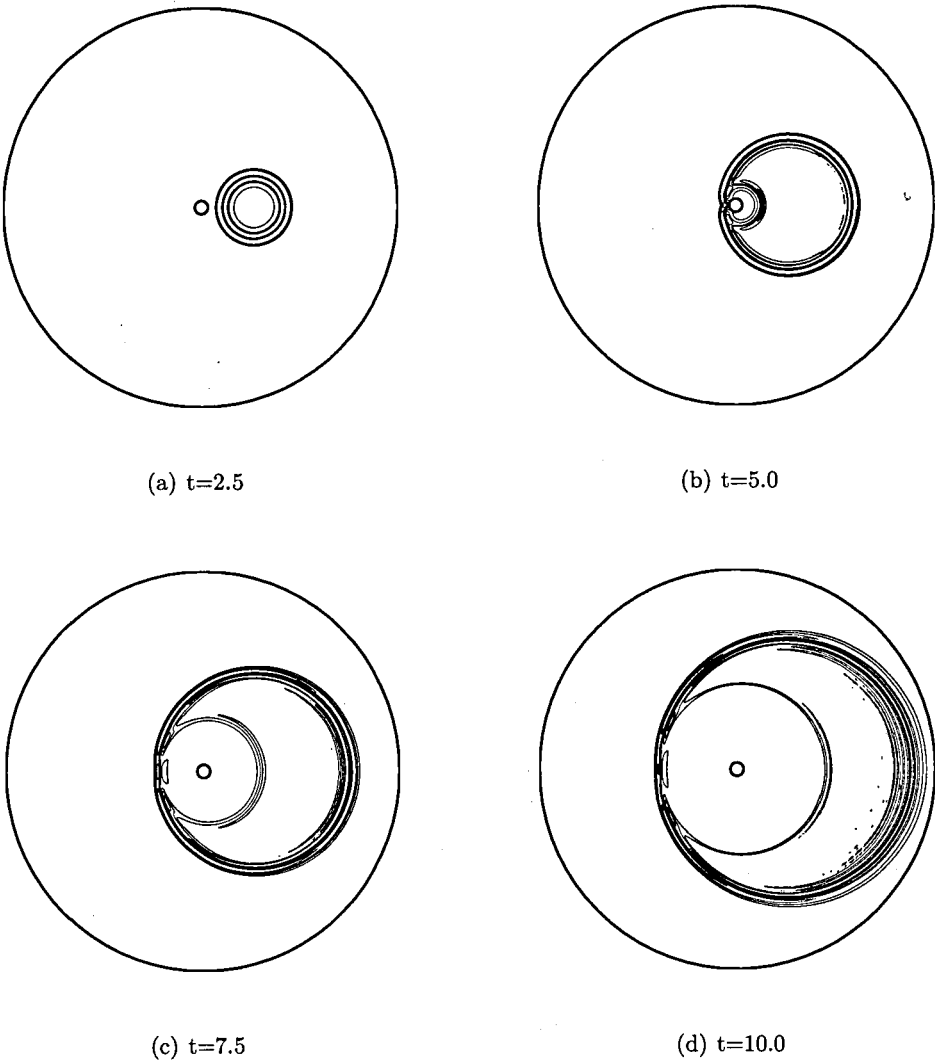
Figure 4.18: Pressure Contours At t=2.5, 5, 7.5 and 10 - TRI Mesh

of the pressure at 9.4 time units.

Overall, the three pressure distributions calculated using the unstructured method on the purely unstructured TRI mesh show a high degree of accuracy in the numerical method. There is little or no dispersive or dissipative errors in any of the three profiles. The pressure traces do not show any larger errors than those encountered with the fourth-order accurate structured method. These results indicate that the error in the previous two test cases is linked directly to the semi-structured form of the NEG and UK meshes. The high accuracy of the TRI mesh test leads to the conclusion that the unstructured method requires the use of a purely unstructured mesh for more complex acoustic phenomena.
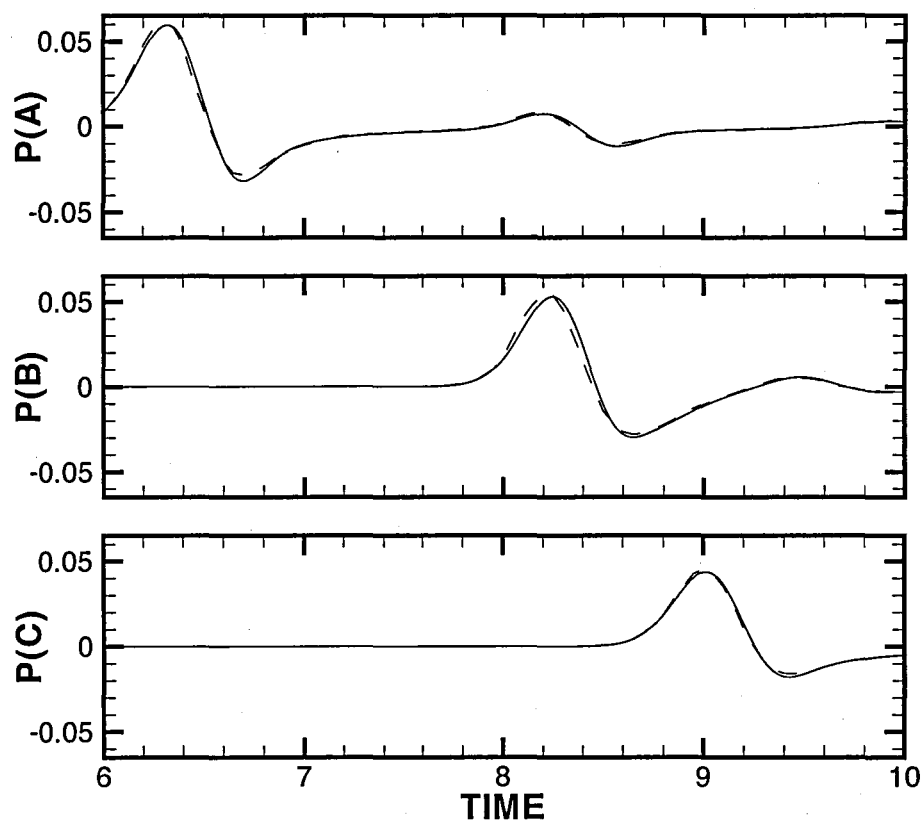
Figure 4.19: Pressure History for Reference Points - TRI Mesh
— Computed, - - - Exact

4.4   Interaction of Pressure Pulse with Solid Boundary

As stated previously, the main purpose of the scattering benchmark problem is to determine the ability of the numerical method to simulate accurately the interaction of a pressure pulse and a solid cylindrical boundary. In order to better understand how the method deals with the solid boundary a closer look at the interaction region is required. With this purpose in mind a series of plots were created showing the effect of the solid boundary on the pressure field and allowing the observation of how the pressure field interacts at several different time steps. The region used is approximately three cylinder diameters in both the x and y directions and is centered at the cylinder. The contours of the pressure fields correspond to seven time steps equally spaced between 3.0 and 6.0 computational time units. This specific range of times was taken because it corresponds to when the leading edge of the pressure pulse impacts with and then reflects off of the cylinder surface. As with previous pressure field plots, the contours are evaluated for signs of dispersion error and dissipation as well as the ability to simulate accurately a simple and symmetrical scattering phenomena.

4.4.1   Structured Mesh Solution

The first series of pressure plots investigated correspond to the structured test case. This test case is taken as the baseline solution as the numerical method used was a high accuracy 4th-order central-differencing approximation. The pressure fields of all seven different time steps shown in Figures 4.20(a) through 4.21(c) show symmetrical contours that remain smooth and continuous as the pressure pulse interacts with the solid cylinder. The leading contours of Figure 4.20(a) break and reform into the smooth pressure wave in Figure 4.21(a) and there appears to be little dissipation and dispersion error. For these series of time steps there are no oscillations created in the initial pressure wave as is passes over the cylinder although Figure 4.20(d) shows some small dispersive error in the contours of the reflected pressure pulse. However, these oscillations are not present 0.5 computational time units later as shown in Figure 4.21(a).

(a) t=3.0   (b) t=3.5

(c) t=4.0   (d) t=4.5
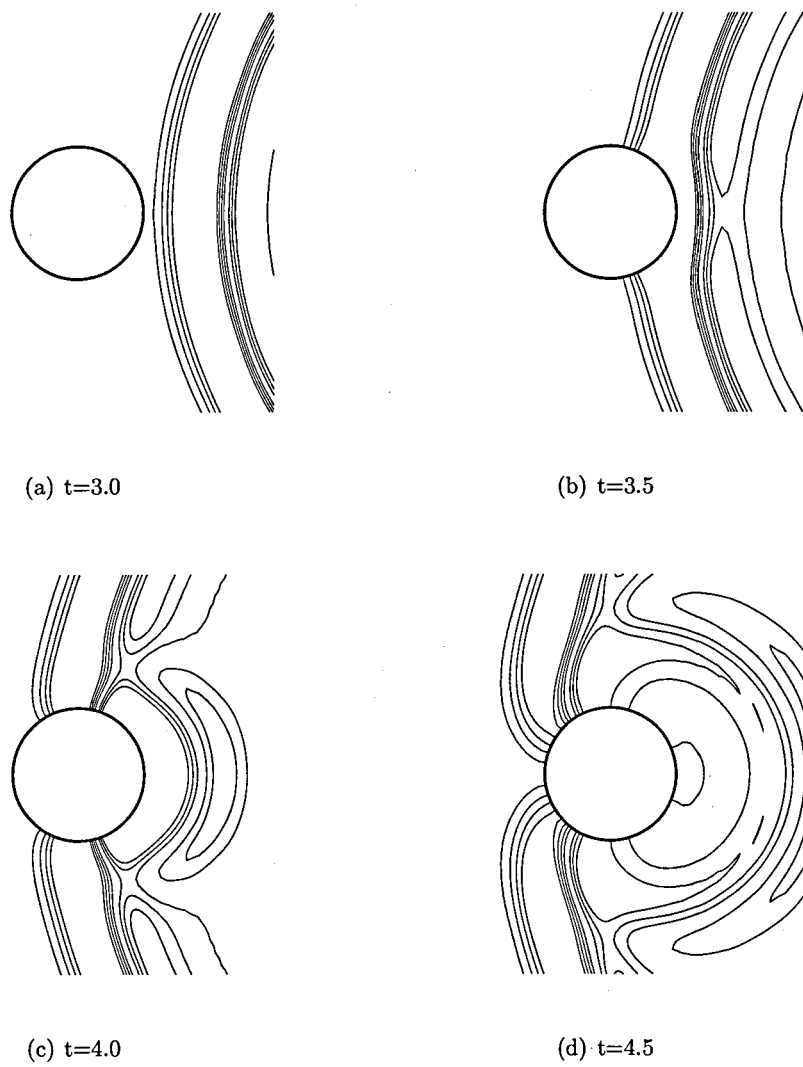
Figure 4.20: Pressure Contours At t=3, 3.5, 4 and 4.5 - Structured Method

(a) t=5.0

(b) t=5.5

(c) t=6.0
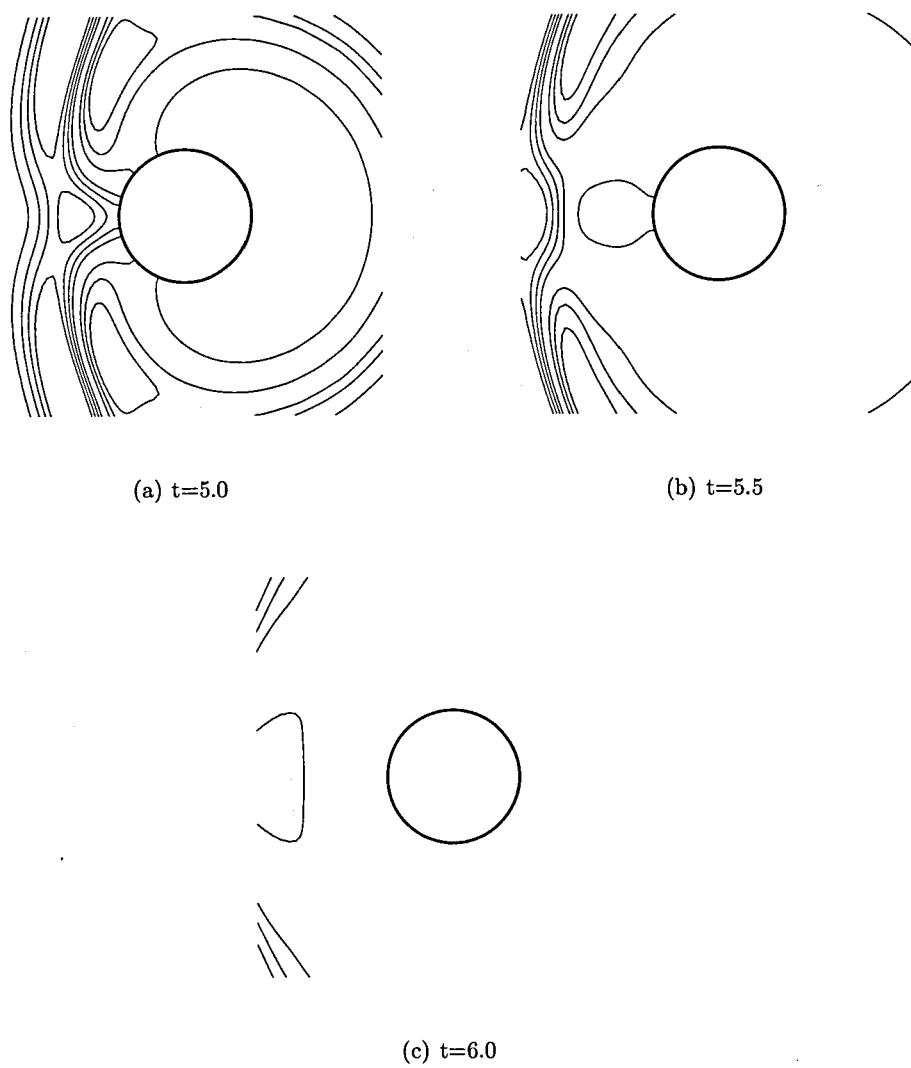
Figure 4.21: Pressure Contours At t=5, 5.5 and 6 - Structured Method

4.4.2 NEG Mesh Solution

This first series of unstructured method pressure field plots were created using the semi-structured NEG mesh. In previous comparisons, such as those above in Section 4.3.2, the pressure contour plots indicate relatively high dissipation and dispersion errors as well as an asymmetrical pressure field. These characteristics are believed to be caused by in part by the semi-structured mesh (the asymmetrical features correspond to the orientation of the mesh cells) but it is not known whether or not the dissipation and dispersion errors are caused by the overall unstructured method or the specific formulation of the solid boundary condition. By looking at the pressure plots at the various time steps in Figures 4.22(a) through 4.23(c) it can be seen that the simple solid boundary condition appears to have a strong dispersive effect. The smooth, continuous pressure contours originally seen in Figure 4.22(a) have dissolved into a series of disconnected loops indicating large dispersive error. The fact that the pressure contours shown in Figures 4.22(a) and 4.22(b) are still smooth indicates that the pressure pulse has been propagated across the domain without the introduction of any dispersive error until the pulse nears the solid boundary. This leads to the conclusion that the dispersion error may be created by the boundary condition and not necessarily the overall unstructured method.

Looking at Figures 4.22(c) and 4.22(d) it can be seen that as the leading edge of the pressure pulse nears the solid boundary the dispersion error is already growing. In Figure 4.23(a) it appears as though the dispersion is growing in several directions. When comparing the NEG mesh pressure field in Figure 4.21(a) with the structured pressure field in Figure 4.23(a) the regions above, below and to the right of the cylinder appear to be showing high levels of dispersive error. This same increased level of dispersive error is obvious when comparing the NEG mesh solution and the structured solution at 6.0 computational time units as in Figures 4.21(c) and 4.23(c).

The asymmetrical contours that were noticed in previous pressure plot comparisons such as those above in Section 4.3.2 are also apparent, to a lesser degree, in these plots. The decreased domain of these pressure field plots do not allow the observation of large regions of asymmetry, but Figures 4.22(d) and 4.23(a) do show definite areas above and below the centerline which are not symmetrical. This indicates that even on this small a scale, the asymmetrical nature of the NEG mesh has a direct negative effect on the solution calculated by the unstructured method.

(a) t=3.0

(b) t=3.5

(c) t=4.0

(d) t=4.5
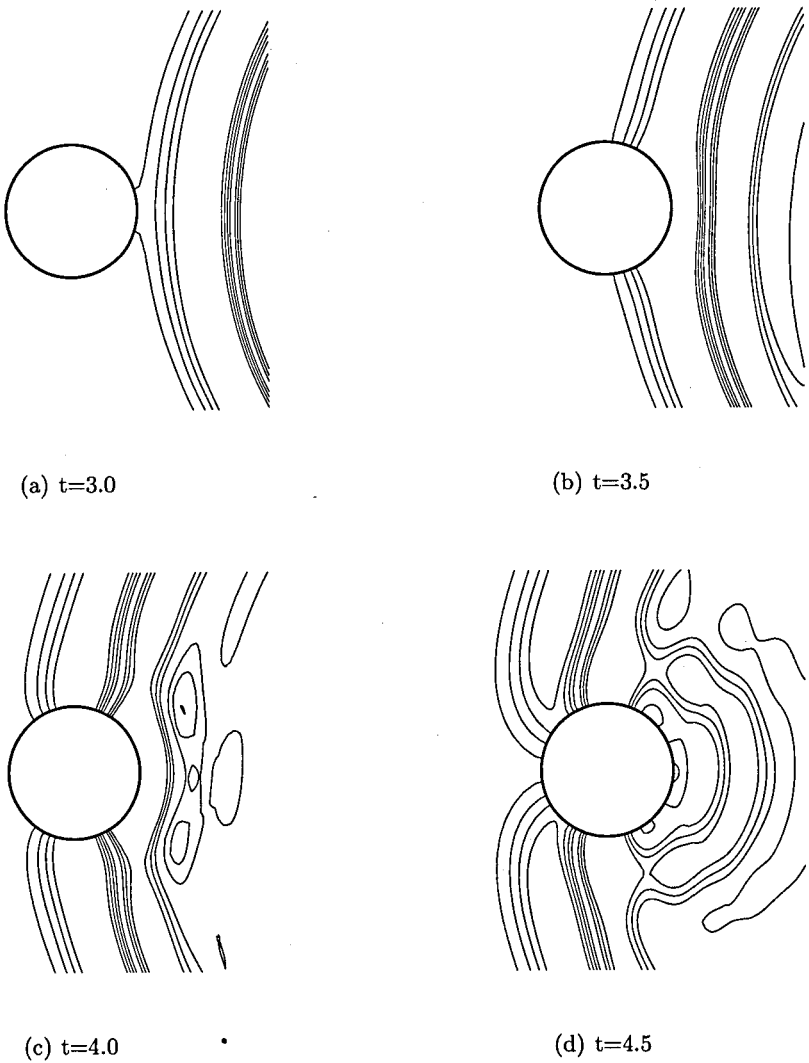
Figure 4.22: Pressure Contours At t=3, 3.5, 4 and 4.5 - NEG Mesh

(a) t=5.0   (b) t=5.5

(c) t=6.0
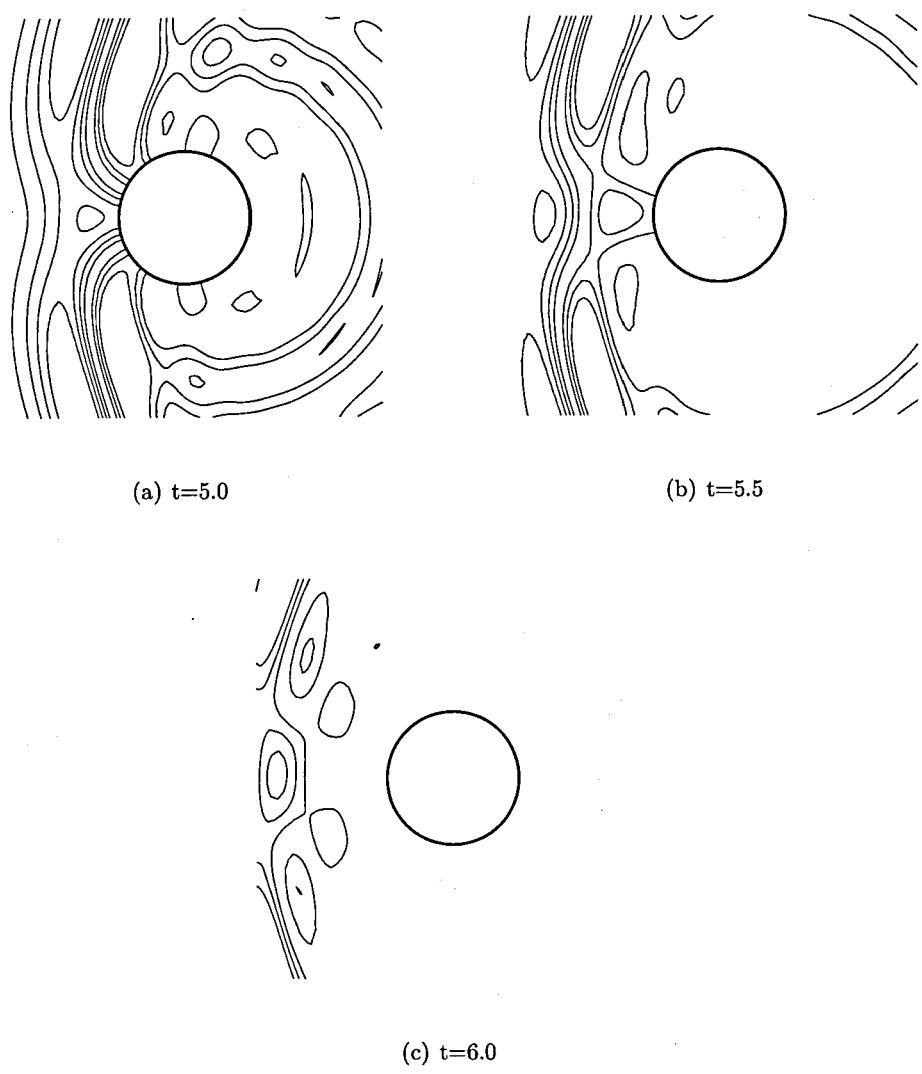
Figure 4.23: Pressure Contours At t=5, 5.5 and 6 - NEG Mesh

4.4.3 UK Mesh Solution

The second set of unstructured method pressure field plots were calculated using the semi-structured UK mesh. For this series of plots the pressure contours were expected to maintain a symmetrical appearance to coincide with the symmetrical nature of the semi-structured UK mesh. On first inspection the plots in Figures 4.24(a) through 4.25(c) appear to display a level of dispersion error similar to that of the NEG mesh solutions while maintaining a symmetrical appearance. As with the NEG mesh results, the pressure contours at 3.0 and 3.5 computational time units (as seen in Figures 4.24(a) and 4.24(b), respectively) reach the cylinder maintaining a smooth and continuous form. The pressure contours at 4.0 and 4.5 computational time units (as seen in Figures 4.24(c) and 4.24(d), respectively) then show dispersive error in the right hand portion of the plot. These findings indicate that the solid boundary condition applied with the unstructured method may be the main cause of the dispersion error, adding more credibility to the conclusion stated in the previous section. The remaining three UK mesh time steps, shown in Figures 4.25(a) through 4.25(c) appear very similar to those of the NEG mesh calculation with a large portion of the pressure contours broken up due to increasing dispersive error.

Overall, this series of pressure plots are very similar to those of the NEG mesh calculation. At all seven time steps, there are distinct similarities between the NEG and UK solution in how the pressure contours interact with the solid boundary and begin to show the dispersion error.

As for the symmetrical nature of the UK mesh test case, all seven of the pressure field plots show a high level of symmetry. Even in the regions of large amounts of dispersion error, the upper portion of the plot closely mirrors the lower portion. This adds further proof that the unstructured method had an inherent sensitivity to the layout of the semi-structured meshes. As with the NEG mesh case, this series of snapshots of the pressure field has a fairly small scope but does agree with the overall characteristics of the solutions as discussed earlier.

(a) t=3.0

(b) t=3.5

(c) t=4.0

(d) t=4.5
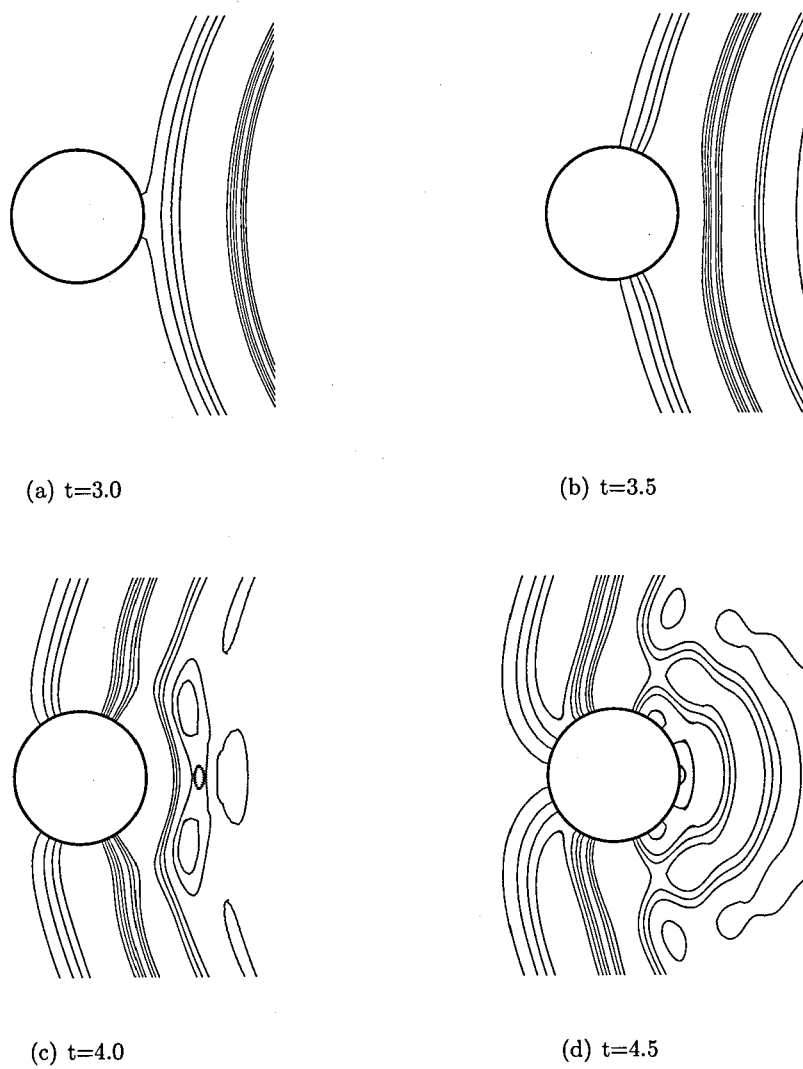
Figure 4.24: Pressure Contours At t=3, 3.5, 4 and 4.5 - UK Mesh

(a) t=5.0

(b) t=5.5

(c) t=6.0
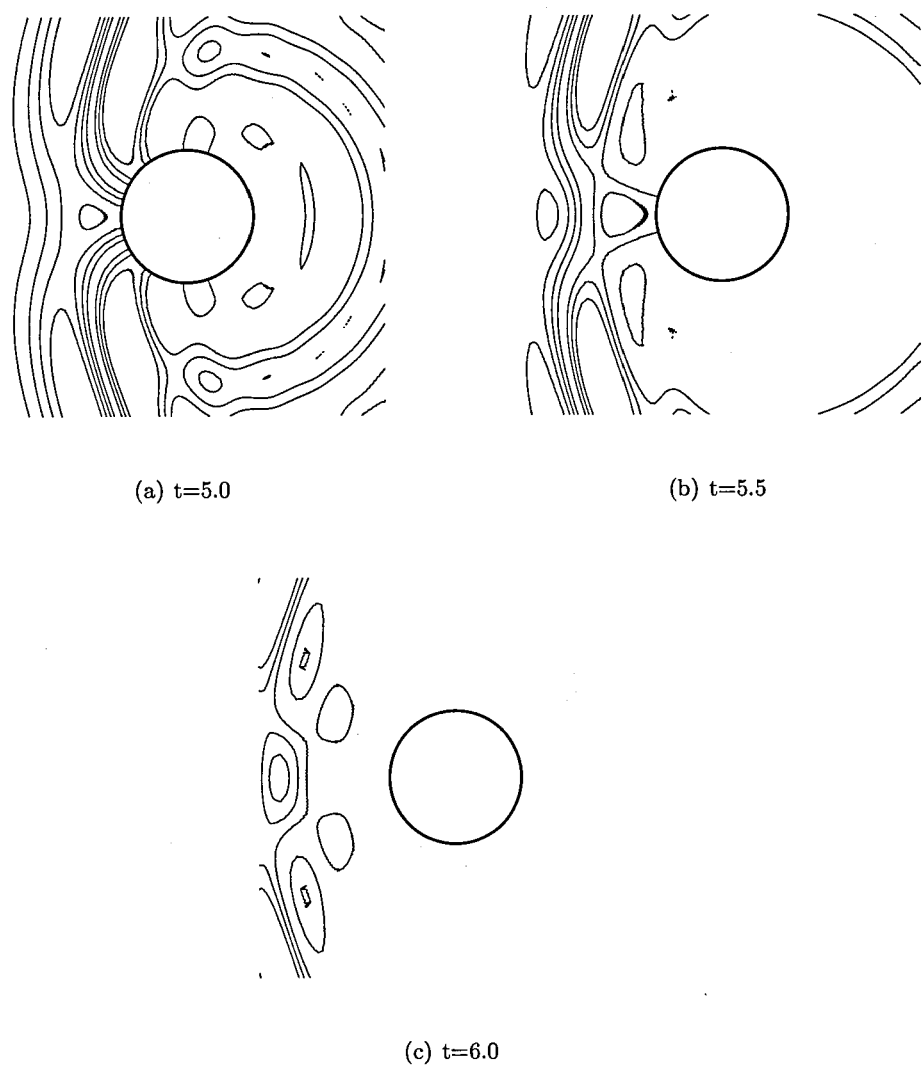
Figure 4.25: Pressure Contours At t=5, 5.5 and 6 - UK Mesh

4.4.4   TRI Mesh Solution

The third and final series of unstructured pressure field plots were completed using the purely unstructured TRI mesh. This mesh has a non-symmetrical distribution of vertices as well as randomly oriented cells. The earlier results discussed in Section 4.3.4 indicated a solution that appeared largely symmetrical with some dispersion error in the outer region. Looking at the interaction of the pressure pulse with the solid cylinder, these earlier results still hold. The pressure field contours shown in Figures 4.26(a) through 4.27(c) appear much more similar to those of the 4th-order accurate structured solution than those of the other unstructured calculations. The contours remain smooth and continuous for all of the time steps and there appears to be little or no dispersive error. In fact for all seven of the different time steps, the interaction of the pressure pulse and the cylinder on the TRI mesh is virtually identical to that of the structured mesh when compared.

As stated previously, the contours remain smooth and continuous and there appears to be no indication of dispersive error. The overall field also appears to have a high level of symmetry. For all of the TRI mesh plots the combination of the simple solid boundary condition and the unstructured method closely mirrors that of the high-order structured method. These results lead to the conclusion that the dispersion error seen with the NEG and UK meshes is not caused by the solid boundary approximation used for the unstructured method but must instead be a result of the use of the semi-structured mesh. The symmetric and low-error contour plots of Figures 4.26(a) through 4.27(c) prove that the dispersion error that does appear at a later time step for this calculation is not caused by the boundary condition. This seems to indicate that the error may be a result of the decreased mesh resolution encountered at the outer region of the domain. These results indicate that this specific formulation has an inherent accuracy, for this particular range of time steps, that nears that of the 4th-order accurate structured method for the interior region of the domain.

(a) t=3.0

(b) t=3.5

(c) t=4.0

(d) t=4.5
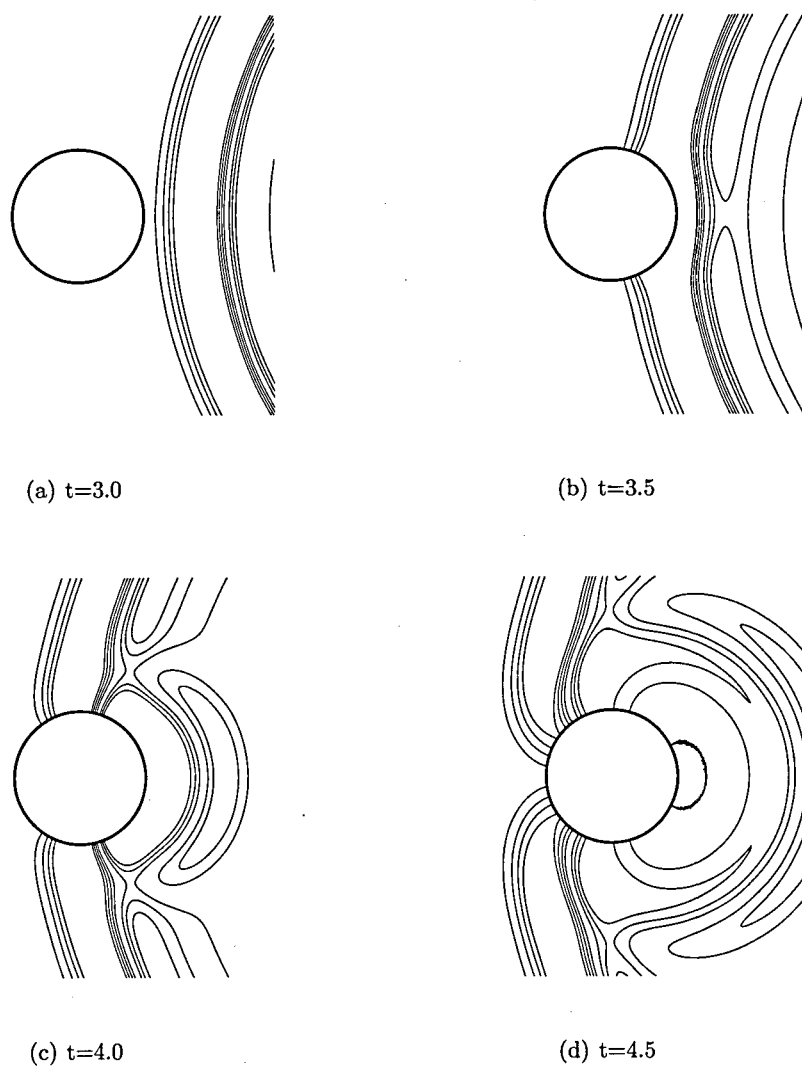
Figure 4.26: Pressure Contours At t=3, 3.5, 4 and 4.5 - TRI Mesh

(a) t=5.0

(b) t=5.5

(c) t=6.0
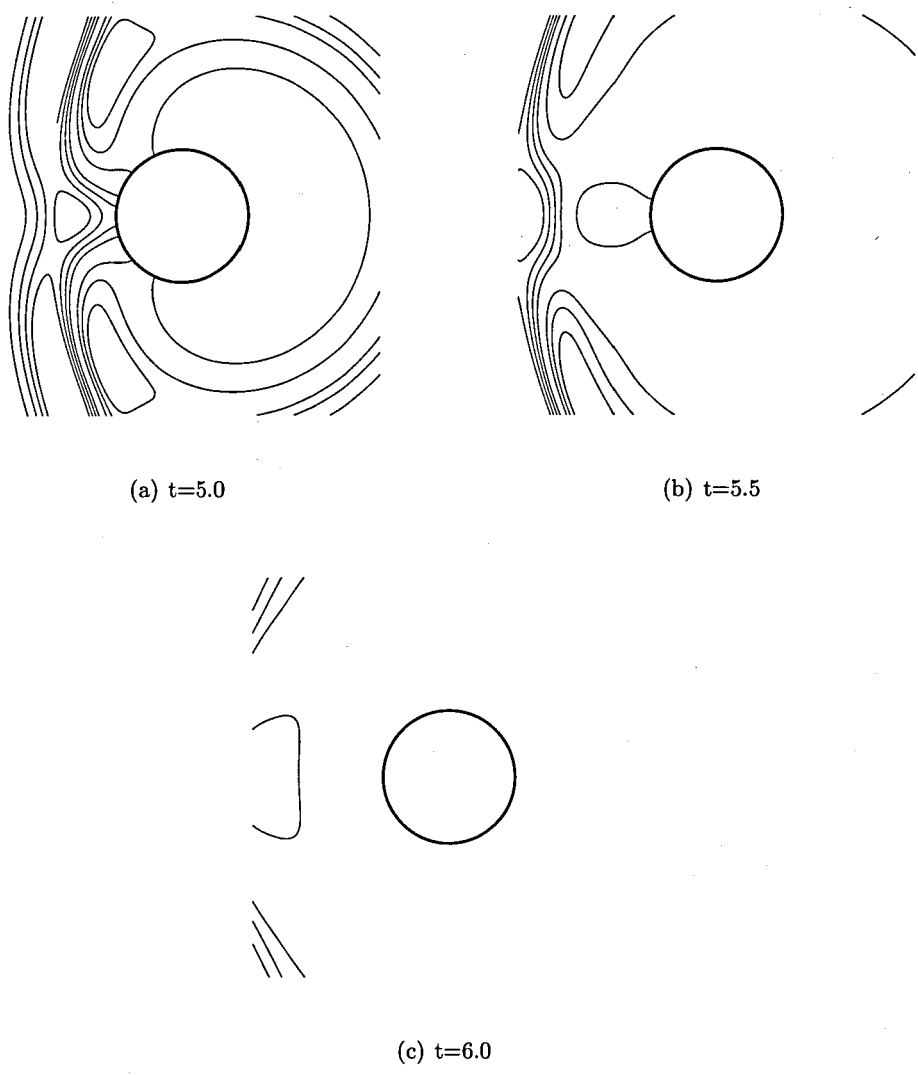
Figure 4.27: Pressure Contours At t=5, 5.5 and 6 - TRI Mesh

4.5 Comparison of Test Case Solutions with Published Results

In the Second CAA Benchmark Workshop Proceedings [64] there were fourteen different researchers that completed calculations for the scattering problem. Of the fourteen, only two did not use structured methods. Those two were the work of Atkins as well as Hsi and Périé. Atkins [5] used a quadrature-free discontinuous Galerkin method to produce results that were highly accurate when compared to the published solution. The method developed by Atkins used a fifth-order approximation of the finite elements along with a standard three step Runge-Kutta time discretisation. The results, reproduced in Figure 4.28, show a high degree of accuracy with only a slight under-prediction of the peaks of the pressure profiles. The method devised by Hsi and Périé [39] employed a commercial finite element package coupled with an explicit time integration algorithm. The commercial package, RADIOSS CFD, used a Lagrangian finite-element approach to calculate the results reproduced in 4.29. The results published by Hsi and Périé show a large amount of dispersive error and very low accuracy. The basic forms of the pressure waves are lost in the each of the profiles corresponding to the three pressure locations. There is very little correlation between the calculated results and the published solution in this case.

Of the remaining structured methods described in the Benchmark Proceedings there are several that show high levels of accuracy but not all. The DRP/LDDRK method of Tam et al. [65] was used to calculate results that show no dispersion or dissipation errors, as with the uniform mean flow problem. The 7-point sixth-order DRP spatial approximation and the tuned coefficients of the LDDRK temporal approximation required the addition of artificial selective dampening to complete a simulation of the scattering problem. The DRP/LDDRK results, reproduced in Figure 4.30 show that the calculated pressure profiles lie directly on the solution profiles. Another accurate method that was used to calculate solutions to the scattering problem was that of Hayder et al. [35]. This method used a combination of spectral methods and a 6th order compact scheme for spatial discretisation and the same LDDRK time stepping algorithm of Tam. The results of Hayder et al. have been reproduced in Figure 4.31. As with the results of Tam et al., the calculated pressure profiles match the solution profiles showing a very high level of accuracy.

For less accurate results, those calculated by Fung [29] using a 3rd-order compact
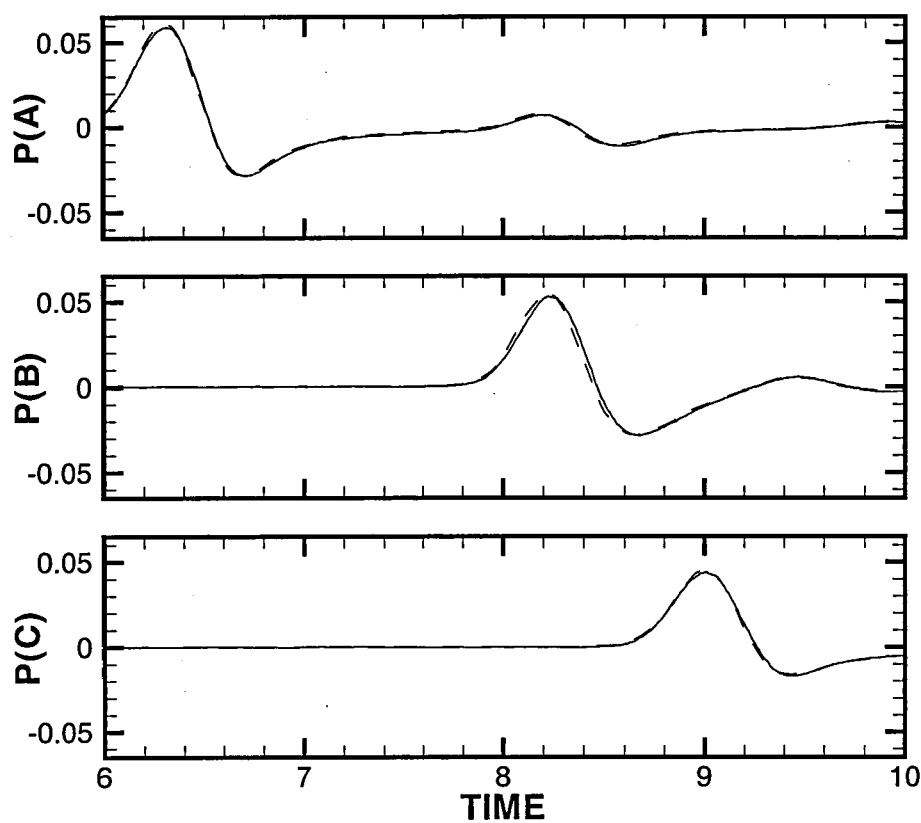
Figure 4.28: Pressure History for Reference Points - Atkins [5]
— Computed, - - - Exact
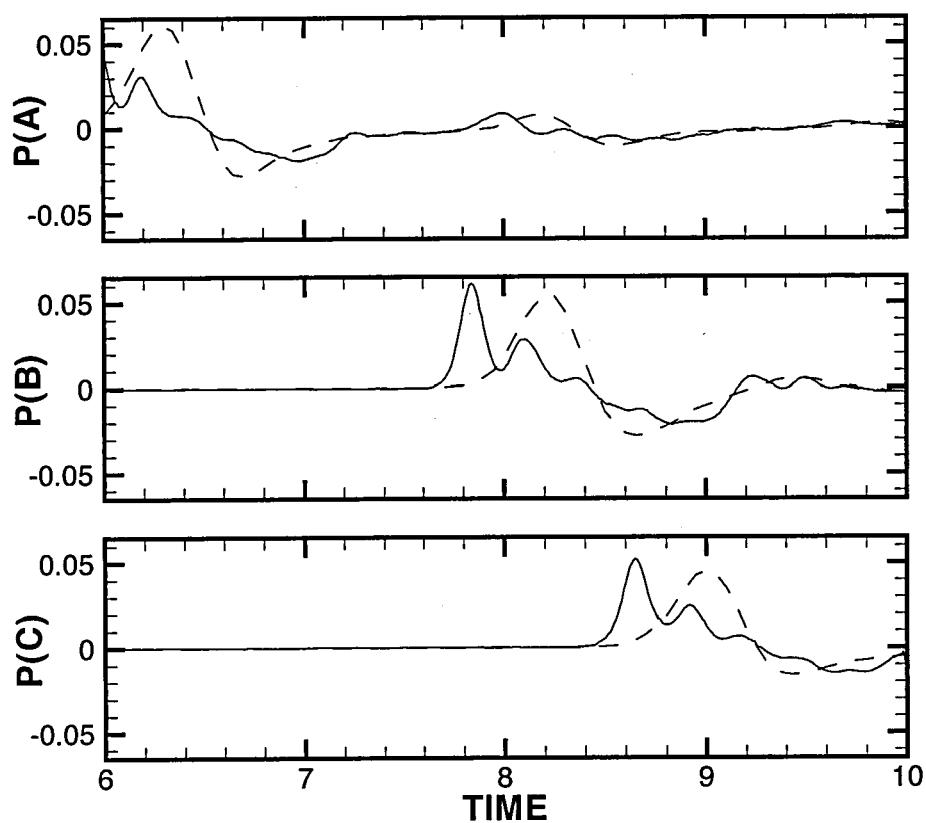
Figure 4.29: Pressure History for Reference Points - Hsi and Périé [39]
— Computed, - - - Exact
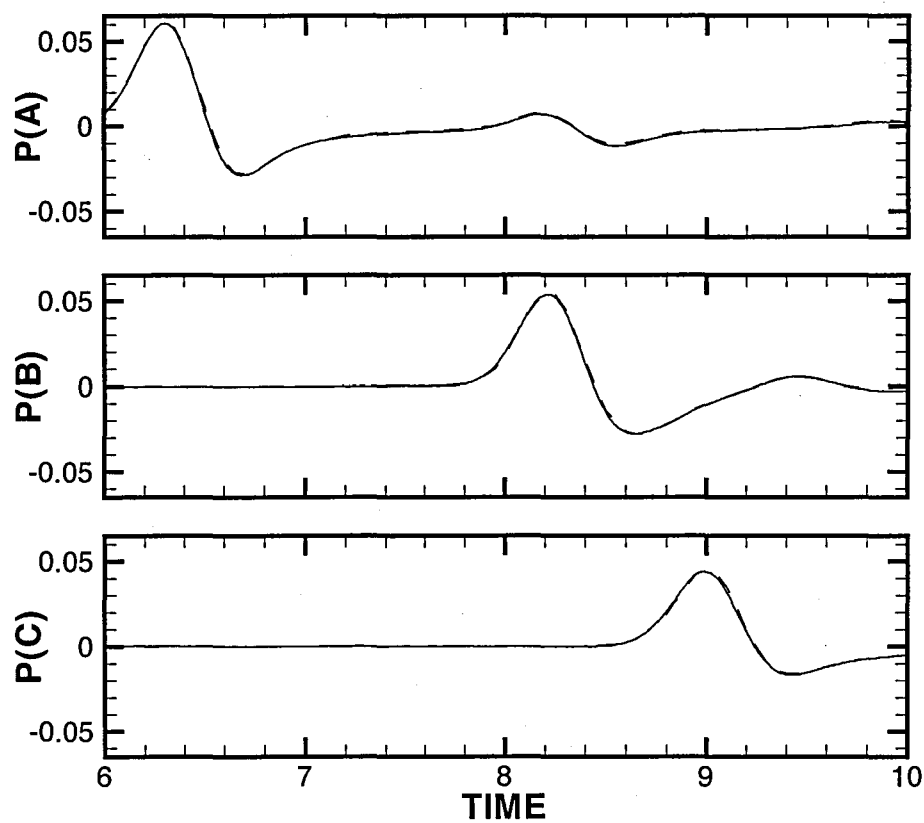
Figure 4.30: Pressure History for Reference Points - Tam et al. [65]
— Computed, - - - Exact
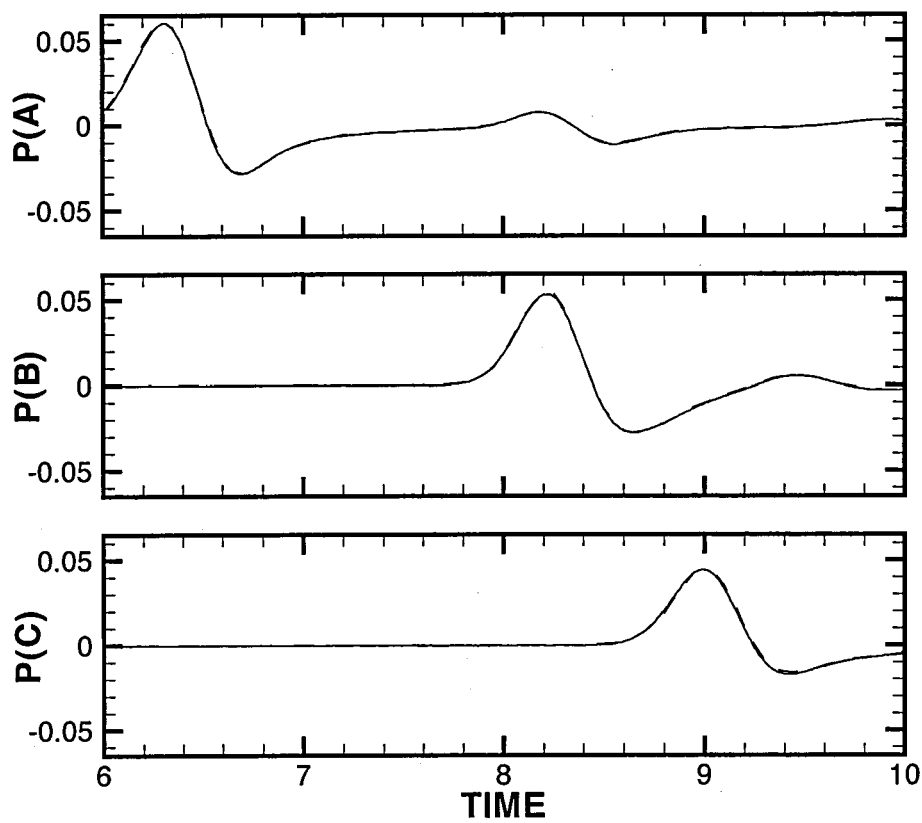
Figure 4.31: Pressure History for Reference Points - Hayder et al. [35]
— Computed, - - - Exact

scheme show dissipation errors that dampen the waveforms of all three of the pressure profiles. The results of Fung have been reproduced in Figure4.32. Another method that showed effects of dissipation and had difficulty remaining accurate were those of Lin and Chan [48]. The method developed by Lin and Chan used a Least Squares spectral element method to approximate the spatial discretisation along with a three level time stepping technique. The results of Lin and Chan are reproduced in Figure 4.33 and show that their method had difficulty in resolving the scattered pressure pulse especially at pressure locations A and C, directly above and behind the cylinder. This selection of results show that even with high-order structured methods the simulation of the scattering problem is not a trivial task and is an important part of the determination of the accuracy of a numerical method for use in computational aeroacoustics.
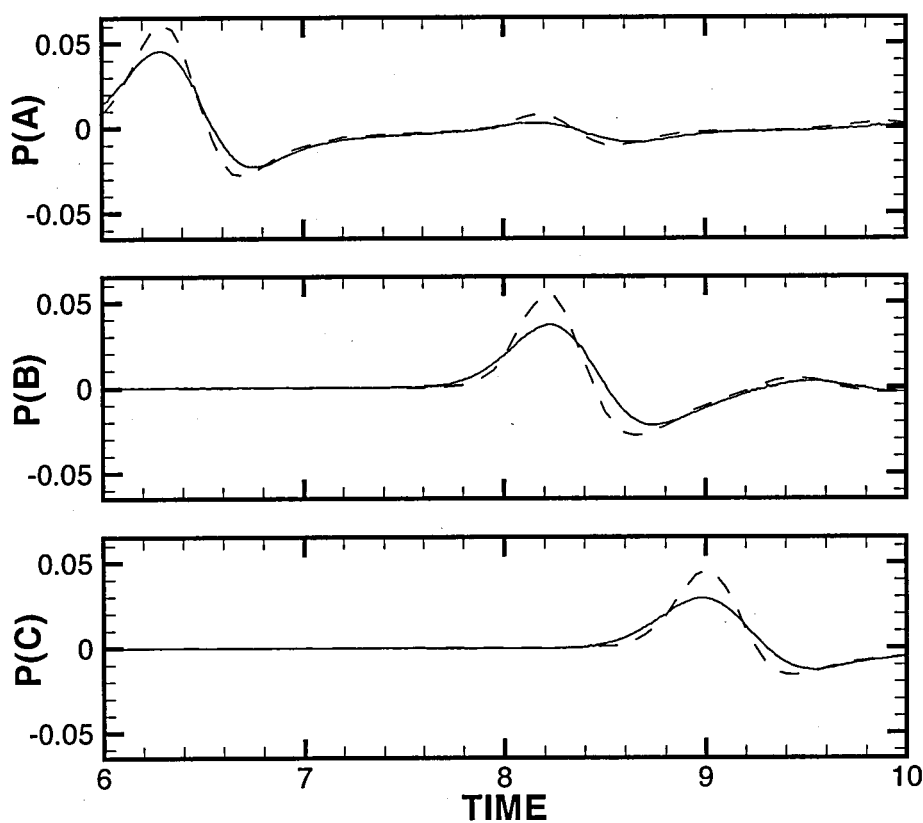
Figure 4.32: Pressure History for Reference Points - Fung [29]
— Computed, - - - Exact
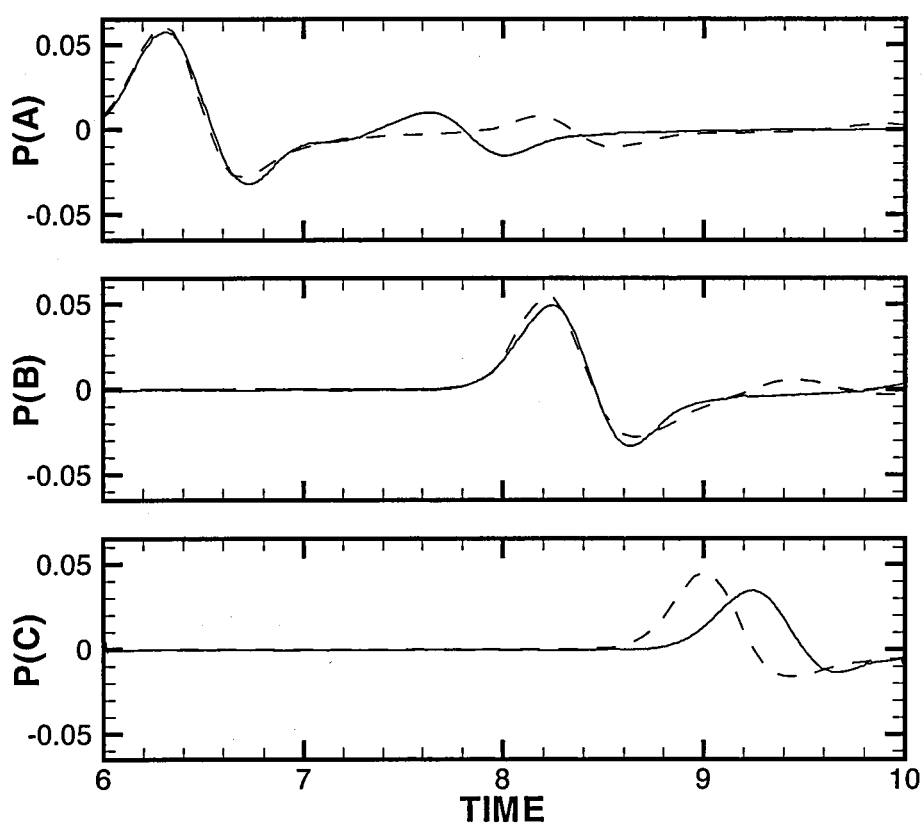
Figure 4.33: Pressure History for Reference Points - Lin and Chan [48]
— Computed, - - - Exact

4.6   Summary of Results

As with the uniform mean flow problem, the unstructured calculations completed for the scattering problem were compared to those of the structured method and the published results both numerically and graphically. The RMS error calculations that provided the numerical comparison showed that while the semi-structured mesh calculations had low accuracy, the accuracy of the purely unstructured TRI mesh calculation was comparable to that of the fourth-order accurate structured method. There was typically an order of magnitude difference between the RMS error of the semi-structured mesh calculations and the TRI mesh calculation. For two of the three pressure profiles, the RMS error of the structured method was approximately half that of the TRI mesh calculation, but for pressure location C the RMS error of the unstructured TRI mesh calculation was better than that of the structured method. This result indicates that for this particular problem, the use of a weighted Least Squares gradient approximation on a purely unstructured mesh performed on par with a basic fourth-order accurate structured method.

When comparing the three unstructured calculations with the structured results and solution, the conclusions remain. The unstructured method appears to have a strong error producing sensitivity to the semi-structured meshes for the scattering problem. The pressure profiles of both the NEG and UK mesh test cases show high levels of dispersive error for all of the pressure point locations. This error is not present with the TRI mesh however. For all three pressure profiles the TRI mesh calculation shows a high level of accuracy. When compared to published results, the unstructured method present here outperforms a 3rd-order compact scheme and a spectral element method. The results of the TRI mesh calculation appear very similar to those of the fourth-order accurate structured calculation.

The formulation of this problem required the use of a solid boundary condition to represent the wall of the cylinder. Since the governing equations and the basic phenomena of the two Benchmark problems are essentially the same it was believed that the inclusion of the solid wall caused the semi-structured meshes to lose the accuracy they displayed with the uniform mean flow problem. With the unstructured method certain characteristics of the meshes were utilized to aid in the application of the solid boundary condition for all three meshes. These characteristics were discussed in Section 2.4.4 of Chapter 2. For the NEG and UK meshes as well as the TRI mesh the repeating pattern and cell structure near the interior boundary was used to simplify the solid wall

boundary condition to a first order approximation. This approximation appears to have had no detrimental effect on the TRI mesh calculation, but seems to be the cause of the error for the NEG and UK mesh cases. As shown in Section 4.4 closer examination of the interaction between the pressure pulse and the solid cylinder indicates that the dispersive error of the TRI test case present at 10.0 computational time units in not caused by the application of the boundary condition. The simulation of the pressure pulse hitting the cylinder using the unstructured method and the TRI mesh appears virtually identical to that of the 4th order accurate structured method calculation. This indicates that the dispersion error is caused sometime after the pulse hits the cylinder wall and seems to indicate that the middle region of the domain is the true cause. All of the unstructured cases show an increasing level of dispersive error at later stages of the calculation as the pressure wave is convected through the middle region of the mesh (approximately halfway between the cylinder and the external boundary). In this region the cells are increasing in size and changing aspect ratio with every step further from the solid cylinder. Since the TRI mesh case shows that the error does not necessarily come from the solid boundary condition but does appear when the pulse reaches a region where the mesh cells are considerably larger, the unstructured method seems to demonstrate a sensitivity not only to the semi-structured nature of the NEG and UK meshes, but an overall sensitivity to mesh cell size. It is believed that when these dispersive errors occur the pressure pulse has not yet interacted with the outer boundary and the error is in fact due to the changing nature of the mesh.

Chapter 5

Conclusions And
Recommendations

5.1   Summary Of Results

5.1.1   Uniform Mean Flow Problem

For the uniform mean flow problem there was a marked difference between solutions calculated using Green-Gauss gradient approximation and solutions calculated using a weighted Least Squares scheme. On two of the three mesh types the RMS error was halved by using the weighted Least-Squares gradient method. It was only on the NEG mesh that the Green-Gauss approximation performed better than the weighted Least Squares method. On both the UK and TRI meshes, the RMS error of the density field calculated using the weighted Least Squares scheme was approximately half that of the Green-Gauss method. In tests using the UK and TRI meshes the standard Least Squares approximation had an RMS error that was slightly lower than that of the Green-Gauss method, but not approaching the level of the weighted Least Squares formulation. On the NEG mesh the Least Squares technique had nearly double the error of the two other approximation methods. When comparing the results of the test cases graphically, there appeared to be an acceleration or compression of the pressure pulse when the Green-Gauss and Least Squares gradient approximation methods were used. This acceleration error was present with all three mesh types and had a greater effect on the downstream portion of the pressure pulse than the upstream portion. These results were the same for both the single and dual quadrature point tests. The uniform mean flow problem

solutions were used to determine the best combination of approximation method and quadrature, that being the use of a single quadrature point with the weighted Least Squares technique. The use of the weighted Least Squares gradient approximation was the only method with noticeable dispersion errors. These errors, though small, were visible on all three mesh types. This dispersive error had little effect on the calculation of the RMS error as the error calculated on the weighted Least Squares test case with the TRI mesh was still the lowest of all the unstructured calculations. For all of the tests completed, the best unstructured solution had an RMS error that was an order of magnitude greater than that of the 6th-order accurate structured method.

5.1.2 Scattering Problem

For the scattering problem the weighted Least Squares approximation method was tested on different mesh types to determine mesh sensitivity and the effect of boundary conditions not present in the previous test case. The most accurate scattering problem solution was completed with the use of the purely unstructured TRI mesh. For each of the three pressure monitoring points the solution of the TRI mesh was the most accurate, and even had a lower RMS error than the 4th-order accurate structured method for one pressure profile. The NEG and UK meshes have similar RMS errors for all three pressure points, but the TRI mesh consistently showed an error an order of magnitude less than that of the other unstructured methods. The decrease in RMS error between the semi-structured NEG/UK and purely unstructured TRI meshes appears to be linked to the application of solid wall boundary conditions. For all of the unstructured mesh calculations a simple solid wall BC was applied that mimicked the condition applied for the structured method and took advantage of the mesh layout along the boundary. The exact same boundary condition was applied to both the NEG and UK mesh test cases, but only a similar boundary condition was applied to the TRI mesh. This was due to the fact that the orientation of the cells along the boundaries differ between the semi-structured and purely unstructured meshes. This change in boundary condition seems to have caused the increase in RMS error and the drastic change in the pressure profile that was calculated at each of the three pressure locations.

After completion of the three unstructured calculations the mesh that was best suited for the more complex scattering Benchmark problem was the purely unstructured TRI mesh. This mesh type was used as a blueprint to created three other similar meshes, all created with the same paving algorithm and all progressively more coarse.

The difference between each of these three new TRI meshes was the number of vertices contained within each mesh. This allows for the calculation of a numerical order of accuracy using mesh coarsening as a control. By using the results obtained using these purely unstructured meshes it was determined that the approximate numerical order of accuracy was different for each of the three pressure profiles calculated. The formulation and analysis involved for the numerical order of accuracy can be seen in Section A.1 of Appendix A. The numerical order of accuracy analysis provided an interesting result. The approximate order of accuracy for two of the three pressure profile calculations was different from that of the third. For pressure profiles associated with locations A and C, the approximation stated 2nd order accuracy. For the pressure profile associated with location B, the approximation gave 1st order accuracy. Not only are the values different, but they are much lower than expected. Normally a 2nd order accurate approximation would not be considered sufficient for CAA scenarios. By comparing the results of the TRI mesh calculation with the 4th order accurate structured case the unstructured method displays an order of accuracy approaching 4th order. The unstructured method results also compared favorably with those of other researchers, displaying an order of accuracy comparable to high order structured methods currently in use.

In their comprehensive paper on the progress of computational approaches for problems in aeroacoustics Colonius and Lele conclude that determining factors used for choosing the best numerical method for CAA problems must include "ease of implementation (and especially imposition of BC)" and the "potential for straight forward implementation in different geometries and flow configurations" [17]. This conclusion is one shared by the majority of researchers in this field and has caused the finite difference methods, especially the high-order accurate and optimized methods, to become the favored methods for computational aeroacoustics. The numerical method used to obtain the results discussed above easily fulfills these requirements. The change from a structured method to an unstructured one successfully addresses the inherent difficulties associated with complex geometries. Also the simple and unique formulation of the boundary conditions have proven to be very successful as shown by the results of Benchmark problems.

Colonius and Lele state how "surprisingly difficult" it is to "maintain high accuracy and computational efficiency for flows in complex geometry (i.e. with unstructured or overlapping body-fitted coordinates)" and that "complex geometry codes can only obtain good accuracy by increasing the resolution" [17]. With the numerical method developed as part of this research the use of a simple Least-Squares approximation, on

a mesh whose nodes correspond exactly to that of the finite difference scheme, provides numerical results which match and in some cases outperform a 4th order accurate structured method. The unstructured method also demonstrates accuracy approaching that of a 6th-order accurate FD scheme. This proves how powerful and unique this combination of discretisation and gradient approximation is. The main purpose of this research was to develop a simple yet accurate unstructured method for CAA applications. The results shown by using this numerical method to calculate solutions for the Benchmark CAA problems prove that the numerical method developed is accurate and demonstrates low dispersive and dissipative error. These results were calculated using a basic Runge-Kutta time discretisation and Least Squares gradient approximation fulfilling the main purpose of creating a simple unstructured numerical method for aeroacoustic applications.

5.2   Achievements and Findings

Referring to the objectives of the present research listed in Section 1.10, the achievements and findings are:

1. A standard high-order central-differencing structured method can be used for basic aeroacoustic simulations. A 6th-order accurate method was used for a uniform mean flow problem and a 4th-order accurate method was used for a scattering problem. Both methods showed high accuracy and low dispersion and dissipation. Both structured methods displayed accuracy on par with other methods currently in use by other researchers in the field.

2. For CAA problems the most accurate unstructured numerical method tested as part of this research included the use of weighted Least Squares gradient approximation with a single quadrature point used for reconstruction. The mesh type best suited for this application was shown to be the purely unstructured TRI mesh.

3. For the scattering problem, the unstructured method described above showed an agreement with the exact solution comparable to (and even surpassing) that of a 4th-order accurate central-differencing structure method. It also showed low dispersion and dissipation error making it a suitable choice for aeroacoustic applications.

4. A spatial convergence analysis showed that the numerical method developed should display approximately second-order accuracy. This level of accuracy was suggested through both analytical and experimental analysis. The results of the test cases showed that the true accuracy was greater than that suggested by the analysis.

5.3 Recommended Future Work

The ultimate goal of this research would be the extension of the numerical method developed into three dimensions and real-life scenarios. It is believed that before that occurs, a more logical and rational testing procedure should be completed. The unstructured code has shown agreement with published results comparable to that of a fourth-order accurate structured method for the scattering problem and low dispersion and low dissipation for both test case problems it has been tested on. The next step is to further test how the method responds to similar but more complex scenarios. The uniform mean flow problems should be adapted to include a two-dimensional flow field at an angle of 45° across the domain. The next step is to change from a uniform mean flow to a complex flow field, although one that is still prescribed analytically and not evolving with the flow. Examples of two-dimensional flow fields that are currently being used in more recent CAA Workshops are the exhaust of a subsonic nozzle and a shear layer [20]. These different flow fields will assess how effective the numerical method is at modeling mean flow refraction. The next step is to use a predicted RANS CFD mean flow field to determine how the numerical method deals with a real-life flow field. This progression from simpler to more complex flow scenarios would give the numerical method proof of its ability to be used in real life situations where the flow field can be complex.

The scattering problem shows that the current method has a reasonable implementation of a solid wall boundary. This should be tested on more complex (but still 2D) shapes such as a square or aerofoil profile. Since the method is already unstructured, it is relatively straightforward to extend it to 3D. A natural progression would be to test the numerical scheme on scattering from a circle in 2D should extend into scattering from a sphere in 3D. A similar problem, that of aeroacoustic shedding over a cylinder in three dimensions was already suggested in the second CAA Workshop [64]. It is believed that the scattering from a sphere is a truer fundamental test of a three-dimensional aeroacoustic method and has been investigated with the use of discontinuous Galerkin

methods [12, 18]. The comparison of the DG test case results with those of this numerical method is of interest and should be undertaken. It is believed that the extension of the method into 3D will prove the effectiveness of the method and lead the way into its application onto more complex geometry and eventually real-life geometries such as landing gear and engine struts.

The numerical method tested here is very similar to many finite volume CFD solvers used to simulate nonlinear flow scenarios so knowledge learned here can be incorporated into existing finite volume unstructured solvers that compute the nonlinear flow field and the acoustics together. There are other examples of Benchmark Workshop test cases that can be used to further explore the numerical abilities of this unstructured method such as the Aeolian tone generation from two cylinders and the sound generation by flow over a cavity [21]. By logically increasing the complexity of the flow field capabilities and the geometric capabilities the unstructured method would be given the opportunity to demonstrate at each step how effectively it deals with the increasing complexity and prove its ability to eventually be an important design tool for real-life, complex flow scenarios.

Appendix A

Analysis of Unstructured Method

After completing the calculations associated with the scattering problem test case, it became apparent that the most accurate formulation of the unstructured numerical method includes the use of a weighted Least Squares gradient approximation on a purely unstructured mesh. In the first series of calculations, the addition of a second quadrature point had little or no effect on the results, therefore only a single quadrature point was used for the reconstruction in the scattering test cases. For both the uniform mean flow and scattering problems, this combination displayed the highest relative accuracy. The next step is to determine an approximate order of accuracy for the unstructured method. This is completed using a numerical determination of accuracy using mesh coarsening as a control.

A.1   Determination of Numerical Order of Accuracy

The numerical order of accuracy is determined using the RMS errors calculated on four different meshes. The function that best describes the relationship between mesh spacing and RMS error is then ascertained using linear regression. This function will then be used as an approximation of the numerical order of accuracy. The four different meshes that are used to determine the numerical order of accuracy are all purely triangular meshes. They were all created using the same method as the original TRI mesh for the scattering problem. The RMS error is taken from the solution of the scattering problem using the weighted Least Squares approximation and single quadrature point reconstruction.

In the scattering problem test case the TRI mesh was created by specifying a boundary vertex distribution and using a paving algorithm to determine the mesh cells. The three additional meshes (TRI2, TRI3 and TRI4) used to determine the numerical order of accuracy were all created the same way, the boundary vertex distributions were specified and then the paving algorithm was used to create the meshes. The statistics of the meshes used are listed in Table A.1 including the number of cells specified along the boundary, the number of vertices as well as the number of primary cells. The number of vertices of the mesh correspond to the number of median dual control volumes. The statistics of the structured mesh used in the calculation of the scattering problem is also listed in Table A.1 for reference.

Mesh Type	No. of Bdy. Vert.	No. of Vertices	No. of Pri. Cells
Structured	600	176055	175160
TRI	600	960863	1920526
TRI2	500	668241	1335482
TRI3	400	427699	854598
TRI4	300	239964	479328

Table A.1: Statistics of Accuracy Test Meshes

Once the solutions to the scattering problem were computed, the RMS error between the calculated pressure distributions and the published solutions was determined and compared. The RMS error for the various TRI mesh calculations can be seen in Figure A.2. The RMS error for the structured method solution to the scattering problem is included in Table A.2 as a reference.

The relationship between the mesh spacing and the RMS error of the pressure distributions can be seen in Figure A.1. The figure shows the log of the mesh spacing (defined below in Equation A.4) plotted against the log of the RMS error of the pressure distributions. The lines for the pressure distributions A,B and C are denoted by the circle ($\bigcirc$),triangle ($\triangle$), and square ($\square$) symbols, respectively.

For each of the three different pressure distributions a straight line approximation of the relationship between mesh spacing and RMS error was determined using a chi-
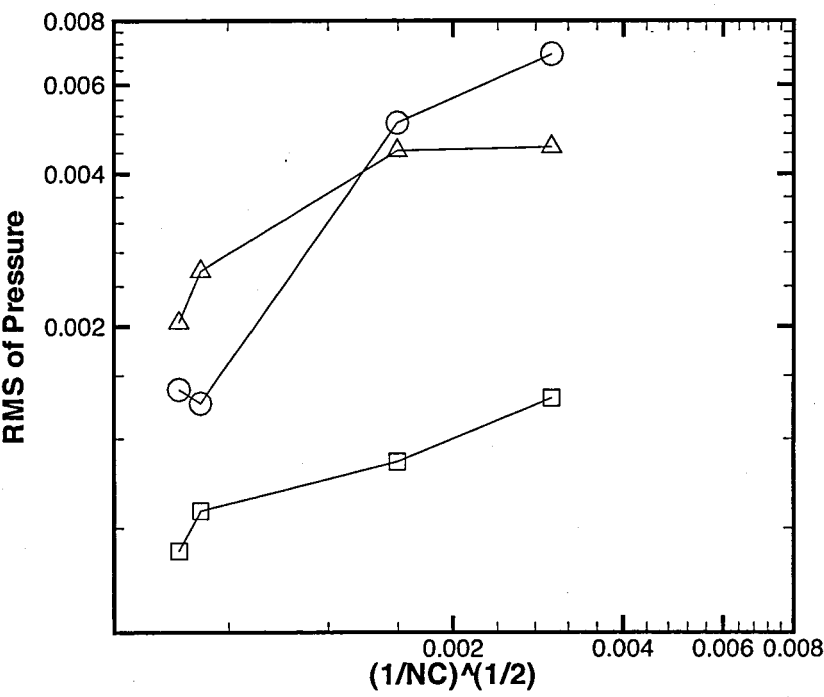
Figure A.1: Linear Regression Data Plot

Mesh	Pressure Location		
Type	A	B	C
Structured	0.9156 E-03	0.1393 E-02	0.9534 E-03
TRI	0.1502 E-02	0.2036 E-02	0.6524 E-03
TRI2	0.1410 E-02	0.2572 E-02	0.7130 E-03
TRI3	0.5041 E-02	0.4441 E-02	0.1595 E-02
TRI4	0.6882 E-02	0.4516 E-02	0.2992 E-02

Table A.2: RMS Error of Accuracy Test Calculations

squared linear regression of the equation

$$y = a + bx \tag{A.1}$$

where y refers to the log of the RMS error of the pressure distribution and x refers to the log of the mesh spacing. Each of the four meshes are used to calculate the linear regression for each pressure point locations, so

$$y_A = \log(\text{RMS}_{P_A}) \, , \; y_B = \log(\text{RMS}_{P_B}) \, , \; y_c = \log(\text{RMS}_{P_C}) \tag{A.2}$$

Looking at one of the pressure distributions, the chi-square merit function [57] can be written as

$$\mathcal{X}^2(a,b) = \sum_{i=1}^{N} \left(\frac{y_i - a - bx_i}{\sigma_i} \right)^2 \tag{A.3}$$

where σ_i is the standard deviation for the data set and is assumed to be constant. The N term refers to the number of points in the data set ($N = 4$) and y_i and x_i refer to the log of the RMS error and log of the mesh spacing, respectively. The mesh spacings for the four TRI meshes are defined using the number of cells as in

$$x_i = \sqrt{\frac{1}{NC_i}} \tag{A.4}$$

Using the merit function the a and b terms of Equation A.1 can be defined as

$$a = \frac{S_{xx} \cdot S_y - S_x \cdot S_{xy}}{\Delta} \tag{A.5}$$

$$b = \frac{S \cdot S_{xy} - S_x \cdot S_y}{\Delta} \tag{A.6}$$

where the regression coefficients are defined as

$$S = \sum_{i=1}^{N} \frac{1}{\sigma_i^2} \tag{A.7}$$

$$S_x = \sum_{i=1}^{N} \frac{x_i}{\sigma_i^2} \tag{A.8}$$

$$S_y = \sum_{i=1}^{N} \frac{y_i}{\sigma_i^2} \tag{A.9}$$

$$S_{xx} = \sum_{i=1}^{N} \frac{x_i^2}{\sigma_i^2} \tag{A.10}$$

$$S_{xy} = \sum_{i=1}^{N} \frac{x_i y_i}{\sigma_i^2} \tag{A.11}$$

and the Δ term is calculated using

$$\Delta = S \cdot S_{xx} - (S_x)^2 \tag{A.12}$$

The RMS error data and mesh statistics are taken from Tables A.1 and A.2 and used to calculated regression functions for each of the three pressure distributions. The coefficients for the three regression functions can be seen in Table A.3.

Pressure	Function Coefficient	
Distribution	a	b
P(A)	5.073	2.533
P(B)	1.212	1.234
P(C)	4.161	2.356

Table A.3: Regression Function Coefficients

For this numerical analysis the slope of the regression functions, term b in Table A.3, can be used as an approximation of the order of accuracy of the unstructured numerical method. This formulation tells us that the method should show a practical order of accuracy of approximately second order. This practical order of accuracy was determined with the full unstructured method for the scattering test case on the actual TRI mesh, not a simplified problem on a basic mesh. For a situation such as this determining a formal order of accuracy can be difficult, however with the combination of the spatial convergence analysis suggesting a second-order accurate method and the

experimental results showing that the calculated solutions show an agreement with the analytical solutions approaching fourth-order accuracy it can be assumed that the method is at least second-order accurate.

Appendix B

Calculated Solutions of Uniform Mean Flow Problem

B.1   Structured Test Case
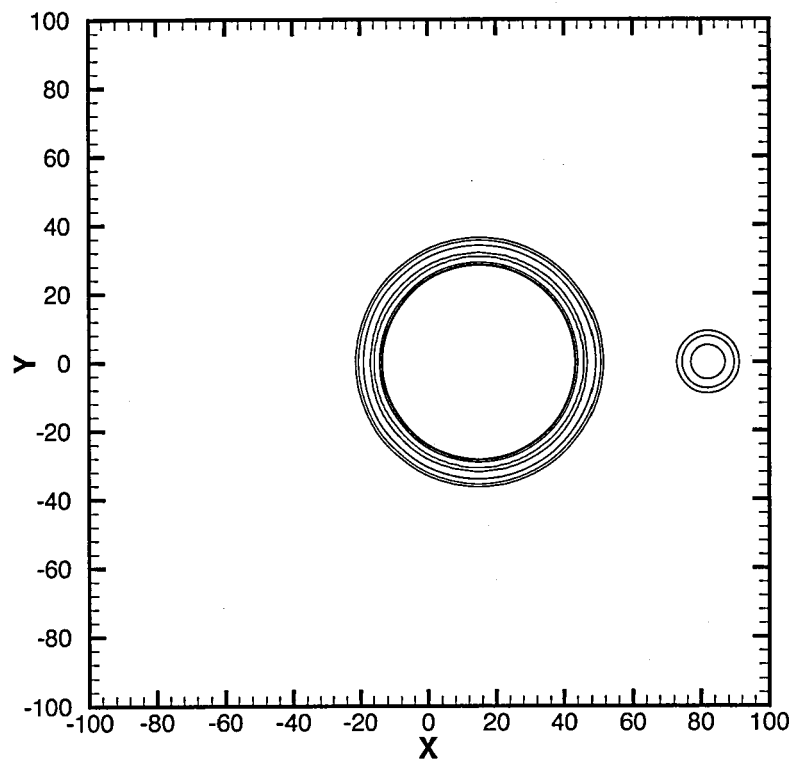
(a) Density Contours at t=30
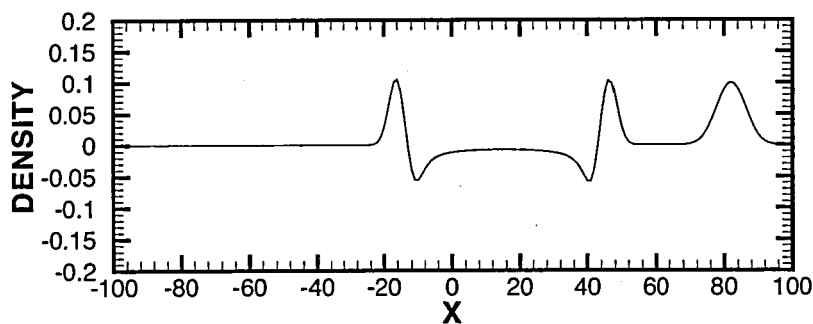
(b) Density Profile Comparison at t=30

Figure B.1: Structured Method (1)
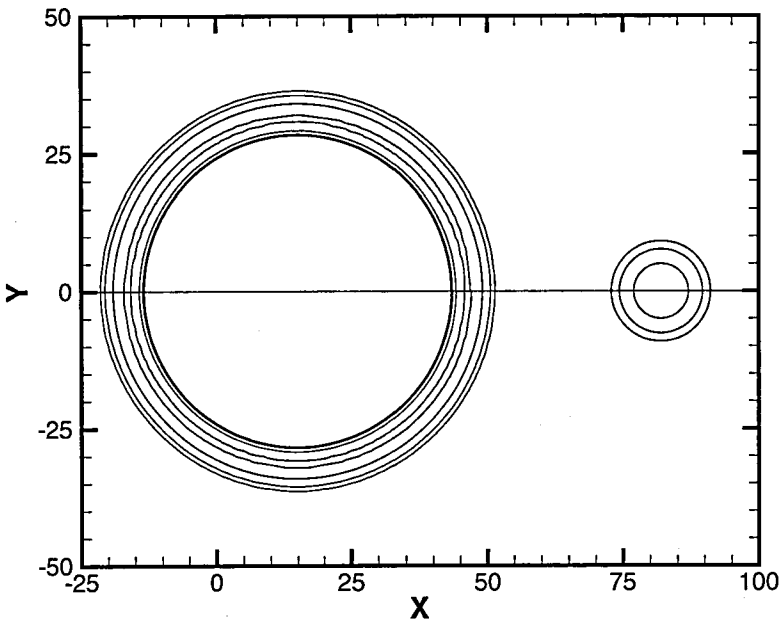
Figure B.2: Structured Method (2)

B.2   NEG Mesh Test Cases

B.2.1   Single Quadrature Point Test Cases
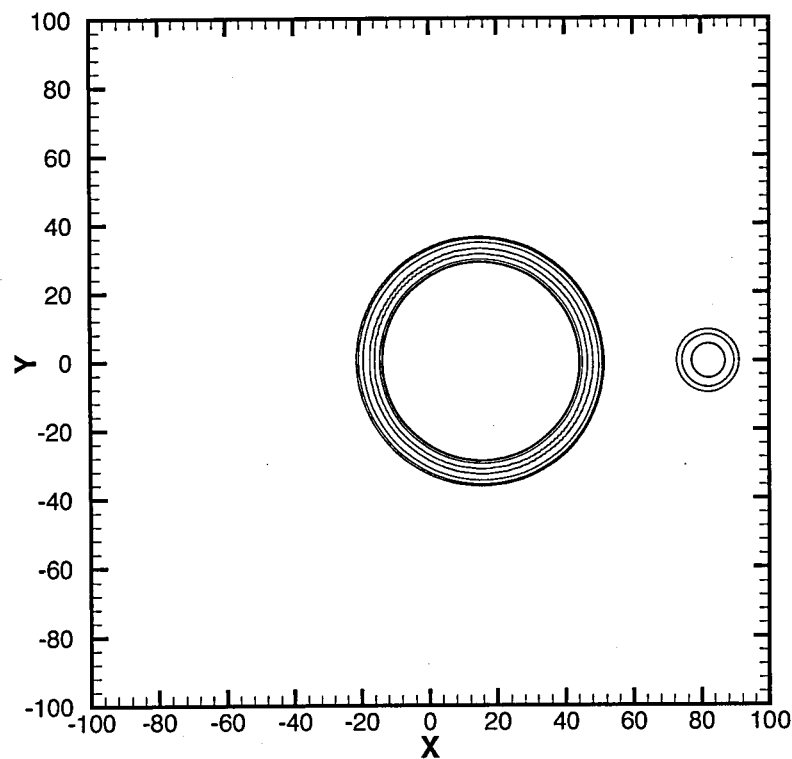
(a) Density Contours at t=30
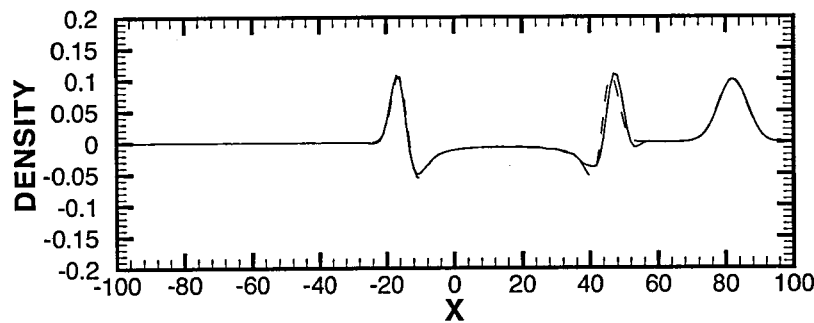
(b) Density Profile Comparison at t=30
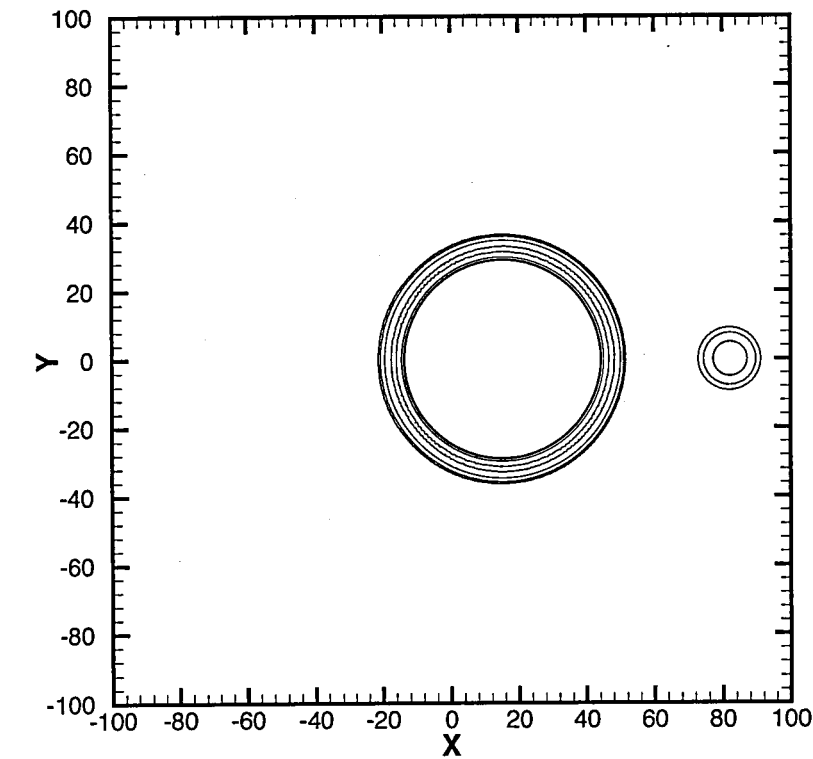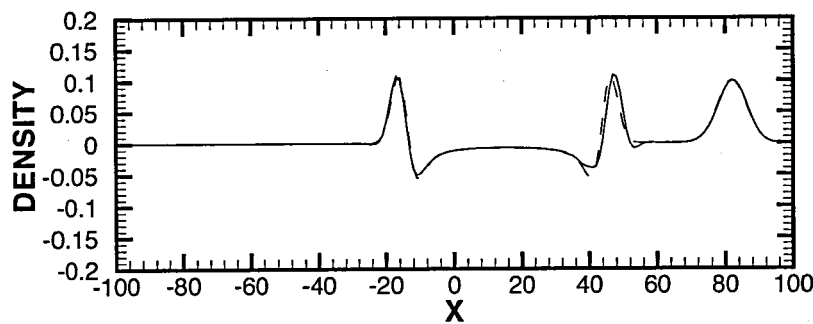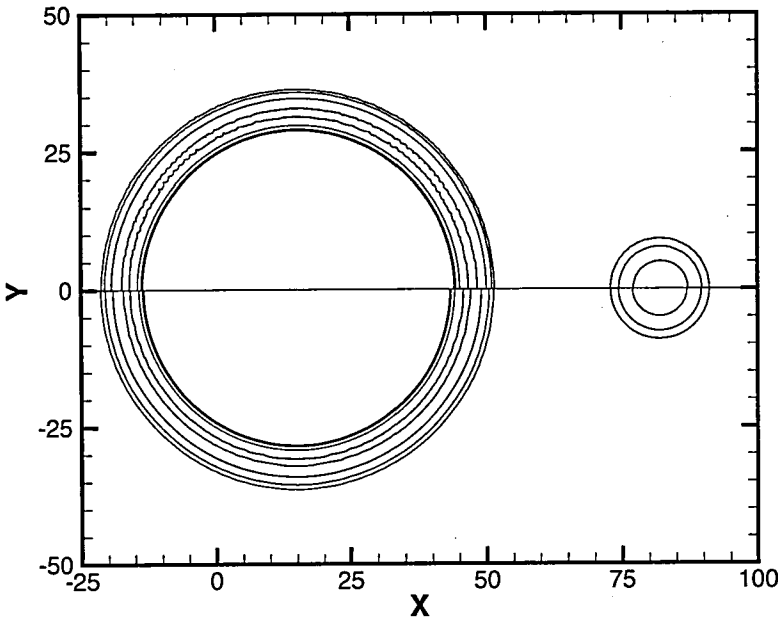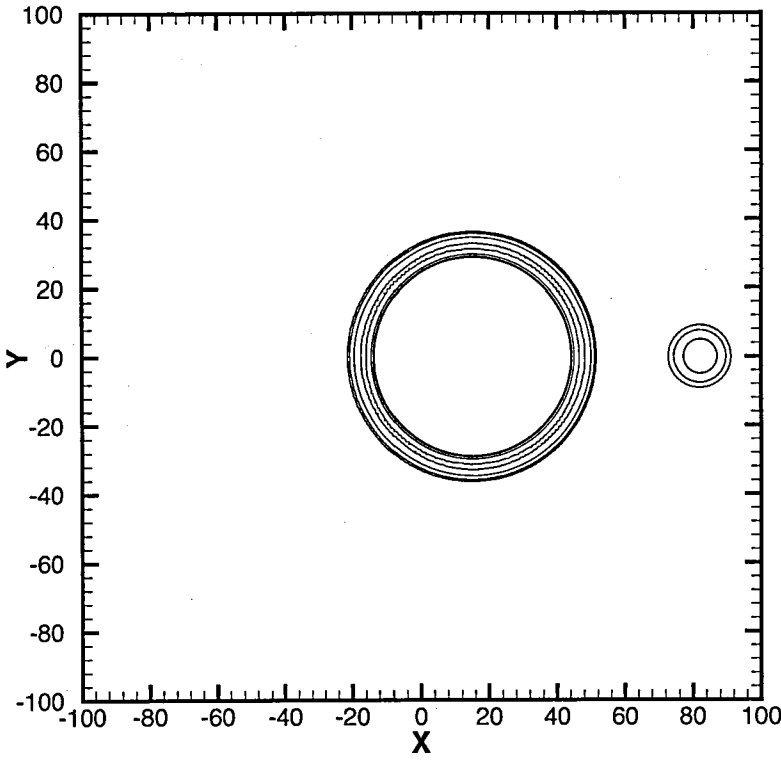
Figure B.3: Green-Gauss Gradient Approximation Method (1)
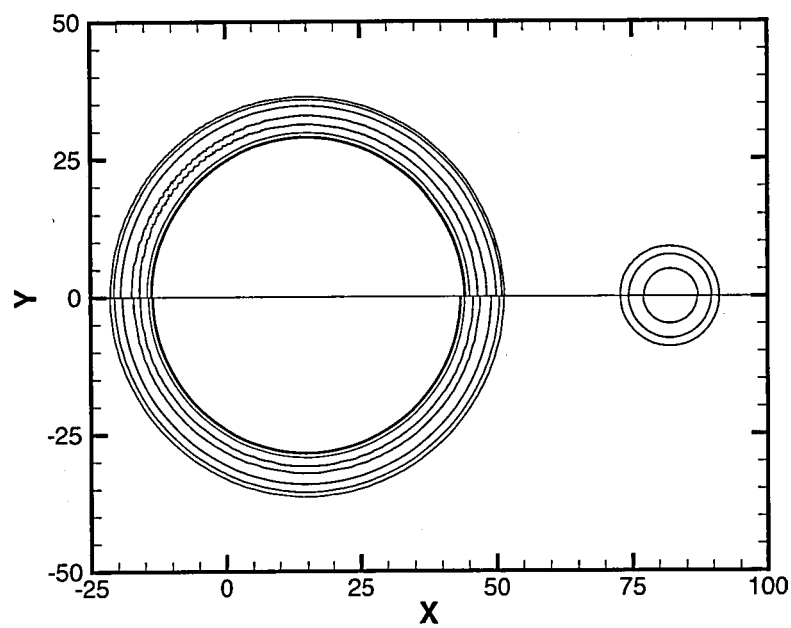
Figure B.4: Green-Gauss Gradient Approximation Method (2)
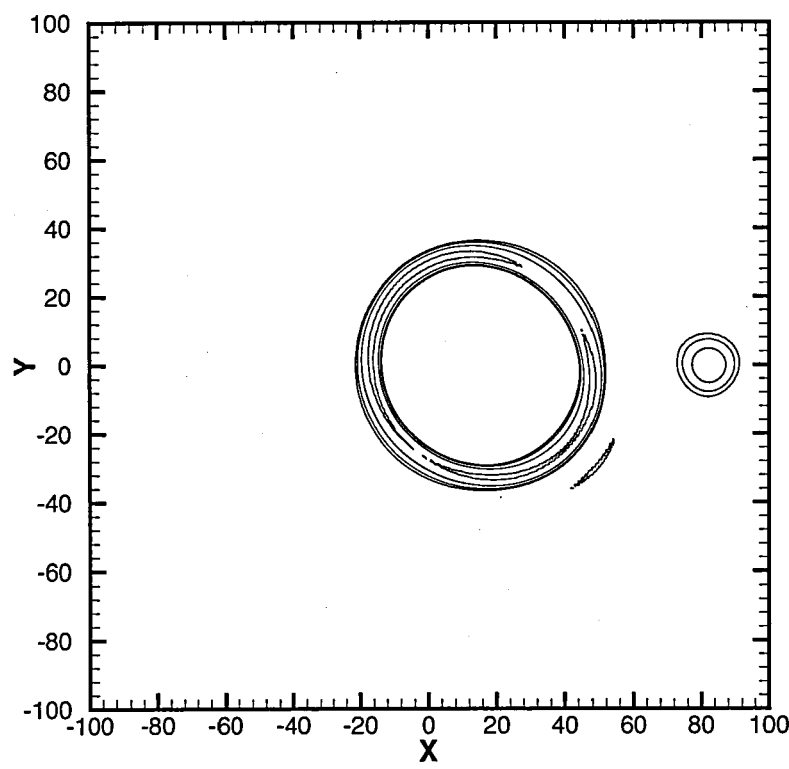
(a) Density Contours at t=30
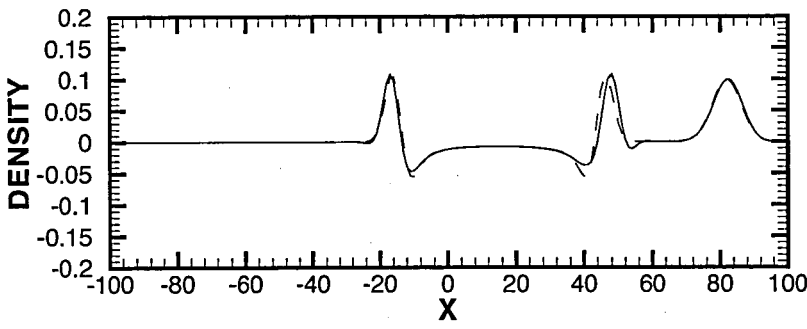
(b) Density Profile Comparison at t=30

Figure B.5: Least Squares Gradient Approximation Method (1)
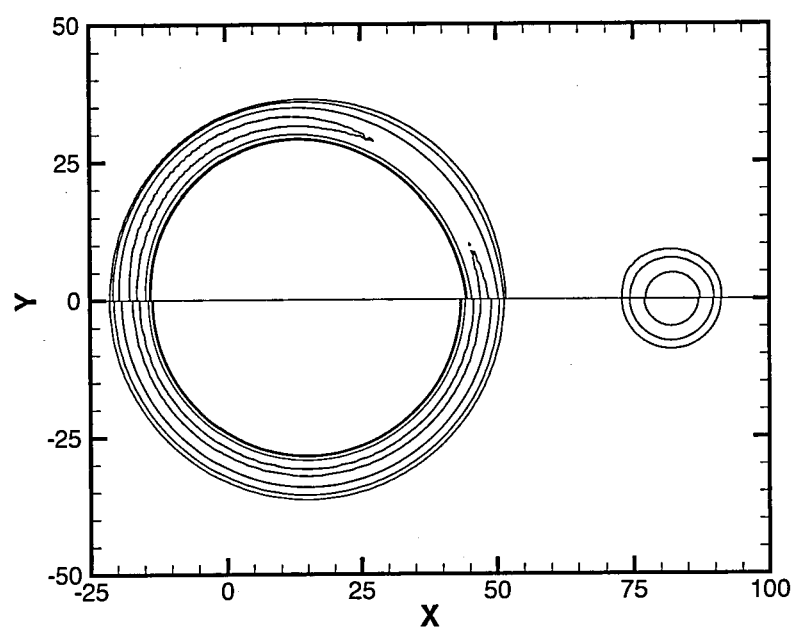
Figure B.6: Least Squares Gradient Approximation Method (2)
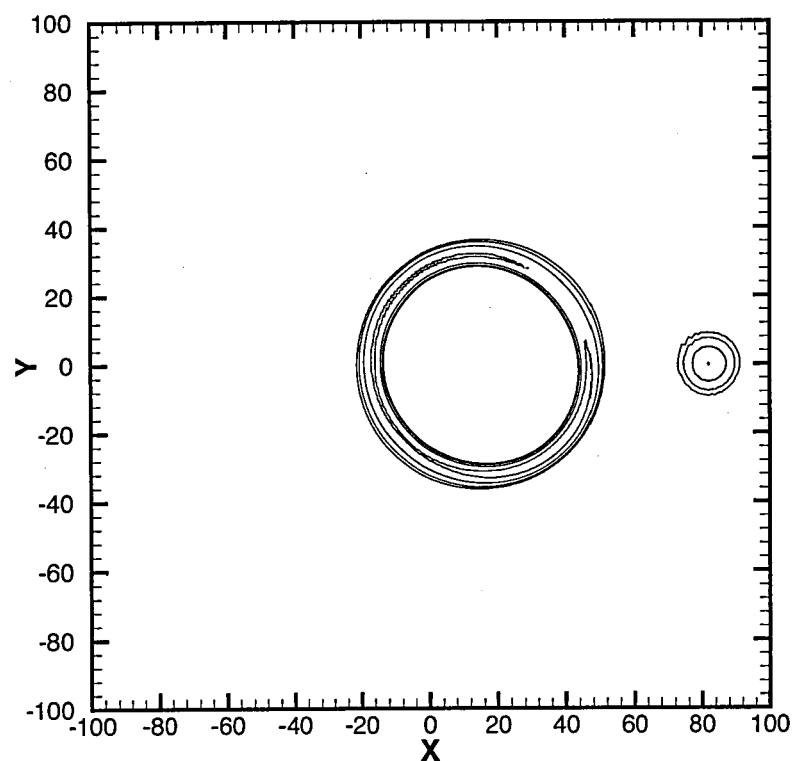
(a) Density Contours at t=30
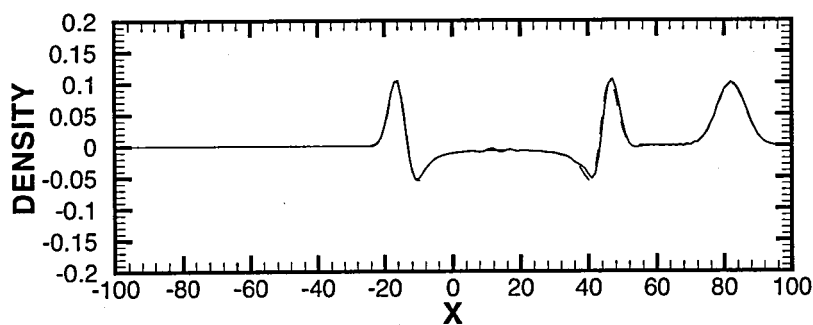
(b) Density Profile Comparison at t=30

Figure B.7: Weighted Least Squares Gradient Approximation Method (1)
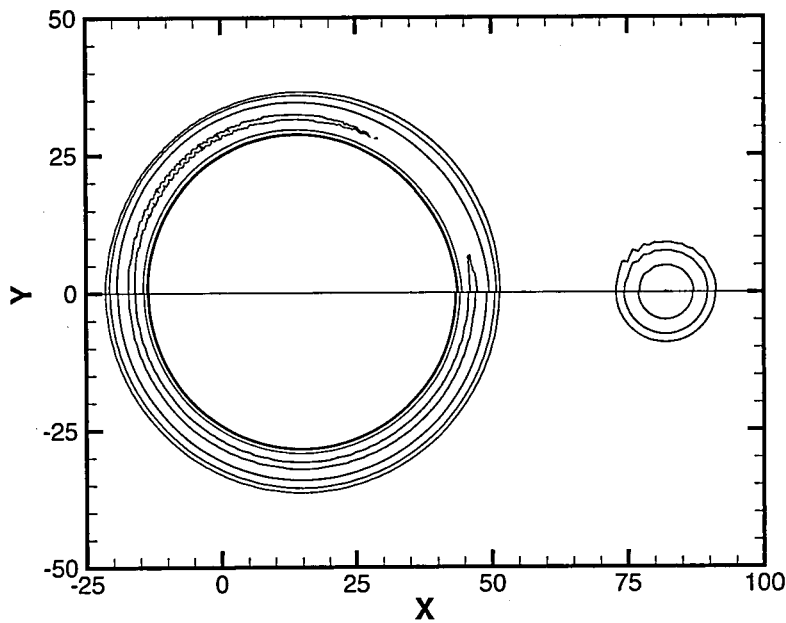
Figure B.8: Weighted Least Squares Gradient Approximation Method (2)

B.2.2   Dual Quadrature Point Test Cases
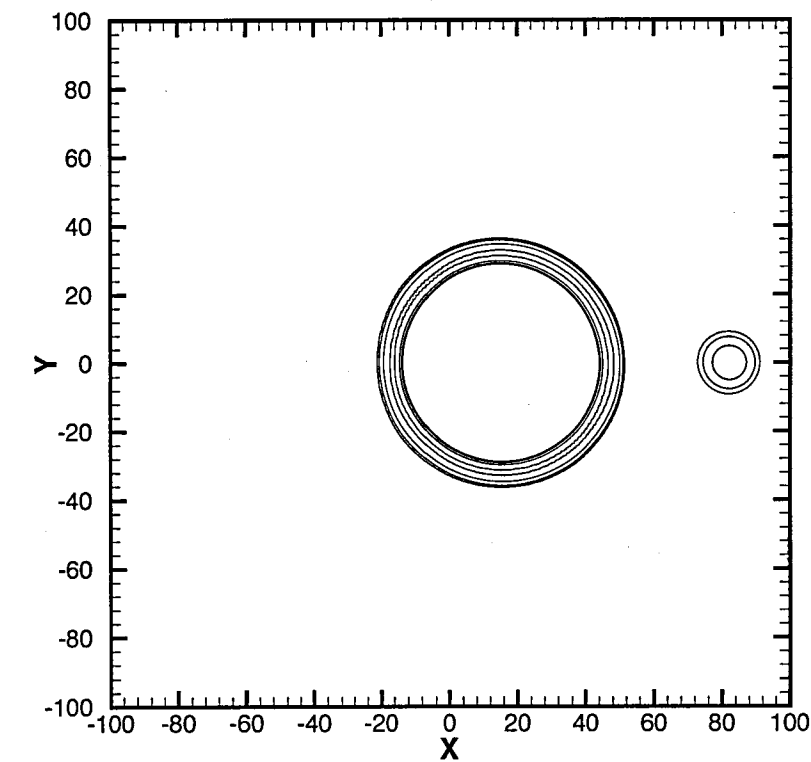
(a) Density Contours at t=30
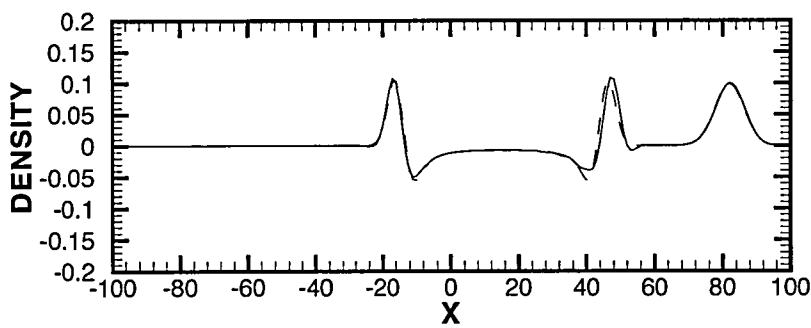
(b) Density Profile Comparison at t=30
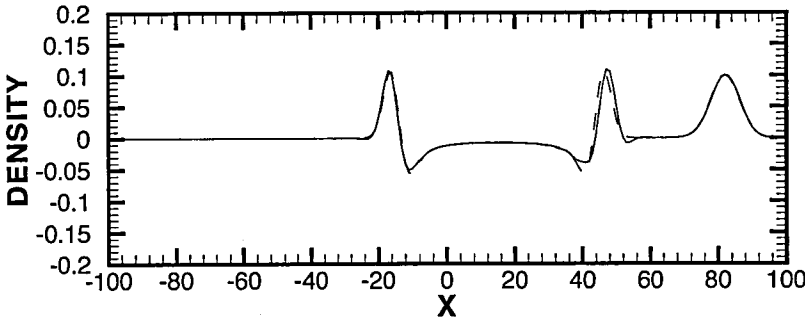
Figure B.9: Green-Gauss Gradient Approximation Method (1)
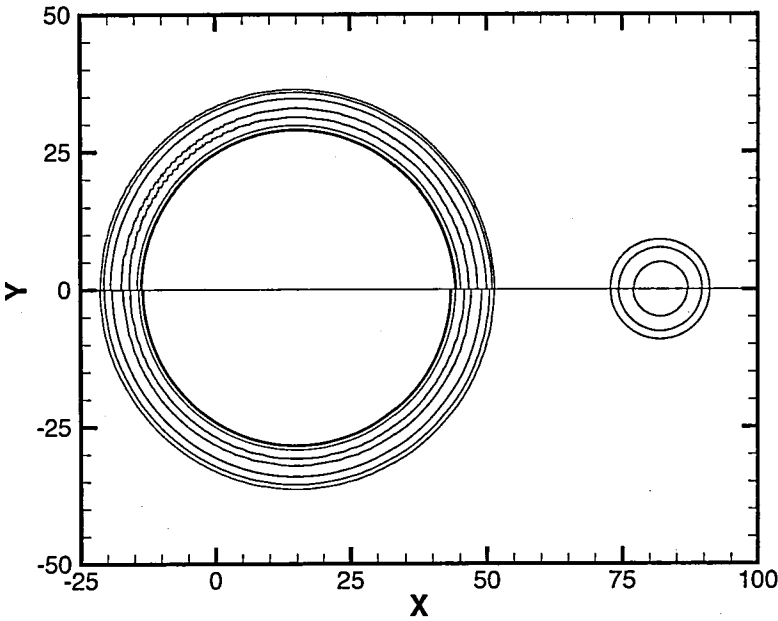
Figure B.10: Green-Gauss Gradient Approximation Method (2)
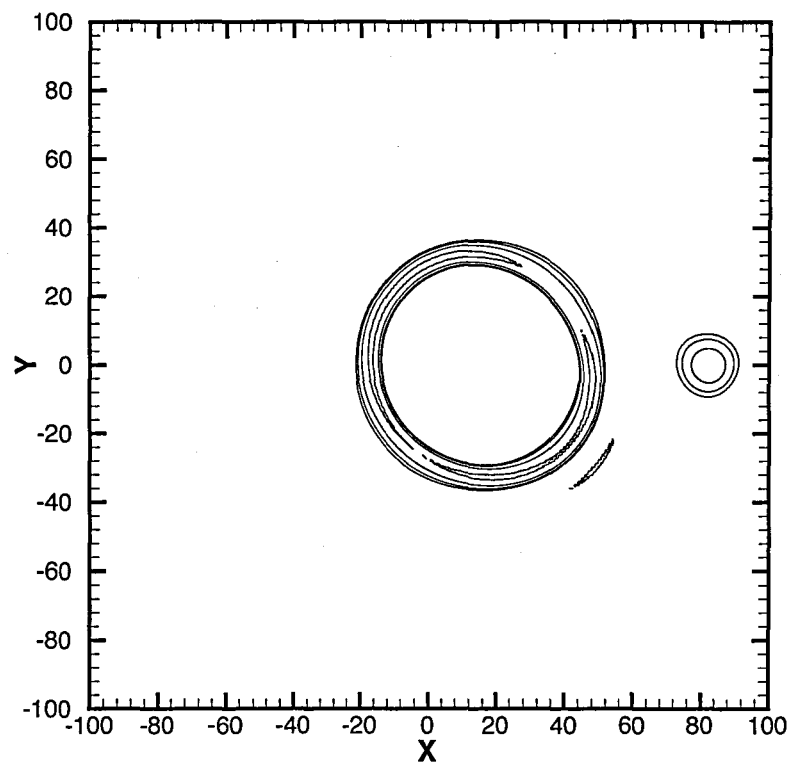
(a) Density Contours at t=30
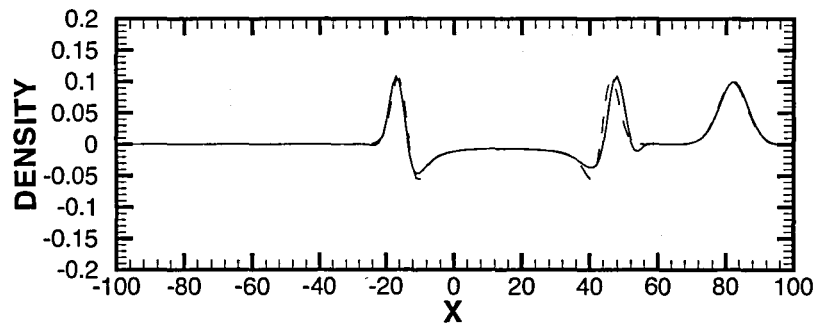
(b) Density Profile Comparison at t=30

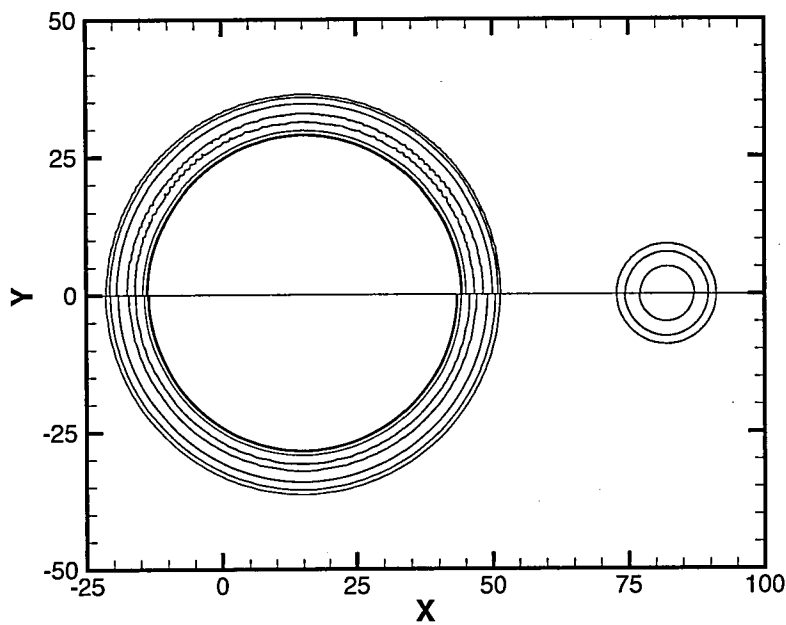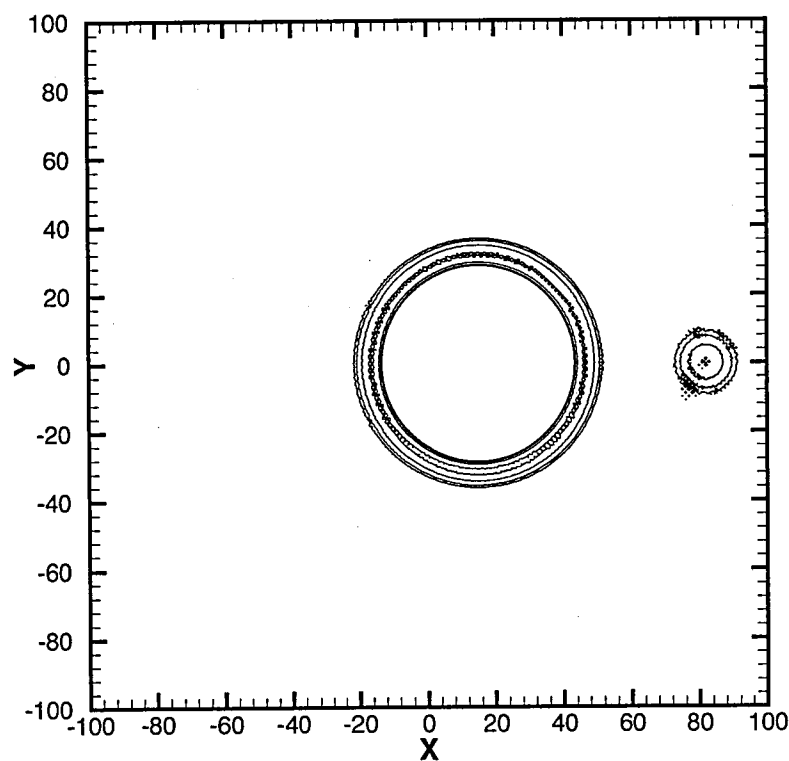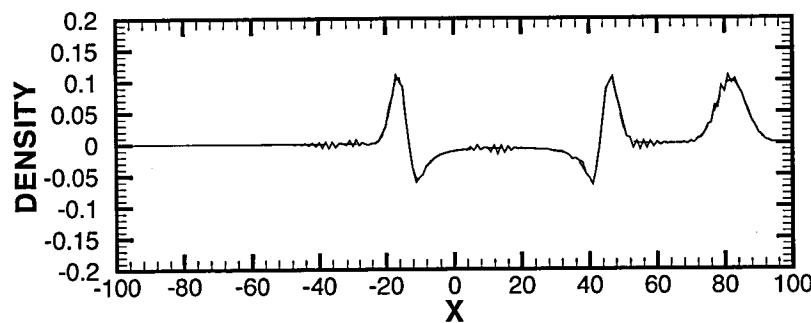Figure B.11: Least Squares Gradient Approximation Method (1)
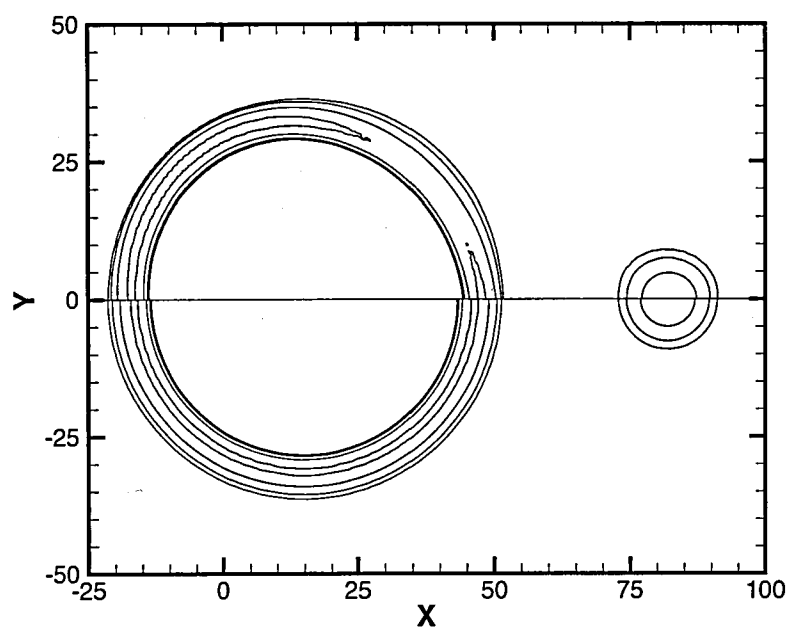
Figure B.12: Least Squares Gradient Approximation Method (2)
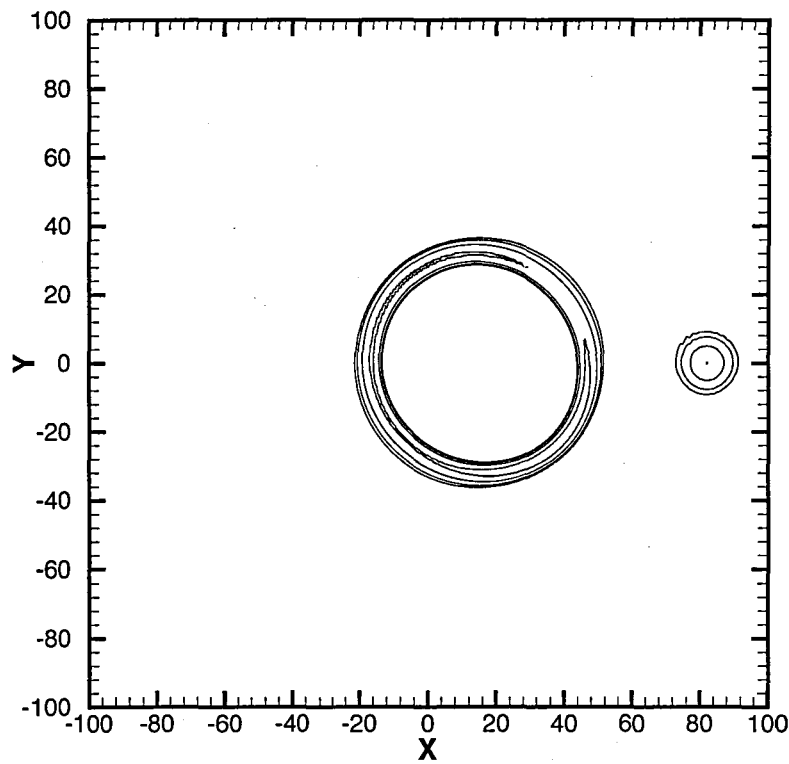
(a) Density Contours at t=30
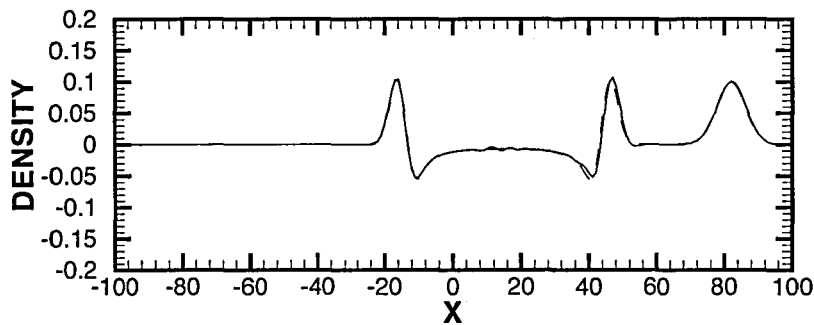
(b) Density Profile Comparison at t=30

Figure B.13: Weighted Least Squares Gradient Approximation Method (1)
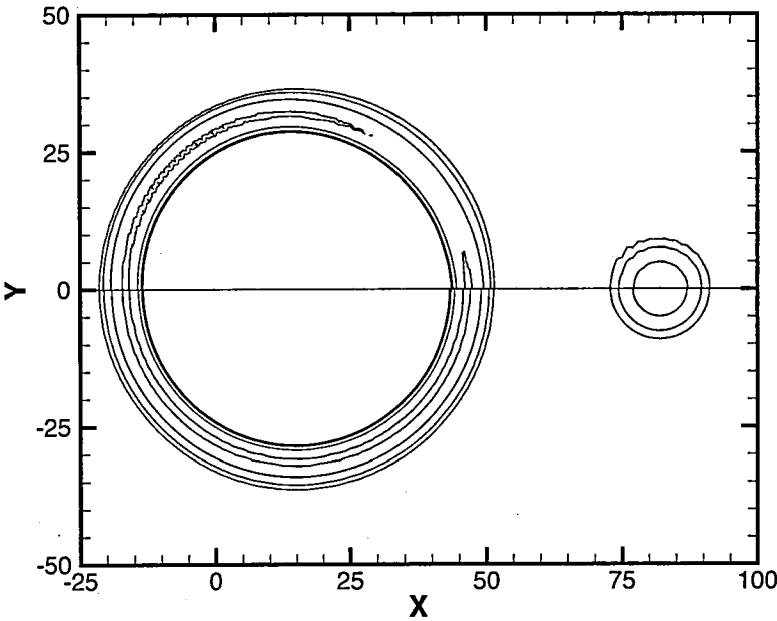
Figure B.14: Weighted Least Squares Gradient Approximation Method (2)

B.3 UK Mesh Test Cases

B.3.1 Single Quadrature Point Test Cases

(a) Density Contours at t=30

(b) Density Profile Comparison at t=30
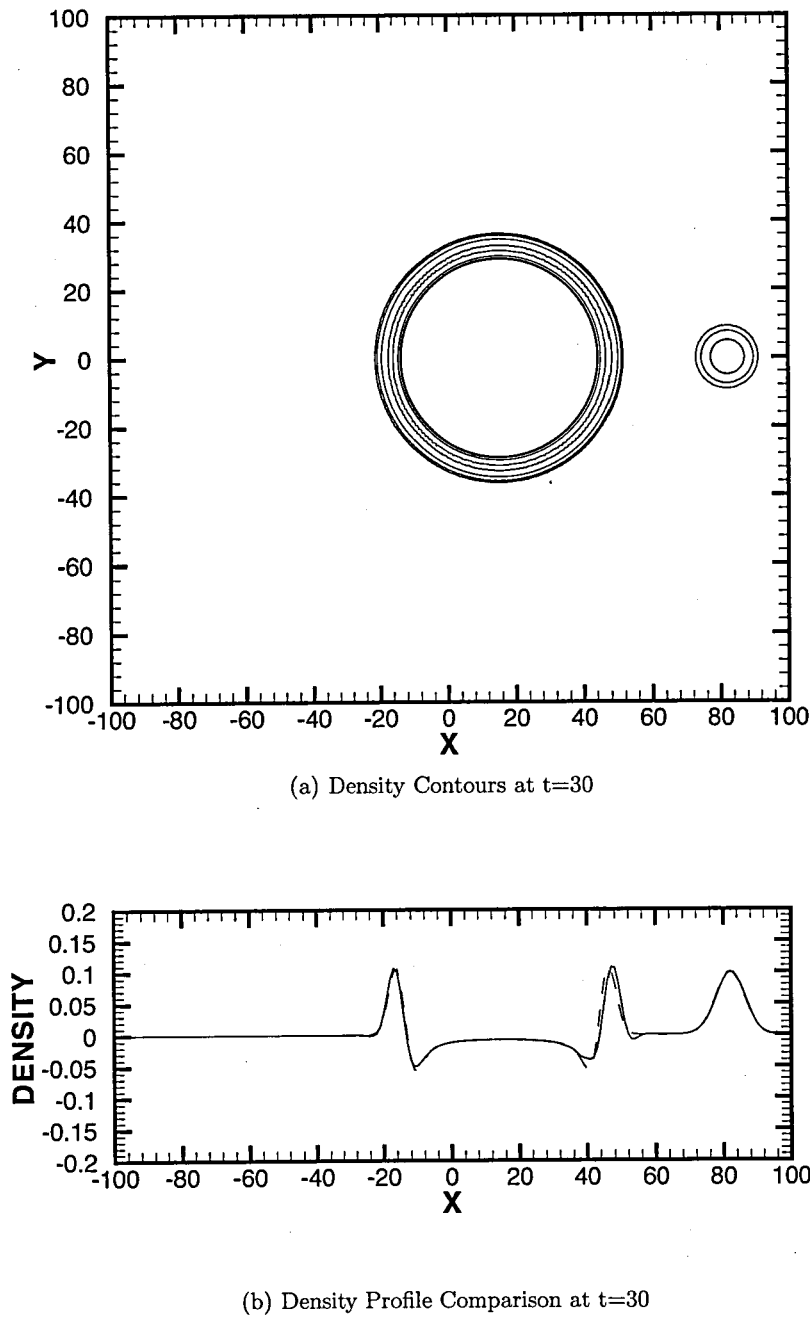
Figure B.15: Green-Gauss Gradient Approximation Method (1)
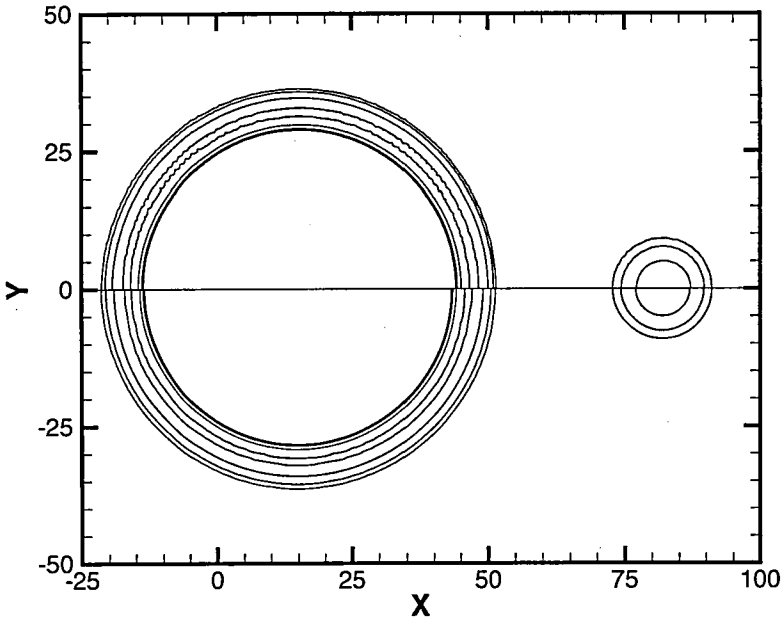
Figure B.16: Green-Gauss Gradient Approximation Method (2)
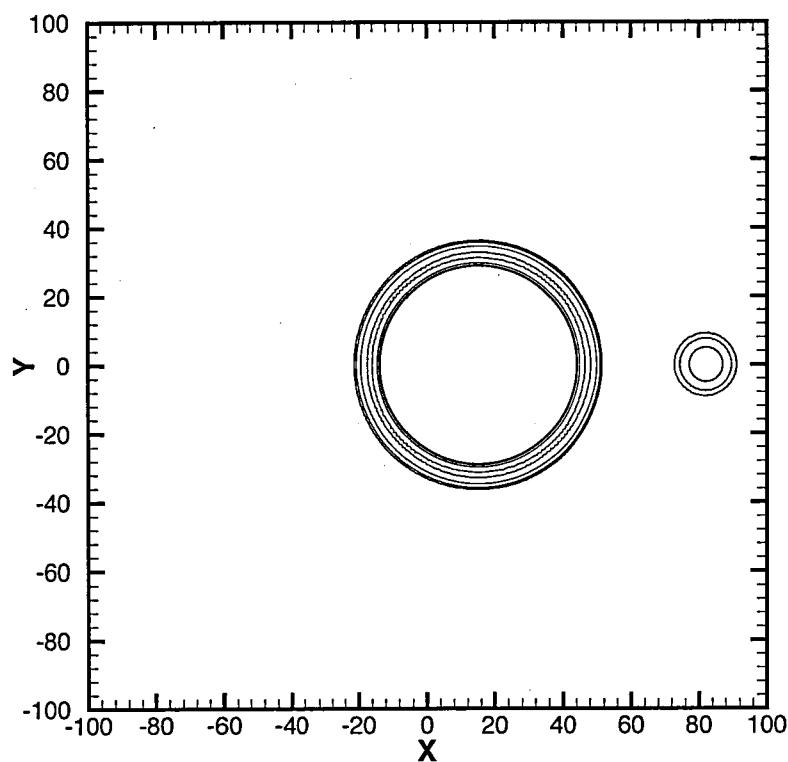
(a) Density Contours at t=30
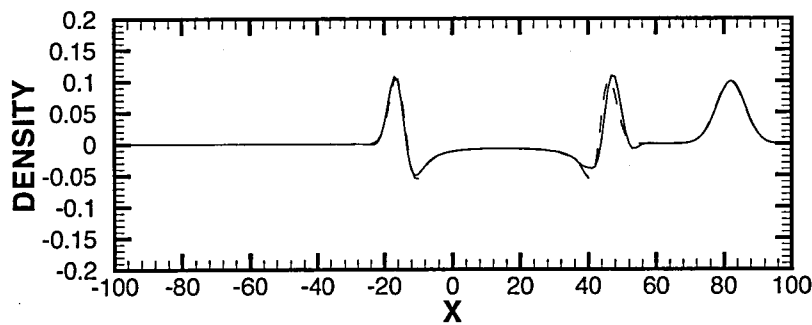
(b) Density Profile Comparison at t=30

Figure B.17: Least Squares Gradient Approximation Method (1)
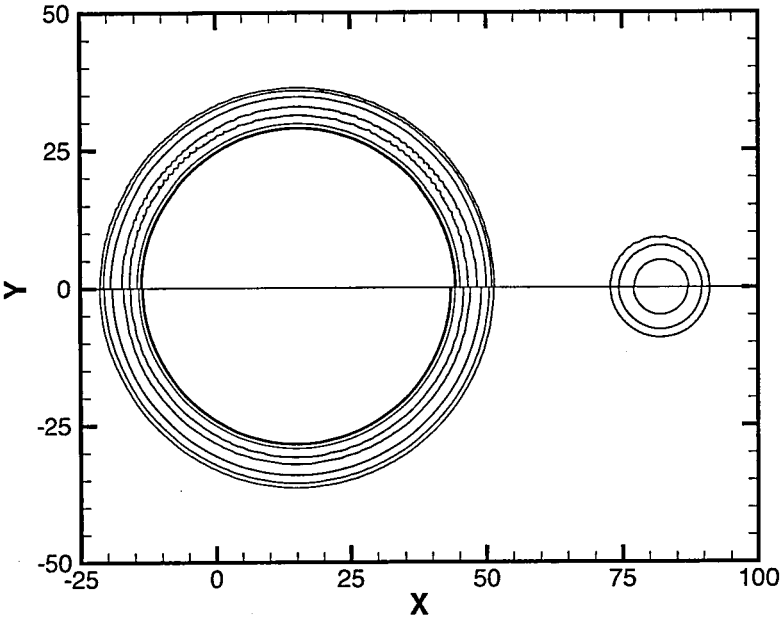
Figure B.18: Least Squares Gradient Approximation Method (2)
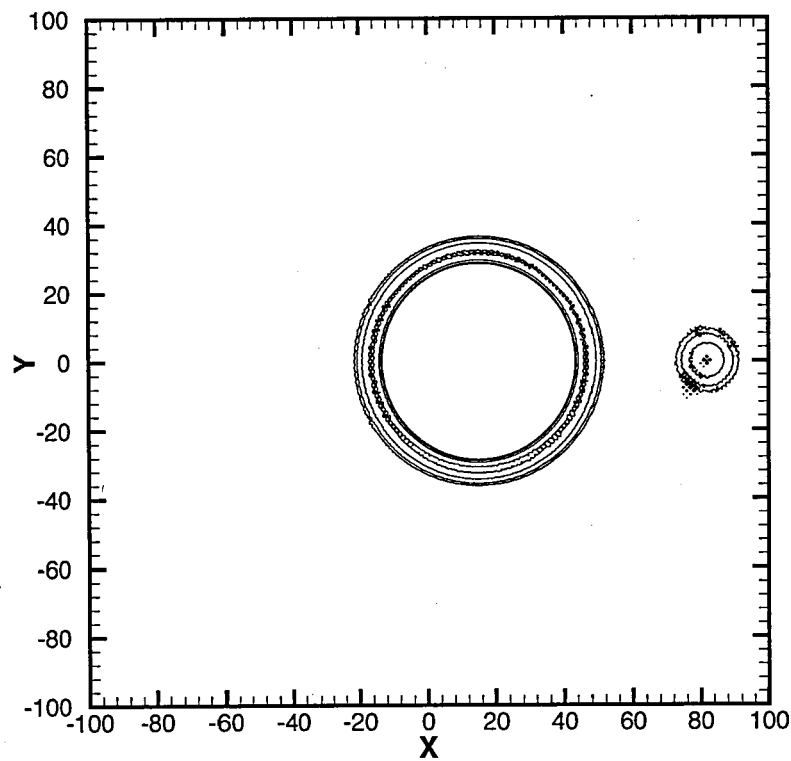
(a) Density Contours at t=30
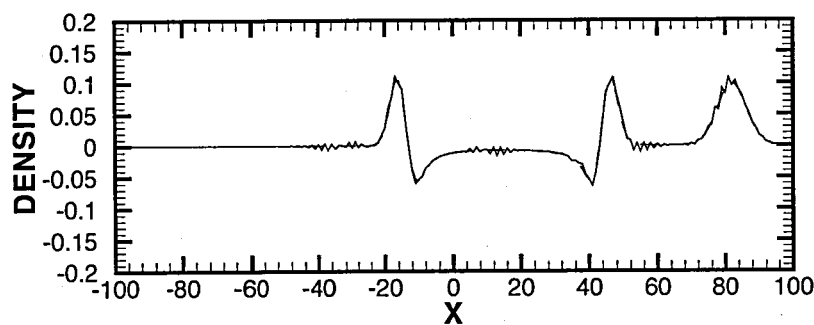
(b) Density Profile Comparison at t=30

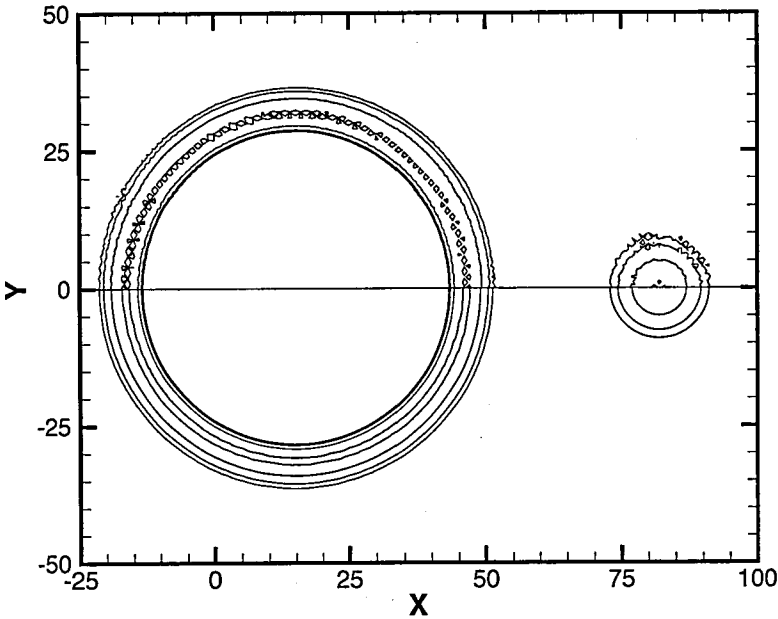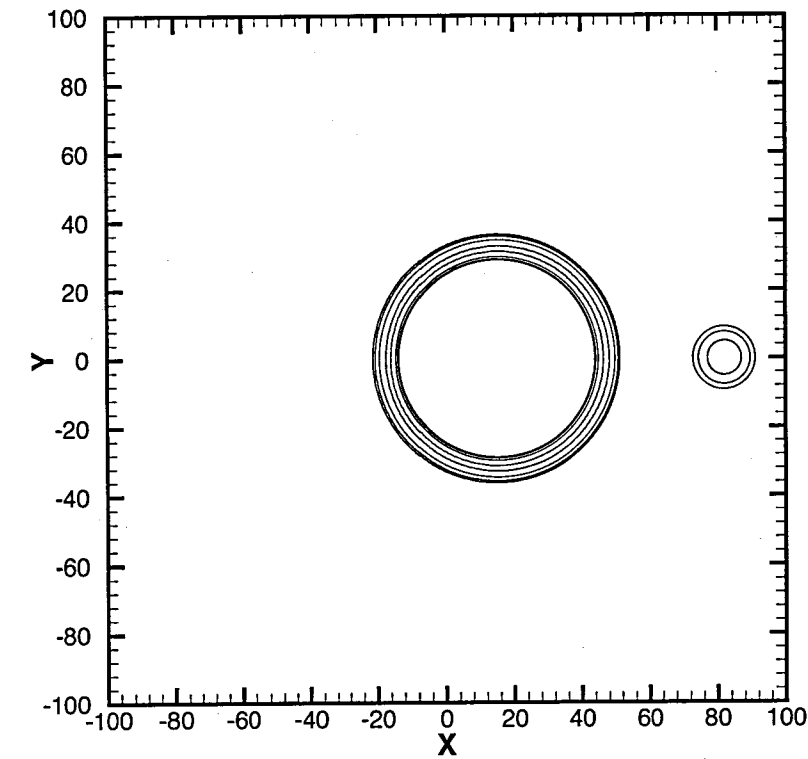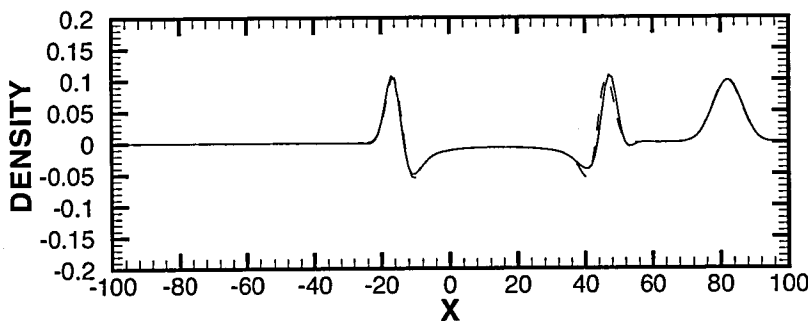Figure B.19: Weighted Least Squares Gradient Approximation Method (1)
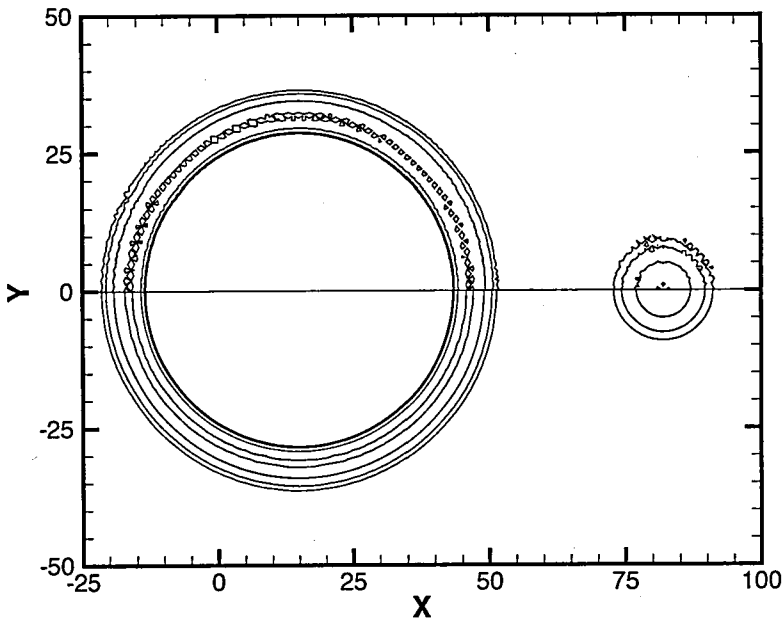
Figure B.20: Weighted Least Squares Gradient Approximation Method (2)

B.3.2   Dual Quadrature Point Test Cases

(a) Density Contours at t=30

(b) Density Profile Comparison at t=30

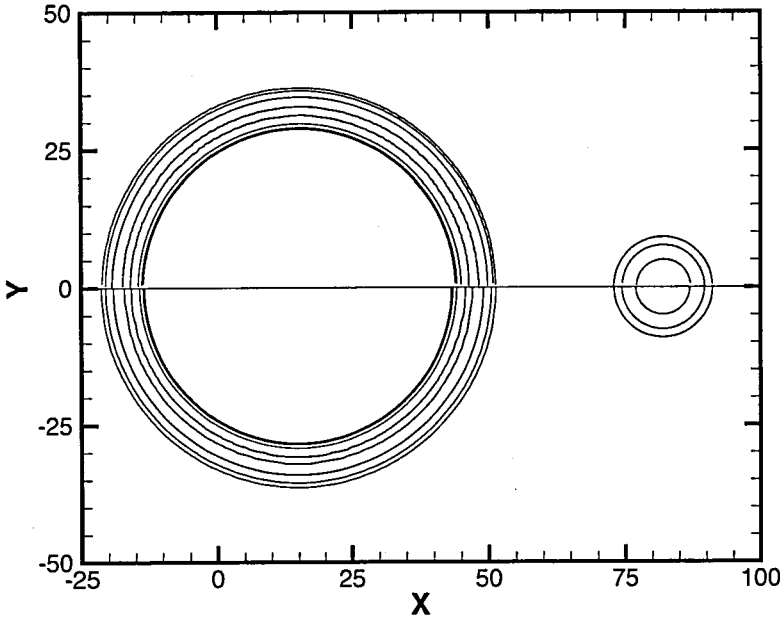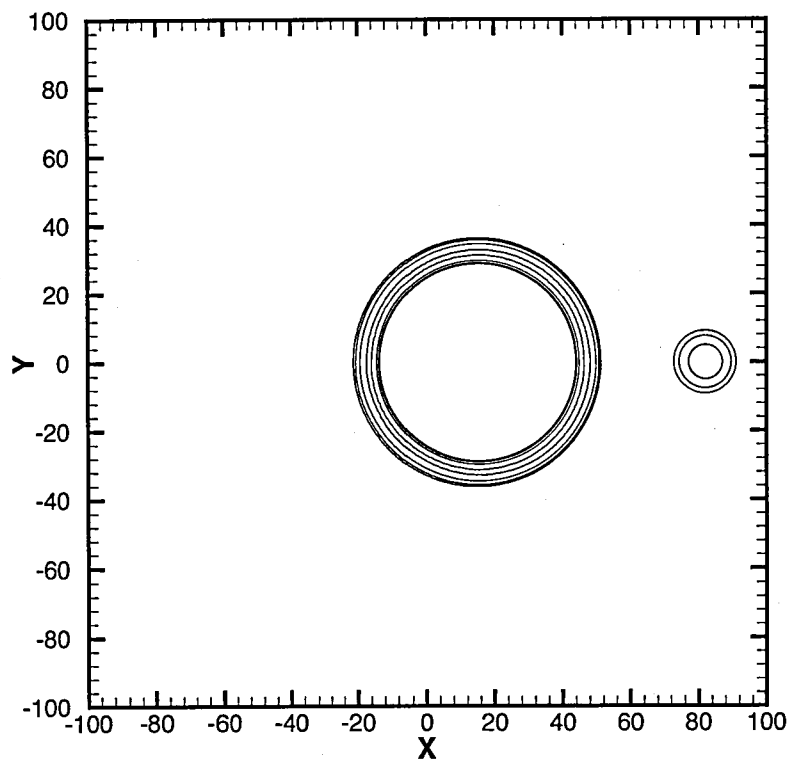Figure B.21: Green-Gauss Gradient Approximation Method (1)

Figure B.22: Green-Gauss Gradient Approximation Method (2)

(a) Density Contours at t=30

(b) Density Profile Comparison at t=30

Figure B.23: Least Squares Gradient Approximation Method (1)

Figure B.24: Least Squares Gradient Approximation Method (2)

(a) Density Contours at t=30

(b) Density Profile Comparison at t=30

Figure B.25: Weighted Least Squares Gradient Approximation Method (1)

Figure B.26: Weighted Least Squares Gradient Approximation Method (2)

B.4 TRI Mesh Test Cases

B.4.1 Single Quadrature Point Test Cases

(a) Density Contours at t=30

(b) Density Profile Comparison at t=30

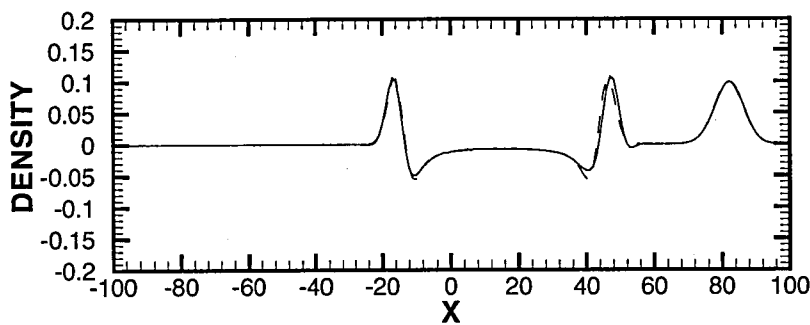Figure B.27: Green-Gauss Gradient Approximation Method (1)

Figure B.28: Green-Gauss Gradient Approximation Method (2)

(a) Density Contours at t=30

(b) Density Profile Comparison at t=30

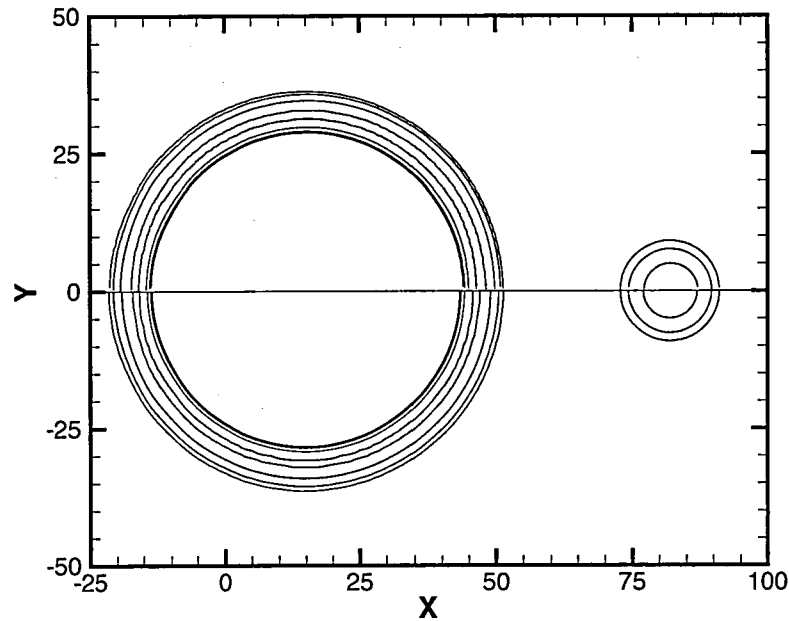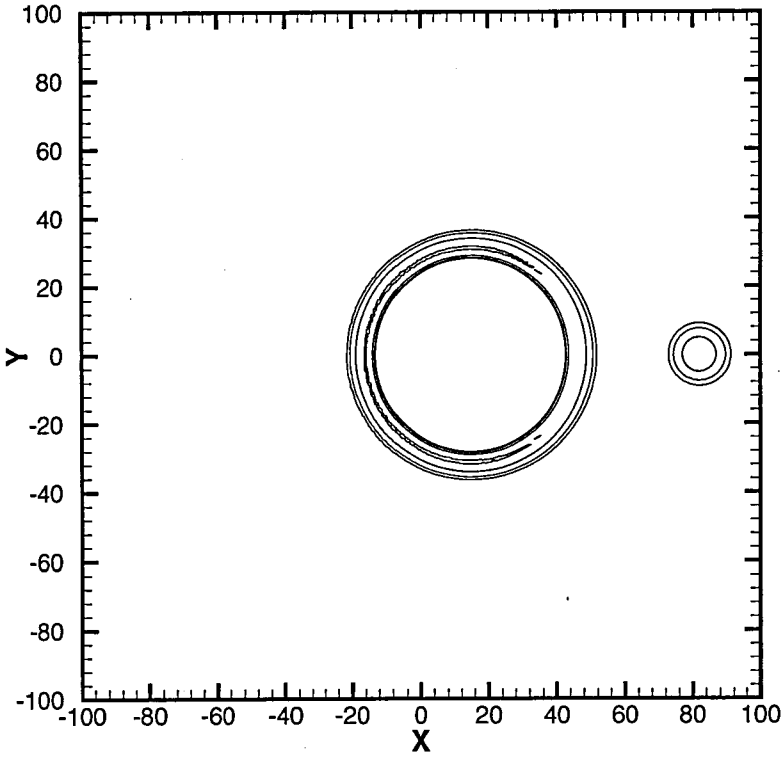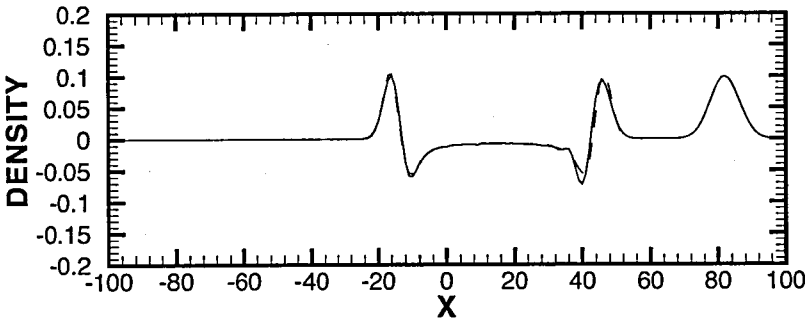Figure B.29: Least Squares Gradient Approximation Method (1)

Figure B.30: Least Squares Gradient Approximation Method (2)

(a) Density Contours at t=30

(b) Density Profile Comparison at t=30

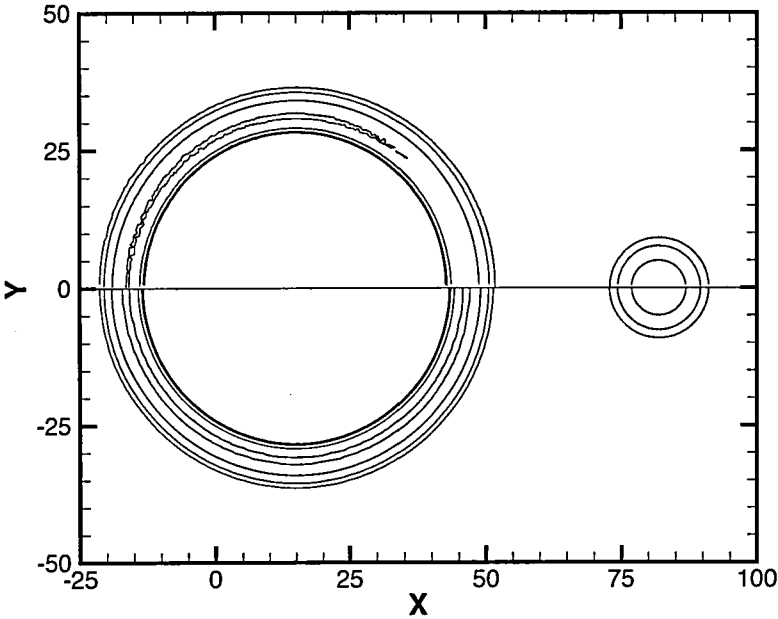Figure B.31: Weighted Least Squares Gradient Approximation Method (1)
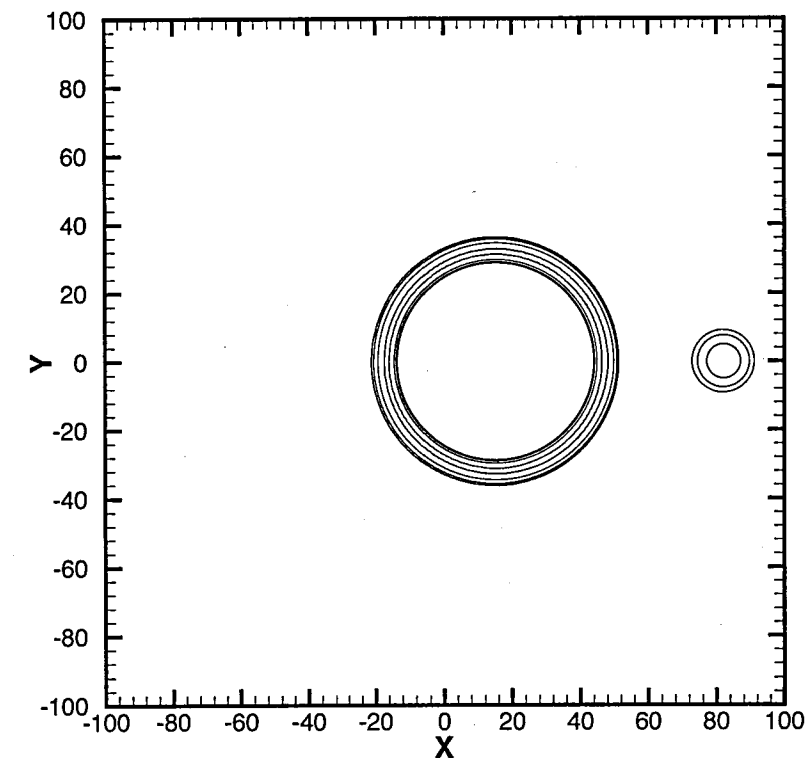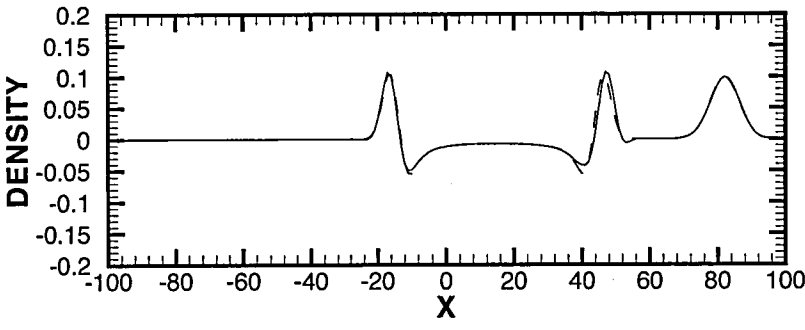
Figure B.32: Weighted Least Squares Gradient Approximation Method (2)

B.4.2 Dual Quadrature Point Test Cases

(a) Density Contours at t=30

(b) Density Profile Comparison at t=30

Figure B.33: Green-Gauss Gradient Approximation Method (1)

Figure B.34: Green-Gauss Gradient Approximation Method (2)

(a) Density Contours at t=30

(b) Density Profile Comparison at t=30

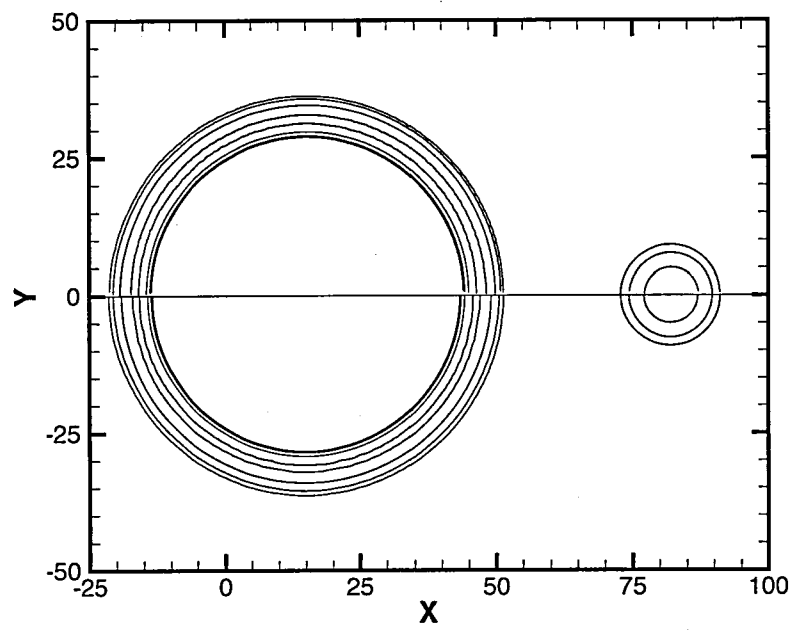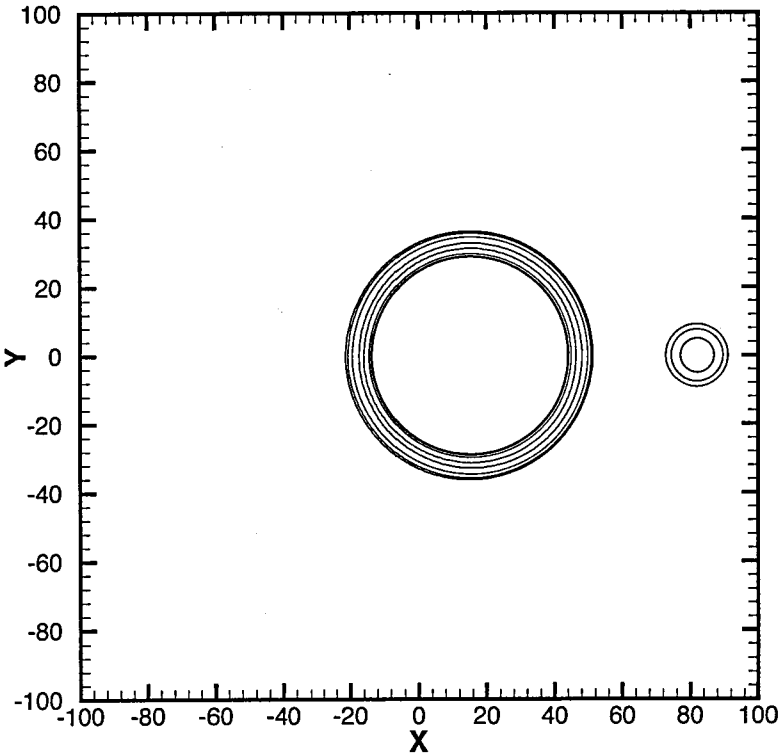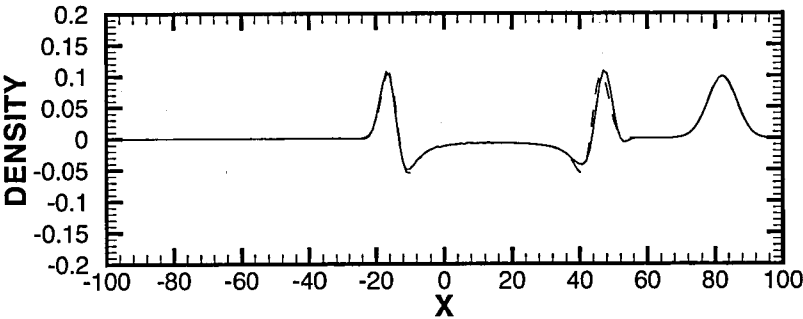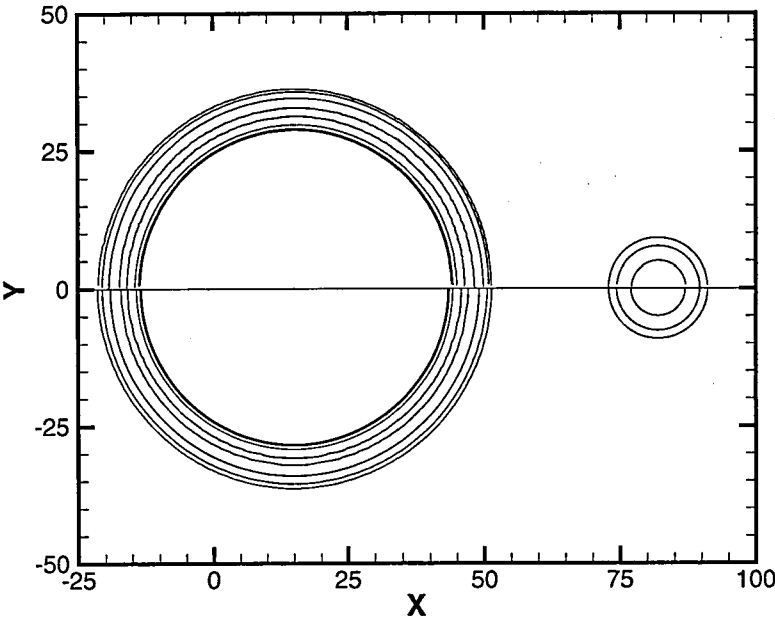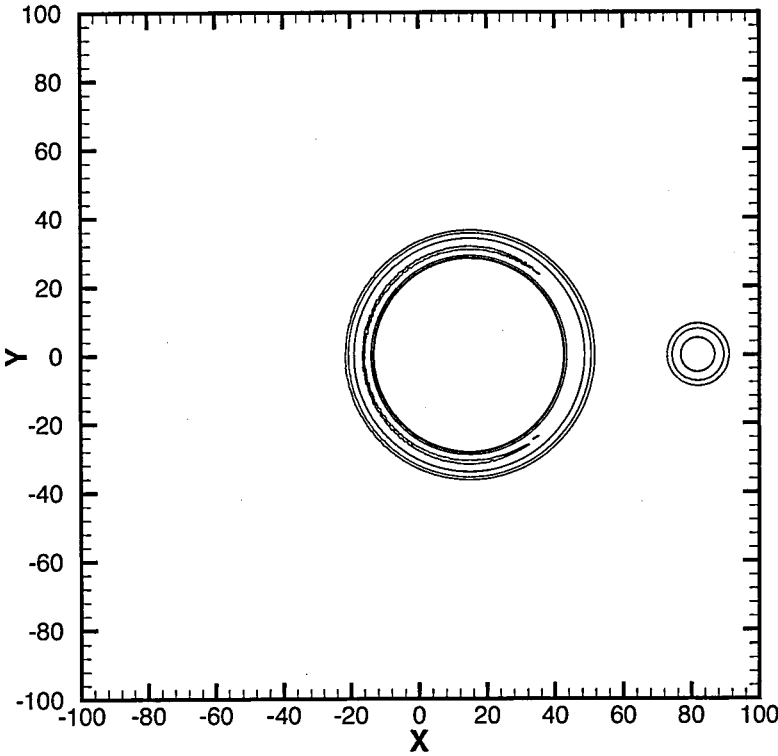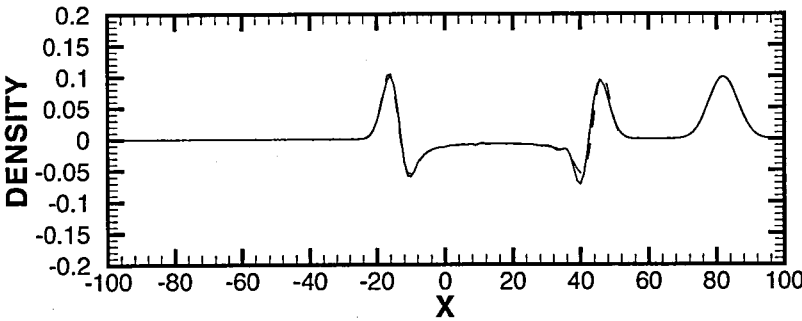Figure B.35: Least Squares Gradient Approximation Method (1)

Figure B.36: Least Squares Gradient Approximation Method (2)

(a) Density Contours at t=30

(b) Density Profile Comparison at t=30

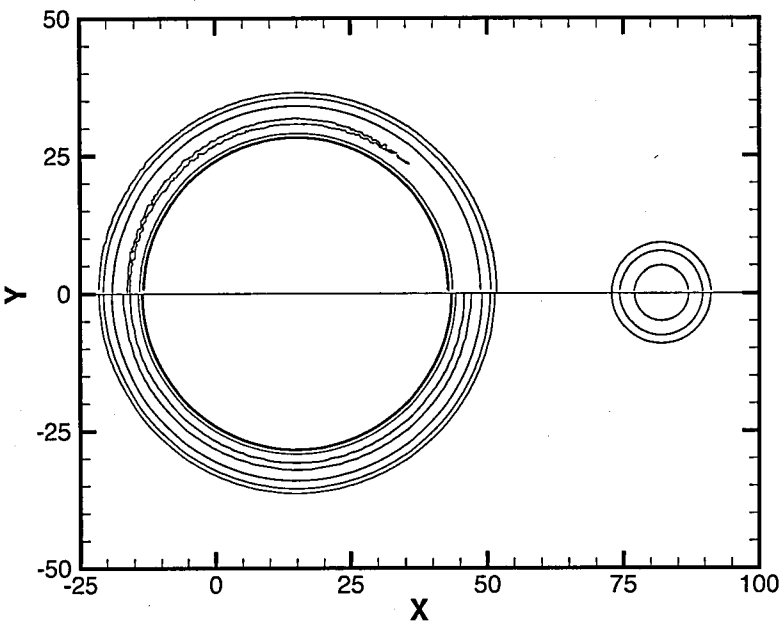Figure B.37: Weighted Least Squares Gradient Approximation Method (1)

Figure B.38: Weighted Least Squares Gradient Approximation Method (2)

Bibliography

[1] European Aviation Safety Agency. *Safer Skies for European Citizens*. [Brochure], Cologne, Germany, December 2004.

[2] J.D. Anderson. *Computational Fluid Dynamics: The Basics with Applications*. McGraw-Hill, Inc., 1995.

[3] W.K. Anderson and D.L. Bonhaus. Airfoil design on unstructured grids for turbulent flows. *AIAA Journal*, 37(2):185–191, February 1999.

[4] H. L. Atkins. Application of essentially nonoscillatory methods to aeroacoustic flow problems. In J.C. Hardin, J.R. Ristorcelli, and C.K.W. Tam, editors, *ICASE/LaRC Workshop on Benchmark Problems in Computational Aeroacoustics (CAA)*, pages 15–26. NASA, May 1995. NASA/CP-3300.

[5] H.L. Atkins. Application of the discontinuous galerkin method to acoustic scatter problems. In C.K.W. Tam and J.C. Hardin, editors, *Second Computational Aeroacoustics (CAA) Workshop on Benchmark Problems*, pages 45–56. NASA, June 1997. NASA CP-3352.

[6] H.L. Atkins. Continued development of the discontinuous galerkin method for computational aeroacoustic applications, AIAA Paper 97-1581, 1997.

[7] H.L. Atkins and D.P. Lockard. A high-order method using unstructured grids for the aeroacoustic analysis of realistic aircraft configurations, AIAA Paper 99-1945, 1999.

[8] H.L. Atkins and C.W. Shu. Qaudrature-free implementation of the discontinuous galerkin method for hyperbolic equations, AIAA Paper 96-1683, 1996.

[9] T.J. Barth and D.C. Jespersen. The design and application of upwind schemes on unstructured meshes, AIAA Paper 89-0366, 1989.

[10] O. Baysal, D.K. Kaushik, and M. Idres. Low-dispersion scheme for nonlinear acoustic waves in nonuniform mean flow, AIAA Paper 97-1582, 1997. 3rd AIAA/CEAS Aeroacoustics Conference.

[11] J.P. Berenger. A perfectly matched layer for the absorption of electromagnetic waves. *Journal of Computational Physics*, 114:185–200, 1994.

[12] M. Bernacki, L. Fezoui, S. Lanteri, and S. Piperno. Parallel discontinuous galerkin unstructured mesh solvers for the calculation of three-dimensional wave propagation problems. *Applied Mathematical Modelling*, 30(8):744–763, 2006.

[13] P.J. Bismuti and D.A. Kopriva. Solution of acoustic scattering problems by a staggered-grid spectral domain decomposition method. In C.K.W. Tam and J.C. Hardin, editors, *Second Computational Aeroacoustics (CAA) Workshop on Benchmark Problems*, pages 69–78. NASA, June 1997. NASA CP-3352.

[14] C. Cheong and S. Lee. Grid-optimized dispersion-relation-preserving schemes on general geometries for computational aeroacoustics. *Journal of Computational Physics*, 174:248–276, 2001.

[15] C. Chung and P.J. Morris. Wave propagation and scattering in computational aeroacoustics. In J.C. Hardin, J.R. Ristorcelli, and C.K.W. Tam, editors, *ICASE/LaRC Workshop on Benchmark Problems in Computational Aeroacoustics (CAA)*, pages 225–232. NASA, May 1995. NASA/CP-3300.

[16] C. Chung and P.J. Morris. Acoustic scattering from two- and three-dimensional bodies. *Journal of Computational Acoustics*, 6(3):357–375, 1998.

[17] T. Colonius and S.K. Lele. Computational aeroacoustics: Progress on nonlinear problems of sound generation. *Progress In Aerospace Sciences*, 40:345–416, 2004.

[18] A. Crivellini and F. Bassi. A three-dimensional parallel discontinuous galerkin solver for acoustic propagation studies. *International Journal of Aeroacoustics*, 2(2):157–174, 2003.

[19] N.A. Cumpsty. *Compressor Aerodynamics*. Longman Group UK Ltd., 1999.

[20] M. D. Dahl. *Third Computational Aeroacoustics (CAA) Workshop on Benchmark Problems*. NASA, August 2000. NASA/CP-2000-209790.

[21] M. D. Dahl. *Fourth Computational Aeroacoustics (CAA) Workshop on Benchmark Problems*. NASA, September 2004. NASA/CP-2004-212954.

[22] G. Djambazov, C.-H. Lai, and K. Pericleous. Development of numerical techniques for near-field aeroacoustic computations. *International Journal for Numerical Methods in Fluids*, 29(6):719–731, 1999.

[23] T. Dong. Industrial applications of caa. In M. D. Dahl, editor, *Third Computational Aeroacoustics (CAA) Workshop on Benchmark Problems*, pages 457–461. NASA, August 2000. NASA/CP-2000-209790.

[24] NASA Facts. Making future commercial aircraft quieter. Technical Report FS-1999-07-003-GRC, NASA Glenn Research Center, July 1999.

[25] Great Britain, Department for Transport. *The Future of Air Transport*. White Paper, London: Stationery Office, December 2003.

[26] Great Britain, Department for Transport. *Transport Statistics Great Britain: 2006 Edition*. National Statistics, London: Stationery Office, November 2006.

[27] K.-Y. Fung. Development of compact wave solvers, AIAA Paper 97-1583, 1997. 3rd AIAA/CEAS Aeroacoustics Conference.

[28] K.-Y. Fung, R.S.O. Man, and S. Davis. An implicit high-order compact algorithm for computational acoustics. *AIAA Journal*, 34(10):2029–2037, October 1996.

[29] K.Y. Fung. Development of compact wave solvers and applications. In C.K.W. Tam and J.C. Hardin, editors, *Second Computational Aeroacoustics (CAA) Workshop on Benchmark Problems*, pages 85–91. NASA, June 1997. NASA CP-3352.

[30] K.Y. Fung, R. S. O. Man, and S. Davis. A compact solution to computational acoustics. In J.C. Hardin, J.R. Ristorcelli, and C.K.W. Tam, editors, *ICASE/LaRC Workshop on Benchmark Problems in Computational Aeroacoustics (CAA)*, pages 59–72. NASA, May 1995. NASA/CP-3300.

[31] P. R. Gliebe. Computational aeroacoustics workshop industry panel discussion. In M. D. Dahl, editor, *Third Computational Aeroacoustics (CAA) Workshop on Benchmark Problems*, pages 425–427. NASA, August 2000. NASA/CP-2000-209790.

[32] G.H. Golub and C.F. Van Loan. *Matrix Computation*. John Hopkins University Press, second edition, 1989.

[33] J.C. Hardin, J.R. Ristorcelli, and C.K.W. Tam. *ICASE/LaRC Workshop on Benchmark Problems in Computational Aeroacoustics (CAA)*. NASA, May 1995. NASA CP-3300.

[34] A.C. Haselbacher. *A Grid-Transparent Numerical Method for Compressible Viscous Flows on Mixed Unstructured Grids*. PhD thesis, Loughborough University, 1999.

[35] M.E. Hayder, G. Erlebacher, and M.Y. Hussaini. Computations of acoustic scattering off a circular cylinder. In C.K.W. Tam and J.C. Hardin, editors, *Second Computational Aeroacoustics (CAA) Workshop on Benchmark Problems*, pages 93–100. NASA, June 1997. NASA CP-3352.

[36] M.E. Hayder, F.Q. Hu, and M.Y. Hussaini. Towards perfectly absorbing boundary conditions for euler equations, AIAA Paper 97-9075, 1997. 13th AIAA CFD Conference.

[37] R. Hixon. Prefactored small-stencil compact schemes. *Journal of Computational Physics*, 165:522–541, 2000.

[38] R. Hixon, S.-H. Shih, and R.R. Mankbadi. Application of an optimized maccormack-type scheme to acoustic scattering problems. In C.K.W. Tam and J.C. Hardin, editors, *Second Computational Aeroacoustics (CAA) Workshop on Benchmark Problems*, pages 101–110. NASA, June 1997. NASA CP-3352.

[39] M.Y. Hsi and F. Périé. Computational aeroacoustics for prediction of acoustic scattering. In C.K.W. Tam and J.C. Hardin, editors, *Second Computational Aeroacoustics (CAA) Workshop on Benchmark Problems*, pages 111–117. NASA, June 1997. NASA CP-3352.

[40] F.Q. Hu. On perfectly matched layer as an absorbing boundary condition, AIAA Paper 96-1664, 1996. 2nd AIAA/CEAS Aeroacoustics Conference.

[41] F.Q. Hu. On constructing stable perfectly matched layers as an absorbing boundary condition for euler equations, AIAA Paper 2002-0227, 2002.

[42] F.Q. Hu and H.L. Atkins. Eigensolution analysis of the discontinuous galerkin method with non-uniform grids, AIAA Paper 2001-2195, 2001.

[43] F.Q. Hu and H.L. Atkins. Two-dimensional wave analysis of the discontinuous galerkin method with non-uniform grids and boundary conditions, AIAA Paper 2002-2514, 2002.

[44] F.Q. Hu, M.Y. Hussaini, and J. Manthey. Low-dissipation and -dispersion runge-kutta schemes for computational acoustics. *Journal of Computational Physics*, 124:177–191, 1996.

[45] J.W. Kim and D.J. Lee. Adaptive nonlinear artificial dissipation model for computational aeroacoustics. *AIAA Journal*, 39(5):810–818, May 2001.

[46] J.W. Kim and D.J. Lee. Generalized characteristic boundary conditions for computational acoustics, part 2. *AIAA Journal*, 42(1):47–55, January 2004.

[47] W.H. Lin. Least-squares legendre spectral element solutions to sound propagation problems. *Journal of the Acoustical Society of America*, 109(2):465–474, February 2001.

[48] W.H. Lin and D.C. Chan. Least-squares spectral element solutions to the caa workshop benchmark problems. In C.K.W. Tam and J.C. Hardin, editors, *Second Computational Aeroacoustics (CAA) Workshop on Benchmark Problems*, pages 165–177. NASA, June 1997. NASA CP-3352.

[49] W. K. Lord. An industry view of caa. In M. D. Dahl, editor, *Third Computational Aeroacoustics (CAA) Workshop on Benchmark Problems*, pages 439–443. NASA, August 2000. NASA/CP-2000-209790.

[50] P.J. Morris, L.N. Long, A. Bangalore, and Q. Wang. A parallel three-dimensional computational aeroacoustics method using nonlinear disturbance equations. *Journal of Computational Physics*, 133:56–74, 1997.

[51] D.M. Nark. The use of staggered schemes and an absorbing buffer zone for computational aeroacoustics. In J.C. Hardin, J.R. Ristorcelli, and C.K.W. Tam, editors, *ICASE/LaRC Workshop on Benchmark Problems in Computational Aeroacoustics (CAA)*, pages 233–244. NASA, May 1995. NASA/CP-3300.

[52] D.M. Nark. A computational aeroacoustics approach to duct acoustics. In C.K.W. Tam and J.C. Hardin, editors, *Second Computational Aeroacoustics (CAA) Workshop on Benchmark Problems*, pages 259–268. NASA, June 1997. NASA CP-3352.

[53] Great Britain, Civil Aviation Authority, Directorate of Airspace Policy. *Aircraft Noise*. Environmental Information Sheet - Number 12, February 2006.

[54] U.S. Department of Transportation, Bureau of Transportation Statistics. *U.S. International Travel and Transportation Trends*. BTS02-03, Washington, D.C., 2002.

[55] U.S. Department of Transportation, Bureau of Transportation Statistics. *2005 Total Airline System Passenger Traffic Up 4.6 Percent From 2004.* BTS20-06, Washington, D.C., 2006.

[56] International Civil Aviation Organization. *Memorandum on ICAO.* [Brochure], Montréal, Canada, 2006.

[57] W.H. Press. *Numerical Recipes in Fortran 77: The Art of Scientific Computing.* Cambridge University Press, second edition, 2001.

[58] Y.B. Radvogin and N.A. Zaitsev. Adequate boundary conditions for unsteady aeroacoustic problems. In C.K.W. Tam and J.C. Hardin, editors, *Second Computational Aeroacoustics (CAA) Workshop on Benchmark Problems*, pages 179–189. NASA, June 1997. NASA CP-3352.

[59] N. N. Reddy. Industry panel presentations and discussions. In J.C. Hardin, J.R. Ristorcelli, and C.K.W. Tam, editors, *ICASE/LaRC Workshop on Benchmark Problems in Computational Aeroacoustics (CAA)*, pages 377–387. NASA, May 1995. NASA CP-3300.

[60] N. N. Reddy. Industry panel presentations and discussions. In C.K.W. Tam and J.C. Hardin, editors, *Second Computational Aeroacoustics (CAA) Workshop on Benchmark Problems*, pages 377–380. NASA, June 1997. NASA CP-3352.

[61] Rolls-Royce. *The Jet Engine.* Rolls-Royce PLC, Derby, fifth edition, 1996.

[62] C.K.W. Tam. Computational aeroacoustics: Issues and methods. *AIAA Journal*, 33(10):1788–1796, October 1995.

[63] C.K.W. Tam and Z. Dong. Solid wall boundary conditions for computational aeroacoustics. *Computational Aero- and Hydro-Acoustics*, 147:63–70, 1993.

[64] C.K.W. Tam and J.C. Hardin. *Second Computational Aeroacoustics (CAA) Workshop on Benchmark Problems.* NASA, June 1997. NASA CP-3352.

[65] C.K.W. Tam, K.A. Kurbatskii, and J. Fang. Numerical boundary conditions for computational aeroacoustics benchmark problems. In C.K.W. Tam and J.C. Hardin, editors, *Second Computational Aeroacoustics (CAA) Workshop on Benchmark Problems*, pages 191–219. NASA, June 1997. NASA CP-3352.

[66] C.K.W. Tam and H. Shen. Direct computation of nonlinear acoustic pulses using high order finite difference schemes, AIAA Paper 93-4325, 1993. 15th AIAA Aeroacoustics Conference.

[67] C.K.W. Tam, H. Shen, K.A. Kurbatskii, L. Auriault, Z. Dong, and J.C. Webb. Solutions of the benchmark problems by the dispersion-relation-preserving scheme. In J.C. Hardin, J.R. Ristorcelli, and C.K.W. Tam, editors, *ICASE/LaRC Workshop on Benchmark Problems in Computational Aeroacoustics (CAA)*, pages 149–171. NASA, May 1995. NASA/CP-3300.

[68] C.K.W. Tam and J.C. Webb. Dispersion-relation-preserving finite difference schemes for computational acoustics. *Journal of Computational Physics*, 107:262–281, 1993.

[69] I.H. Tristanto. *A Mesh Transparent Numerical Method for Large-Eddy Simulation of Compressible Turbulent Flows*. PhD thesis, Loughborough University, 2004.

[70] K. Viswanathan and M. C. Joshi. Use of computational methods for noise/vibration problems. In M. D. Dahl, editor, *Third Computational Aeroacoustics (CAA) Workshop on Benchmark Problems*, pages 445–450. NASA, August 2000. NASA/CP-2000-209790.

[71] Z.J. Wang. Evaluation of high-order spectrral volume method for benchmark computational aeroacoustic problems. *AIAA Journal*, 43(2):337–348, February 2005.

[72] D. S. Weir. Relevance of caa to regional and business aircraft engine design. In M. D. Dahl, editor, *Third Computational Aeroacoustics (CAA) Workshop on Benchmark Problems*, pages 433–437. NASA, August 2000. NASA/CP-2000-209790.

[73] M. Zhuang and R. Chen. Applications of the optimized upwind dispersion-relation-preserving schemes for multi-dimensional acoustic problems, AIAA Paper 98-2367, 1998. 4th AIAA/CEAS Aeroacoustics Conference.

[74] D. Zingg and H. Lomax. Finite-difference schemes on regular triangular grids. *Journal of Computational Physics*, 108(2):306–313, 1993.